ADVANCED PHOTONICS

Theme Issue on

Photonics with Thin Film Lithium Niobate

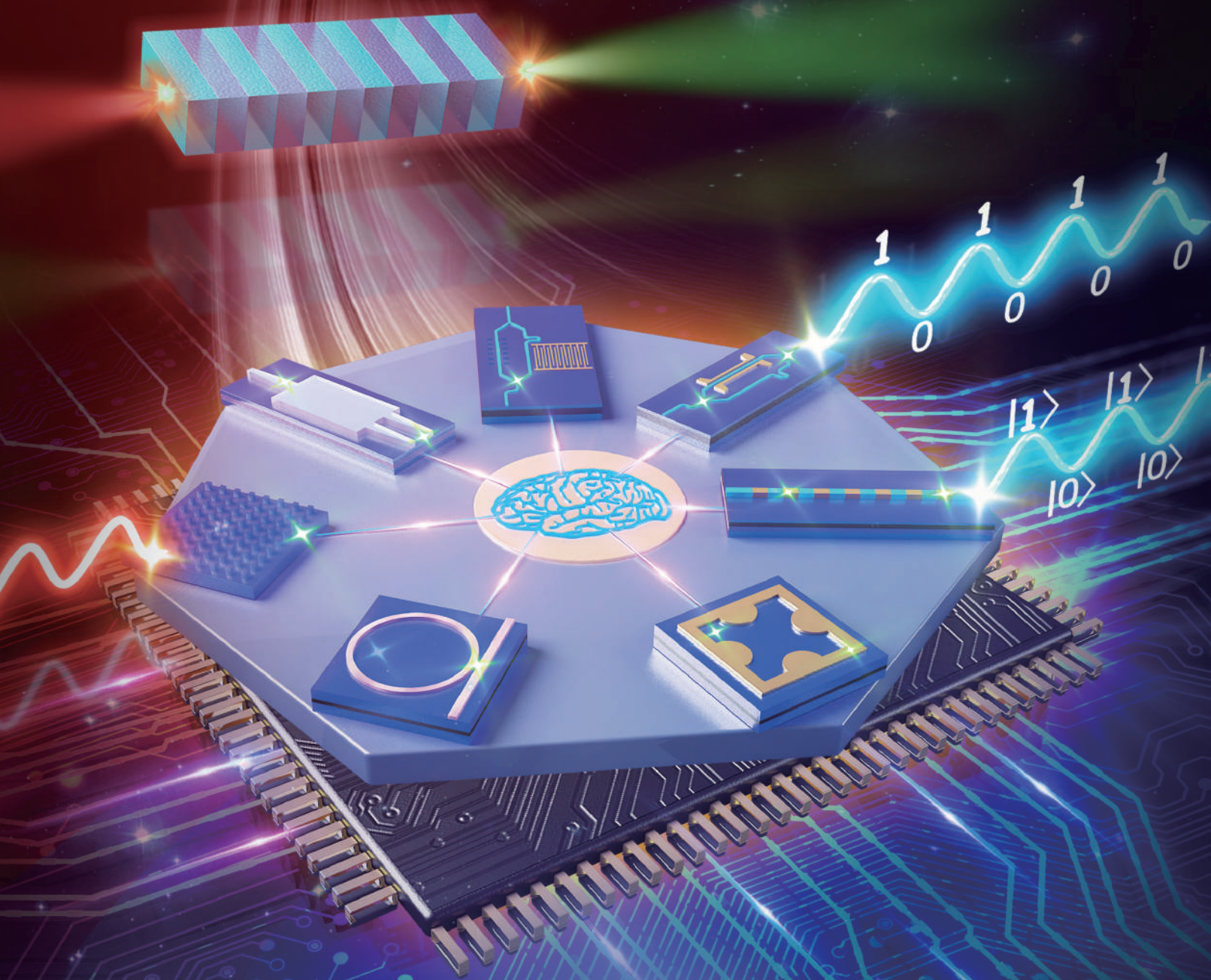

CHINESE LASER PRESS 中国激光杂志社 | SPIE.

CONTENTS

ADVANCED PHOTONICS

Photonics with Thin Film Lithium Niobate

On the cover — The image illustrates a roadmap of the development of lithium niobate photonics, from the typical bulk lithium niobate photonics to the newly developed thin-film lithium niobate photonics, as well as various functional devices.

Photonics with Thin Film Lithium Niobate

Siyuan Yu
Sun Yat-sen University, Department of Electronics and Information Engineering, Guangzhou, China

Siyuan Yu, Sun Yat-sen University

Thin film lithium niobate (TFLN) has the potential to revolutionize photonic integrated circuit (PIC) technology, due to its ability to combine low optical loss, tight optical confinement, and active optical functions. In particular, the readily available electro-optic effect and 2nd order nonlinear effect afford more unique functionalities to TFLN compared to other, more mature, PIC materials, including silicon (Si), silicon nitride (SiN_x), silicon dioxide (SiO_2) and indium phosphide (InP), while the refractive index contrast between TFLN waveguide and typical cladding materials such as SiO_2 is sufficiently large to support relatively tight bending, leading to small component sizes.

Over the past few years, research on TFLN-based PICs has blossomed. TFLN electro-optic modulators in particular have benefitted hugely from the natural advantage of its electro-optic effect and are now being commercialized, with several start-up companies worldwide already publicizing small-size, low-drive voltage prototypes. The research attention is now moving on to other, more challenging aspects of TFLN technology. These include on-chip laser sources and devices based on its nonlinear optical effects. In addition to the classical optical information applications including communications and sensing, TFLN PICs exploiting high quality on-chip laser sources and nonlinear devices are also promising candidates for integrated quantum photonics.

To spotlight advances in TFLN technology, we present a special collection published across *Advanced Photonics* and its sister journal *Advanced Photonics Nexus*. This collection includes two review articles and two original research articles. We feature a wide-ranging review article which we hope may help those new to the field to attain a comprehensive overview of photonics based on TFLN (https://doi.org/10.1117/1.AP.4.3.034003). We also feature a review article focused on the nonlinear photonics in TFLN to enable an in-depth inspection of this research area (https://doi.org/10.1117/1.AP.4.3.034001). The two research articles, one combining the generation of very narrow linewidth laser emission with tunability provided by the electro-optic effect (https://doi.org/10.1117/1.AP.4.3.036001) and the other on the generation of optical frequency combs exploiting nonlinear effects (https://doi.org/10.1117/1.APN.1.1.016001), represent distinctive progress in light sources based on TFLN.

We hope our readers enjoy these articles and find them useful. For greater insight and enrichment, we also offer an interview with TFLN innovator and pioneer Marko Lončar (https://doi.org/10.1117/1.AP.4.3.030503) and a perspective by Zhenda Xie and Shining Zhu (https://doi.org/10.1117/1.AP.4.3.030502).

$LiNbO_3$ crystals: from bulk to film

Zhenda Xie[a,b,c,*] **and Shining Zhu**[a,b,c,*]

[a]Nanjing University, College of Engineering and Applied Sciences, School of Physics, School of Electric Science and Engineering, National Laboratory of Solid State Microstructures, Nanjing, China

[b]Nanjing University, Ministry of Education, Key Laboratory of Intelligent Optical Sensing and Manipulation, Nanjing, China

[c]Collaborative Innovation Center of Advanced Microstructures, Nanjing, China

Lithium niobate[1,2] is a ferroelectric crystal that features superior electro-optical, nonlinear optical, and acoustic optical performance, and it is thus prominent in various optoelectronic applications. Recent breakthroughs in the fabrication of thin film lithium niobate (TFLN) combine the unique features of the bulk crystal onto an integrated platform with submicron light confinement, driving new records in reducing the energy consumption for high-speed electro-optical modulation,[3–5] the footprint for acoustic wave filtering,[6] and the power requirement for efficient optical frequency conversion.[7–9] TFLN is mainly fabricated using the smart cut technique,[10,11] which was developed for silicon-on-insulator materials[12] and is known for its capability for manufacturing high-quality, large-sized crystalline wafer. Revolutionary performances are expected by moving from bulk to TFLN, e.g., in the form of lithium-niobate-on-insulator (LNOI) optical communication and wireless communication devices, and this trend may also lead to fundamental breakthroughs in optical computation, microwave photonics, and quantum optics, as discussed below.

Lithium-niobate-based electro-optical modulators (EOMs) have been the choice of long-distance optical communication for decades. However, their relatively large size and high cost make them only applicable for the backbone connections. LNOI EOM, however, is capable of the same high modulation speed and CMOS-compatible low drive voltage in a much smaller package. Power consumption as low as 0.37 fj/bit has been demonstrated.[3] These performances make the LNOI EOM not only a direct alternate to the bulk lithium niobate EOM, but also a promising candidate for optical links in/between data centers and local area networks at the data rates of 200-800 Gbps and above, therefore driving the next generation optical communication technology. It is worth noting that laser sources and amplifiers have been demonstrated using rare-earth-ion-doped LNOI chips,[13] which may enable a fully integrated optical communication module. Hybridization with laser-active materials or silicon is another attractive approach towards full integration that adds a light source or driving electronics capabilities.[14] Such hybrid integration can also enable simultaneous signal processing and memory operations, leading toward artificial intelligence applications.[15]

Optical computation may change the power-hungry nature of modern electronic computation technology, in both classical[16] and quantum approaches,[17] by demonstration of computation speed acceleration and quantum supremacy. In either approach, larger scale photonic circuitry is required, with phase sensitive optical paths as the interaction mechanism. The low loss nature of lithium niobate qualifies LNOI for such large-scale photonic integration, achieving a level of 2.7 dB per meter in different demonstrations.[18,19] A further crucial challenge for optical computation is circuit reconfigurability, and LNOI is the only mature material to combine fast and accurate phase control using electro-optical modulation, acoustic-optical modulation, or thermal-optical modulation.

Microwave photonics has been a long-chased dream to bring optical accuracy and bandwidth into microwave technology. Photonic integration is key to push complex microwave photonics systems, including high-bandwidth electro-optic modulators, low-noise frequency synthesizers, and chip signal processors, into practice.[20] The LNOI platform contains the most powerful toolbox, including the EOM and dispersive Kerr soliton (DKS) frequency combs.[21] Self-referencing is necessary to further stabilize DKS comb. With high nonlinear coefficients in both $\chi^{(2)}$ and $\chi^{(3)}$, octave-spanning supercontinuum generation[22] and efficient frequency doubling[9] have been reported separately using LNOI, and self-referencing can be expected combining these processes on the same chip. The only missing parts are the photodetector and control electronics in the on-chip signal processing, and their integration relies on the hybrid integration technology.

Domain engineered bulk lithium niobate crystal, also known as optical superlattice,[23] has been a great success for nonclassical light generation and photon state manipulation, for quantum optics research. However, photonic integration is the key to the practical application of quantum information technology. Compared to other photonics integration platforms, LNOI features high nonlinearity in $\chi^{(2)}$ and fast EOM for photon state modulation. Ultrabright photon pair generation has been reported in both straight waveguide and micro-resonator using LNOI to achieve revolutionary photon generation rates of 2.79×10^{11} Hz/mW[24] and 2.7 MHz/μW,[25] respectively. Together with the low-loss waveguide and other passive devices, larger scale on-chip photon state manipulation can be expected.

On one hand, the above important advances may be seen as incremental steps toward practical application of quantum information technology that are expected directly from the high nonlinearity of LNOI. On the other hand, the practical application of quantum information relies on sources of the deterministic multiqubit state, which is the multiphoton state in photonics quantum systems. While such a problem is yet to be resolved, a theoretical study shows that LNOI may be the only candidate for such deterministic multiphoton state generation considering the material limitations.[26] Deterministic nonlinear interaction is possible at single photon level, and the required quality factor is on the order of 10^7 to 10^8 for domain engineered micro-ring resonators, within the reach of existing fabrication limits.[26]

In summary, from bulk devices to chips, LNOI technology has shown its capability to push the performance of optoelectronic devices to new heights, for electro-optical modulation and acoustic wave filtering functions in next-generation optical and wireless communications. In conjunction with hybrid integration, LNOI can also be an enabling technology for optical computation, microwave photonics, and quantum information, with large-scale photonic integration, high optical reconfigurability, and strong nonlinear interaction at the single photon level. To make these happen, large-size low-defect TFLN wafer and high-performance device fabrication techniques are key areas of future research.

*Address all correspondence to Zhenda Xie xiezhenda@nju.edu.cn; Shining Zhu zhusn@nju.edu.cn

References

1. J. Sun et al., "Brief review of lithium niobate crystal and its applications," *J. Synth. Cryst.* **49**(6), 947–964 (2020).
2. B. Gao et al., "Long-lived lithium niobate: history and progress," *J. Synth. Cryst.* **50**(7), 1183–1199 (2021).
3. C. Wang et al., "Integrated lithium niobate electro-optic modulators operating at CMOS-compatible voltages," *Nature* **562**(7725), 101–104 (2018).
4. M. He et al., "High-performance hybrid silicon and lithium niobate Mach–Zehnder modulators for 100 Gbit s-1 and beyond," *Nat. Photonics* **13**(5), 359–364 (2019).
5. M. Li et al., "Lithium niobate photonic-crystal electro-optic modulator," *Nat. Commun.* **11**, 4123 (2020).
6. L. Shao et al., "Microwave-to-optical conversion using lithium niobate thin-film acoustic resonators," *Optica* **6**(12), 1498–1505 (2019).
7. C. Wang et al., "Ultrahigh-efficiency wavelength conversion in nanophotonic periodically poled lithium niobate waveguides," *Optica* **5**(11), 1438–1441 (2018).
8. J.-Y. Chen et al., "Ultra-efficient frequency conversion in quasi-phase-matched lithium niobate microrings," *Optica* **6**(9), 1244 (2019).
9. Y. Niu et al., "Optimizing the efficiency of a periodically poled LNOI waveguide using in situ monitoring of the ferroelectric domains," *Appl. Phys. Lett.* **116**(10), 101104 (2020).
10. G. Poberaj et al., "Lithium niobate on insulator (LNOI) for micro-photonic devices," *Laser Photonics Rev.* **6**(4), 488–503 (2012).
11. Y. Jia, L. Wang, and F. Chen, "Ion-cut lithium niobate on insulator technology: recent advances and perspectives," *Appl. Phys. Rev.* **8**(1), 011307 (2021).
12. A. E. Lim et al., "Review of silicon photonics foundry efforts," *IEEE J. Sel. Top. Quantum Electron.* **20**(4), 405–416 (2014).
13. S. Dutta et al., "Integrated photonic platform for rare-earth ions in thin film lithium niobate," *Nano Lett.* **20**(1), 741–747 (2020).
14. D. Zhu et al., "Integrated photonics on thin-film lithium niobate," *Adv. Opt. Photon.* **13**(2), 242–352 (2021).
15. L. Tong et al., "2D materials–based homogeneous transistor-memory architecture for neuromorphic hardware," *Science* **373**(6561), 1353–1358 (2021).
16. Y. Shen et al., "Deep learning with coherent nanophotonic circuits," *Nature Photonics* **11**(7), 441–446 (2017).
17. H.-S. Zhong et al., "Quantum computational advantage using photons," *Science* **370**(6523), 1460–1463 (2020).
18. M. Zhang et al., "Monolithic ultra-high-Q lithium niobate microring resonator," *Optica* **4**(12), 1536–1537 (2017).
19. J. Zhou et al., "Electro-optically switchable optical true delay lines of meter-scale lengths fabricated on lithium niobate on insulator using photolithography assisted chemo-mechanical etching," *Chin. Phys. Lett.* **37**(8), 084201 (2020).
20. D. Marpaung, J. Yao, and J. Capmany, "Integrated microwave photonics," *Nat. Photonics* **13**(2), 80–90 (2019).
21. Y. He et al., "Self-starting bi-chromatic $LiNbO_3$ soliton microcomb," *Optica* **6**(9), 1138 (2019).
22. M. Jankowski et al., "Ultrabroadband nonlinear optics in nanophotonic periodically poled lithium niobate waveguides," *Optica* **7**(1), 40–46 (2020).
23. S. Zhu, Y. Zhu, and N. Ming, "Quasi-phase-matched third-harmonic generation in a quasi-periodic optical superlattice," *Science* **278**(5339), 843–846 (1997).
24. G.-T. Xue et al., "Ultrabright multiplexed energy-time-entangled photon generation from lithium niobate on insulator chip," *Phys. Rev. Appl.* **15**(6), 064059 (2021).
25. Z. Ma et al., "Ultrabright quantum photon sources on chip," *Phys. Rev. Lett.* **125**(26), 263602 (2020).
26. H.-Y. Liu et al., "A scheme for deterministic N-photon state generation using lithium niobate on insulator device," https://doi.org/10.48550/arXiv.2205.14956 (2022).

New opportunities with an old optical material: an interview with Professor Marko Lončar

Guoqing Chang
Chinese Academy of Sciences, Institute of Physics, Shanghai, China

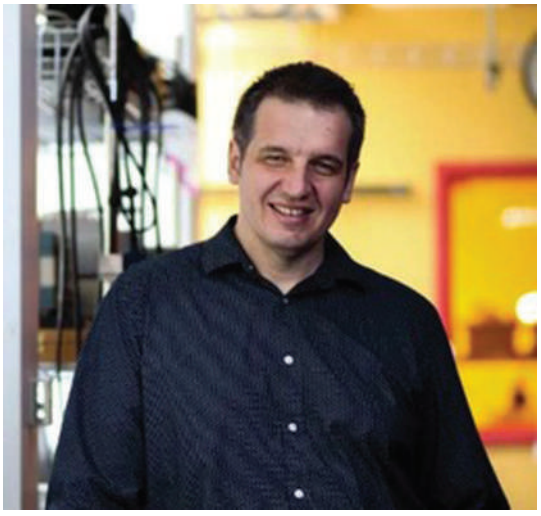

Marko Lončar, Tiantsai Lin Professor of Electrical Engineering at Harvard's John A. Paulson School of Engineering and Applied Sciences (SEAS).

Guoqing Chang spoke with Marko Lončar of Harvard University about his innovative work in thin film lithium niobate.

Chang: How did you become interested in researching nanoscale optics?
Lončar: I obtained my bachelor's degree in electrical engineering from University of Belgrade in 1997 and the same year I went to Caltech to pursue my PhD. I initially wanted to conduct research in power electronics. However, after meeting friends who were taking quantum and photonics-related courses I was intrigued… These courses sounded very interesting to me, so at the end of my first year, I switched to the group of Axel Scherer, who was working on nanofabrication and integrated optics. I started working in the field of photonic crystals, first waveguides then nanolasers, and finally nanocavities for sensing and quantum electrodynamics applications.

Chang: Thank you! Our topic today is lithium niobate. It's an old optical material, in use for more than 50 years. Recently, you started to work on thin-film lithium niobate (TFLN). How did you start to work on this material?
Lončar: When I was studying at Caltech, I attended my first CLEO conference in 2000. There, I saw a talk by Rick Osgood's group at Columbia University, focused on making thin lithium niobate films—they were slicing bulk LN crystals into slabs and doing fun stuff with it. A few years later, when I was a postdoc with Federico Capasso at Harvard, I reached out to Rick and he was kind to send me some of their LN material. I was curious to see if I can etch this material and make devices in it. Then, as well as now, my interest has been in developing nanostructuring strategies for materials that have unique optical properties but are hard to fabricate devices in. And lithium niobate certainly satisfies both of these criteria: it is a very important electro-optic material, but also a very hard material to etch!

I have to say that my initial efforts largely failed… I was able to make some photonic crystals using focused ion beam milling but devices never really worked properly. Still, integrated lithium niobate photonics was an important part of my research proposal as I was applying for faculty positions in 2005/06, and I was determined to continue research in this direction. Several years later, I learned about a new company in China—NanoLN—that was commercializing thin film LN. I believe they were emailing everybody trying to sell their wafers, but most people ignored them at the time, it seems. My student Cheng Wang (now a professor at City University of Hong Kong) happened to be going back to China for summer vacation that year, and I asked him to visit NanoLN to see if they were "legit."

Cheng visited the company and was impressed! They were indeed making a series of products related to thin-film crystals. At that time, we decided to purchase a few TFLN wafers. But procuring wafers was only half of the job. The biggest challenge was to develop nanostructuring techniques for TFLN that can make ultra low-loss devices. Cheng worked for 2-3 years in Harvard's clean room, exploring the processing methods, and trying to figure out the fabrication recipes. (I have to give credit to Harvard's Center for Nanoscale Systems that is very open to new materials and processes, unlike more traditional shared clean rooms.) Cheng was later joined by my former postdoc Mian Zhang (now CEO of HyperLight corporation) and together they were able to figure the fab recipe that can result in ultra-low loss TFLN photonic devices. The rest is history 😊

Chang: What are the advantages of TFLN over bulk LN?
Lončar: TFLN has many advantages, in my opinion. The main advantage, which was our original motivation, is to reduce the driving voltage for modulators. In bulk LN, waveguides are made by either proton exchange or doping to locally change the refractive index. This results in a very low index contrast between the core and the cladding. It's a similar situation to what you'd have in an optical fiber, for example. Since the index contrast is very small, the mode is very large. Thus, if you're making a modulator, you need to put the electrodes very far away from the waveguide core, which means that when you want to change the refractive via electro-optic effect, you need to apply a large voltage to get an appreciable electric field.

The benefit of TFLN is that you can make tightly confined waveguides using etching—similar approach that is used in e.g. silicon photonics. This allows us to place electrodes closer to the waveguide thus allowing the same electric field to be achieved using much smaller voltage. This is an old and simple idea, but the main challenge was to figure out an etching process that results in a very low loss waveguide. During this process, we also realized that the bandwidth of the modulator could be very large, because matching between phase velocity of applied

electrical signal and group velocity of light can be matched by adjusting the thickness of oxide layer underneath LN device layer. Interestingly, this approach has been used for bulk LN modulators as well, however the oxide layer is placed between the electrodes and the LN waveguide. Thus, in the conventional LN modulators there is a trade-off between the modulation efficiency/operating voltage and operating bandwidth, but TFLN eliminates this trade-off. In fact, TFLN allows you to have extremely high bandwidth and low operating voltage, while ensuring low loss and better transmission efficiency.

Chang: Many researchers are also keen on silicon-based photonic modulation devices. Compared with silicon-based devices, what are the advantages of TFLN platform?
Lončar: In my opinion, lithium niobate is a much better material than silicon for photonics. It has an intrinsic electro-optic effect that allows you to apply an electric field to change the refractive index, which is essential for modulators and many other devices. Silicon doesn't have an electro-optic effect, and you need to inject or deplete carriers in order to use carrier dispersion to control the refractive index. But carrier dispersion comes with a drawback: free-carrier absorption. So that's one issue.

Another merit is that TFLN can handle a lot of power and has less transmission loss for light. Its wider bandgap makes it less susceptible to multiphoton absorption effects. Also, it can operate over a wider wavelength range than silicon.

A drawback of lithium niobate, on the other hand, is that it's a photorefractive material. So if you operate it at short wavelengths at high optical powers this can be a problem. We're working on mitigating these issues.

Another drawback is that LN devices are much bigger than silicon ones, for example. While the electro-optic effect is essentially loss-less, it results in the small change of refractive index which means very large devices. By contrast, silicon devices are more compact—but they have the disadvantages of loss, lower-speed transmission, and much less power-handling capability.

Of course, another big advantage for silicon is established fabrication practices. But I would like to think that we have addressed that for lithium niobate to a great extent.

Chang: I see. In your opinion, what are the important devices that can be fabricated based on TFLN?
Lončar: TFLN has a fascinating potential. Broadly, in my group we are working on two or three different areas. One of them is radio frequency (RF)/ microwave/ millimeter wave photonics, of interest for e.g. radar remoting and 5G–6G communications applications, where electrical signals are sent via optical carriers and thus require excellent analog modulators. We need to have very good low-voltage, high-performance, high-linearity modulators—and lithium niobate is really good for that. State-of-the-art microwave photonic systems consist of discrete components, including e.g. lasers, LN modulators, fibers, filters, detectors, and thus suffer from insertion losses of each component which then requires amplifiers, and makes the system more complex and expensive. We are working on integrating all of these components on a TFLN chip to improve the system performance while significantly minimizing its size and cost.

Interestingly, with small modifications our platform can be used to realize state-of-the-art tunable lasers, including ultra-fast ones, as well as broad and stable frequency combs. We are actively working on these, and exploring their applications in precision measurements and optical communications.

TFLN has huge potential in quantum science and technology, and this is another very active area of research in our group. For example, we are making quantum transducers that can interface superconducting qubits with optical photons, as well as multiplexed quantum repeaters that can extend the reach of quantum networks. The latter combines our activities in TFLN and diamond quantum memories.

Chang: Your team recently published an article in *Nature* about on-chip electro-optical frequency shifters and beam splitters. How do they work, and why are they important?
Lončar: The frequency shifter consists of two coupled ring resonators that result in so-called split resonances. Using laser we can excite one of these resonances, for example the longer wavelength one. Then, when we apply RF field with the same frequency as the resonance splitting, we can transfer photons to the shorter wavelength resonance. Importantly, if you control the amount of RF that you're applying, you can move 10%, 50%, or even 99% of light from one resonance to the other. Thus, our device, as my student Yaowen Hu demonstrated, enables frequency domain beam splitting or shifting functionalities, and is a frequency domain analogue of e.g. a tunable directional coupler.

The main interest in this for us was so-called "frequency-domain photonic quantum computing," which is basically a form of linear optical quantum computing, but now in the frequency domain. Usually, people use conventional phase modulators to realize frequency domain beam splitters. These, however, result in many sidebands, beyond those of interest, that then need to be mitigated using additional discrete components (e.g., wave shapers, modulators) which increases the loss and complexity. The frequency domain beam splitting that we have demonstrated overcomes these problems.

Another application that we are considering is control of emission wavelength of lasers used for addressing trapped atoms and color centers in diamond, for example. Conventional approaches to achieve this rely on single-sideband modulation using IQ modulators or serodyne approach using a phase modulator, and are lossy or require complex microwave sources. Our approach simplifies this and allows for frequency shifting using only single tone microwave signal.

Chang: What do you think are the unique advantages of TFLN in the context of on-chip nonlinear nanophotonics?
Lončar: There are so many interesting things that the community is now working on! The biggest advantage of TFLN is that it combines strong second and third order nonlinearities that can be engineered using periodic poling and dispersion engineering. Combined with TFLN's wide bandwidth this is truly amazing for nonlinear photonics applications that typically require large optical powers. Good examples are stabilized and self-referenced frequency combs.

The ultimate goal of nonlinear optics would be achieving nonlinear response at single-photon level. Beyond scientific curiosity, this would enable realization of photonic quantum computers, for example. Based on theoretical predictions, this could be achieved by increasing the quality factor of TFLN ring resonators by 1 to 2 orders of magnitude and/or by engineering the nonlinearities using periodic poling. Both are hard, but possible. For example, we have recently estimated that the TFLN platform can allow Q factors about 20 to 30 times larger than state-of-the-art TFLN devices (10 million) So that's encouraging but further fabrication improvements are needed.

Chang: Your group recently achieved femtosecond pulse generation via integrated EO time lens. Why is such an on-chip femtosecond laser source so important?
Lončar: Femtosecond sources play a pivotal role in nonlinear optics and other fields of science and technology. My original interest was generating flat comb for communication applications. Maybe the

spectral aspect of this device was more interesting to me at the time than the temporal aspect. My former postdoc, now professor at USC—Mengjie Yu—was the one to suggest that we could integrate all components of the time lens—temporal analogue of the conventional lens—on single TFLN chip. To accomplish this, we start with CW laser and then use the electro-optic amplitude and phase modulation to generate optical pulse, and then we use dispersion-engineered photonic crystals to compress the pulse down to 500 femtosecond. Going forward, we plan to use periodic poling to broaden the spectrum, and integrated detectors and feedback to stabilize the comb. This would provide a stable femtosecond light source that would have many interesting applications in spectroscopy and metrology.

Chang: Integrating lasers on tiny chips is exciting. Your group recently demonstrated a tiny laser with an output power of 60 mW. Can you give us a brief introduction about this work and your plans for the next step?
Lončar: In fact, since that work was published, my student Amirhassan Shams Ansari has improved the process and now we have several devices that can reach more than 100 mW of on-chip power. We are currently working on increasing the laser power, ideally reaching 1 W soon, as well as reducing the laser linewidth to kHz range. In parallel, we have already started using these devices for RF photonics and telecom applications.

Chang: Why do you care about TFLN devices operating in the visible light band?
Lončar: For us, the main driver for developing TFLN for visible wavelength range are quantum applications. For example, quantum memories in diamond, that we have been working on for several years already, emit at 737 nm. However, to be able to use these in quantum networks, the wavelength needs to be shifted to e.g. 1300-nm or 1500-nm wavelength range. That can be accomplished using frequency mixing in TFLN. At the same time, phase modulators and frequency shifters we talked about earlier, but now operating in visible, could be used to overcome inhomogeneous broadening of quantum memories.

Chang: When will TFLN devices move from laboratory to large-scale foundry production?
Lončar: In some sense this is already happening. Good news is that, owing to LN's amazing material properties, fabrication steps involved are much simpler than in the case of Si photonics. Bad news is that Li is considered to be a contaminant for CMOS processing, and thus many large foundries were reluctant to start processing TFLN wafers. However, this has started to change.

Chang: What are the major challenges in the field of TFLN integrated processing?
Lončar: One is to further increase the quality factor of the resonator, that is, reduce the losses. Another one is very-low frequency operation and DC bias drifts for modulators. This has been a problem for conventional modulators as well, but has been successfully addressed. We are working on overcoming this issue in the case of TFLN modulators as well. For nonlinear optics applications, thickness uniformity of currently available wafers can be an issue too. Small thickness variations can significantly affect the phase matching conditions which can be a huge problem. Also, ion slicing process used to create TFLN from congruent bulk LN crystal can be a problem and limiting for ultra-high-performance operation. There have been some activities, however, on MBE (molecular beam epitaxy) to grow very high-quality LN layers.

Chang: What breakthroughs do you expect for this field in the coming 10 years?
Lončar: I am very optimistic about the development of TFLN in 10 years. In fact let me be controversial and say, you can quote me, that within 10 years, TFLN will replace silicon photonics for all high-performance optoelectronic applications, and definitely those in datacom. For example, as reported at OFC by HyperLight and collaborators, transceiver modules with TFLN chips replacing the silicon photonic ones could reduce the power consumption by 20-30%. This is huge! I also predict that TFLN will be the dominant platform for quantum photonics, and will of course continue to dominate microwave photonic applications.

Chang: You mentioned your startup company HyperLight. What's the mission of this company?
Lončar: HyperLight is commercializing TFLN photonic integrated circuits, with particular focus on inter- and intra-data center optical interconnects. At the same time, HyperLight already has customers in telecom, quantum, and microwave photonic space, and will start offering foundry services. The latter will enable broad scientific community to have access to TFLN photonics. I'm proud that even though it's a young startup, HyperLight already has a lot of customers and significant revenues. The latter is not common for early-stage semiconductor-based startups.

Chang: Will it happen that in 10 years from now somewhere in the US will be named Lithium-Niobate Valley?
Lončar: Let's hope! I'm fairly optimistic about this and I would very much like this to be somewhere in the US. However, my feeling is that, unless the US changes attitude towards semiconductor manufacturing, the new Valley will be somewhere in Taiwan or mainland China.

Chang: Thank you for accepting my interview in your busy schedule.
Lončar: It's a pleasure to chat with you. Thank you for giving me the opportunity to share with you my passion for TFLN photonics. Hopefully, your readers will find this informative and even more people will start working with this exciting platform.

Review Article

ADVANCED PHOTONICS

Applications of thin-film lithium niobate in nonlinear integrated photonics

Milad Gholipour Vazimali[a] and Sasan Fathpour[a,b,*]
[a]University of Central Florida, CREOL, College of Optics and Photonics, Orlando, Florida, United States
[b]University of Central Florida, Department of Electrical and Computer Engineering, Orlando, Florida, United States

Abstract. Photonics on thin-film lithium niobate (TFLN) has emerged as one of the most pursued disciplines within integrated optics. Ultracompact and low-loss optical waveguides and related devices on this modern material platform have rejuvenated the traditional and commercial applications of lithium niobate for optical modulators based on the electro-optic effect, as well as optical wavelength converters based on second-order nonlinear effects, e.g., second-harmonic, sum-, and difference-frequency generations. TFLN has also created vast opportunities for applications and integrated solutions for optical parametric amplification and oscillation, cascaded nonlinear effects, such as low-harmonic generation; third-order nonlinear effects, such as supercontinuum generation; optical frequency comb generation and stabilization; and nonclassical nonlinear effects, such as spontaneous parametric downconversion for quantum optics. Recent progress in nonlinear integrated photonics on TFLN for all these applications, their current trends, and future opportunities and challenges are reviewed.

Keywords: lithium niobate; thin-film lithium niobate; nonlinear integrated optics; photonic integrated circuits.

Received Mar. 15, 2022; revised manuscript received Apr. 13, 2022; accepted for publication May 3, 2022; published online May 30, 2022.

[DOI: 10.1117/1.AP.4.3.034001]

1 Introduction

The excellent electro-optic (EO) and nonlinear optical properties of lithium niobate ($LiNbO_3$ or LN) have long established it as a prevailing photonic material for the long-haul telecom modulator and wavelength-converter markets. Indeed, the first nonlinear experiment in any waveguide platform was a demonstration of Cherenkov radiation from titanium-diffused LN.[1] Conventional LN waveguides are most commonly formed by in-diffusion of titanium (Ti) dopants[2] or by the proton exchange process.[3] However, these conventional lithium niobate optical waveguides have a low index-contrast, hence are bulky compared with modern integrated platforms, such as silicon photonics. The bulkiness impedes photonic circuit implementations and imposes high optical power requirements for nonlinear applications.

Achieving thin films of LN (with a thickness of a few hundred nanometers) that reside on an insulator cladding with a much lower index (e.g., silicon dioxide, SiO_2)— along with methods to achieve low-loss ridge or channel waveguides on the thin films—can address the above issues and yield high-contrast waveguides. Thin-film lithium niobate (TFLN) wafers on silicon (Si) substrates and high-contrast waveguides (with submicron cross-sectional dimensions) were developed for the first time at CREOL in 2013.[4] Since the commercialization of TFLN wafers by a few vendors,[5–7] efforts by several research teams have tremendously advanced the field of TFLN-integrated photonics. A plethora of ultracompact linear and nonlinear optical devices and circuits (waveguides, microring resonators, modulators, grating couplers, wavelength converters, entangled photon sources, isolators, supercontinuum, and comb sources) with unprecedented or significantly superior performances than the conventional (bulk) LN counterparts have been demonstrated. The combined efforts have rejuvenated LN for EO, nonlinear-, and quantum-optics applications, and the material is considered to be among the top candidates for heterogeneous integrated photonics. That is when multiple materials are monolithically integrated on the same substrate (preferably silicon), while each material is chosen for the functionalities that it suits the best.

*Address all correspondence to Sasan Fathpour, fathpour@creol.ucf.edu

TFLN is still under investigation for a better understanding of its fundamental properties, such as crystal defects, optical damage,[8] and the photorefractive effect.[9] First-principle studies have also been used to explore new capabilities of the material.[10,11] Dry etching of LN is challenging in bulky conventional waveguides with deep sidewalls, hence diffusion or implantation of dopants is typically preferred. Etching appeared to be challenging in the early years of TFLN, thus rib-loading techniques were adopted,[4,12,13] which is indeed advantageous for EO devices in some respects.[14] However, direct etching of LN is preferred for nonlinear-optic applications. Partially due to the shallow etching required in TFLN waveguides, optical propagation losses as low as 0.027 dB/cm,[15] as well as intrinsic Q-factors beyond 10^8,[16] have been achieved. Even at the wafer level, a propagation loss of 0.27 dB/cm has been demonstrated,[17] which is an important milestone for large-scale integration. Progress in fabrication processes on TFLN is reviewed elsewhere.[18,19]

Numerous studies have also been conducted on the technological improvement of the platform such as domain engineering,[18,20–23] which is particularly important for nonlinear devices based on periodic poling. Increasing numbers of functionalities are being demonstrated on TFLN and are rendering it a fully functional integrated platform. For example, light sources including rare-earth ion-doped[24–29] and Raman lasers[30,31] as well as heterogeneously integrated electrically pumped III-V lasers[32,33] have been demonstrated. Shams et al.[33] adopted flip-chip bonding and demonstrated electrically pumped DFB lasers on TFLN with up to 60 mW of optical power coupled to the TFLN waveguide. The performance of EO modulators is still being further improved,[34,35] with a recently reported data transmission rate of 1.96 Tb/s at a single wavelength with a 110 GHz 3-dB bandwidth and <1 V of driving voltage.[36] Progress has been made in design and experimental results to enhance the EO bandwidth of TFLN modulators into the subterahertz regime.[14,37] Other components, such as highly efficient couplers,[38] tunable filters,[39] optical isolators,[40] and programmable spatial light modulators,[41] have also been reported. This review paper, however, primarily covers research studies related to nonlinear optics.

Nonlinear optical processes have numerous applications in spectroscopy, quantum optics, and optical communication, among others. Since the first demonstration of second-harmonic generation (SHG) over six decades ago,[42] a vast variety of materials and platforms have been explored for nonlinear optics applications.[43] This review paper exclusively focuses on recent advancements in nonlinear integrated photonics on TFLN. Overviews of early developments of nonlinear effects in TFLN devices and recent progress on other materials can be found elsewhere.[44–46]

2 Second-Order Nonlinearity in Thin-Film Lithium Niobate

LN has been the primary material of choice for second-order nonlinear optics, owing to its large optical susceptibility ($\chi^{(2)}$) with the largest coefficient of it being diagonal, relatively large refractive index ($n_o = 2.21$ and $n_e = 2.14$ at $\lambda = 1550$ nm), low optical absorption, ultraviolet to mid-infrared optical transmission, and its ferroelectric property, which allows for efficient nonlinear processes through domain reversal. Several other materials have been traditionally considered for second-order nonlinear applications (e.g., see Table 1.5.3 in Ref. 43). For integrated solutions and in addition to LN, materials such as AlN,[47] (Al)GaAs,[48,49] and GaN,[50] have lent themselves to thin film on insulator waveguide platforms. Their nonlinear coefficients and refractive indices are listed in Table 1 and compared with LNs. GaAs has a very high d_{36} value but it is not a ferroeletric material, hence modal-phase matching (PM) is typically pursued, which, as argued later, is less favorable than quasi-PM among fundamental guided modes.

Table 1 Optical properties of some of the materials used for second-order nonlinear applications.

Material	Largest d coefficient	Refractive index at 1550 nm
$LiNbO_3$[51]	$d_{33} = 27$ pm/V	~2.2
AlN[52]	$d_{33} = 4.7$ pm/V	~2.1
GaAs[51]	$d_{36} = 119$ pm/V	~3.4
GaN[53]	$d_{33} = 16.5$ pm/V	~2.3

Initially, bulk material and conventional waveguides were used to explore the capabilities of LN for nonlinear applications.[54–57] Conventional waveguides, based on proton-exchange or titanium-diffusion, have demonstrated phenomenal performance and have been commercially available for several years.

Shortly after the emergence of TFLN on silicon substrates,[4] it was realized that this new platform could take the performance of nonlinear devices to a much higher level.[13,58] As shown in Fig. 1, owing to the compactness of TFLN waveguides provided by the high index contrast, optical mode sizes are remarkably smaller than those in conventional counterparts, hence much higher intensities can be achieved for the same optical power. Moreover, the overlap integral between the interacting optical modes at different wavelengths with the same parity is much larger. These differences result in significant improvements in efficiencies of various nonlinear processes. For example, the normalized conversion efficiency of second harmonic generation (SHG) has a direct relation to the overlap integral of the fundamental and second harmonic modes and an inverse relation to mode areas.[46] Moreover, bending radii in the TFLN platform are much smaller than in the conventional LN because of its high index contrast, hence efficient and ultracompact microresonator structures can be easily realized on this platform for integrated nonlinear applications.

Single-pass straight microwaveguides and resonant-based structures, such as microrings, microdisks, racetracks, and photonic crystals, have been used to investigate nonlinear integrated photonics on the TFLN platform. Classical second-order nonlinearities, such as SHG, sum-frequency generation (SFG), difference-frequency generation (DFG), optical parametric amplification (OPA), optical parametric oscillation (OPO), and the nonclassical spontaneous parametric downconversion (SPDC) process have been demonstrated, which are all covered in more details in the following sections.

It is well known that for an efficient nonlinear process, both the energy and momentum conservation conditions should be satisfied, the latter of which is not trivial due to waveguide and material dispersion. For example, SFG requires $\omega_1 + \omega_2 = \omega_3$ and $k_1 + k_2 = k_3$ or $n_1\omega_1/c + n_2\omega_2/c = n_3\omega_3/c$, where ω_i denotes the angular frequencies of the participating signals in the nonlinear process, and k_i and n_i are the corresponding wavevector and refractive index, respectively.[43] For the case of SHG, in which $\omega_1 = \omega_2$, $k_1 = k_2$, and $n_1 = n_2$, the energy and

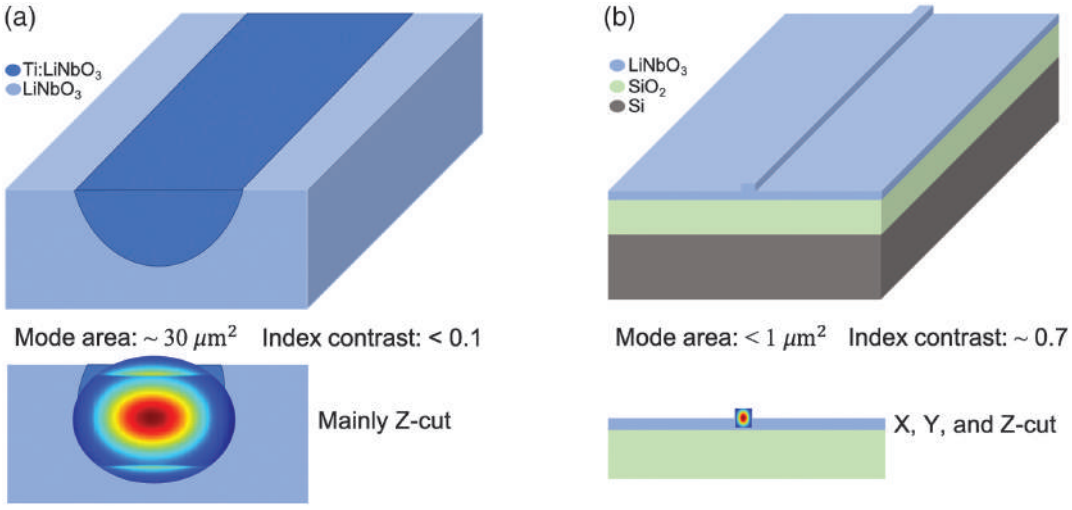

Fig. 1 Comparison of optical mode areas, index contrast, and crystal orientations in (a) conventional LN waveguides and (b) thin-film LN waveguides.

momentum conservation conditions are simplified to $\omega_3 = 2\omega_1$, $k_3 = 2k_1$, or $n(\omega_1) = n(2\omega_1)$. Similarly, these conditions should be fulfilled for other efficient nonlinear processes. In the presence of a wavevector mismatch (or as often referred to as phase mismatch), e.g., $\Delta k = k_1 + k_2 - k_3 \neq 0$ for SFG, the power oscillates between the participating frequencies instead of efficiently generating the targeted frequency. Therefore, PM becomes the most critical aspect of any nonlinear process. In addition, and in resonant-based structures, all the frequencies involved in an efficient nonlinear process should meet the resonance condition.

Various phase-matching methods are covered in Sec. 2.1 for SHG, which can be similarly applied to other three-wave mixing processes in TFLN. It is worth mentioning that for all these methods and considering the crystal orientation, the preferred polarization is, if possible, the one that utilizes the largest element in the $\chi^{(2)}$ tensor of LN, i.e., d_{33}. For instance, Fig. 2 shows the crystal orientation and preferred polarization for periodic poling and modal PM methods for straight waveguides. As shown in this figure, TFLN wafers are available in X-, Y-, and Z-cut orientations, and the desired polarization is chosen accordingly.

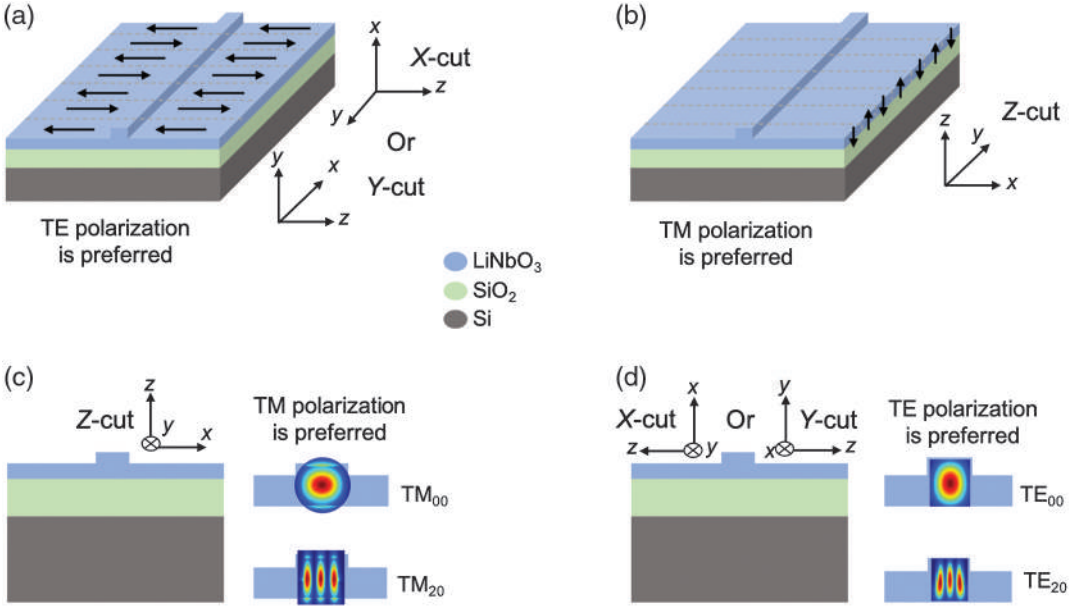

Fig. 2 Crystal orientations and corresponding preferred polarization to achieve maximum efficiency for nonlinear processes in TFLN using [(a), (b)] quasi phase matching via periodic poling and [(c), (d)] modal phase matching.

2.1 Second-Harmonic Generation in TFLN

SHG is considered the most fundamental three-wave mixing process, and it is commonly used to evaluate the performance of new materials and platforms. Hence, it is not surprising that SHG accounts for a sizable portion of the published works on three-wave mixing in TFLN. SHG can be used in applications such as light generation at inconvenient wavelengths for conventional semiconductor light sources, ultrashort pulse width measurement, and second-harmonic microscopy. This section reviews influential SHG studies that use straight waveguides, as well as resonator-based with various phase-matching methods. It is noted that for SHG, when the polarizations of both the pump (fundamental) and the second harmonic (SH) waves are the same and along the extraordinary axis, the PM method is called type-0 PM; otherwise, it is called type-I PM.

Several phase-matching methods have been adopted or developed on TFLN (see Fig. 3). They can be divided into two broad categories.[46] The first group is perfect PM, which achieves $\Delta k = 0$ by keeping the refractive indices for the fundamental and SH modes equal. Birefringent PM (BPM) and modal PM (MPM) are two examples of perfect PM methods. Cyclic PM (CMP), which is used in microrings and microdisks, meets the $\Delta k = 0$ condition for perfect PM in certain azimuthal angles. The second category is quasi-PM (QPM), $\Delta k \neq 0$, which is based on perturbing the nonlinear process to compensate for phase mismatches and includes grating-assisted QPM (GA-QPM) and periodic poling. Using metasurfaces, PM-free SHG is also possible.

The power relation of SHG in a lossless medium follows $P_2 \propto (P_1 L)^2$, where P_1 and P_2 are the pump and SH powers, respectively, and L is the device length.[43] Therefore, a normalized conversion efficiency is defined as $\eta = P_2/(P_1^2 L^2)$ with the unit of $\%\,\mathrm{W}^{-1}\,\mathrm{cm}^{-2}$. However, the proportionality to L^2 is rarely held in practical waveguides, since the relation is only valid in the low-loss regime.[46] Therefore, it is worth considering the efficiency in units of $\%\ \mathrm{W}^{-1}$ as well for better performance evaluation and comparison. Such a normalized conversion efficiency, i.e., P_2/P_1^2, is typically reported for resonant-based structures. However, this again can lead to absurdly large numbers if P_1 is very small, but without useful P_2 values. It appears

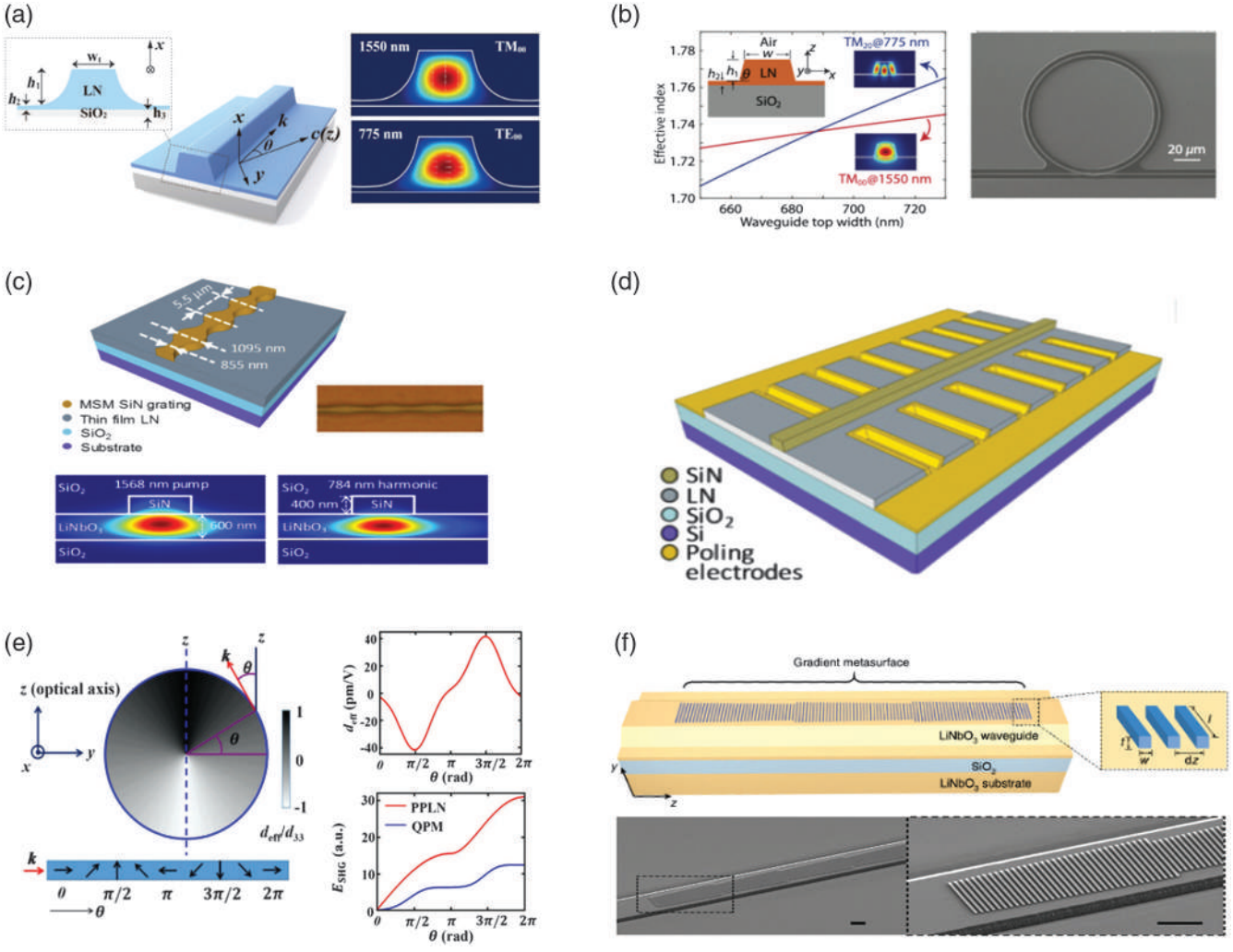

Fig. 3 Various phase-matching methods used on the TFLN platform. (a) Birefringent phase-matching.[59] (b) Modal phase matching.[60] (c) Grating-assisted quasi phase matching or mode shape modulation.[61] (d) PPLN on a straight waveguide.[13] (e) Natural quasi phase matching, which is conceptually similar to cyclic phase-matching.[62] (f) Phase-matching-free metasurface.[63]

that the unitless absolute ratio of the output–input powers, P_2/P_1 (expressed in %), may be the ultimate meaningful efficiency for most practical applications.

2.1.1 Birefringent phase matching

BPM can be attained in anisotropic materials by polarizing the fundamental and SH waves along different axes (type-I) to match the refractive indices at these frequencies and satisfy perfect PM. Although LN is a birefringent material, it is uncommon to use this method for SHG on TFLN, since it precludes the process from taking advantage of the largest element in the $\chi^{(2)}$ tensor, corresponding to the nonlinear coefficient $d_{33} = 27$ pm/V. This is in addition to the spatial walk-off issue and practical difficulties in implementing BPM, particularly in integrated chips. Nonetheless, Lu et al.[59] adopted an idea to demonstrate BPM on *X*-cut TFLN with an LN thickness of 10 μm. The refractive index of the TM_{00} mode at the C-band fundamental wavelength was matched to that of the TE_{00} mode at the SH by deviating the 20-mm-long straight waveguide from the optical axis of LN by an angle of $\theta = 52$ deg. Furthermore, the strong birefringence thermo-optic effect of LN was used to demonstrate a wide thermal tunability at a rate of 1.06 nm/K. The normalized conversion efficiency was, however, low (2.7% W^{-1} cm^{-2}). It seems that this design concept can be harnessed in other integrated birefringent materials, where QPM is not easily accessible.

2.1.2 Modal phase matching

In MPM, the dispersion of a multimode waveguide is engineered to accomplish equal effective refractive indices for the fundamental mode at the pump wavelength and a higher-order mode at the SH wavelength. Nonlinear devices based on MPM are easy to fabricate and are functional after forming the waveguide or the microring without the need for postprocessing steps, such as periodic poling. MPM has been employed for straight waveguides[64,65] and microresonator structures[60,66] in both type-0 and type-I configurations. The type-I implementation leverages the strong thermo-optic birefringence of LN and can tune the wavelength efficiently over a wide span at the expense of using the $d_{31} = 4.7$ pm/V coefficient, which is more than five times smaller than d_{33}. However, even in the type-0 configuration, the SHG efficiency is limited due to using higher-order modes at the SH wavelength, which are less confined, have a higher propagation loss, and have a much weaker overlap integral with the fundamental mode at the pump wavelength. Luo et al.[65] demonstrated a type-I MPM in an 8-mm-long straight waveguide with a normalized SHG conversion efficiency of $\eta = 7.3\%\,W^{-1}\,cm^{-2}$ and a tuning slope of 0.84 nm/K from 1560 to 1620 nm. Wang et al.[64] reported an $\eta = 41\%\,W^{-1}\,cm^{-2}$ for a 1-mm-long device using type-0 MPM. Usually, the third-order mode is used at the SH wavelength, since the overlap integral between modes with different parities is equal to zero in a homogeneous waveguide. However, by adding complexity to the fabrication process and by having inhomogeneous waveguides consisting of TiO_2 on LN, the TE_{00} mode for the pump and the TE_{01} mode for the SH were utilized with much stronger overlap integral, resulting in $\eta = 650\%\,W^{-1}\,cm^{-2}$ in a 2.35-mm-long device.[67] Chen et al.[66] employed type-0 MPM and observed a 10-fold enhancement in SHG efficiency in a microring with 80 μm radius compared with a 1-mm-long straight waveguide with the same cross-section. A relatively high conversion efficiency of 1500% W^{-1} was demonstrated in a microring resonator with a 50 μm radius using type-0 MPM.[60] MPM has been used in microdisk resonators as well, in type-0 configuration on a *Z*-cut TFLN.[68–70] However, the efficiencies in microdisks are much lower than microrings, and one of the best reported values for the normalized conversion efficiency appears to be ~11% W^{-1}.[68]

2.1.3 Grating-assisted quasi phase matching

In GA-QPM, also known as mode shape modulation,[61] guided modes are periodically perturbed to induce an extra phase term and compensate for the phase mismatch. Rao et al.[61] implemented a sinusoidal width variation in a TFLN waveguide rib-loaded with SiN, which resulted in an estimated η of ~1% W^{-1} cm^{-2} for a 4.9-mm-long waveguide. Wang et al.[64] employed direct etching of TFLN to form periodically grooved waveguides with a groove depth of 80 nm and obtained $\eta = 6.8\%\,W^{-1}\,cm^{-2}$ for a 500-μm-long device.

2.1.4 Periodic poling in straight waveguides

Periodic poling, demonstrated first on bulk LN devices over a few decades ago,[71] is the most common and efficient QPM technique on LN, especially for straight waveguides, despite $\Delta k \neq 0$. In this method, to compensate for Δk, the sign of the relevant nonlinear coefficient is periodically altered in the areas that the power is supposed to be converted back to the pump frequency. A periodicity of $\Lambda = 2\pi/\Delta k$ with a 50% duty cycle prevents power oscillation between interactive waves and facilitates a much more efficient power transfer from the pump to the targeted frequency. Devices made with this technique are called periodically poled lithium niobate (PPLN) and have been commercialized for many years. Poling is accomplished by utilizing the ferroelectric property of LN through domain inversion by applying electric fields greater than the coercive field. For congruent bulk LN, the coercive field value is ~21 V/μm.[72] This value is higher in TFLN (~40 to 48 V/μm), which is possibly related to the interface of SiO_2/LN bonding[73] or the annealing step of the wafer fabrication process and the subsequent out-diffusion of Li^+ ions.[74] PPLN devices typically utilize d_{33} in a type-0 PM configuration in which the fundamental modes can be used for both the pump and SH wavelengths, resulting in a strong overlap integral and enhanced overall conversion efficiency. Extensive studies have been conducted to optimize the poling process parameters, e.g., preheat treatment, temporal waveform, and electric field strength for achieving a stable and uniform ~50% duty cycle throughout the entire device.[21–23,75] Recently, several groups have successfully demonstrated submicron poling periods,[76–78] which are capable of compensating for large values of Δk and are of high demand, particularly for short-wavelength nonlinear devices and counter-propagating processes. Also, nondestructive measurement methods, such as piezo-response force microscopy (PFM), SH confocal microscopy,[79] and far-field diffraction,[80] are employed to visualize and evaluate the poling quality.

In 2016, PPLN devices were demonstrated for the first time on the TFLN platform on LN[73] and Si[13] substrates. Both devices relied on silicon nitride (SiN) rib-loaded waveguides on TFLN. Using SiN rib-loaded waveguides and by engineering the lateral leakage, a normalized conversion efficiency of 1160% W^{-1} cm^{-2} was achieved in 2019 for a 4.8-mm-long device.[81] Figure 4 shows various types of PPLN devices demonstrated in TFLN, such as straight waveguides and resonator structures.

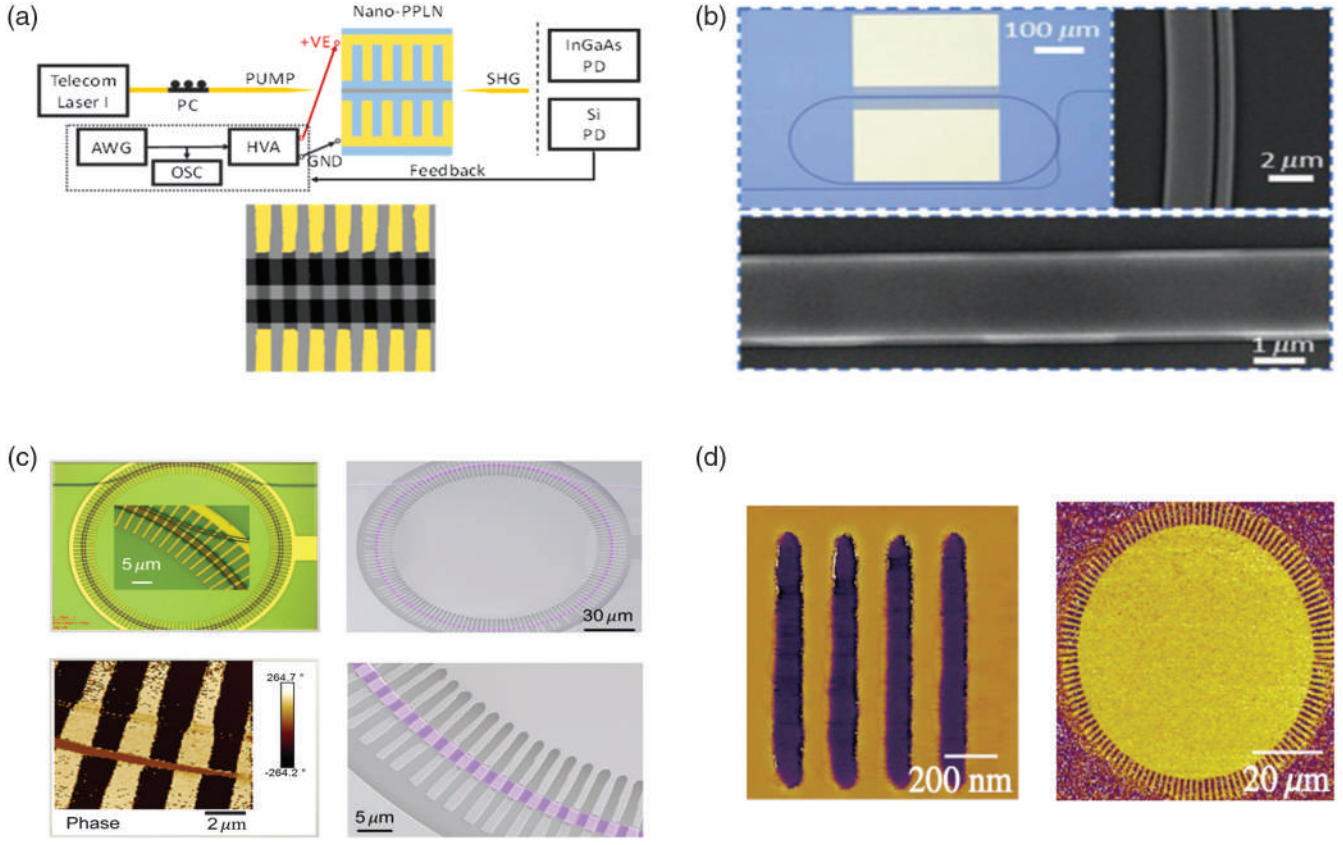

Fig. 4 PPLN devices in different structures. (a) Straight waveguide.[82] (b) Racetrack resonator that is poled on one of the straight arms.[83] (c) Radially poled microring resonator.[84] (d) Radially poled microdisk, poled using the PFM technique in which they also demonstrated a poling period as small as 200 nm.[85]

Following the development of low loss etching processes,[15] ultrahigh efficient nonlinear processes on TFLN using direct etching emerged. In 2018, using direct etching on a MgO-doped *X*-cut TFLN, Wang et al.[86] reported normalized SHG conversion efficiencies of 2600 and 2300% W^{-1} cm^{-2} for 4-mm-long devices on two different waveguide widths operating at two distinct wavelengths. MgO-doping mitigates any potential photorefractive effects in LN, and hence enables high-power operation. Chen et al.[87] achieved a very similar performance on an undoped *X*-cut TFLN with an η of 2200% W^{-1} cm^{-2} for a 4-mm-long device. In 2019, our group showed a record high normalized SHG conversion efficiency to date of 4600% W^{-1} cm^{-2} on a 300-μm-long device by actively monitoring the poling process and by performing multiple iterative cycles of poling and depoling.[82] In 2020, another very high η of 3757% W^{-1} cm^{-2} was reported on a longer device length of 5 mm.[88] Recently, a normalized conversion efficiency of ~320% W^{-1} cm^{-2} was reported for a 20-mm-long device corresponding to ~1280% W^{-1},[89] which is relatively high for conversion efficiencies reported to this date in units of % W^{-1} for straight waveguides (see Table 2).

2.1.5 Periodic poling in microresonators

Combining highly efficient PPLN devices with the intensified light–matter interaction in resonant-based structures has led to a new front in nonlinear processes. In 2019, Chen et al.[83] utilized a doubly resonant microcavity in a racetrack shape on *X*-cut MgO-doped TFLN and periodically poled the 300-μm-long straight waveguide on one arm to achieve a normalized conversion efficiency of 230,000% W^{-1} with only 5.6 μW of pump power and a moderate *Q*-factor of 3.7×10^5. Lu et al.[90] radially poled a doubly resonant microring resonator on a *Z*-cut TFLN and were able to demonstrate $\eta = 250{,}000\%\mathrm{W}^{-1}$. This is while they employed d_{31} by using TE_{00} for the pump mode and TM_{00} for the SH mode due to the difficulty of poling, since the poling period of type-0 PM would have been almost three times smaller. By utilizing d_{33} in the type-0 configuration through overcoming the poling issues and by improving the *Q*-factor of resonators, the same group reached 5,000,000% W^{-1} conversion efficiency at the low power regime with a pump power of ~10 μW.[84] As mentioned above, such very high efficiencies in % W^{-1} are possible because the ratio P_2/P_1^2 would increase inversely with a decrease of the pump power for the same order of absolute power efficiency (see Table 3). Nonlinear optics at such low pump powers is a welcome development. However, as mentioned before, in most practical applications, the amount of the generated output power is more important and the absolute power efficiency, P_2/P_1 in %, is therefore a more relevant figure of merit.

With a high single-photon coupling rate of 1.2 MHz and a reasonably low dissipation rate of 184.6 MHz, the previously cited work[84] reached a single-photon anharmonicity of 0.7%,[84] which could find application in integrated quantum photonics.[92,93] Periodically poled whispering-gallery resonators

Table 2 Performance of various devices based on straight waveguide structure for SHG using different phase-matching methods. Power values for the pump and SH wavelength and the absolute conversion efficiency (in %) correspond to the maximum normalized conversion efficiency and are not necessarily the maximum reported numbers in these papers.

PM method	Pump/SH power	Length	$\%\,W^{-1}\,cm^{-2}$	$\%\,W^{-1}$	Absolute %
BPM type-I[59]	25 mW/67 μW	2 cm	2.7	10.7	~0.27
MPM type-0[67]	630 μW/140 nW	2.35 mm	650	36	~0.022
PPLN type-0[82]	3 mW/370 nW	300 μm	4600	4.14	~0.012
PPLN type-0[88]	530 μW/2.7 μW	5 mm	3757	939.25	~0.5
PPLN type-0[86]	1.5 mW/9.4 μW	4 mm	2600	416	~0.6
PPLN type-0[87]	2.95 mW/31.6 μW	4 mm	2200	352	~1
PPLN type-0[89]	~6 mW/550 μW	20 mm	~320	~1280	~9

Table 3 Comparison of resonant-based structures for SHG using different phase-matching methods.

Structure	PM method	Pump/SH power	Q_L at FW	$\%\,W^{-1}$	Absolute %
Microring[60]	MPM type-0	440 μW/2.9 μW	1.4×10^5	1500	~0.65
Microring[84]	PPLN type-0	1.05 μW/56 nW	1.8×10^6	5×10^6	~5.3
Microring[90]	PPLN type-I	55 μW/7.5 μW	8×10^5	2.5×10^5	~13.5
Racetrack[83]	PPLN type-0	5.6 μW/73 nW	3.7×10^5	2.3×10^5	~1.3
Microdisk[91]	CPM type-I	10 mW/110 μW	1.1×10^5	~110	~1.1
Microdisk[16]	NQPM type-0	30 μW/4.2 μW	7.5×10^7	4.7×10^5	~14

and microdisks are also demonstrated,[85,94,95] but with much lower conversion efficiencies. Nonetheless, the developed poling techniques for microdisks using PFM are invaluable and pave the way for reaching poling periods below 100 nm[95] [see Fig. 4(d)].

2.1.6 Cyclic phase matching

The CPM method[96] is used in microresonators on *X*- and *Y*-cut TFLN in a type-I configuration.[91,97,98] Since the ordinary refractive index of LN is larger than the extraordinary value, the pump signal is polarized perpendicularly to the optical axis and hence holds a constant ordinary refractive index while the SH wave is in-plane and experiences an oscillating refractive index between the ordinary and extraordinary indices as it rotates around the resonator structure. Accordingly, the PM condition is met at four different azimuthal angles at each round. The normalized conversion efficiency for the CPM method has a record of only $110\%\,W^{-1}$.[91] However, it benefits from wider PM bandwidths[97] and does not require periodic poling.

In 2019, a method very similar to CPM, but in type-0 configurations, was demonstrated and was called natural QPM.[62] Herein, the in-plane waves on *X*- or *Y*-cut TFLN undergo different effective nonlinear coefficients as they rotate around the resonator structure, which resembles the domain inversion and QPM without periodic poling. Using this method, a broad PM bandwidth with a normalized conversion efficiency of $9900\%\,W^{-1}$ was reported.[62] Recently and partially due to a record high intrinsic Q of above 10^8, natural QPM with a conversion efficiency of $470{,}000\%\,W^{-1}$ was achieved in an ultrabroadband nonlinear device.[16] Also, an absolute conversion efficiency of 23% was reported at a saturation pump power of 110 μW.

2.1.7 Metasurfaces and photonic crystals

Phase-matching-free SHG is also possible using metasurface structures, which usually can operate over a wide range of wavelengths. This has been done, for example, by utilizing Mie-type resonant structures,[63,99,100] optical anapole modes,[101] and resonant waveguide gratings.[102,103] Among these, one of the best performances so far ($\eta_{max} = 1660\%\,W^{-1}\,cm^{-2}$) belongs to phased-array antennas forming a gradient metasurface, which provides a unidirectional wavevector and deprives the SH of converting back to the pump wavelength. A more detailed review on SHG using metasurface structures can be found elsewhere.[104]

Also, photonic crystals can be potentially very efficient in nonlinear processes due to their extremely small mode sizes and a strong light–matter interaction.[105,106] However, they require an elaborate doubly resonant design to overcome their typical low Q-factors and external coupling at SH, which remains a challenging task.

2.1.8 Summary and concluding remarks on SHG

Tables 2 and 3 summarize the performance of various devices for SHG using different phase-matching methods for straight waveguides and resonant-based structures, respectively. In these tables, maximum normalized conversion efficiencies along with the corresponding on-chip optical power at the fundamental and SH wavelengths and the absolute conversion efficiency are reported. The power values are mostly extracted from the related

plots in these published works. It is noted that some of these studies reported higher absolute conversion efficiencies at the high-power regime, where SH and pump powers do not follow the quadratic relation anymore and hence the normalized conversion efficiency is lower. In straight waveguides, PPLN devices have demonstrated the best performance in all conversion efficiency units. In resonant-based structures, again PPLN devices have exhibited a superior performance. However, the best absolute conversion efficiency belongs to a microdisk working with the natural QPM method,[16] which originates from the record-high loaded Q-factor of this resonator that is almost two orders of magnitude higher than the PPLN-based counterparts.

Comparing the two tables shows that conversion efficiencies reported in units of $\%\,\mathrm{W}^{-1}$ are mostly orders of magnitude larger for resonant-based structures. This notable difference is arising from the fact that straight waveguides are usually pumped at milliwatt levels, while resonant-based structures often work at microwatt levels. The absolute conversion efficiency is also higher in resonant-based structures. However, straight waveguides can handle very high powers, which can result in large absolute conversion efficiency values. For instance, an absolute conversion efficiency of 53% has been reported with 117 mW at SH when it was pumped with 220 mW in a MgO-doped TFLN waveguide.[86] Generation of SH at such high power levels is desired for many applications. Moreover, from the practical perspective, straight waveguides are generally less sensitive to thermal, vibrational, and other environmental fluctuations and have higher fabrication yield compared with resonant-based structures, which are very sensitive to fabrication errors. Finally, most of the high-performance resonant structures were pumped with TM polarized light on a Z-cut TFLN to utilize d_{33}, which can be a limiting factor for an ultimate integrated photonic chip, since semiconductor quantum-well lasers typically emit TE-polarized light and hence a polarization rotator is required for TM pumping.

2.2 Other Three-Wave Mixing Processes in TFLN

Other second-order nonlinearities, such as SFG, DFG, optical parametric oscillation/amplification (OPO/OPA), and SPDC, have been demonstrated on TFLN. Moreover, various three-wave mixing processes have been cascaded on this platform and resulted in outstanding performances for processes such as low (third and fourth) harmonic generation. All these processes will be briefly reviewed in the following sections.

2.2.1 Sum-frequency generation

The SFG process is very similar to SHG, in principle, with the ability to mix two distinct wavelengths, which makes it suitable for numerous applications. SFG can be used to generate light at frequency ranges where SHG cannot be utilized due to the lack of efficient lasers. It is also very common to use SFG for upconversion detection. For instance, low-power mid-infrared (mid-IR) light, down to a single-photon,[107] can be converted to visible wavelengths and detected using low-noise and high-performance visible detectors. SFG on TFLN has been demonstrated on both straight waveguides[82,108] and resonant-based structures.[105,109,110]

Our team demonstrated an SFG bandwidth of ~20 nm in a TFLN PPLN device with a normalized conversion efficiency of $\sim 900\%\,\mathrm{W}^{-1}\,\mathrm{cm}^{-2}$ when one of the lasers was at a fixed wavelength and the other one was swept within its tuning range.[82] In addition, swiping both lasers resulted in an SFG from 1460 to 1620 nm. In microdisk resonators, a conversion efficiency of $2.2 \times 10^{-3}\ \mathrm{W}^{-1}$ is reported with a relatively low Q of 1.8×10^5 using the MPM method.[110] Ideally, the conversion efficiencies four times larger than SHG should be achieved for SFG.[111] Therefore, having state-of-the-art values for Q and utilizing natural QPM or PPLN—as the most efficient PM methods for resonators so far—can notably boost the efficiency of SFG.

SFG can be combined with other second-order nonlinear phenomena, such as SHG, to obtain highly efficient higher-order nonlinear processes through cascading,[62,69,112–115] which will be discussed later in a separate subsection. Moreover, SFG has been cascaded with the EO effect, which is in principle a second-order nonlinear process as well. This is very useful for low-power and high-speed control of an SFG.[116]

2.2.2 Difference-frequency generation and parametric amplification and oscillation

DFG, OPA, and OPO share similar working principles. DFG has been extensively used for generating terahertz and mid-IR sources on other platforms.[117,118] On the TFLN platform, DFG has been demonstrated using both straight waveguides[40,119] and resonant-based structures.[60] A new hybrid TFLN/Si platform is proposed by providing numerical simulation results to utilize DFG for terahertz generation,[120] though it appears to be challenging to be realized from the fabrication perspective. Using periodically poled TFLN on sapphire—with a transparency window up to 4.5 μm—mid-infrared generation up to 3.66 μm with a DFG normalized conversion efficiency of $200\%\,\mathrm{W}^{-1}\,\mathrm{cm}^{-2}$ is demonstrated.[119] Sapphire helps with circumventing the high absorption loss of the oxide layer at wavelengths longer than 2.5 μm.[58,119] Cascaded SHG/DFG is used to demonstrate effective four-wave mixing on a microdisk on TFLN using MPM.[70] In collaboration with Johns Hopkins University, we have utilized DFG in a TFLN PPLN device and spectral filtering to demonstrate an optical isolator concept based on nonlinear optics.[40] The isolator has a wide bandwidth (>150 nm) with 40 dB transmittance difference between forward and backward-propagating waves.

OPAs have been recently pursued on TFLN.[121,122] On-chip amplification, combined with phenomenal properties of LN, opens the door wide open for applications in sensing, communications, and quantum information processing, among others. Recently, using dispersion engineered PPLN devices, Ledezma et al.[123] reported on a phase-sensitive gain of 11.4 dB on a 2.5-mm-long device (~45 dB/cm) with a pump pulse energy of 0.8 pJ. They also demonstrated optical parametric generation with a 110 dB/cm gain with <6 pJ of pump pulse energy and more than 600 nm gain bandwidth. Jankowski et al.[124] circumvented the group-velocity dispersion and temporal walk-off effects via delicate dispersion engineering in a TFLN PPLN device and reported on a 118 dB/cm of unsaturated parametric gain over 1 μm of bandwidth with 4 pJ pulse energies. They also achieved a saturated gain of 146 dB/cm and a conversion efficiency of 15% for pulse energies above 10 pJ. These gain values are comparable with the state-of-the-art semiconductor optical amplifiers but with a much higher bandwidth that can potentially initiate numerous applications for TFLN.

OPOs can be utilized as a classical source for the generation of coherent radiations throughout a wide range of frequencies or as a nonclassical source for purposes such as quantum random number generation. Ultralow threshold (30 μW) integrated OPO

devices are recently reported on the TFLN platform using a radially poled PPLN microring.[125] This OPO is widely tunable through varying the temperature and the pump wavelength and showed an 11% conversion efficiency at a pump power of 93 μW.

2.2.3 Spontaneous parametric downconversion

SPDC is a nonclassical three-wave mixing process in which a pump photon generates two entangled photons, i.e., signal and idler, at lower frequencies.[126] For over three decades, SPDC has been used as a source in various quantum mechanical experiments, such as quantum cryptography[127] and quantum teleportation,[128] and it is usually more efficient than the third-order counterpart of spontaneous four-wave mixing.

TFLN is a propitious candidate for integrated quantum photonics. SPDC has been demonstrated on straight PPLN waveguides,[87,129–133] as well as on resonant-based structures.[97,134] In collaboration with Northwestern University, our team has reported quantum-correlated photon pairs with a high coincidence-to-accidental ratio (CAR) of beyond 10^3 over 140 nm[129] (on the same discussed PPLN devices with 300 μm lengths that exhibited an SHG efficiency of 4600% $W^{-1}\,cm^{-2}$).[82] In another publication, we demonstrated correlated photon pairs using cascaded SHG and SPDC in a single 4-mm-long PPLN device.[130] A comprehensive review of integrated quantum photonics on the TFLN platform can be found elsewhere.[135]

Over the past two years, several high-performance SPDC devices based on PPLN structures are demonstrated. Zhao et al.[132] reported a CAR of ~67,000 at a pair flux of 76 kHz and a CAR of ~670 at a pair flux of 11.4 MHz for a 5-mm-long PPLN waveguide. A spectral brightness of 5.6×10^7 Hz nm^{-1} mW^{-1}, visibility of >99%, and heralded single-photon autocorrelation of $g_H^{(2)}(0) < 0.025$ were measured for this device as well. Xue et al.[131] showed an ultrahigh pair flux rate and a spectral brightness of 2.79×10^{11} Hz mW^{-1} and 1.53×10^9 Hz nm^{-1} mW^{-1}, respectively, on a 6-mm-long PPLN waveguide at the expense of a lower CAR value of about 600. This device possessed 160 nm of bandwidth and maximum visibility of ~99%. Recently, Javid et al.[133] demonstrated a record high bandwidth of 800 nm (100 THz) in a 5-mm-long dispersion engineered PPLN waveguide. A CAR of >150,000 at a pair flux of 176 kHz, a spectral brightness of 3.8×10^7 Hz nm^{-1} mW^{-1}, and a visibility of 98.8% were reported for this device. Using a radially poled microring resonator on the TFLN platform, Ma et al.[134] demonstrated pair fluxes of 36.3 and 8.5 MHz at pump powers as low as 13.4 and 3.4 μW, respectively. Also, a maximal CAR of ~15,000 and a minimal $g_H^{(2)}(0)$ of 0.008 were reported for this PPLN microring. These devices have already met or in some cases surpassed the performance of other materials, such as Si, SiN, AlN, and bulk LN. Therefore, a bright future is expected for quantum integrated photonics on TFLN.

2.2.4 Cascading second-order nonlinear processes

Higher-order harmonics and wave mixing effects can occur by cascading $\chi^{(2)}$ processes in a single or multiple TFLN devices. Furthermore, effective third-order nonlinearities can be realized through cascading $\chi^{(2)}$ processes.[136] This is specifically very intriguing for the TFLN platform since $\chi^{(2)}$ of LN is much stronger than its other nonlinearities. Cascading $\chi^{(2)}$ processes has been extensively studied on the TFLN platform to further improve the performance of other nonlinear processes.[69,70,89,114,115,130,137–139]

There are several methods to achieve such cascading effects (see Fig. 5). A straightforward method is by placing two or more different periodically poled sections, each being responsible for a specific $\chi^{(2)}$ process. For instance, our group demonstrated two devices (each with two cascaded PPLN sections) for low-harmonic generation, namely third- and fourth- harmonic generations (THG and FHG). For THG, the first PPLN segment was designed for SHG while the second PPLN was responsible for SFG, resulting in a cascaded SHG/SFG ($\omega + \omega \rightarrow 2\omega / 2\omega + \omega \rightarrow 3\omega$). For FHG, both PPLN segments were poled for SHG, resulting in SHG/SHG ($\omega + \omega \rightarrow 2\omega / 2\omega + 2\omega \rightarrow 4\omega$).[137] Another method is to have more than one period in a PPLN device and generate a wider range of k-vectors to compensate for different phase-mismatching required for various nonlinear processes. This has been done in a chirped PPLN straight waveguide, which resulted in illustration of high-harmonics up to the 13th harmonic.[115] Also, a PPLN microdisk with a dual period was utilized for THG and FHG.[95] In addition, it is possible to achieve cascading in a single PPLN waveguide for THG and FHG via pulse pumping and by slightly detuning the pump wavelength from the QPM wavelength.[82,89,139] This latter method was used to demonstrate self-phase modulation with an effective nonlinear refractive index, i.e. $n_{2,\text{eff}}$, that is almost 200 times larger than the intrinsic n_2 of LN in a dispersion-engineered PPLN waveguide.[139] The effective $\chi^{(3)}_{\text{eff}}$ reported in this paper is larger than that of other well-known photonic Kerr-based platforms (such as Si and SiN) and proves the effectiveness of the cascading process. Moreover, in the first reported cascaded $\chi^{(2)}$ for THG in a resonator, it was shown that natural BPM can be employed to observe both SHG and THG at higher values of pump power.[69]

2.3 Applications of Second-Order Nonlinearity in Optical Frequency Combs

An optical frequency comb (OFC) consists of a large number of equidistant teeth in the optical spectra with potential applications in accurate optical clocks, optical communication, detection and ranging, spectroscopy, and sensing.[140] TFLN in particular is a very attractive platform for OFCs since dispersion engineering is fairly easy on this platform, and it enables OFC generation through different processes, such as $\chi^{(3)}$, cascaded $\chi^{(2)}$, and the EO effect. Moreover, TFLN can leverage other phenomenal properties of LN to provide additional devices, such as self-referencing components, EO modulators, frequency converters, and filters to materialize a fully functional integrated chip for OFC generation.

The most common method for OFC generation is based on the Kerr effect, which is a third-order nonlinear process and will be discussed in Sec. 3.2. In another approach, OFC generation through only $\chi^{(2)}$ processes is also possible and is called quadratic frequency combs. This can be done through an OPO cascaded with SHG/SFG or the other way around. In other words, quadratic frequency combs leverage LN's large second-order nonlinear coefficients and can result in a lower threshold and higher efficiency compared with Kerr combs. Moreover, the frequency shifting nature of this process makes it possible to generate OFCs at the mid-IR or ultraviolet wavelengths using the commonly available visible and near-IR lasers. On-chip integration of $f-2f$ self-referencing is feasible as well. However, such combs have been mostly demonstrated on table-top systems.[141] Recently, an on-chip quadratic frequency comb with

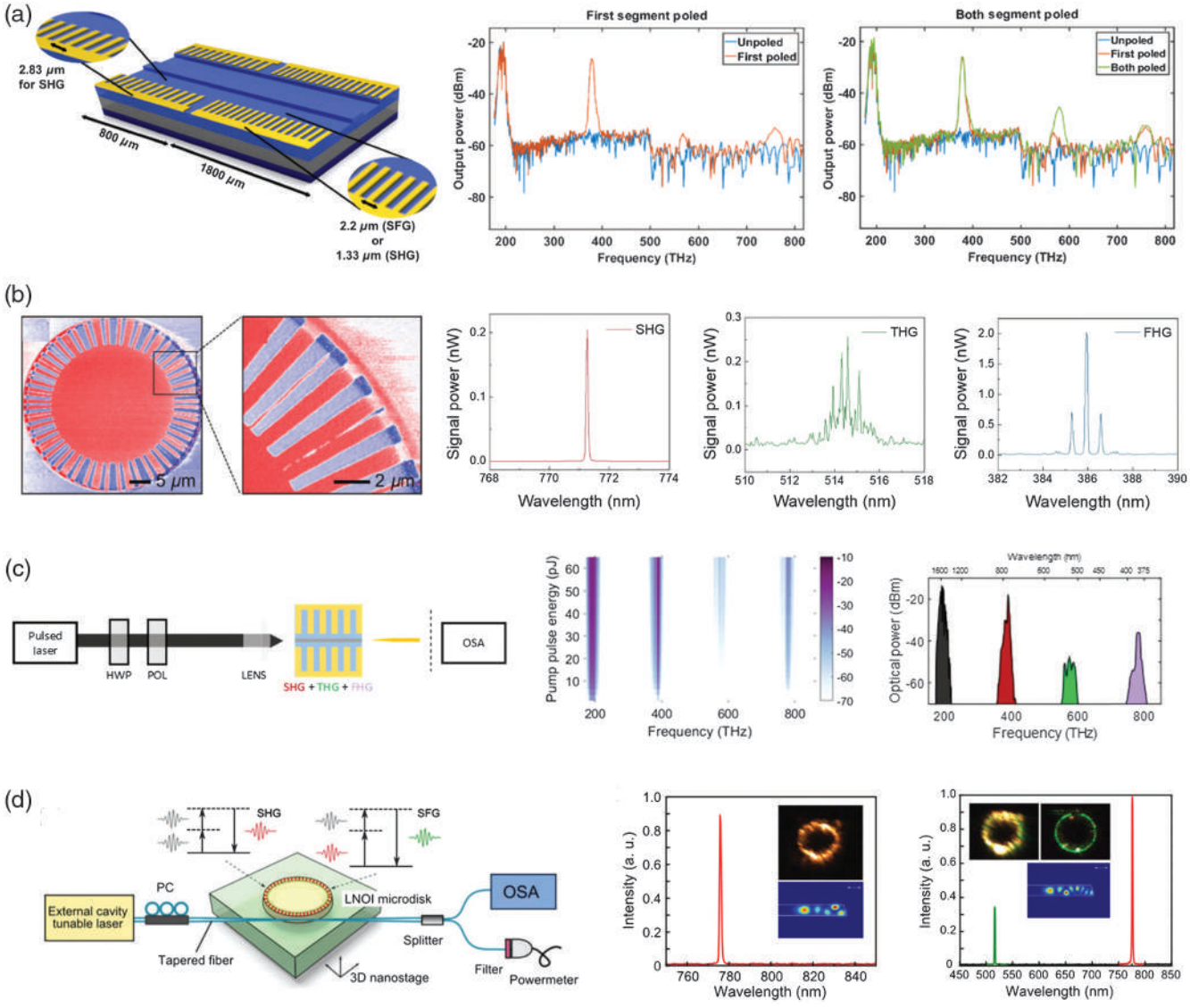

Fig. 5 Some of the schemes used for implementing cascaded $\chi^{(2)}$ processes in TFLN and the corresponding harmonic generations. (a) Two PPLN sections with different poling periods to enable SHG/SFG cascading for a THG device and SHG/SHG for an FHG device.[137] (b) Dual-period PPLN microdisk with demonstrated THG and FHG.[95] (c) THG and FHG on a single PPLN device via pulse pumping.[82] (d) SHG and THG on a microdisk through cascaded SHG/SFG by taking advantage of the natural BPM.[69]

a soliton state was illustrated in an AlN platform.[142] Quadratic OFCs, operating in the modulation instability regime, have been reported on conventional LN chips using PPLN waveguides and a microresonator[143–147] [Fig. 6(a)]. This type of OFC has yet to be demonstrated on the TFLN platform.

EO combs are another alternative for OFC generation. Although EO is fundamentally a $\chi^{(2)}$ nonlinear process, the EO combs are not regarded as a variant of the quadratic frequency combs discussed above, since their working principle is different. In the EO scheme, comb lines are formed by generating sidebands of the pump signal through phase modulation.[149] To increase the number of lines, usually a resonator structure such as a Fabry–Pérot cavity[150] or a microresonator[151] is used in which the frequency of the applied RF signal matches an integer number of the resonator's free-spectral range. The line spacings of these OFCs are tunable, and the spectral flatness compared with Kerr combs can be achieved on them by proper designs. However, due to the small frequency spacing compared with Kerr combs, EO combs have limited bandwidths. A review on the advancement of integrated EO combs on different platforms can be found elsewhere.[152]

On the TFLN platform and by proper dispersion engineering in a microresonator structure with $Q \approx 1.5 \times 10^6$, Zhang et al.[151] were able to expand the spectral span of an EO comb to 80 nm with a spectral slope of ~1 dB/nm and a pump to comb conversion efficiency of ~0.3%. The spectra comprised more than 900 comb lines with a repetition rate of ~10.45 GHz. Recently, the same group used two coupled resonators that were critically coupled when applying the RF modulation signal and hence transferred the pump power much more efficiently

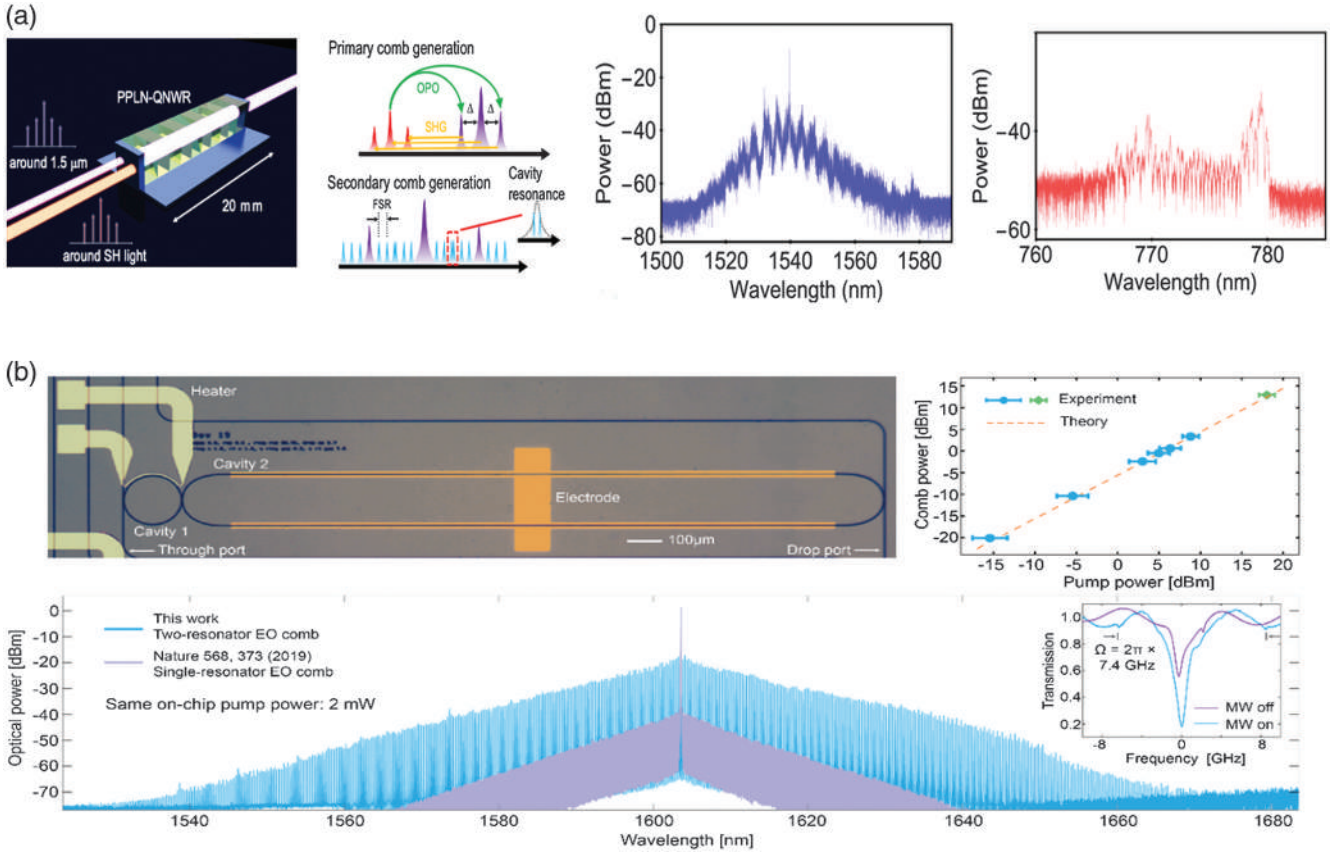

Fig. 6 Using second-order nonlinear processes for generating OFCs on lithium niobate. (a) Quadratic frequency comb generation on conventional LN[143] using cascaded $\chi^{(2)}$ processes, which has yet to be demonstrated on the TFLN platform. (b) Electro-optic frequency comb generation in TFLN using coupled microring and racetrack resonators and the resulting spectrum exhibiting a high conversion efficiency.[148]

into the microresonator.[148] This new configuration resulted in conversion efficiency of 30% with a spectral span of 132 nm and a comb line spacing of ~31 GHz [Fig. 6(b)]. In addition, it was shown that this EO comb, with such bandwidth and conversion efficiency, can be used as a high peak power ultrafast pulse source (~336 fs pulse duration) for other on-chip nonlinear processes including Kerr comb generation.

3 Third-Order Nonlinear Processes in TFLN

Although the third-order nonlinear coefficient of LN (1.6×10^{-21} m^2/V^2) is not as exceptionally high as its second-order coefficient compared with other materials, it is still very large and comparable to SiN, which is a popular choice for third-order nonlinear applications. Utilizing LN $\chi^{(3)}$ coefficients, combined with the recently achieved ultralow propagation loss and compact mode sizes of TFLN, makes the platform appealing for high-performance third-order nonlinear devices.

Among several well-known third-order nonlinear interactions, e.g., four-wave mixing,[153] stimulated Brillouin scattering,[154] and Raman processes,[155] some have been demonstrated on the TFLN platform.[30,156] However, due to the limited space, this work only covers supercontinuum generation (SCG) and Kerr effect in resonant structures, with an emphasis on their applications in OFCs.

3.1 Supercontinuum Generation

SCG is a nonlinear process where an ultrashort pulse with enough intensity experiences spectral broadening after propagating a certain distance through a third-order nonlinear medium.[140] SCG typically requires anomalous group velocity dispersion (GVD). However, it can be also achieved in the marginally normal GVD regime at the expense of higher pulse powers.[157] Spectral broadening of more than one octave is particularly useful for OFCs, since the wide spectrum allows stabilization of the carrier-envelope offset (CEO) frequency, f_{CEO}, through the $f-2f$ self-referencing method. SCG on integrated platforms benefits from ease of dispersion engineering and compact waveguide sizes and hence operates at lower energies. TFLN is a great platform for SCG as it offers a strong $\chi^{(2)}$ nonlinearity in addition to the required $\chi^{(3)}$, hence enables on-chip $f-2f$ self-referencing[158] [Fig. 7(c)].

Lu et al.[160] demonstrated SCG with 1.5 octaves of bandwidth using 800 pJ of pulse energy in a 10-mm-long *Z*-cut TFLN waveguide. In another work, 2.58 octaves of bandwidth using a pulse energy of 185 pJ was achieved in a 5-mm-long waveguide on an *X*-cut TFLN[159] [Fig. 7(a)]. In addition to SCG, SHG and SFG were observed in this study, which were attributed to MPM at higher-order spatial modes. With the SCG spectrum overlapping with that of SHG, the f_{CEO} beat-note was directly detected with a 30-dB signal-to-noise ratio (SNR). Jankowski

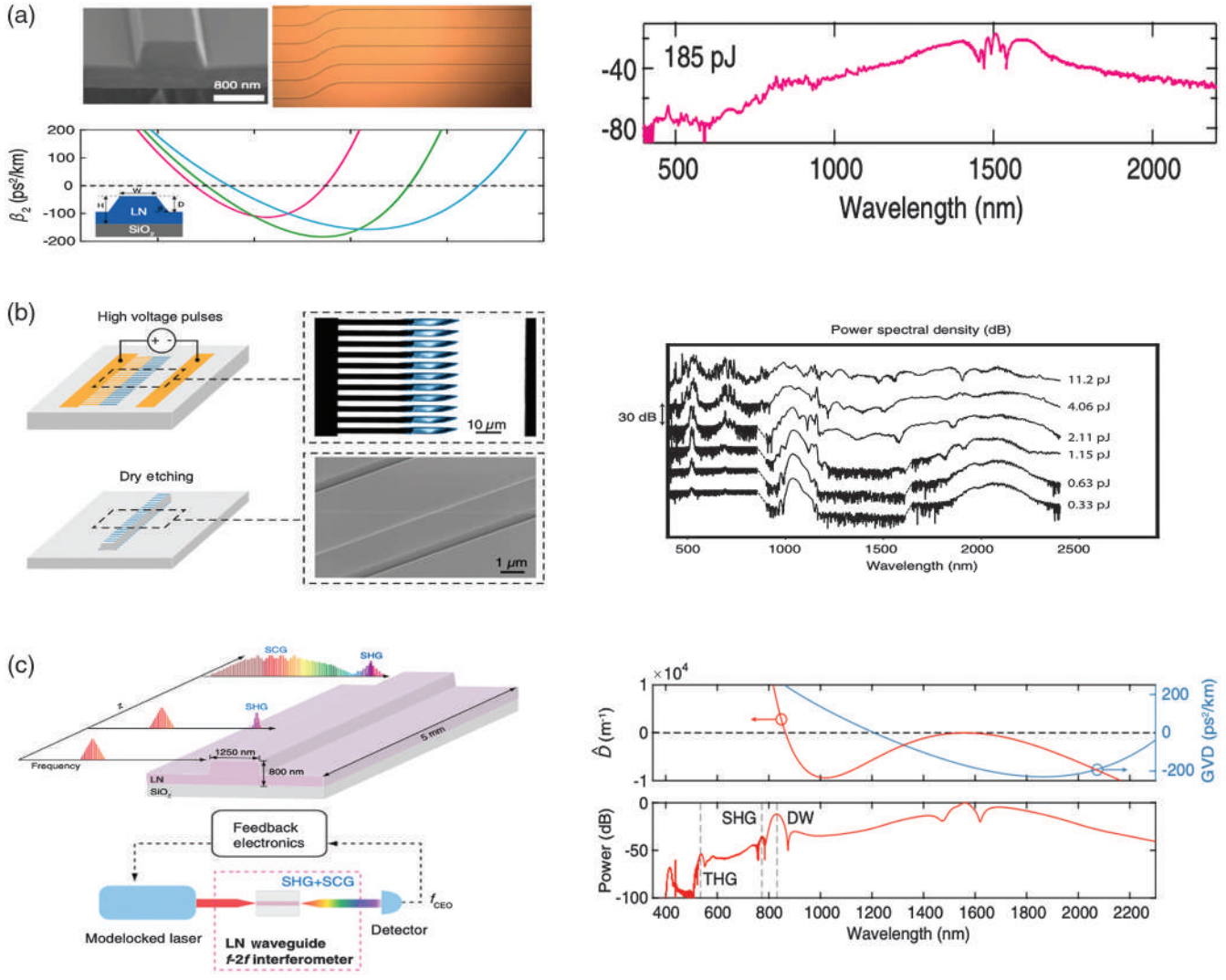

Fig. 7 SCG on the TFLN platform. (a) SCG spanning over two octaves in a dispersion engineered straight waveguide without poling.[159] (b) SCG on a periodically poled straight waveguide with a span of more than two octaves at a pulse energy of ~11 pJ.[139] (c) Using cascaded SCG and SHG for on-chip $f-2f$ self-referencing, which is of great importance for realization of on-chip OFCs.[158]

et al.[139] used a 6-mm-long PPLN waveguide to take advantage of cascaded $\chi^{(2)}$ processes and achieved more than two orders of magnitude improvement in self-phase modulation compared with that of Kerr nonlinearities. This resulted in an SCG with >2.5 octaves span at only ~11 pJ of pulse energy. To confirm the coherency of the SCG, they measured the f_{CEO} beat-note with an SNR of 35 dB.

3.2 Kerr Effect in Microresonators for Optical Frequency Comb Generation

Soliton OFCs can be generated over a wide bandwidth in microresonator structures with anomalous dispersion and by relying on the Kerr ($\chi^{(3)}$) nonlinearity. Using these combs, as the conceptual schematic in Fig. 8(a) suggests, versatile properties of TFLN can be utilized for the realization of fully integrated soliton combs on a single chip with providing all the necessary components.[161] He et al.[161] demonstrated soliton microcombs with a comb teeth spacing of ~200 GHz over a >200 nm spanning range around $\lambda = 1550$ nm in a Z-cut microring resonator with a Q of 2.2×10^6. They also showed that the photorefractive effect of LN (which acts in the opposite direction of the thermo-optic effect) permits the soliton mode-locking process to self-start and, more importantly, makes switching between the soliton states possible through both up- and down-tuning of the laser frequency. In a very similar work, operating around $\lambda = 2$ μm to reduce the impact of stimulated Raman scattering (SRS) on Kerr comb generation, Gong et al.[164] illustrated a line spacing of ~200 GHz over a span of ~300 nm. Wang et al.[165] made an integrated chip with filters and modulators to manipulate the output of the generated OFC. They designed a microring resonator capable of supporting both TE and TM polarizations with anomalous dispersion for both cases and reported on OFC generation spanning over 700 and 300 nm for TE and TM polarizations, respectively, with ~250 GHz spacing. However, the soliton state was not achieved, and the generated combs were attributed to modulation instability due to the Raman effect. Therefore, the strong Raman effect needs to be

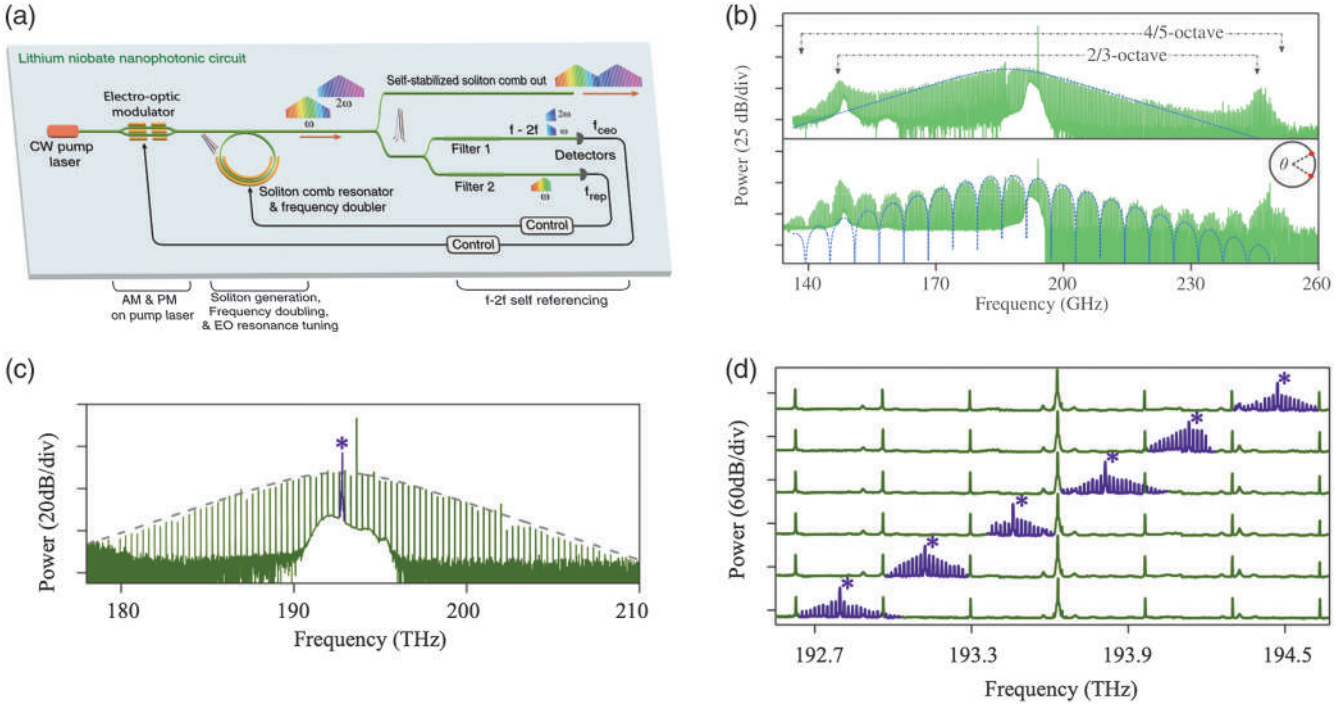

Fig. 8 OFC generation in TFLN using the Kerr effect. (a) Conceptual schematic of a fully integrated soliton comb system in TFLN with all the required functionalities.[161] (b) Soliton Kerr comb generation spanning near one octave.[162] (c) Cascaded Kerr and EO combs with green lines corresponding to Kerr comb lines spanning over 200 nm.[163] (d) Zoomed in spectra of the cascaded Kerr and EO combs demonstrating that EO combs with much lower repetition rates fill the gap between Kerr combs.[163]

circumvented to have frequency combs in soliton states. Gong et al.[162] accomplished this goal by increasing the threshold energy for SRS to more than that of the soliton through a delicate design of the external coupling rate with respect to the intrinsic decay rate. As a result, soliton frequency combs spanning over 4/5 octaves, with a spacing of ~335 GHz, were demonstrated [see Fig. 8(b)]. Pushing the span over an octave enables highly desired $f-2f$ self-referencing for this type of OFCs on the TFLN platform. It should be noted that the conversion efficiency from pump to comb lines is currently low for practical applications and further improvements are required for on-chip Kerr combs. The same group recently demonstrated a cascaded Kerr and EO comb, where the EO comb lines with much lower repetition rates filled the gap between Kerr soliton combs [Figs. 8(c) and 8(d)].[163] In addition, this could facilitate the stabilization of Kerr combs.

4 Conclusions and Outlook

Some of the initial research studies and recent developments in nonlinear photonics on the TFLN platform were reviewed. The improvements are magnificent for such a relatively short period of time, reaching or surpassing the performance of prior platforms for nonlinear applications. Despite outstanding demonstrated performances, this platform is still in its early years of development and will have a lot more to offer in the future.

There is plenty of room left for improvement of the TFLN platform before it becomes a fully functional integrated photonic platform. Fabrication needs to ultimately reach a point that reproducible, high-yield, and wafer-scale processing can be accomplished in foundries, while pushing the propagation losses down to the material absorption limit.

There are more essential photonic components that must be incorporated to the platform either monolithically or through heterogeneous integration. As mentioned before, progress has been made in heterogeneously integrated semiconductor lasers in TFLN.[32,33] Similar methods could be adopted for integration of semiconductor photodetectors on this platform. Other examples include cointegration of second- and third-order materials. As discussed, LN has a relatively high third-order Kerr optical susceptibility. But in some applications, such as OFCs, it is still sensible to utilize other materials—such as SiN or chalcogenide glass—that may be advantageous in terms of nonlinear coefficient, optical loss, dispersion management, cost, compatibility with silicon foundry fabrication, etc. To this end, our team and collaborators have made progress in heterogeneous integration of TFLN and chalcogenide glass waveguides on the same silicon substrates.[166,167]

Furthermore, besides improving the performance of devices based on different optical and other functionalities (e.g., EO, second- and third-order nonlinearities and piezoelectricity), all of them may need to be integrated on the same chip to fully utilize the capabilities of this versatile platform.

A lot of further milestones can be accomplished for nonlinear photonics on TFLN. Material properties, such as the photorefractive effect, need to be more accurately studied. For second-order nonlinearities, QPM using periodic poling still appears to be the most efficient method. The poling process can be perfected and standardized at the foundry level to achieve

high-yield and high-performance PPLN devices with <100 nm poling periods. Such small poling periods compensate for large phase mismatches, which can be very functional especially for counterpropagating QPM processes. With the reported performances for PPLN microring devices and considering their small footprint and low power consumption, they could be promising devices for $\chi^{(2)}$ processes in certain applications. However, one caveat for PPLN microrings is that the most efficient devices are made on *Z*-cut TFLN and operate in the TM polarization, which may not be the best option for ultimate fully integrated chips since the output of semiconductor lasers is usually TE-polarized, thus on-chip TE-to-TM polarization rotators will be required. Nonetheless, passive on-chip TM-to-TE polarization rotators[168] and polarization rotator-splitters[169,170] have been recently reported in TFLN. It is expected that reliable, low-loss, and high extinction ratio passive TE-to-TM polarization rotators will be demonstrated in the platform in the future. Furthermore, and as mentioned before, straight-waveguide PPLNs can typically handle higher powers and are more tolerant to fabrication errors and environmental fluctuations.

On-chip amplification in TFLN has been accomplished using heterogeneously integrated semiconductor optical amplifiers,[32] Er-doped amplifiers,[171–173] and OPAs.[123,124] Cascaded $\chi^{(2)}$ processes are anticipated to be much more sophisticated that can be used for efficient frequency conversion in the ultraviolet and mid-IR wavelength ranges as well as generating broadband OFC and SCG sources. The current high demand for OFCs, along with the miniaturization and robustness that comes with integrated OFC on the TFLN platform, will push the limits for this type of devices to have higher conversion efficiencies and SNR with self-referencing incorporated in them. Also, EO devices are envisioned to be effectively integrated with all types of nonlinear devices for fast tuning or high-speed modulation.

Finally, considering the current progress in the efficiency of nonlinear processes, especially second-order effects, it is expected to achieve very high absolute conversion efficiencies in the future. Reaching large values in absolute efficiency will be a major step forward for integrated nonlinear photonics and its applications. Integrated quantum photonics will be severely pursued at that point since nonlinearity at the single photon level will be accessible.

In summary, TFLN has emerged as a mature platform for integrated photonics on a ferro-electric material with high second- and third-order nonlinearity. The high-contrast and low-loss waveguides on TFLN make them ideal for realization of compact nonlinear devices operating at low powers compared with conventional waveguides on the same material or on other materials. Several applications, such as optical spectroscopy, wavelength conversion for light generation at inconvenient wavelengths, digital optical synthesizers, and quantum optics, can be realized using the discussed efficient nonlinear devices and circuits on TFLN.

Acknowledgments

Some of the results by the authors' group were funded by Office of Naval Research (N000141712409); Division of Emerging Frontiers in Research and Innovation (1741694) and under the Defense Advanced Research Project Agency (DARPA) DODOS project, Grant No. HR0011-15-C-0057. The views, opinions, and/or findings expressed are those of the authors and should not be interpreted as representing the official views or policies of the Department of Defense or the U.S. Government. The authors have no conflicts of interest to disclose.

References

1. N. Uesugi and T. Kimura, "Efficient second-harmonic generation in three-dimensional $LiNbO_3$ optical waveguide," *Appl. Phys. Lett.* **29**(9), 572–574 (1976).
2. R. Schmidt and I. Kaminow, "Metal-diffused optical waveguides in $LiNbO_3$," *Appl. Phys. Lett.* **25**(8), 458–460 (1974).
3. J. L. Jackel, C. Rice, and J. Veselka, "Proton exchange for high-index waveguides in $LiNbO_3$," *Appl. Phys. Lett.* **41**(7), 607–608 (1982).
4. P. Rabiei et al., "Heterogeneous lithium niobate photonics on silicon substrates," *Opt. Express* **21**(21), 25573–25581 (2013).
5. Partow Technologies, LLC, http://www.partow-tech.com/ (accessed: March 2022).
6. NanoLN, http://www.nanoln.com/ (accessed: March 2022).
7. Ngk insulators, Ltd., https://www.ngk-insulators.com/ (accessed March 2022).
8. Y. Kong et al., "Recent progress in lithium niobate: optical damage, defect simulation, and on-chip devices," *Adv. Mater.* **32**(3), 1806452 (2020).
9. Y. Xu et al., "Mitigating photorefractive effect in thin-film lithium niobate microring resonators," *Opt. Express* **29**(4), 5497–5504 (2021).
10. A. L. Kozub et al., "Polaronic enhancement of second-harmonic generation in lithium niobate," *Phys. Rev. B* **104**(17), 174110 (2021).
11. M. Boukhtouta et al., "Predictions on structural, electronic, optical and thermal properties of lithium niobate via first-principle computations," *Philos. Mag.* **100**(9), 1150–1171 (2020).
12. A. Rao et al., "Heterogeneous microring and Mach-Zehnder modulators based on lithium niobate and chalcogenide glasses on silicon," *Opt. Express* **23**(17), 22746–22752 (2015).
13. A. Rao et al., "Second-harmonic generation in periodically-poled thin film lithium niobate wafer-bonded on silicon," *Opt. Express* **24**(26), 29941–29947 (2016).
14. A. Honardoost et al., "Towards subterahertz bandwidth ultra-compact lithium niobate electrooptic modulators," *Opt. Express* **27**(5), 6495–6501 (2019).
15. M. Zhang et al., "Monolithic ultra-high-*Q* lithium niobate microring resonator," *Optica* **4**(12), 1536–1537 (2017).
16. R. Gao et al., "Broadband highly efficient nonlinear optical processes in on-chip integrated lithium niobate microdisk resonators of *Q*-factor above 10^8," *New J. Phys.* **23**(12), 123027 (2021).
17. K. Luke et al., "Wafer-scale low-loss lithium niobate photonic integrated circuits," *Opt. Express* **28**(17), 24452–24458 (2020).
18. J. Lin et al., "Advances in on-chip photonic devices based on lithium niobate on insulator," *Photonics Res.* **8**(12), 1910–1936 (2020).
19. Y. Jia, L. Wang, and F. Chen, "Ion-cut lithium niobate on insulator technology: recent advances and perspectives," *Appl. Phys. Rev.* **8**(1), 011307 (2021).
20. D. Sun et al., "Microstructure and domain engineering of lithium niobate crystal films for integrated photonic applications," *Light: Sci. Appl.* **9**(1), 197 (2020).
21. Y. Jiao et al., "Improvement on thermal stability of nano-domains in lithium niobate thin films," *Crystals* **10**(2), 74 (2020).
22. M. Younesi et al., "Periodic poling with a micrometer-range period in thin-film lithium niobate on insulator," *J. Opt. Soc. Am. B* **38**(3), 685–691 (2021).
23. B. J. Stanicki et al., "Surface domain engineering in lithium niobate," *OSA Contin.* **3**(2), 345–358 (2020).
24. Y. Liu et al., "On-chip erbium-doped lithium niobate microcavity laser," *Sci. China Phys. Mech. Astron.* **64**(3), 234262 (2021).

25. R. Gao et al., "On-chip ultra-narrow-linewidth single-mode microlaser on lithium niobate on insulator," *Opt. Lett.* **46**(13), 3131–3134 (2021).
26. Q. Luo et al., "On-chip erbium-doped lithium niobate microring lasers," *Opt. Lett.* **46**(13), 3275–3278 (2021).
27. X. Liu et al., "Tunable single-mode laser on thin film lithium niobate," *Opt. Lett.* **46**(21), 5505–5508 (2021).
28. D. Yin et al., "Electro-optically tunable microring laser monolithically integrated on lithium niobate on insulator," *Opt. Lett.* **46**(9), 2127–2130 (2021).
29. R. Zhang et al., "Integrated lithium niobate single-mode lasers by the Vernier effect," *Sci. China Phys. Mech. Astron.* **64**(9), 294216 (2021).
30. M. Yu et al., "Raman lasing and soliton mode-locking in lithium niobate microresonators," *Light: Sci. Appl.* **9**(1), 9 (2020).
31. D. Zhu et al., "Integrated photonics on thin-film lithium niobate," *Adv. Opt. Photonics* **13**(2), 242–352 (2021).
32. C. O. de Beeck et al., "III/V-on-lithium niobate amplifiers and lasers," *Optica* **8**(10), 1288–1289 (2021).
33. A. Shams-Ansari et al., "Electrically pumped laser transmitter integrated on thin-film lithium niobate," *Optica* **9**(4), 408–411 (2022).
34. A. Honardoost, K. Abdelsalam, and S. Fathpour, "Rejuvenating a versatile photonic material: thin-film lithium niobate," *Laser Photonics Rev.* **14**(9), 2000088 (2020).
35. Y. Qi and Y. Li, "Integrated lithium niobate photonics," *Nanophotonics* **9**(6), 1287–1320 (2020).
36. M. Xu et al., "Dual-polarization thin-film lithium niobate in-phase quadrature modulators for terabit-per-second transmission," *Optica* **9**(1), 61–62 (2022).
37. F. Arab Juneghani et al., "Demonstration of non-symmetric thin-film lithium niobate modulator with a 3-dB bandwidth beyond 100 GHz," in *CLEO: Sci. and Innov.*, Optical Society of America (2022).
38. C. Hu et al., "High-efficient coupler for thin-film lithium niobate waveguide devices," *Opt. Express* **29**(4), 5397–5406 (2021).
39. K. Abdelsalam et al., "Tunable dual-channel ultra-narrowband Bragg grating filter on thin-film lithium niobate," *Opt. Lett.* **46**(11), 2730–2733 (2021).
40. K. Abdelsalam et al., "Linear isolators using wavelength conversion," *Optica* **7**(3), 209–213 (2020).
41. X. Ye et al., "High-speed programmable lithium niobate thin film spatial light modulator," *Opt. Lett.* **46**(5), 1037–1040 (2021).
42. P. Franken et al., "Generation of optical harmonics," *Phys. Rev. Lett.* **7**(4), 118–119 (1961).
43. R. W. Boyd, *Nonlinear Optics*, Academic Press (2020).
44. A. Rao and S. Fathpour, "Second-harmonic generation in integrated photonics on silicon," *Phys. Status Solidi A* **215**(4), 1700684 (2018).
45. A. Rao and S. Fathpour, "Heterogeneous thin-film lithium niobate integrated photonics for electrooptics and nonlinear optics," *IEEE J. Sel. Top. Quantum Electron.* **24**(6), 8200912 (2018).
46. S. Fathpour, "Heterogeneous nonlinear integrated photonics," *IEEE J. Quantum Electron.* **54**(6), 6300776 (2018).
47. W. H. P. Pernice et al., "Second harmonic generation in phase matched aluminum nitride waveguides and micro-ring resonators," *Appl. Phys. Lett.* **100**(22), 223501 (2012).
48. S. May et al., "Second-harmonic generation in AlGaAs-on-insulator waveguides," *Opt. Lett.* **44**(6), 1339–1342 (2019).
49. L. Chang et al., "Heterogeneously integrated GaAs waveguides on insulator for efficient frequency conversion," *Laser Photonics Rev.* **12**(10), 1800149 (2018).
50. C. Xiong et al., "Integrated GaN photonic circuits on silicon (100) for second harmonic generation," *Opt. Express* **19**(11), 10462–10470 (2011).
51. D. N. Nikogosyan, *Nonlinear Optical Crystals: A Complete Survey*, Springer Science & Business Media (2006).
52. N. Li et al., "Aluminium nitride integrated photonics: a review," *Nanophotonics* **10**, 2347–2387 (2021).
53. H. Zhang et al., "Study of nonlinear optical effects in GaN: Mg epitaxial film," *Appl. Phys. Lett.* **69**(20), 2953–2955 (1996).
54. J. Webjorn, F. Laurell, and G. Arvidsson, "Fabrication of periodically domain-inverted channel waveguides in lithium niobate for second harmonic generation," *J. Lightwave Technol.* **7**(10), 1597–1600 (1989).
55. E. Lim, M. Fejer, and R. Byer, "Second-harmonic generation of green light in periodically poled planar lithium niobate waveguide," *Electron. Lett.* **25**(3), 174–175 (1989).
56. L. E. Myers et al., "Multigrating quasi-phase-matched optical parametric oscillator in periodically poled $LiNbO_3$," *Opt. Lett.* **21**(8), 591–593 (1996).
57. G. Miller et al., "42%-efficient single-pass CW second-harmonic generation in periodically poled lithium niobate," *Opt. Lett.* **22**(24), 1834–1836 (1997).
58. S. Fathpour, "Emerging heterogeneous integrated photonic platforms on silicon," *Nanophotonics* **4**(1), 143–164 (2015).
59. C. Lu et al., "Highly tunable birefringent phase-matched second-harmonic generation in an angle-cut lithium niobate-on-insulator ridge waveguide," *Opt. Lett.* **47**(5), 1081–1084 (2022).
60. R. Luo et al., "Optical parametric generation in a lithium niobate microring with modal phase matching," *Phys. Rev. Appl.* **11**(3), 034026 (2019).
61. A. Rao et al., "Second-harmonic generation in single-mode integrated waveguides based on mode-shape modulation," *Appl. Phys. Lett.* **110**(11), 111109 (2017).
62. J. Lin et al., "Broadband quasi-phase-matched harmonic generation in an on-chip monocrystalline lithium niobate microdisk resonator," *Phys. Rev. Lett.* **122**(17), 173903 (2019).
63. C. Wang et al., "Metasurface-assisted phase-matching-free second harmonic generation in lithium niobate waveguides," *Nat. Commun.* **8**(1), 2098 (2017).
64. C. Wang et al., "Second harmonic generation in nano-structured thin-film lithium niobate waveguides," *Opt. Express* **25**(6), 6963–6973 (2017).
65. R. Luo et al., "Highly tunable efficient second-harmonic generation in a lithium niobate nanophotonic waveguide," *Optica* **5**(8), 1006–1011 (2018).
66. J.-Y. Chen et al., "Modal phase matched lithium niobate nanocircuits for integrated nonlinear photonics," *OSA Contin.* **1**(1), 229–242 (2018).
67. R. Luo et al., "Semi-nonlinear nanophotonic waveguides for highly efficient second-harmonic generation," *Laser Photonics Rev.* **13**(3), 1800288 (2019).
68. C. Wang et al., "Integrated high quality factor lithium niobate microdisk resonators," *Opt. Express* **22**(25), 30924–30933 (2014).
69. S. Liu, Y. Zheng, and X. Chen, "Cascading second-order nonlinear processes in a lithium niobate-on-insulator microdisk," *Opt. Lett.* **42**(18), 3626–3629 (2017).
70. S. Liu et al., "Effective four-wave mixing in the lithium niobate on insulator microdisk by cascading quadratic processes," *Opt. Lett.* **44**(6), 1456–1459 (2019).
71. E. Lim et al., "Blue light generation by frequency doubling in periodically poled lithium niobate channel waveguide," *Electron. Lett.* **25**(11), 731–732 (1989).
72. L. E. Myers et al., "Quasi-phase-matched optical parametric oscillators in bulk periodically poled $LiNbO_3$," *J. Opt. Soc. Am. B* **12**(11), 2102–2116 (1995).
73. L. Chang et al., "Thin film wavelength converters for photonic integrated circuits," *Optica* **3**(5), 531–535 (2016).
74. J. T. Nagy and R. M. Reano, "Reducing leakage current during periodic poling of ion-sliced x-cut MgO doped lithium niobate thin films," *Opt. Mater. Express* **9**(7), 3146–3155 (2019).
75. A. Boes et al., "Efficient second harmonic generation in lithium niobate on insulator waveguides and its pitfalls," *J. Phys.: Photonics* **3**(1), 012008 (2021).

76. J. Zhao et al., "Poling thin-film x-cut lithium niobate for quasi-phase matching with sub-micrometer periodicity," *J. Appl. Phys.* **127**(19), 193104 (2020).
77. B. Slautin et al., "Domain structure formation by local switching in the ion sliced lithium niobate thin films," *Appl. Phys. Lett.* **116**(15), 152904 (2020).
78. J. T. Nagy and R. M. Reano, "Submicrometer periodic poling of lithium niobate thin films with bipolar preconditioning pulses," *Opt. Mater. Express* **10**(8), 1911–1920 (2020).
79. S. Reitzig et al., ""Seeing is believing"—in-depth analysis by co-imaging of periodically-poled x-cut lithium niobate thin films," *Crystals* **11**(3), 288 (2021).
80. R. K. Prasath et al., "Measurement of the internal electric field in periodically poled congruent lithium niobate crystals by far-field diffraction," *Appl. Opt.* **60**(13), 3791–3796 (2021).
81. A. Boes et al., "Improved second harmonic performance in periodically poled LNOI waveguides through engineering of lateral leakage," *Opt. Express* **27**(17), 23919–23928 (2019).
82. A. Rao et al., "Actively-monitored periodic-poling in thin-film lithium niobate photonic waveguides with ultrahigh nonlinear conversion efficiency of 4600% W^{-1} cm^{-2}," *Opt. Express* **27**(18), 25920–25930 (2019).
83. J.-Y. Chen et al., "Ultra-efficient frequency conversion in quasi-phase-matched lithium niobate microrings," *Optica* **6**(9), 1244–1245 (2019).
84. J. Lu et al., "Toward 1% single-photon anharmonicity with periodically poled lithium niobate microring resonators," *Optica* **7**(12), 1654–1659 (2020).
85. Z. Hao et al., "Second-harmonic generation using d_{33} in periodically poled lithium niobate microdisk resonators," *Photonics Res.* **8**(3), 311–317 (2020).
86. C. Wang et al., "Ultrahigh-efficiency wavelength conversion in nanophotonic periodically poled lithium niobate waveguides," *Optica* **5**(11), 1438–1441 (2018).
87. J.-Y. Chen et al., "Efficient parametric frequency conversion in lithium niobate nanophotonic chips," *OSA Contin.* **2**(10), 2914–2924 (2019).
88. J. Zhao et al., "Shallow-etched thin-film lithium niobate waveguides for highly-efficient second-harmonic generation," *Opt. Express* **28**(13), 19669–19682 (2020).
89. C. Lu et al., "Second and cascaded harmonic generation of pulsed laser in a lithium niobate on insulator ridge waveguide," *Opt. Express* **30**(2), 1381–1387 (2022).
90. J. Lu et al., "Periodically poled thin-film lithium niobate microring resonators with a second-harmonic generation efficiency of 250,000%/W," *Optica* **6**(12), 1455–1460 (2019).
91. J. Lin et al., "Phase-matched second-harmonic generation in an on-chip $LiNbO_3$ microresonator," *Phys. Rev. Appl.* **6**(1), 014002 (2016).
92. M. Li et al., "Photon-photon quantum phase gate in a photonic molecule with $\chi^{(2)}$ nonlinearity," *Phys. Rev. Appl.* **13**(4), 044013 (2020).
93. M. Heuck, K. Jacobs, and D. R. Englund, "Controlled-phase gate using dynamically coupled cavities and optical nonlinearities," *Phys. Rev. Lett.* **124**(16), 160501 (2020).
94. R. Wolf et al., "Quasi-phase-matched nonlinear optical frequency conversion in on-chip whispering galleries," *Optica* **5**(7), 872–875 (2018).
95. L. Zhang et al., "Dual-periodically poled lithium niobate microcavities supporting multiple coupled parametric processes," *Opt. Lett.* **45**(12), 3353–3356 (2020).
96. G. Lin et al., "Wide-range cyclic phase matching and second harmonic generation in whispering gallery resonators," *Appl. Phys. Lett.* **103**(18), 181107 (2013).
97. R. Luo et al., "On-chip second-harmonic generation and broadband parametric down-conversion in a lithium niobate microresonator," *Opt. Express* **25**(20), 24531–24539 (2017).
98. R. Wu et al., "Lithium niobate micro-disk resonators of quality factors above 10^7," *Opt. Lett.* **43**(17), 4116–4119 (2018).
99. A. Fedotova et al., "Second-harmonic generation in resonant nonlinear metasurfaces based on lithium niobate," *Nano Lett.* **20**(12), 8608–8614 (2020).
100. J. Ma et al., "Nonlinear lithium niobate metasurfaces for second harmonic generation," *Laser Photonics Rev.* **15**(5), 2000521 (2021).
101. Y. Li et al., "Optical anapole mode in nanostructured lithium niobate for enhancing second harmonic generation," *Nanophotonics* **9**(11), 3575–3585 (2020).
102. F. Renaud et al., "Second-harmonic-generation enhancement in cavity resonator integrated grating filters," *Opt. Lett.* **44**(21), 5198–5201 (2019).
103. S. Yuan et al., "Strongly enhanced second harmonic generation in a thin film lithium niobate heterostructure cavity," *Phys. Rev. Lett.* **127**(15), 153901 (2021).
104. Y. Li et al., "Recent progress of second harmonic generation based on thin film lithium niobate," *Chin. Opt. Lett.* **19**(6), 060012 (2021).
105. H. Jiang et al., "Nonlinear frequency conversion in one dimensional lithium niobate photonic crystal nanocavities," *Appl. Phys. Lett.* **113**(2), 021104 (2018).
106. M. Li et al., "High-Q 2D lithium niobate photonic crystal slab nanoresonators," *Laser Photonics Rev.* **13**(5), 1800228 (2019).
107. J. S. Dam, P. Tidemand-Lichtenberg, and C. Pedersen, "Room-temperature mid-infrared single-photon spectral imaging," *Nat. Photonics* **6**(11), 788–793 (2012).
108. G. Li et al., "Broadband sum-frequency generation using d_{33} in periodically poled $LiNbO_3$ thin film in the telecommunications band," *Opt. Lett.* **42**(5), 939–942 (2017).
109. Z. Hao et al., "Sum-frequency generation in on-chip lithium niobate microdisk resonators," *Photonics Res.* **5**(6), 623–628 (2017).
110. X. Ye et al., "Sum-frequency generation in lithium-niobate-on-insulator microdisk via modal phase matching," *Opt. Lett.* **45**(2), 523–526 (2020).
111. A. K. Hansen et al., "Highly efficient single-pass sum frequency generation by cascaded nonlinear crystals," *Opt. Lett.* **40**(23), 5526–5529 (2015).
112. T. Sjaardema, A. Rao, and S. Fathpour, "Third-and fourth-harmonic generation in cascaded periodically-poled lithium niobate ultracompact waveguides on silicon," in *CLEO: Sci. and Innov.*, Optical Society of America, p. STh1J-1 (2019).
113. S. Lauria and M. F. Saleh, "Mixing second- and third-order nonlinear interactions in nanophotonic lithium-niobate waveguides," *Phys. Rev. A* **105**(4), 043511 (2021).
114. R. Wolf et al., "Cascaded second-order optical nonlinearities in on-chip micro rings," *Opt. Express* **25**(24), 29927–29933 (2017).
115. D. D. Hickstein et al., "High-harmonic generation in periodically poled waveguides," *Optica* **4**(12), 1538–1544 (2017).
116. D. Wang et al., "Cascaded sum-frequency generation and electro-optic polarization coupling in the PPLNOI ridge waveguide," *Opt. Express* **27**(11), 15283–15288 (2019).
117. Y. J. Ding, "Progress in terahertz sources based on difference-frequency generation," *J. Opt. Soc. Am. B* **31**(11), 2696–2711 (2014).
118. C. Erny et al., "Mid-infrared difference-frequency generation of ultrashort pulses tunable between 3.2 and 4.8 μm from a compact fiber source," *Opt. Lett.* **32**(9), 1138–1140 (2007).
119. J. Mishra et al., "Mid-infrared nonlinear optics in thin-film lithium niobate on sapphire," *Optica* **8**(6), 921–924 (2021).
120. J. Yang and C. Wang, "Efficient terahertz generation scheme in a thin-film lithium niobate-silicon hybrid platform," *Opt. Express* **29**(11), 16477–16486 (2021).
121. F. Kaufmann et al., "On-chip optical parametric amplification in subwavelength lithium niobate nanowaveguides," in *Integr.*

Photonics Res., Silicon and Nanophotonics, Optical Society of America, p. JTu5A-52 (2018).
122. J.-Y. Chen et al., "Phase-sensitive amplification in nanophotonic periodically poled lithium niobate waveguides," in *CLEO: Sci. and Innov.*, Optical Society of America, p. SM3L-5 (2020).
123. L. Ledezma et al., "Intense optical parametric amplification in dispersion engineered nanophotonic lithium niobate waveguides," arXiv:2104.08262 (2021).
124. M. Jankowski et al., "Quasi-static optical parametric amplification," *Optica* **9**(3), 273–279 (2022).
125. J. Lu et al., "Ultralow-threshold thin-film lithium niobate optical parametric oscillator," *Optica* **8**(4), 539–544 (2021).
126. D. C. Burnham and D. L. Weinberg, "Observation of simultaneity in parametric production of optical photon pairs," *Phys. Rev. Lett.* **25**(2), 84–87 (1970).
127. T. Jennewein et al., "Quantum cryptography with entangled photons," *Phys. Rev. Lett.* **84**(20), 4729–4732 (2000).
128. D. Bouwmeester et al., "Experimental quantum teleportation," *Nature* **390**(6660), 575–579 (1997).
129. B. S. Elkus et al., "Generation of broadband correlated photon-pairs in short thin-film lithium-niobate waveguides," *Opt. Express* **27**(26), 38521–38531 (2019).
130. B. S. Elkus et al., "Quantum-correlated photon-pair generation via cascaded nonlinearity in an ultra-compact lithium-niobate nano-waveguide," *Opt. Express* **28**(26), 39963–39975 (2020).
131. G.-T. Xue et al., "Ultrabright multiplexed energy-time-entangled photon generation from lithium niobate on insulator chip," *Phys. Rev. Appl.* **15**(6), 064059 (2021).
132. J. Zhao et al., "High quality entangled photon pair generation in periodically poled thin-film lithium niobate waveguides," *Phys. Rev. Lett.* **124**(16), 163603 (2020).
133. U. A. Javid et al., "Ultrabroadband entangled photons on a nanophotonic chip," *Phys. Rev. Lett.* **127**(18), 183601 (2021).
134. Z. Ma et al., "Ultrabright quantum photon sources on chip," *Phys. Rev. Lett.* **125**(26), 263602 (2020).
135. S. Saravi, T. Pertsch, and F. Setzpfandt, "Lithium niobate on insulator: an emerging platform for integrated quantum photonics," *Adv. Opt. Mater.* **9**(22), 2100789 (2021).
136. G. I. Stegeman, D. J. Hagan, and L. Torner, "$\chi^{(2)}$ cascading phenomena and their applications to all-optical signal processing, mode-locking, pulse compression and solitons," *Opt. Quantum Electron.* **28**(12), 1691–1740 (1996).
137. T. Sjaardema et al., "Low-harmonic generation in cascaded thin-film lithium niobate waveguides," *Adv. Photonics Res.* **2022**, 2100262 (2022).
138. M. Wang et al., "Strong nonlinear optics in on-chip coupled lithium niobate microdisk photonic molecules," *New J. Phys.* **22**(7), 073030 (2020).
139. M. Jankowski et al., "Ultrabroadband nonlinear optics in nanophotonic periodically poled lithium niobate waveguides," *Optica* **7**(1), 40–46 (2020).
140. M. Malinowski et al., "Towards on-chip self-referenced frequency-comb sources based on semiconductor mode-locked lasers," *Micromachines* **10**(6), 391 (2019).
141. S. Mosca et al., "Modulation instability induced frequency comb generation in a continuously pumped optical parametric oscillator," *Phys. Rev. Lett.* **121**(9), 093903 (2018).
142. A. W. Bruch et al., "Pockels soliton microcomb," *Nat. Photonics* **15**(1), 21–27 (2021).
143. R. Ikuta et al., "Frequency comb generation in a quadratic nonlinear waveguide resonator," *Opt. Express* **26**(12), 15551–15558 (2018).
144. X. Wang et al., "2 μm optical frequency comb generation via optical parametric oscillation from a lithium niobate optical superlattice box resonator," *Photonics Res.* **10**(2), 509–515 (2022).
145. N. Amiune et al., "Optical-parametric-oscillation-based $\chi^{(2)}$ frequency comb in a lithium niobate microresonator," *Opt. Express* **29**(25), 41378–41387 (2021).
146. I. Hendry et al., "Experimental observation of internally pumped parametric oscillation and quadratic comb generation in a $\chi^{(2)}$ whispering-gallery-mode microresonator," *Opt. Lett.* **45**(5), 1204–1207 (2020).
147. J. Szabados et al., "Frequency comb generation via cascaded second-order nonlinearities in microresonators," *Phys. Rev. Lett.* **124**(20), 203902 (2020).
148. Y. Hu et al., "High-efficiency and broadband electro-optic frequency combs enabled by coupled micro-resonators," arXiv: 2111.14743 (2021).
149. T. Ren et al., "An integrated low-voltage broadband lithium niobate phase modulator," *IEEE Photonics Technol. Lett.* **31**(11), 889–892 (2019).
150. M. Xu et al., "Integrated lithium niobate modulator and frequency comb generator based on Fabry-Perot resonators," in *CLEO: Appl. and Technol.*, Optical Society of America, p. JTh2B-27 (2020).
151. M. Zhang et al., "Broadband electro-optic frequency comb generation in a lithium niobate microring resonator," *Nature* **568**(7752), 373–377 (2019).
152. H. Sun et al., "Recent progress in integrated electro-optic frequency comb generation," *J. Semicond.* **42**(4), 041301 (2021).
153. R. Normandin and G. I. Stegeman, "Nondegenerate four-wave mixing in integrated optics," *Opt. Lett.* **4**(2), 58–59 (1979).
154. B. J. Eggleton et al., "Brillouin integrated photonics," *Nat. Photonics* **13**(10), 664–677 (2019).
155. R. Loudon, "The Raman effect in crystals," *Adv. Phys.* **13**(52), 423–482 (1964).
156. L. Cai et al., "Acousto-optical modulation of thin film lithium niobate waveguide devices," *Photonics Res.* **7**(9), 1003–1013 (2019).
157. A. L. Gaeta, M. Lipson, and T. J. Kippenberg, "Photonic-chip-based frequency combs," *Nat. Photonics* **13**(3), 158–169 (2019).
158. Y. Okawachi et al., "Chip-based self-referencing using integrated lithium niobate waveguides," *Optica* **7**(6), 702–707 (2020).
159. M. Yu et al., "Coherent two-octave-spanning supercontinuum generation in lithium-niobate waveguides," *Opt. Lett.* **44**(5), 1222–1225 (2019).
160. J. Lu et al., "Octave-spanning supercontinuum generation in nanoscale lithium niobate waveguides," *Opt. Lett.* **44**(6), 1492–1495 (2019).
161. Y. He et al., "Self-starting bi-chromatic $LiNbO_3$ soliton microcomb," *Optica* **6**(9), 1138–1144 (2019).
162. Z. Gong et al., "Near-octave lithium niobate soliton microcomb," *Optica* **7**(10), 1275–1278 (2020).
163. Z. Gong et al., "Monolithic Kerr and electro-optic hybrid microcombs," arXiv:2202.02920 (2022).
164. Z. Gong et al., "Soliton microcomb generation at 2 μm in z-cut lithium niobate microring resonators," *Opt. Lett.* **44**(12), 3182–3185 (2019).
165. C. Wang et al., "Monolithic lithium niobate photonic circuits for Kerr frequency comb generation and modulation," *Nat. Commun.* **10**(1), 978 (2019).
166. A. Honardoost et al., "Cascaded integration of optical waveguides with third-order nonlinearity with lithium niobate waveguides on silicon substrates," *IEEE Photonics J.* **10**(3), 4500909 (2018).
167. G. F. C. Gonzalez et al., "Design of a hybrid chalcogenide-glass on lithium-niobate waveguide structure for high-performance cascaded third-and second-order optical nonlinearities," *Appl. Opt.* **58**(13), D1–D6 (2019).
168. Y. Zhao et al., "Compact lithium-niobate-on-insulator polarization rotator based on asymmetric hybrid plasmonics waveguide," *IEEE Photonics J.* **13**(4), 4800105 (2021).
169. Z. Chen et al., "Broadband adiabatic polarization rotator-splitter based on a lithium niobate on insulator platform," *Photonics Res.* **9**(12), 2319–2324 (2021).
170. X. Wang et al., "Efficient polarization splitter-rotator on thin-film lithium niobate," *Opt. Express* **29**(23), 38044–38052 (2021).

171. M. Cai et al., "Erbium-doped lithium niobate thin film waveguide amplifier with 16 dB internal net gain," *IEEE J. Sel. Top. Quantum Electron.* **28**(3), 8200608 (2021).
172. Q. Luo et al., "On-chip erbium-doped lithium niobate waveguide amplifiers," *Chin. Opt. Lett.* **19**(6), 060008 (2021).
173. J. Zhou et al., "On-chip integrated waveguide amplifiers on erbium-doped thin-film lithium niobate on insulator," *Laser Photonics Rev.* **15**(8), 2100030 (2021).

Milad Gholipour Vazimali is a PhD candidate at CREOL, the College of Optics and Photonics at the University of Central Florida (UCF). He received his BS degree in electrical engineering from Sharif University of Technology in 2014. He received his first MS degree in semiconductor devices from the University of Tehran in 2017 and his second MS degree in optics from UCF in 2020. His current research interests include photonic integrated circuits, nonlinear optics, and optoelectronic devices.

Sasan Fathpour is a professor at CREOL, the College of Optics and Photonics at UCF with a secondary joint appointment at the Department of Electrical and Computer Engineering. He received his PhD in electrical engineering from the University of Michigan, Ann Arbor, in 2005. His current research interests include heterogeneous integrated photonics, nonlinear integrated optics, silicon photonics, and unconventional photonic platforms operating in the mid-wave- and near-infrared and visible wavelength ranges. He has received the US National Science Foundation CAREER Award (2012) and the Office of Naval Research Young Investigator Program Award (2013). He is a coauthor of over 190 publications, including about 80 journal papers, 6 book chapters, and 3 patents. He coedited the book *Silicon Photonics for Telecommunications and Biomedicine*, CRC Press (2012). He is the cofounder of Partow Technologies, LLC. He is an associate editor of Optica and has been a guest editor for the SPIE *Journal of Nanophotonics*. He is a fellow of Optica, a senior member of SPIE and IEEE, and a member of MRS.

Review Article

ADVANCED PHOTONICS

Advances in lithium niobate photonics: development status and perspectives

Guanyu Chen,[a] Nanxi Li,[b] Jun Da Ng,[a] Hong-Lin Lin,[a] Yanyan Zhou,[b] Yuan Hsing Fu,[b] Lennon Yao Ting Lee,[b] Yu Yu,[c,*] Ai-Qun Liu,[d] and Aaron J. Danner[a,*]

[a]National University of Singapore, Department of Electrical and Computer Engineering, Singapore
[b]A*STAR (Agency for Science, Technology and Research), Institute of Microelectronics, Singapore
[c]Huazhong University of Science and Technology, School of Optical and Electronic Information, Wuhan National Laboratory for Optoelectronics, Wuhan, China
[d]Nanyang Technological University, Quantum Science and Engineering Centre, Singapore

Abstract. Lithium niobate (LN) has experienced significant developments during past decades due to its versatile properties, especially its large electro-optic (EO) coefficient. For example, bulk LN-based modulators with high speeds and a superior linearity are widely used in typical fiber-optic communication systems. However, with ever-increasing demands for signal transmission capacity, the high power and large size of bulk LN-based devices pose great challenges, especially when one of its counterparts, integrated silicon photonics, has experienced dramatic developments in recent decades. Not long ago, high-quality thin-film LN on insulator (LNOI) became commercially available, which has paved the way for integrated LN photonics and opened a hot research area of LN photonics devices. LNOI allows a large refractive index contrast, thus light can be confined within a more compact structure. Together with other properties of LN, such as nonlinear/acousto-optic/pyroelectric effects, various kinds of high-performance integrated LN devices can be demonstrated. A comprehensive summary of advances in LN photonics is provided. As LN photonics has experienced several decades of development, our review includes some of the typical bulk LN devices as well as recently developed thin film LN devices. In this way, readers may be inspired by a complete picture of the evolution of this technology. We first introduce the basic material properties of LN and several key processing technologies for fabricating photonics devices. After that, various kinds of functional devices based on different effects are summarized. Finally, we give a short summary and perspective of LN photonics. We hope this review can give readers more insight into recent advances in LN photonics and contribute to the further development of LN related research.

Keywords: lithium niobate; etching; photonics; integrated optics; nanotechnology; devices.

Received Jan. 16, 2022; revised manuscript received Apr. 12, 2022; accepted for publication Apr. 26, 2022; published online Jun. 8, 2022.

[DOI: 10.1117/1.AP.4.3.034003]

1 Introduction

Lithium niobate ($LiNbO_3$, LN) is one of the most important artificial materials and has been widely used in the photonics area since it was first discovered to have a ferroelectric property in 1949.[1] Compared with other material systems, LN has various superior characteristics, such as a wide transparency window (400 nm to 5 μm) and large electro-optic (EO)/nonlinear-optic (NLO)/acousto-optic (AO)/pyroelectric coefficients, as well as stable chemical and physical properties.[2–9] Based on these effects, various kinds of photonics devices have been demonstrated. For example, the large EO property of LN can be used for the realization of high-speed modulators. As there is no carrier dynamic process involved, such as the case in its counterparts including silicon (Si)[10] and indium phosphide (InP),[11] both the speed and linearity of LN modulators show advantages compared with other kinds of modulators. Therefore, in current fiber-optic communication systems, LN-based modulators have been widely used.[3] The second- and third-order nonlinear effects

*Address all correspondence to Yu Yu, yuyu@mail.hust.edu.cn; Aaron J. Danner, adanner@nus.edu.sg

in LN can also be used for various nonlinear optic conversions, covering both classical and quantum application scenarios.[12–15] Other properties of LN are also widely utilized for fabricating high-performance functional devices.[16–18]

For LN photonics, one of the challenges is how to effectively confine the light and thus enhance its interaction with the LN crystal. In a typical bulk LN (planar device), light is confined inside a planar waveguide formed by ion-in diffusion or proton exchange (PE).[19–21] In such a method, the refractive index contrast is usually very small (~0.02), therefore bulk LN-based devices have a large feature size and relatively poor performance even though they have been successfully used for decades. The problem of a poor index contrast hampers further development of LN photonics as high power and large device sizes are not compatible with desired trends in energy efficiency and integration. In the meantime, integrated platforms, such as silicon photonics,[22–28] have gotten more attention as silicon photonics in particular has become one of LN's strongest competitors due to its complementary metal oxide semiconductor (CMOS) compatibility, even though it lacks EO effects. This situation may yet change, though, as high-quality thin film LN (TFLN) with a controlled thickness has become available through the lapping and polishing[29,30] and crystal ion slicing (CIS) methods.[8,9] These high-quality TFLNs can be bonded onto an insulator with a lower refractive index (such as silicon oxide), and then an LN on insulator (LNOI) structure similar to silicon on insulator (SOI) is realized. The principal benefit from the large refractive index contrast of LNOI is that much more compact devices can be integrated on the same single chip by patterning three-dimensional (3D) structures using various developed etching technologies.[31–33] In addition, TFLN can also be bonded to other material platforms that are lithographically patterned, where LN serves as a thin layer of unpatterned film and the light from waveguides or devices fabricated in the bonded platform interacts with it.[34,35] Relying on developed processing technologies, LN-based photonics devices with a high performance, especially integrated devices, have experienced a rapid development during recent years and many different structures for various application scenarios have been demonstrated,[2–9] showing that an era of LN photonics is coming.

In this review, we try to comprehensively summarize recent advances of LN photonics. The content of this review is not only focused on the integrated LN photonics devices that have appeared in recent years, but rather some bulk LN-based devices and related processing technologies; in this way, the research community can reach a better, comprehensive understanding of the technology evolution of LN photonics. We hope readers may be inspired by this review and then contribute to the further development of LN photonics. This review is organized as follows. In Sec. 2, we first introduce the material properties of LN, which form the basis of different kinds of applications. Then, we introduce several key processing technologies of LN photonics in Sec. 3. In Sec. 4, various kinds of functional devices are demonstrated, ranging from passive to active and innovative devices. Last, we give a summary and outlook of LN photonics. An illustration of the overall content of this review is shown in Fig. 1.

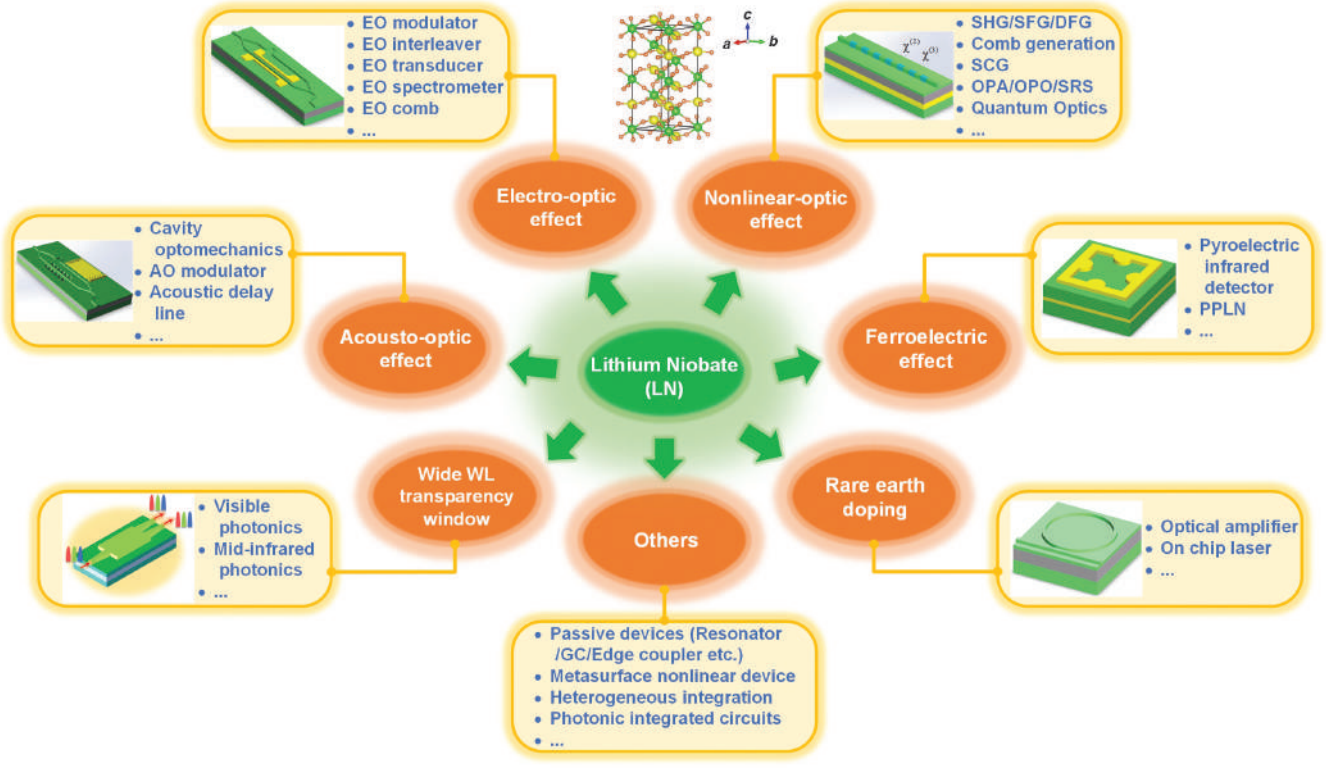

Fig. 1 Overview of LN photonics. Top middle inset is LN crystal structure. EO, electro-optic; SHG, second harmonic generation; SFG/DFG, sum/difference frequency generation; SCG, supercontinuum generation; OPA/OPO, optical parametric amplification/oscillation; SRS, stimulated Raman scattering; PPLN, periodically poled lithium niobate; GC, grating coupler; WL, wavelength; AO, acousto-optic.

2 Material Properties

LN does not exist in the natural world and is a purely artificial inorganic material. It is composed of lithium, niobium, and oxygen. People usually refer to LN as a distorted perovskite type of crystal. In 1966, Bell Labs demonstrated single crystal LN and analyzed its material properties comprehensively.[36–40] LN has a trigonal crystal structure (as shown in Fig. 1; top middle inset) and lacks inversion symmetry. There are many unique features of LN, such as a wide operational wavelength window, electro-optic (Pockels) effect, nonlinear optical polarizability, AO effect, rare earth doping possibility, pyroelectric effect, etc. These effects can be used for various applications, especially in photonics devices.

2.1 Basic Properties

LN is a birefringent crystal, and its ordinary (n_o) and extraordinary (n_e) refractive indices are 2.341 and 2.2547 at 500 nm wavelength,[41] respectively. It has a wide wavelength transparency window, covering from the visible (400 nm) to the mid-infrared (5 μm),[42] which makes it an attractive platform for many different applications. In the visible range, some applications, such as frequency metrology, quantum communication/computation, and light detection and ranging (LiDAR), can be realized based on the LN platform.[42] While in the short infrared range, especially near 1550 nm which is important for telecommunications, LN has been widely used for light modulation based on both bulk LN and TFLN.[31,43] For longer infrared wavelengths, some nonlinear optic conversions can be realized using LN.[44] Ferroelectric LN has a large bandgap, which is calculated to be about 4.71 eV.[45] A summary of LN material properties is shown in Table 1. Some details of these properties will be discussed in the remaining subsections and more details related to functional devices that exploit the various properties shown in Table 1 can be found in Sec. 4.

2.2 Electro-Optic Properties

In an anisotropic material, the coefficients of the impermeability tensor $(1/n^2)_i$, which change with increasing electric field strength, can be described by Eq. (1), where r_{ij} are known as the EO coefficients. As LN is a class 3m (ditrigonal-pyramidal) crystal, the EO coefficients can be described according to Eq. (2). The largest (z-oriented) refractive index changes with respect to an applied (z-oriented) voltage can be described by Eq. (3), where n_e is the extraordinary refractive index and E_z is the applied positive electrical field. As the relation between the refractive index change and the applied electrical field is linear, such an effect is also recognized as a linear EO effect or Pockels effect. By controlling the direction of the electric field, either an increase or a decrease in refractive index change can be obtained. For LN, r_{33} (~30.9 pm/V) is most widely used for the design of EO devices,[41] and this relatively high value is one of its main advantages. Many different kinds of modulators and EO tuning devices are reported based on such a property:[31,52]

$$\Delta\left(\frac{1}{n^2}\right)_i = \sum_i r_{ij}E_j, \tag{1}$$

Table 1 Material property summary of LN.

Category	Typical values/characteristics	Reference
Crystal structure	Trigonal	38
Refractive index	n_o/n_e: 2.341/2.2547 @ 500 nm	41
Transparency window	400 to 5000 nm	42
Bandgap	4.71 eV	45
Electro-optic coefficients	$r_{13} = 9.6$ pm/V; $r_{22} = 6.8$ pm/V; $r_{33} = 30.9$ pm/V; $r_{42} = 32.6$ pm/V	41
Second-order nonlinear susceptibility	d_{22} (1.058 μm) $= 2.46 \pm 0.23$ pm/V; d_{31} (1.058 μm) $= -4.64 \pm 0.66$ pm/V; d_{33} (1.058 μm) $= -41.7 \pm 7.8$ pm/V	46
Third-order nonlinear susceptibility	$\chi^{(3)} = (0.61 \pm 0.092) \times 10^4$ pm^2/V^2 @ 1.047 μm	47
Photo-elastic constants	$p_{11} = -0.026$; $p_{12} = 0.09$; $p_{13} = 0.133$; $p_{14} = -0.075$; $p_{31} = 0.179$; $p_{33} = 0.071$; $p_{41} = -0.151$; $p_{44} = 0.146$ (dimensionless)	2
Pyroelectric coefficient	-4×10^{-9} C $\cdot$ cm^{-2} $\cdot$ °C^{-1} at 25°C	48
Thermal conductivity	~5.234 W/(m $\cdot$ K) (a- or c-oriented)	49
Thermo-optic coefficient	$\sim 2.5 \times 10^{-6}$ K^{-1} (337 K, 1523 nm, ordinary) $\sim 4 \times 10^{-5}$ K^{-1} (337 K, 1523 nm, extraordinary)[a]	50
Piezoelectric strain coefficients	$d_{15} = 6.8 \times 10^{-11}$ C $\cdot$ N^{-1}; $d_{22} = 2.1 \times 10^{-11}$ C $\cdot$ N^{-1}; $d_{31} = -0.1$ C $\cdot$ N^{-1}; $d_{33} = 0.6$ C $\cdot$ N^{-1}	51

[a]Extracted from the measured data shown in the figures of Ref. 50.

$$r_{ij} = \begin{bmatrix} 0 & -r_{22} & r_{13} \\ 0 & r_{22} & r_{13} \\ 0 & 0 & r_{33} \\ 0 & r_{42} & 0 \\ r_{42} & 0 & 0 \\ r_{22} & 0 & 0 \end{bmatrix}, \tag{2}$$

$$\Delta n = -\frac{1}{2} n_e^3 r_{33} E_z. \tag{3}$$

2.3 Nonlinear Optic Properties

Another attractive property of LN is its high second- ($\chi^{(2)}$) and third-order ($\chi^{(3)}$) nonlinear susceptibilities. The second-order non-susceptibility of LN can be described by the two dimensional (2D) matrix shown in Eq. (4), where P_x, P_y, P_z are the electric polarization components, E_x, E_y, E_z are the electric field components, and d_{ij} are the second-order nonlinear susceptibility coefficients. For LN, typical values of d_{22}, d_{31}, and d_{33} are 2.46, −4.64, and −41.7 pm/V,[46] respectively. In addition, the third-order nonlinearity coefficient ($\chi^{(3)}$) of LN is estimated to be around $(0.61 \pm 0.092) \times 10^4$ pm^2/V^2.[47] Both the high second- and third-order nonlinearities make LN an attractive platform for various kinds of applications, such as second harmonic generation (SHG),[12,13,53–66] sum frequency generation (SFG),[67,68] difference frequency generation (DFG),[44] third harmonic generation (THG),[62,69] optical parametric amplification/oscillation (OPA/OPO),[70,71] stimulated Raman scattering (SRS),[72,73] frequency comb,[74–77] supercontinuum generation (SCG),[64,78,79] and photon pair generation.[80–83] Section 4 discusses these applications in detail.

$$\begin{pmatrix} P_x \\ P_y \\ P_z \end{pmatrix} = 2 \times \begin{pmatrix} 0 & 0 & 0 & 0 & d_{31} & -d_{22} \\ -d_{22} & d_{22} & 0 & d_{31} & 0 & 0 \\ d_{31} & d_{31} & d_{33} & 0 & 0 & 0 \end{pmatrix} \begin{pmatrix} E_x^2 \\ E_y^2 \\ E_z^2 \\ 2E_zE_y \\ 2E_zE_x \\ 2E_xE_y \end{pmatrix}. \tag{4}$$

2.4 Acousto-Optic Properties

When acoustic waves pass through a medium, they will cause elongation and local compression of the medium to produce elastic strain. The strain changes periodically with space and time, causing a medium to appear dense and then rare, just like a phase grating. Diffraction will appear when light passes through such a medium disturbed by acoustic waves, which is known as the AO effect (sometimes, it is also regarded as the photoelastic effect). The anisotropic AO relationship between the strain and the refractive index can be described by Eq. (5),[2] where $\Delta(1/n^2)_{ij}$ is a second rank tensor describing the refractive index change, S_{kl} is the second rank strain tensor, and p_{ijkl} is the fourth rank AO/photoelastic tensor. The detailed photoelastic coefficients of LN are shown in Table 1. The large photoelastic coefficients of LN together with its significant piezoelectric effect (for efficient acoustic waves launching) make multiphysics functional devices possible, such as AO modulators. Different from EO modulators, an AO modulator has bandpass frequency selectivity, which can complement low pass EO modulators:

$$\Delta\left(\frac{1}{n^2}\right)_{ij} = \sum_{k,l} p_{ijkl} S_{kl}. \tag{5}$$

2.5 Ferroelectric Properties

LN was reported to have ferroelectric properties as early as 1949,[1] which means it exhibits spontaneous polarization characteristics with a nonzero electric dipole moment when there is no external electrical field. Such a property is commonly used for photonics application. For example, periodically inverting the crystal polarization direction of LN by applying a high electric field (∼22 kV/mm) to form periodically poled LN (PPLN) can be used for improving nonlinear conversion (examples are discussed in Sec. 4.3).[80] For ferroelectric materials such as LN, the relationship between temperature variation and polarization intensity is usually described by the pyroelectric effect.[2] In a pyroelectric crystal, varying the temperature will modify the positions of the atoms within the crystal structure; thus, its spontaneous material polarization will change correspondingly. Such a change in polarization state will result in a voltage rise across the crystal.[2] If two surfaces (such as the top and bottom surfaces of Z-cut LN) of a crystal are covered with electrodes, there can be a current in the externally connected circuit. Such a current is proportional to the rate of temperature change and can be described by Eq. (6),[84] where I is the current, $P(T)$ is the pyroelectric coefficient, A is the surface area, and $\mathrm{d}T/\mathrm{d}t$ is the temperature change rate. For LN, $P(T)$ was measured to be -4×10^{-9} C · cm^{-2} · °C^{-1} at 25°C.[48] An intrinsically high pyroelectric coefficient in LN makes it a suitable platform for low cost and uncooled pyroelectrical photodetectors.

$$I = P(T) A \frac{\mathrm{d}T}{\mathrm{d}t}. \tag{6}$$

2.6 Thermo-Optic Properties

The thermal-optic (TO) coefficient of LN can be described by Eq. (7),[50] where n_i is the refractive index ($i = o$ represents ordinary, $i = e$ represents extraordinary), T is the temperature, λ_L is the wavelength, l is the etalon length, $\Delta T_{\pi/2}$ is the temperature variation needed for complete detuning of the optical cavity, and $\alpha(T)$ is the thermal expansion of LN along the light propagation direction. Due to the birefringence property of LN, the thermal optical coefficient of LN is different for ordinary and extraordinary light. According to one measured result,[50] the thermal optical coefficients of LN at around 337 K and 1523 nm are about 2.5×10^{-5} and 4×10^{-5} K^{-1} for ordinary and extraordinary light, respectively. The thermal conductivity of LN can be calculated according to Eq. (8), where κ is the thermal conductivity, ρ is the density, C_p is the specific heat, and η is the thermal diffusion coefficient. The thermal conductivity of LN is also crystal orientation dependent. However, the difference is

too small to distinguish. A typical value of thermal conductivity for either a- or c-oriented LN is around 5.234 $\mathrm{W}/(\mathrm{m}\cdot\mathrm{K})$.[49] Although these properties are not the highest among other materials, the TO effect in LN has still attracted some attention as it has a higher tuning efficiency and superior DC stability than the EO effect.[85–87] Slower TO effect-based devices can be good complements to EO devices, especially in some areas where switching speed is not the primary consideration, such as in the case during calibration or tuning. One example is that the thermal tuning blocks can be used as phase shifters to control modulation bias points of an IQ modulator.[88] For TFLN devices, the thermal tuning efficiency can also be improved by etching away underlying oxide.[85,87] With the development of integrated LN photonics, TO-based devices will have more and more application scenarios.

$$\frac{\mathrm{d}n_i}{\mathrm{d}T}=\frac{\lambda_L}{4l\Delta T_{\pi/2}}n_i\alpha(T), \tag{7}$$

$$\kappa=\rho C_p\eta. \tag{8}$$

2.7 Rare Earth Doping

Rare earth ions are solid state emitters with stable optical transitions with long lifetimes, making them good gain materials for optical amplification and lasers.[89] In a typical fiber optic communication system, the silica fiber is doped with rare earth ions to form a fiber-optic amplifier/laser. Recently, rare earth doped integrated lasers, including different rare earth elements and laser cavity designs, have also been demonstrated on silicon photonics platforms.[90] LN can also be doped with rare earth ions to realize interesting devices.[91] With the development of TFLN technology, rare earth doped amplifiers[92] and lasers[93] have been demonstrated that can solve the chip-scale light source problem and pave the way toward large-scale photonic integrated circuits (PICs). The doping with these rare earth ions can take place either during the crystal growth phase[94] or with postprocessing.[95] More details about rare earth doped devices can be found in Sec. 4.5.

3 Processing Technology

3.1 Planar Device Technology

Light confinement is a fundamental problem in photonics applications generally. The refractive index of LN is around $2.341(n_o)/2.2547(n_e)$.[41] Optical confinement and waveguiding require index contrast. In a typical planar bulk LN crystal, methods to introduce a refractive index contrast to form waveguides or other confinement structures can be divided into four main types:[96] (1) Li-out diffusion, (2) metal ion-in diffusion, (3) PE, and (4) ion implantation. All of them form a planar device configuration.

3.1.1 Li-out diffusion

The Li-out diffusion method was first demonstrated by Kaminow and Carruthers.[97] As LN can crystallize in a slightly nonstoichiometric form $(\mathrm{Li_2O})_y(\mathrm{Nb_2O_5})_{1-y}$, its extraordinary index n_e will increase linearly when the alloying variable y decreases within a narrow range between 0.48 and 0.5. The change of y can be realized by the Li-out diffusion of $\mathrm{Li_2O}$ from the LN surface since the lithium ion has high mobility. Therefore, by applying a thermal treatment of an LN sample for several hours at high temperature, the refractive index will be changed in an LN target area as Li is diffused away.[96] This method has two main disadvantages. One is that the refractive-index change occurs only in n_e, and the other is that it is difficult to achieve selective diffusion.[98] Therefore, although Li-out diffusion is proposed in principle and has been demonstrated in experiment,[97,99,100] it is seldom used for photonics device fabrication. Alternatively, ion-in diffusion is more frequently adopted for LN device fabrication.[19]

3.1.2 Metal ion-in diffusion

During the metal ion-in diffusion process, a thin layer of metal is first evaporated onto an LN crystal surface, and then the crystal is heated at a temperature in a nonreactive atmosphere for several hours to make the metal diffuse into the crystal.[19,98,101–112] A schematic of a photonic waveguide fabrication process based on ion-in diffusion is shown in Fig. 2(a). Different metals have been used for ion-in diffusion. Some of these are summarized in Table 2. The most widely used metal is titanium (Ti).[19] The metal ion-in diffusion method is an easy and economical method for fabricating photonics devices. For experimental demonstration, as shown in Table 2, propagation loss below 1 dB/cm in photonics wires using such method has been realized.[98,113–115] Before the appearance of TFLN devices, metal ion-in diffusion was widely used in photonic device fabrication. However, the refractive index difference formed by this method is very small (normally < 0.02). Another method called PE can result in a slightly larger refractive index contrast,[20,21] although also not very high overall.

3.1.3 Proton exchange

In 1981, PE was first used to fabricate optical waveguides in LN.[20,21] Different from metal ion-in diffusion, hydrogen ions are diffused into an LN crystal and are then exchanged with lithium ions during the PE process. The lithium ions then diffuse out of the crystal and finally the LN crystal is partially transformed into a new chemical with composition $\mathrm{H}_x\mathrm{Li}_{1-x}\mathrm{NbO}_3$ within a certain surface depth. The $\mathrm{H}_x\mathrm{Li}_{1-x}\mathrm{NbO}_3$ compound has several different phase states depending on the component proportion (x), as validated by X-ray rocking curve analysis results and some other techniques.[116] Several proton sources have been used for the PE process, such as benzoic, octanoic, adipic, glutaric, stearic acids, and their mixtures.[117–119] Among them, benzoic acid is the most widely used proton source, as it has a high boiling point and stability throughout its liquid phase.[116] A typical process flow for photonic device fabrication using PE is shown in Fig. 2(b). Compared with the metal ion-in diffusion method, the PE process has a much higher photorefractive damage threshold for visible light confining and transmission,[120] as well as a higher resulting refractive index contrast.[121] The PE process has been widely used to fabricate photonics devices in LN crystals with different orientations.[116,121–126] Other than PE, a few other ions have also been used in such an exchange process with lithium to realize a refractive index change in LN.[127–130] For example, Shah et al. demonstrated a kind of LN waveguide by immersing X-cut LN crystals in silver nitrate at 360°C temperature for several hours, and lithium/silver ion exchange was observed.[127] Although with the more recent development of TFLN, direct dry etching has recently received more attention as it results in a much larger index contrast than either PE or

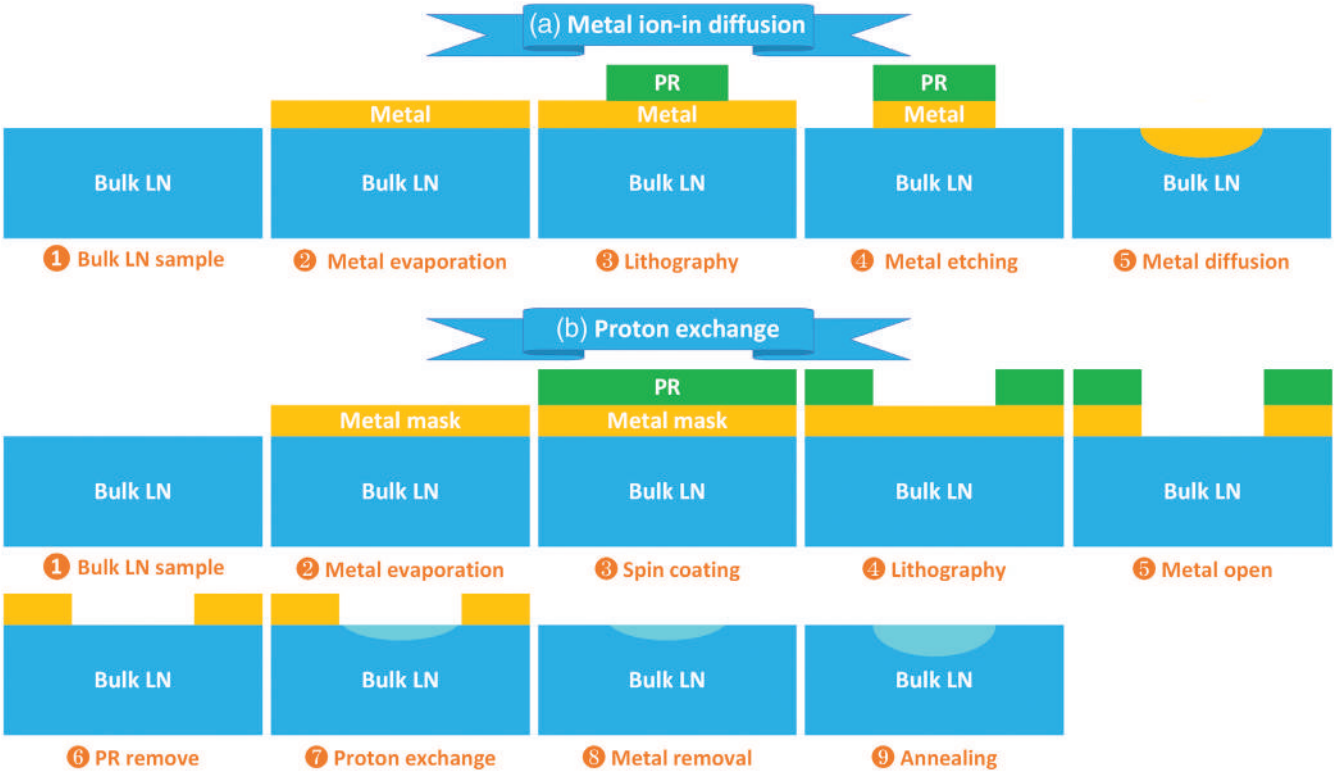

Fig. 2 Process flow of planar LN device fabrication. Illustration of (a) metal ion-in diffusion and (b) PE methods for planar photonic device fabrication in bulk LN crystals (dimensions are not drawn to scale). PR, photoresist.

Table 2 Summaries of metal ion-in diffusion method. *T*, temperature; TE, transverse electric; TM, transverse magnetic; N.A., not available/applicable; Zn, Zinc.

Year	Metal	Depth (Å)	Atmosphere	Time (h)	*T* (°C)	$\Delta n_o/n_e$	Loss	Ref.
1974	Ti/V/Ni	500	Argon (Ar)	6	960/970/800	Ti: 0.01/0.04 V: 0.0005/0.004 Ni: 0.0095/0.006	1 dB/cm at 630 nm	19
1975	TiO_2	200	Oxygen	10	900 to 1150	0.002	TE: 0.8 dB/cm TM: 0.7 dB/cm	98
1977	Co, Ni, Cu, Zn	10,000	Air	N.A.	900 to 1100	N.A.	N.A.	101
1978	Ti	400 to 600	Air	5	1050	N.A.	2 dB/cm at 633 nm	102
1978	Ti	500	Air	10	1000 to 1100	0.0077/0.0105	N.A.	103
1979	Ti	500	N.A.	5.5	1060	N.A.	1.25 dB/cm	104
1979	Ti	75	Ar	4.5	940	N.A.	N.A.	105
1980	Ti	500	Air	5	975 to 1075	0.005	0.5 dB/cm	113
1982	Ti	740	Ar	6	1050	0.00051/0.00049	0.62 dB/cm at 1.3 μm	114
1983	Ti	950	O_2 and H_2O	6	1050	N.A.	N.A.	106
1984	TiO_2	50 to 150	Oxygen	5 to 10	1000	N.A.	N.A.	107
1994	Ti/Ni	200/180	N.A.	8/2.5	1050/960	N.A.	N.A.	108
1995	Ni	220	N.A.	1.5	800	0.0112	N.A.	109
1996	Ni	100	N.A.	4 to 6	900	~0.002 to 0.016	TE: 0.7 dB/cm TM: 1.4 dB/cm	110
1999	Zn	N.A.	N.A.	N.A.	700 to 800	~0.0033 to 0.0077	N.A.	111
2006	Zn	N.A.	Zn	2	500	0.0012	N.A.	112
2019	Ti	700	Wet oxygen	Several	1010	N.A.	0.5 dB/cm	115

ion-in diffusion, the PE method still has certain advantageous application scenarios, especially to assist dry/wet etching technologies to realize some innovative photonic devices.[131]

3.1.4 Ion implantation

Ion implantation can also be used for fabricating waveguides in LN crystals.[132–137] Different from the above-mentioned methods, ion implantation results in a decrease of refractive index around the target area. Destefanis et al. implanted helium (He) ions into LN surfaces with about 1 to 2 MeV energies.[132] They formed a low refractive index layer in the 2 to 4 μm range just below the LN surface. Such a region of lower refractive index can form sufficient refractive index contrast for light confinement. It is worth mentioning that such a low index layer is very easy to etch by wet etchant, compared with these areas without damage. Therefore, such a buried layer can also be etched away to obtain a much larger refractive index difference.[138] We will introduce this method again when we discuss wet etching. Other than the He ion, other ions have also been demonstrated for ion implantation of LN.[133,135] Although a very large index difference can be obtained based on such methods, many more crystal defects will also be produced during the physical bombardment. Therefore, ion implantation has not been widely used for the formation of photonics devices in LN crystals. But He ion implantation is widely used in CIS technology, which is used for fabrication of TFLN. More details about TFLN process technologies are introduced in the subsequent sections.

3.2 Thin Film Lithium Niobate Fabrication Technology

Though bulk LN devices have been widely adopted during the past decades, their low index contrast and therefore weak light confinement have severely limited its further development toward large scale and dense integration. TFLN is thus proposed and developed to meet the advanced requirements of future devices. There are many different methods that have been proposed to create the TFLN. For example, TFLN can be directly sputtered onto a glass substrate,[139] or grown on GaAs by pulsed laser deposition,[140] or grown on a lithium tantalate substrate by the chemical vapor deposition (CVD) method.[141] However, the directly grown/sputtering method may cause damage to the crystal quality as the measured EO properties are not as good as the bulk counterpart.[139–141]

3.2.1 Crystal ion slicing

In contrast, CIS technology can realize high-quality single crystal TFLN wafers and has widely been used since 1998.[5,142–146] Figure 3(a) shows a schematic of CIS technology. The processing starts from a bulk LN wafer, which is usually grown using the Czochralski method.[147] Then, the bulk LN is implanted with He ions to a specific layer thickness (which depends on the desired TFLN thickness) to form a sacrificial layer. Helium (He) implantation is performed using an ordinary ion implanter. The He ion is the most widely used ion due to its small atomic mass.[142] As the ion implantation will cause LN crystal damage that results in a different subsequent etch rate or thermal properties compared with undamaged areas, it can be comparatively easy to separate the top thin film layer from a bulk LN using a simple etching method, such as hydrofluoric acid (HF) etching. Then, the thin film layer is bonded to a bottom insulator layer using mature wafer bonding methods.[9] Usually, the bottom insulator is selected to be a material with a lower refractive index, such as silicon oxide. The large resulting refractive index contrast between the LN and the bottom insulator enables strong

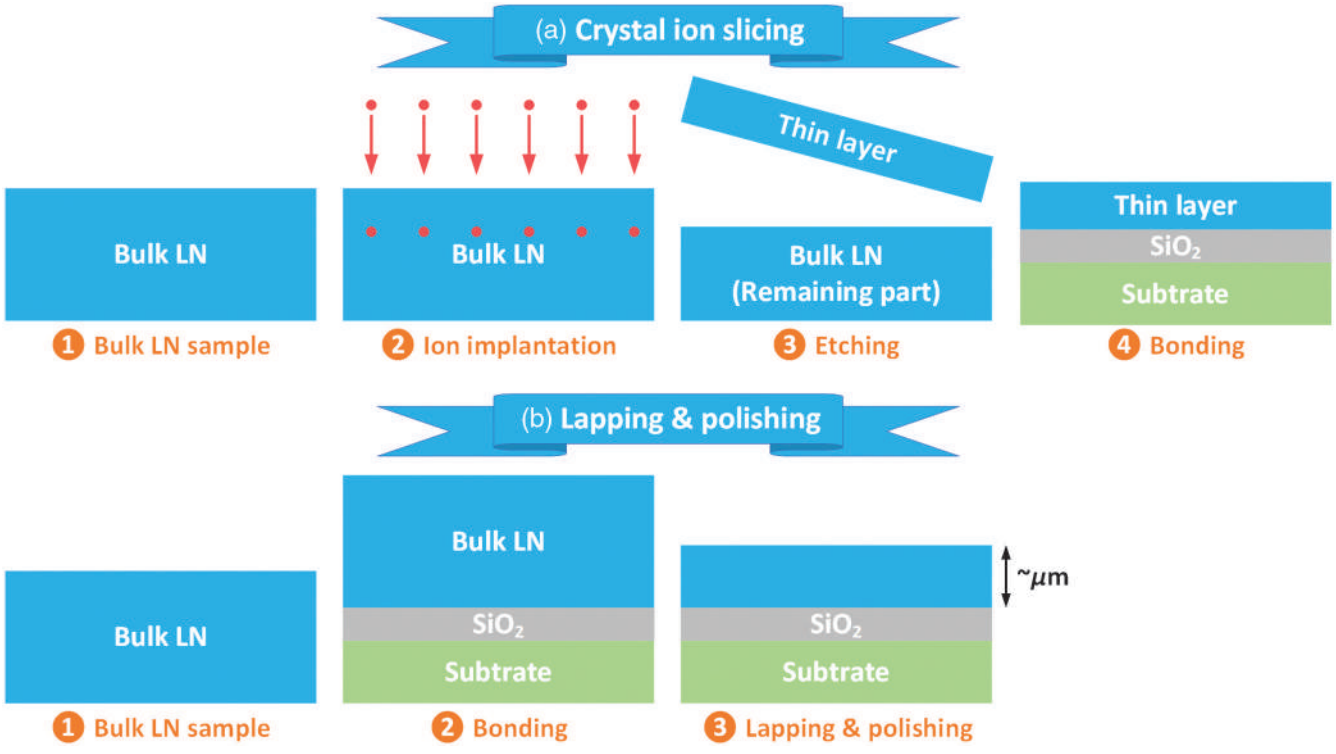

Fig. 3 Process flows of (a) CIS and (b) lapping and polishing technologies. Dimensions are not drawn to scale.

light confinement within the LN layer. It is worth mentioning that the bottom substrate is not only restricted to LN, glass or Si is also possible. Furthermore, a thin layer of metal can also be inserted between the substrate and insulator layer to form a bottom metal electrode.

3.2.2 Lapping and polishing

In addition to CIS technology, the lapping and polishing method has also been developed for LN film fabrication. Figure 3(b) shows the process flow of the lapping and polishing method. The thick bulk LN wafer is first bonded onto a substrate with an insulator (of lower refractive index) inserted between them. Then, the top LN layer is thinned down to a few microns thickness by successive lapping and polishing.[29,30] Compared with the CIS method, the LN film thickness after lapping and polishing is a little bit thick (typically around a few microns) and thus results in a larger device size. However, there are some advantages of LN films made by this technology. First, lapping and polishing is a purely mechanical process and thus has a smaller influence on crystal quality compared with CIS technology. In addition, the larger waveguide core in thick LN films enables a better coupling efficiency and a much higher laser-damaged threshold compared with thinner LN films.[29,30,148–154] Therefore, lapping and polishing is a good complement to CIS technology.

3.3 Heterogeneous Integration

In the previous subsection, we introduced a kind of TFLN by wafer bonding a thin layer of LN onto an insulator with a lower refractive index (LNOI structure). In such a structure, 3D waveguides are directly etched to enable light transmission, and thus most of the optical field can be confined within the LN layer. There is another way to realize interaction of light with LN crystal, though, where the LN is not patterned at all. We refer to such a method as heterogeneous integration of LN with other material systems. As far back in 2009, Solmaz et al. demonstrated a type of integrated As_2S_3 ring with Ti-diffused LN. As the refractive index of As_2S_3 is very close to LN (As_2S_3 is 2.4, LN is 2.2), the transmitted light inside a Ti diffused LN waveguide can be vertically coupled into an As_2S_3 waveguide.[155] Since then, various kinds of heterogeneous integration schemes have been demonstrated, as summarized in Table 3.

These schemes can be divided into two categories. The first involves directly bonding/growing TFLN onto other mature material platforms,[156,157,160,161,166,170] such as SOI wafers. Here, the light is confined inside these mature material layers with patterned structures, and the optical mode is designed to partially overlap with a top bonded/grown LN layer. Figures 4(a)–4(c) show an example of an LN on silica hybrid micro-resonator.[161] About 15.47-nm root mean square (RMS) surface roughness is

Table 3 Summary of heterogeneous integration of LN with other material systems. ALD, atomic layer deposition; N.A., not available/applicable; a-Si, amorphous silicon.

Year	Cut	Structure	Thickness	Device	Integration method	Ref.
2009	X-cut	As_2S_3/Ti:LN	470 nm/N.A.	Ring	Magnetron sputtering	155
2011	Z-cut	LN/Si/SiO_2	~1 μm/250 nm/2 μm	Ring	Bonding	156
2012	Z-cut	LN/Si/SiO_2	600 nm/250 nm/2 μm	Ring *E*-field sensor	Bonding	157
2013	Y-cut	Ta_2O_5/LN/SiO_2	200 nm/400 nm/1.6 μm	Ring modulator	Bonding and deposition	158
2014	X-cut	a-Si:H/LN	90 nm/N.A.	MZI modulator	PECVD	159
2014	Z-cut	LN/Si/SiO_2	1 μm/250 nm/1 μm	Ring modulator	Bonding	160
2015	N.A.	LN/silica	290 nm/2 μm	Whispering-gallery-mode resonator	Excimer laser ablation	161
2015	X-cut	SiN_x/LN/SiO_2	260 nm/700 nm/2 μm	MZI modulator	PECVD	162
2015	Z-cut	TiO_2/LN/SiO_2	95 nm/600 nm/N.A.	Waveguide	Magnetron sputtering	163
2015	Y-cut	$Ge_{23}Sb_7S_{70}$/LN/SiO_2	350 nm/400 nm/2 μm	MZI modulator	Bonding and E-beam evaporation	164
2016	X-cut	SiN/LN/SiO_2	390 nm/700 nm/2 μm	PPLN waveguide	Magnetron sputtering	54
2016	Y -cut	SiN/LN/SiO_2	500 nm/400 nm/2 μm	MZI modulator	Bonding and PECVD	165
2017	X-cut	LN/Si_3N_4/SiO_2	300 nm/850 nm/N.A.	Waveguide	LPCVD and Bonding	166
2017	X-cut	Si/LN	145 nm/N.A.	Resonator	Bonding	167
2019	X-cut	a-Si/LN/SiO_2	100 nm/300 nm/2 μm	Photodetector	PECVD	34
2020	X-cut	SiN_x/LN/SiO_2	220 nm/300 nm/4 μm	MZI modulator	PECVD	168
2020	X-cut	SiN_x/LN/SiO_2	200 nm/300 nm/4.7 μm	MZI modulator	LPCVD	169
2020	X-cut	LN/SiN_x/SiO_2	200 nm/225 nm/N.A.	MZI modulator	Bonding	170
2020	X-cut	Si_3N_4/LN/SiO_2	200 nm/300 nm/N.A.	Spectrometer	PECVD	171
2020	Z-cut	NbN/HfO_2/LN/SiO_2	5 nm/10 nm/615 nm/2 μm	Superconducting SPD	ALD	172
2020	N.A.	Polymer/LN/SiO_2	500 nm/400 nm/N.A.	Mode (de)multiplexer	Spin coating	35

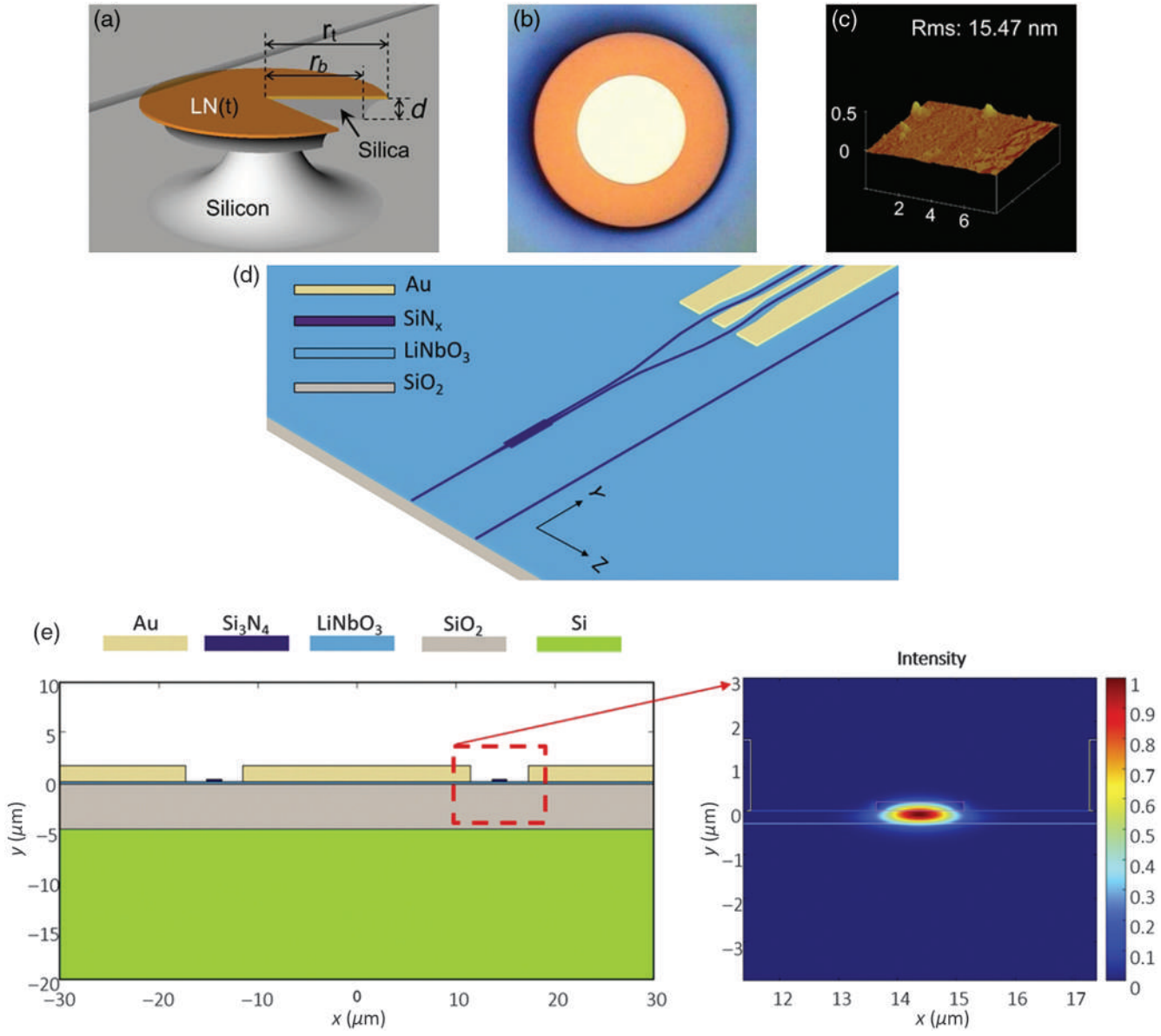

Fig. 4 Heterogeneous integrated LN devices. (a) Schematic structure, (b) optical, and (c) atomic force microscopic images of an LN on silica hybrid micro-resonator. (a)–(c) Adapted from Ref. 161 © 2015 Wiley-VCH Verlag GmbH and Co. (d) 3D schematic structure, (e) cross section and optical field distribution of a SiN_x on LN hybrid MZI modulator. (d) and (e) Adapted from Ref. 169; all article content, except where otherwise noted, is licensed under a Creative Commons Attribution (CC BY) license.

measured, which supports highly efficient EO application. The other scheme involves integrating or depositing a thin layer of a specific material (which is typically easier to dry etch than LN itself) that has a similar refractive index with LN above/onto the TFLN.[34,35,54,155,158,159,162–165,167–169,171–174] Usually, these materials are directly grown on the LN surface, with a method such as magnetron sputtering,[54,155,163] plasma-enhanced chemical vapor deposition (PECVD),[34,159,162,168,171] or low-pressure chemical vapor deposition (LPCVD).[166,169] As shown in Figs. 4(d) and 4(e), by patterning the deposited SiN_x above the LN, the optical mode can be confined well inside the waveguide and an EO modulator can thus be realized.[169] In such a scenario, the introduced material together with the LN layer forms the light confinement structure. Thus, the overlap of the optical mode and the LN layer is designed to be large. In addition, an etchless TFLN platform with photonic bound states in the continuum (BIC) has also been demonstrated recently through direct patterning of the above integrated organic polymer.[35,173,174] In both methods, the LN layer is usually not patterned, and the geometry of the structure is defined in the other material with a more mature processing technology. Therefore, these methods avoid the well-known problem of LN crystals being difficult to etch.[175] When there are no good etching solutions of LN available, heterogeneous integration becomes a good choice. Various types of devices have been realized based on these two schemes, as shown in Table 3. It is worth noting that the applications presented are not limited to

active devices, as passive devices can also be realized. For example, hybrid grating couplers (GCs) for light coupling based on patterned Si[176] and gold (Au)[177] have been demonstrated. As the propagating optical field is only partially overlapping the LN crystal, the interactions between the light and LN are not maximized relative to what they would be if the light were instead fully confined within the LN. However, such methods are still attractive as they combine both the advantages of LN and the other well-developed material platform chosen, while avoiding difficulties associated with LN fabrication processes.

3.4 Etching Technology

3.4.1 Dry etching

For both bulk LN and TFLN, there are strong motivations toward direct etching to form 3D structures.[178] Dry etching is one of the main methods to realize such a goal. The plasma of a chemically active gas together with an inert ion plays the main roles during dry etching. As summarized in Table 4, many different kinds of dry etching methods have been demonstrated during the past decades. These demonstrations can be divided into three categories. One involves using the plasma of pure halogen ions,[179,180,182,183,194,196] such as sulfur hexafluoride (SF_6), carbon tetrafluoride (CF_4), and boron trichloride (BCl_3). As halogen ions will chemically react with the lithium, the reactant produced in the process of dry etching will be a problem and later affect device performance. Figures 5(a) and 5(b) show the scanning electron microscopy (SEM) image and current changed along the etching depth in end point detection after SF_6 etching, which clearly shows the byproduct layer.[182] Nagata et al. tried to remove the reactant using an additional wet etching method.[179] The second category involves mixing the halogen ions with argon (Ar) in the plasma.[178,182,185,186,188,189,191,193,195] Ar ion-based etching is a pure physical bombardment process. By engineering the gas flow ratio between the Ar and halogen element, the etch rate, profile, and surface conditions can be improved. In such a method, the halogen ions can still be a problem and affect the etching quality. Therefore, people have developed the third category of using pure Ar gas for etching.[175,184,190,195] Compared with the first two methods, pure Ar-based etching has a lower etching rate, as the ion bombardment is a pure physical process. Its advantages are flat and clear surface condition, as evidenced by the SEM, AFM, and X-ray photoelectron spectroscopy (XPS) results shown in Figs. 5(c)–5(e).[175] By using Ar-based etching, nearly vertical side walls[52,175,197] and ultralow propagation loss[197] have been observed; this method can then find wide use for photonics device fabrication. During such dry etching processes, a hard mask is typically used in addition to photoresist to improve the etching selectivity, as summarized in Table 4.

Table 4 Summary of LN dry etching technologies. PMMA, polymethyl methacrylate; HSQ, hydrogen silsesquioxane; MMA, methyl methacrylate; N.A., not available/applicable; RIE, reactive ion etching; ICP, inductively coupled plasma.

Year	Cut	Type	Etch gas	Resist	Mask	Etch rate	Selectivity[a]	Etch type	Ref.
1981	X-cut	Bulk	CCl_2F_2, Ar, O_2	AZ 1350-J	Ni/Cr	55 nm/min	~4[b]	RIE	178
1998	Z-cut	Bulk	CF_4	N.A.	Ni	800 nm/h	N.A.	Plasma etching	179
2000	X-cut	Bulk	CF_4	N.A.	SIO_2	~60 nm/min[c]	N.A.	Plasma etching	180
2007	Z-cut	TFLN	Ar	SU-8	N.A.	N.A.	N.A.	Plasma etching	181
2008	X/Y/Z-cut	Bulk	CF_4, $O_2/SF_6/SF_6$, O_2	N.A.	Ni/NiCr	2 to 3/10 to 53/37 to 195 nm/min	3–10	RIE/ICP/ICP	182
2009	Y-cut	Bulk	SF_6	TI09 XR	Ni	20 to 50 nm/min	20	RIE	183
2009	Z-cut	TFLN	Ar	OIR 907-17	N.A.	7.67 nm/min[c]	N.A.	ICP	184
2010	X-cut	Bulk	CHF_3, Ar	AZ5214	Cr	97.5 nm/min	8.1–16	ICP	185
2010	X-cut	Bulk	CHF_3, Ar	N.A.	Cr	92.5 nm/min	N.A.	ICP	186
2011	X-cut	Bulk	SF_6, CF_4, He	PMMA	Cr	280 nm/min	N.A.	ICP	187
2012	Z-cut	Bulk	SF_6, Ar	AZ5214E	Cr	98.6 nm/min	12	ICP	188
2015	Z-cut	Bulk	BCl_3, Ar	N.A.	Ni	100 nm/min	7	ICP	189
2016	X-cut	TFLN	Ar	S1828	N.A.	12 nm/min	N.A.	ICP	190
2018	Z-cut	TFLN	CHF_3, Ar	N.A.	Cr	N.A.	7	Plasma etching	191
2018	X-cut	TFLN	Ar	N.A.	N.A.	N.A.	N.A.	RIE	192
2019	Z-cut	TFLN	Cl_2, BCl_3, Ar	PMMA	SIO_2	200 nm/min	0.69	RIE	193
2019	X-cut	TFLN	Ar	HSQ	N.A.	N.A.	N.A.	ICP	52
2019	Z-cut	Bulk	SF_6, O_2	N.A.	Cr/Cu	812 nm/min	77	ICP	194
2021	X/Z-cut	TFLN	Ar	ma-N 1400	Cr	15 to 30 nm/min	1.4	ICP	175
2021	X-cut	TFLN	CF_4, Ar; Cl_2, Ar; Ar	MMA/PMMA	Cr	35 to 50 nm/min; 20 to 33 nm/min; 12 to 18 nm/min;	N.A.	ICP	195

[a]Selectivity is defined by the etch rate ratio between LN and the mask.
[b]Extracted from demonstrated pictures.
[c]Calculated based on the demonstrated data.

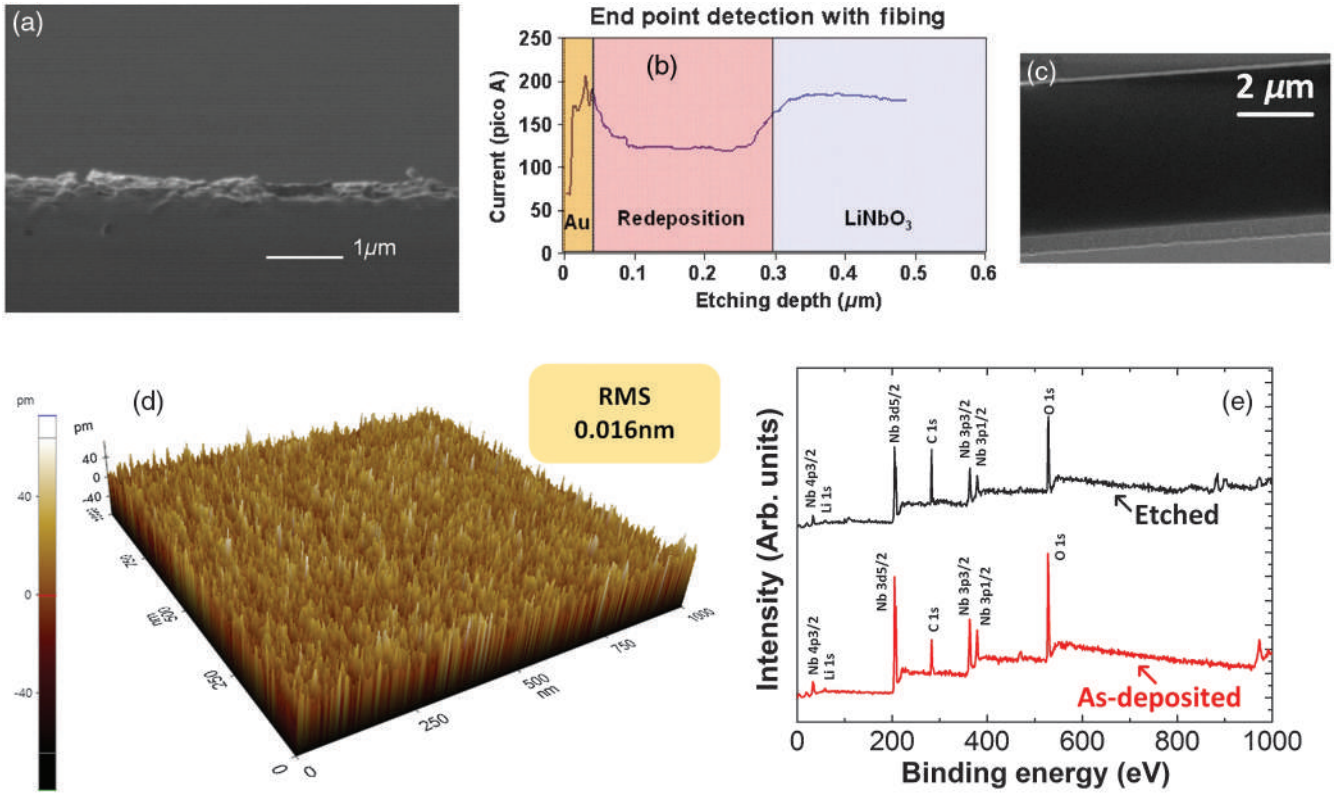

Fig. 5 Dry etching results of LN. (a) SEM image of the LN cross section and (b) current changed along etching depth in end point detection after SF_6 based etching. (a) and (b) Adapted from Ref. 182 © 2008 American Institute of Physics (AIP). (c) SEM, (d) AFM, and (e) XPS images of LN sample after Ar-based dry etching. (c)–(e) Adapted with permission from Ref. 175.

3.4.2 *Wet etching*

LN can also be etched by the wet etching method. Compared with dry etching, wet etching can realize a more uniform surface and much higher etch rates.[198] In addition, wet etching is an economical and simple method compared with other etching technologies and is widely used in other material systems.[109] It has been demonstrated that after the PE process, for instance, LN shows a larger etch rate using the mixture of HF and nitric acid (HNO_3), compared with LN areas that are not subjected to the PE process.[199] Therefore, the combination of PE and a mixture of HF and HNO_3 etchant is widely used for LN wet etching.[109,199–204] Compared with dry etching, its etched sidewall is not too deep and there can be an underetching problem. Ting et al. demonstrated that the etching depth and aspect ratio can be improved using a diluted PE source with a lithium compound.[198] By optimizing different molar percentages of adipic acid and lithium compounds, a very high aspect ratio [defined as etched depth D divided by horizontal distance of the slant H, as shown in Figs. 6(a)–6(f)] has been realized. Such an improvement can be clearly seen from the SEM images shown in Figs. 6(a)–6(f). The underetching problem can be alleviated by annealing (improve the adhesion of hard mask), as demonstrated by Hu et al.[205] Some researchers also demonstrated that by adding some ethanol into the $HF-HNO_3$ mixture, the etched surface of LN can be much smoother.[205] PE is not the only way to cause a subsequent LN etching rate difference. Wang et al. found that O^+ and Si^+ ion implanted regions can be etched more easily than those protected by a photoresist mask using a mixture of HF and HNO_3 at room temperature.[206] Si et al. demonstrated that He ion implantation caused crystal damage in LN, which consequently also showed a higher chemical etching rate,[138] and photonic crystal waveguides were successfully realized using such a method, as shown in Fig. 6(g). Using an ion beam enhanced etching method, a similar damaged layer can also be obtained.[207] Copper (Cu) ion implantation with the assistance of HF solution has also been validated as a good way to achieve wet etching of LN crystals, and an etching rate of around 100 nm/s has been observed.[32] Up until now, most of the reported wet etching methods have been demonstrated in bulk LN crystals. But we believe wet etching is also suitable for TFLN devices, especially in some scenarios where cantilever structures are needed.

3.4.3 *Other patterning/etching technologies*

In addition to the above-mentioned methods, some other methods have also been used for the patterning/etching of LN. Most of them have been based on the physical polishing/milling process, such as focused ion beam (FIB) milling,[208–211] dicing,[212,213] femtosecond laser micromachining,[214–218] and chemomechanical polish lithography (CMPL).[214,215,217,219–223] FIB itself is a pure mechanical milling process, which either can be used along[208,209,211] or together with other dry etching methods for layout patterning.[208,210] For prototype validation, FIB is a good choice. But it will not be suitable for mass production of devices

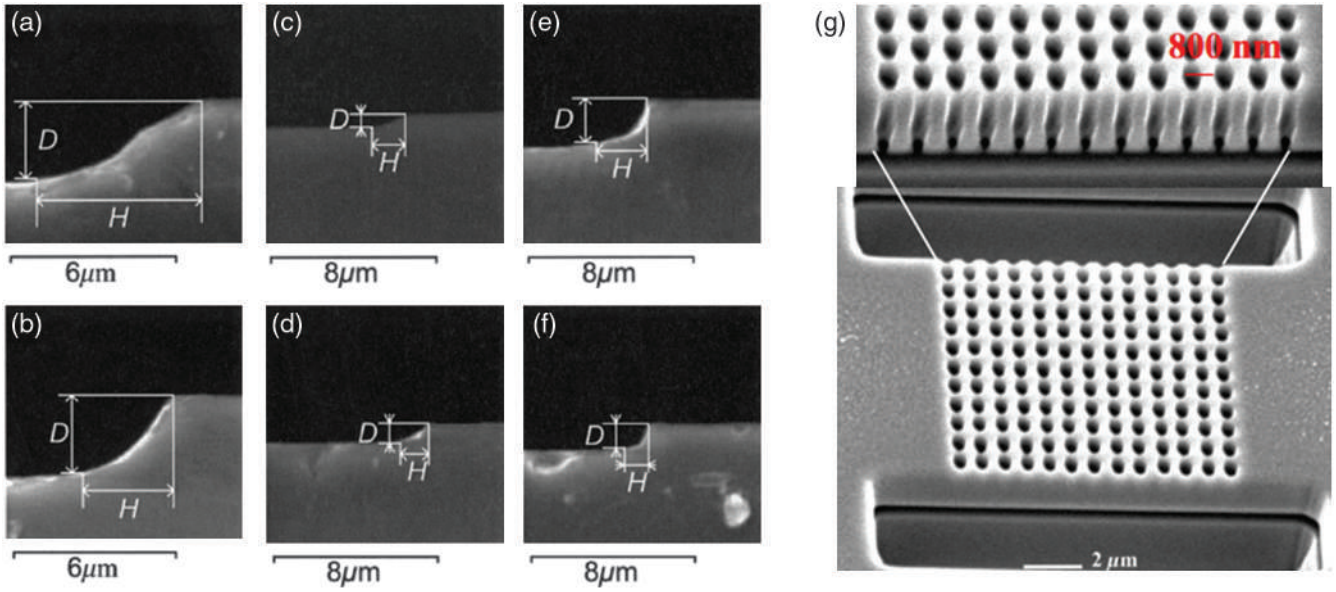

Fig. 6 Wet etching results of LN. SEM images of the LN etched cross section using undiluted (a) 0% and (b) 20% of adipic acid, (c) 0% and (d) 20% of adipic acid with 0.6% of lithium benzoate, (e) 20% and (f) 30% of adipic acid with 0.3% of lithium carbonate (concentrations in percent represent mole fractions). (a)–(f) Adapted from Ref. 198 © 2006 Wiley Periodicals, Inc. (g) SEM image of photonic crystals (PhCs) using ion implantation and wet etching. Adapted with permission from Ref. 138 © 2010 American Vacuum Society.

of any type due to economic and operability considerations. By contrast, dicing is an efficient method for quick fabrication of optical waveguides, as it can realize smooth sidewalls and a high aspect ratio.[212,213] Recently, femtosecond laser ablation combined with FIB[214–218] or CMPL[214,215,217,219–221] has also been demonstrated for LN crystal patterning, which has received wide attention. Such a method can be divided into three steps. First, the LN crystal or metal mask is ablated with tightly focused femtosecond laser pulses, which is usually performed in water to reduce the possibility of debris and cracks.[215] Second, the LN crystal is polished by the FIB or CMPL process. Third, the underlying oxide is partially etched using a wet etching method. Very high quality factor (Q factor) ($\sim 10^8$) microresonators have been demonstrated based on such a method,[224] which proves the very high quality of the etched sidewall. These mechanical milling methods together with the above introduced processing technologies pave the way for the fabrication of various LN photonics devices.

4 Functional Devices

Compared with other materials systems, LN has many unique features, such as large EO, NLO, and AO effects. The details of these effects are described in Sec. 2. For a long time, LN-based photonics devices were demonstrated only in bulk LN crystals, such as the Ti diffused EO modulator that is widely used in current fiber-optic communication systems due to its large bandwidth and superior linear EO response.[3] The recently developed high-quality TFLN together with various etching technologies, however, has made significant headway toward integrated LN photonics. Many different kinds of photonics devices fabricated in bulk LN have now been demonstrated in TFLN, including passive devices, EO devices, nonlinear optical devices, AO devices, rare earth doping devices, pyroelectric devices, TO devices, etc.

In this section, we will give a review of functional devices demonstrated in LN during recent years. These devices cover both bulk LN and TFLN, which make use of the effects discussed in Sec. 2 and some key technologies demonstrated in Sec. 3. Here, bulk LN based devices are introduced for comparison with TFLN devices and will not be the main focus as they have been widely discussed in other reviews.[2,3] From a comprehensive history of LN device evolution, we hope readers can be inspired to achieve improved designs of high-performance devices in the future and contribute to the further development of LN photonics generally.

4.1 Passive Devices

The waveguide is the most basic photonic device, as it confines light inside a specific region through refractive index contrast. As discussed in Sec. 2, there are many different ways to realize such a refractive index contrast. In a typical bulk LN crystal, ion-in diffusion, PE, and ion implantation are mostly used to define planar waveguides, while for TFLN, direct etching, including dry etching, wet etching, and a few other types of physical etching can be used to form waveguides for light confinement. Compared with ion-in diffused or PE bulk LN, the large refractive index contrast present at the interface of the top LN layer and the underlying bottom insulator in TFLN makes some compact and low loss devices possible. Researchers have developed several ways to characterize waveguide loss, such as cutback, sliding-prism, Fabry–Perot resonance, and scattered light methods.[225,226] In addition, the propagation loss can also be extracted from the Q factor of a microresonator,[42,192] which is inversely proportional to the Q factor of the microresonator.

4.1.1 Microresonator

In past years, various kinds of microresonators have been demonstrated both in bulk LN and TFLN platforms.[43,181,192,193,197,214–218,221,222,224,227–240] In bulk periodically poled Z-cut LN crystals, a high Q factor of 2×10^7 was measured by mechanically polishing the LN crystal,[227] as shown in Fig. 7(a). The Q factor of the TFLN-based microresonator is increased gradually. In 2014, Wang et al. demonstrated a kind of microdisk in TFLN using Ar-based electron-cyclotron resonance (ECR) reactive ion etching (RIE), and its measured Q factor was around 10^5 [Fig. 7(b)].[228] This was just at the early stage of TFLN devices. Such a value can be further improved by optimizing design and processing technologies. For example, a microring with a Q factor up to 10^7 was demonstrated in 2017 using an optimized Ar-based dry etching process, which corresponds to a propagation loss as low as 2.7 dB/cm.[192] An SEM image of this kind of etched microring and its corresponding measured transmission spectrum are shown in Figs. 7(c) and 7(d), respectively. These results validate the fact that Ar-based etching is a suitable method for TFLN patterning. Meanwhile, many other groups have also demonstrated high $\sim 10^5$ Q factor based on such a method.[197,230,231,234,236,237] More recently, a record-high Q factor up to 10^8 (calibrated by considering transmission rates of modes) at 1550 nm wavelength was achieved using the femtosecond laser-assisted CMPL method[224] [as shown in Figs. 7(e) and 7(h)], which indicates a propagation loss of around 0.28 dB/m. Such a result is realized using a pure mechanical polishing process, thus avoiding the possible ion-induced lattice damage. This ultralow loss device opens up many prospects toward broad application of LN photonics, especially for various nonlinear applications. Compared with bulk LN devices, low loss or high Q factors are not the main advantages of TFLN-based microresonator, however, as ultrahigh Q factors have also been demonstrated in bulk LN devices.[227] More advantageous is the fact that the larger refractive index contrast in TFLN enables various microresonator forms that are ordinarily extremely difficult or impossible to realize in bulk LN. Here, our discussion on microresonators is limited to microrings or microdisks. Actually, some other types of microresonators have also been demonstrated in LN (mainly TFLN), such as photonics crystal (PhC)[241] and distributed Bragg reflector (DBR)-based Fabry–Perot (DBR-FP)[242,243] resonators. Recent progress of EO modulators based on PhC and Fabry–Perot microresonators is discussed in Sec. 4.2.1.

4.1.2 Grating coupler

Due to the strong mode confinement in TFLN, many other passive blocks have subsequently been demonstrated.[85,131,176,177,223,244–269] The fiber to chip interface is a basic function as it determines how much light can be coupled into a photonic device. There are two types of methods to couple the external light into a chip. One is vertical coupling of light onto a chip using a GC.[176,177,245,247,248,252,254,259,265,266,268,269] The other is based on edge coupling,[223,246,249,258] which couples light into a chip horizontally. According to the operation principle, GCs can also be divided into two categories, one is the one-dimensional (1D) GC and the other is the 2D GC, both of which have been demonstrated in the LN platform. For a 1D GC, the design strategy is to optimize the periodic structure to realize the phase matching condition for best coupling efficiency. A high coupling efficiency of $-1.42/-2.1$ dB ($\sim 72\%/61.6\%$) has been realized in Z-cut TFLN with a bottom Au reflector, and the grating has been designed with a chirped structure to improve its coupling efficiency,[259] as shown in Figs. 8(a)–8(c). The typical coupling efficiency of a 1D GC is between -3 and -7 dB.[176,177,245,247,248,252,254,268,269] A 2D GC is more functional as it can realize the demultiplexing of orthogonal polarization multiplexed signals while coupling light into on-chip devices.[270] Although there are many reports about 2D GC in other material systems, similar research is very limited in TFLN. Chen et al. demonstrated a kind of 2D GC in TFLN with measured coupling efficiencies of -5.13 dB at 1561 nm for P-polarized light and -7.6 dB at 1568 nm for S-polarized light,[265] as shown in Figs. 8(d)–8(f). Their measured 1-dB bandwidths for both P- and S-polarized lights are around 30 nm. Such demonstrated results are far from comparable to those of its counterparts and hence need more efforts to improve. Both 1D and 2D GCs allow for wafer scale on-chip testing without the need of chip dicing. GCs are more difficult to realize in bulk LN compared with TFLN due to its smaller refractive index contrast.

4.1.3 Edge coupler

Compared with the vertical GC, an edge coupler is less sensitive to polarization, has a larger operating bandwidth, and enables lower insertion loss. Its main drawbacks are that accurate facet polishing and sample dicing are needed. For edge coupling, the main optical loss mechanism is the mode mismatch between the fiber and on-chip waveguide. Therefore, design strategies are to tailor both the fiber and waveguide modes to reduce the mode mismatch and thus improve the coupling efficiency. By adiabatically tapering a standard single-mode fiber to match a specially designed LN waveguide, Yao et al. demonstrated a measured $-1.32/-1.88$ dB coupling efficiency for transverse electric (TE)/magnetic (TM) modes.[223] Using a monolithic bilayer mode size converter, He et al. also demonstrated a measured 1.7-dB/facet coupling loss,[246] as shown in Figs. 9(a)–9(c). By combining a silicon oxynitride cladding waveguide with the bilayer LN taper, the coupling efficiency is further reduced to 0.54/0.59 dB per facet at 1550 nm for TE/TM light.[266] A multiple layer mode size converter shows a possible solution for low loss edge coupling in TFLN. Compared with the SOI platform, the refractive index contrast in TFLN is smaller and thus results in weaker mode confinement and larger waveguide bending radii. However, a comparable low coupling loss can also be obtained in TFLN by reducing the mode size mismatch between the fiber and waveguide. We believe there is still room for performance enhancement of edge coupling in the LN platform, as lower coupling loss (<0.5 dB/facet) has already been demonstrated in ion-in diffused bulk LN devices.[271]

4.1.4 Other passive devices

In addition, mode-related devices,[131,244,250,251,255,261,262,267] TO-based devices,[85–87] Bragg grating filters,[253,256,257,264] optical true delay lines,[263] and optical phased arrays[260] have also been demonstrated in the LN platform. Most of them rely on the large refractive index contrast available in TFLN. Similar to its counterpart, which is SOI, these passive blocks can be combined together to form more powerful chip scale PICs. And researchers have already tried to do so. For example, a two-mode (de)multiplexer is realized by combining a passive Mach–Zehnder interferometer (MZI) and an EO tuning electrode.[131] This will be a trend as PICs can solve power consumption and device size problems that are inherent in conventional bulk LN devices.

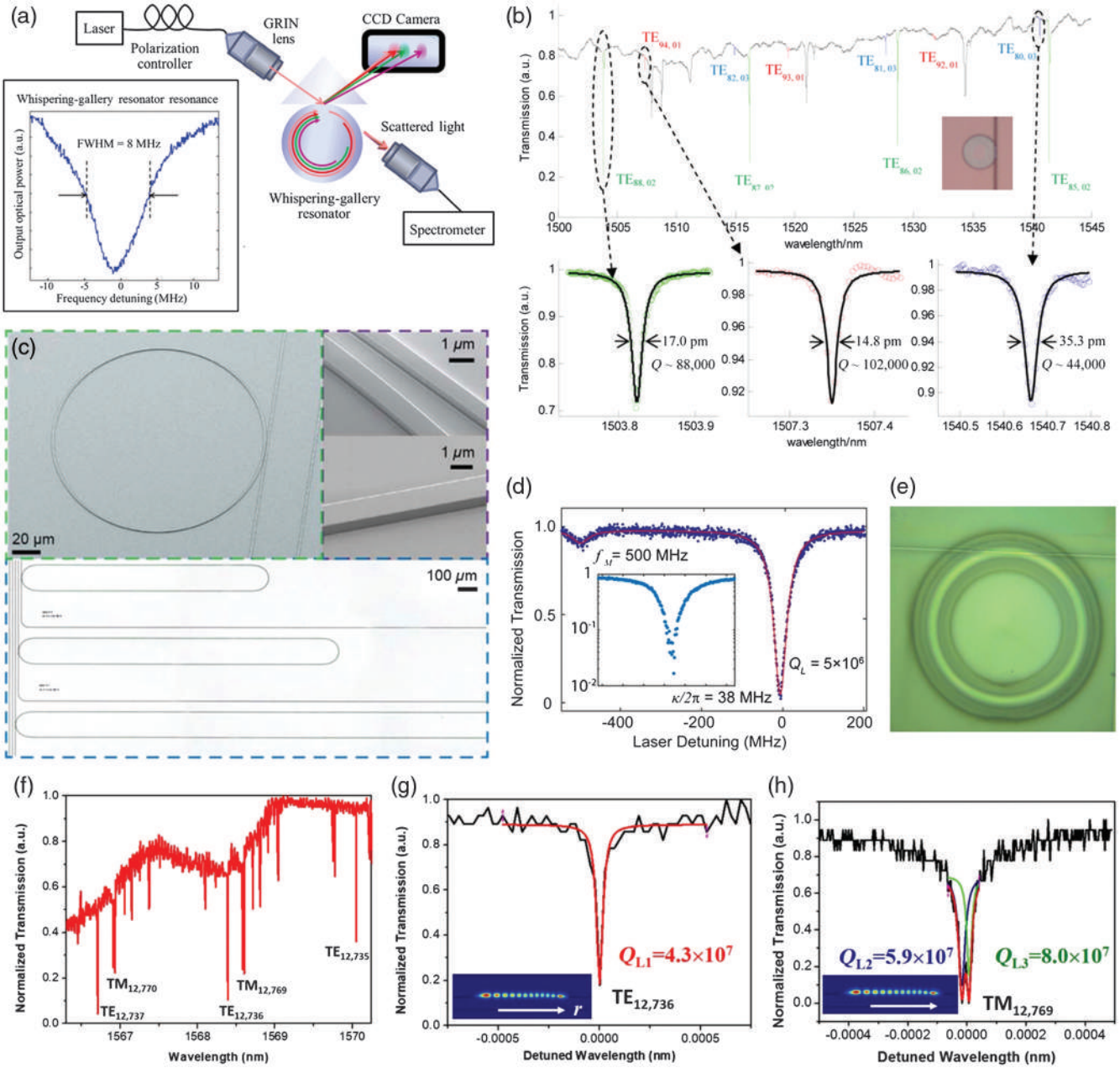

Fig. 7 LN-based microresonators. (a) Schematic experimental setup for characterizing a mechanical polishing bulk LN whispering-gallery resonator and its corresponding measured Q factor. Adapted from Ref. 227 © 2011 AIP. (b) Resonance spectra of the fabricated microdisk using ECR RIE technology in TFLN. Inset shows the microscope image of tapered fiber coupling on top of the device. Zoom in views are the details of representative resonance dips. Adapted with permission from Ref. 228 © 2014 Optical Society of America (OSA). (c) SEM (top) and microscopic images (bottom) of microring and microracetrack ring with various lengths, and (d) its measured transmission spectrum. (c) and (d) Adapted with permission from Ref. 192 © 2017 OSA. (e) Microscope image of the waveguide coupled TFLN microring and (f) its measured transmission spectrum. The Q factors for (g) TE and (h) TM modes fitted by Lorentz-shape curves. (e)–(h) Adapted with permission from Ref. 224 © 2022 Chinese Optical Society (COS).

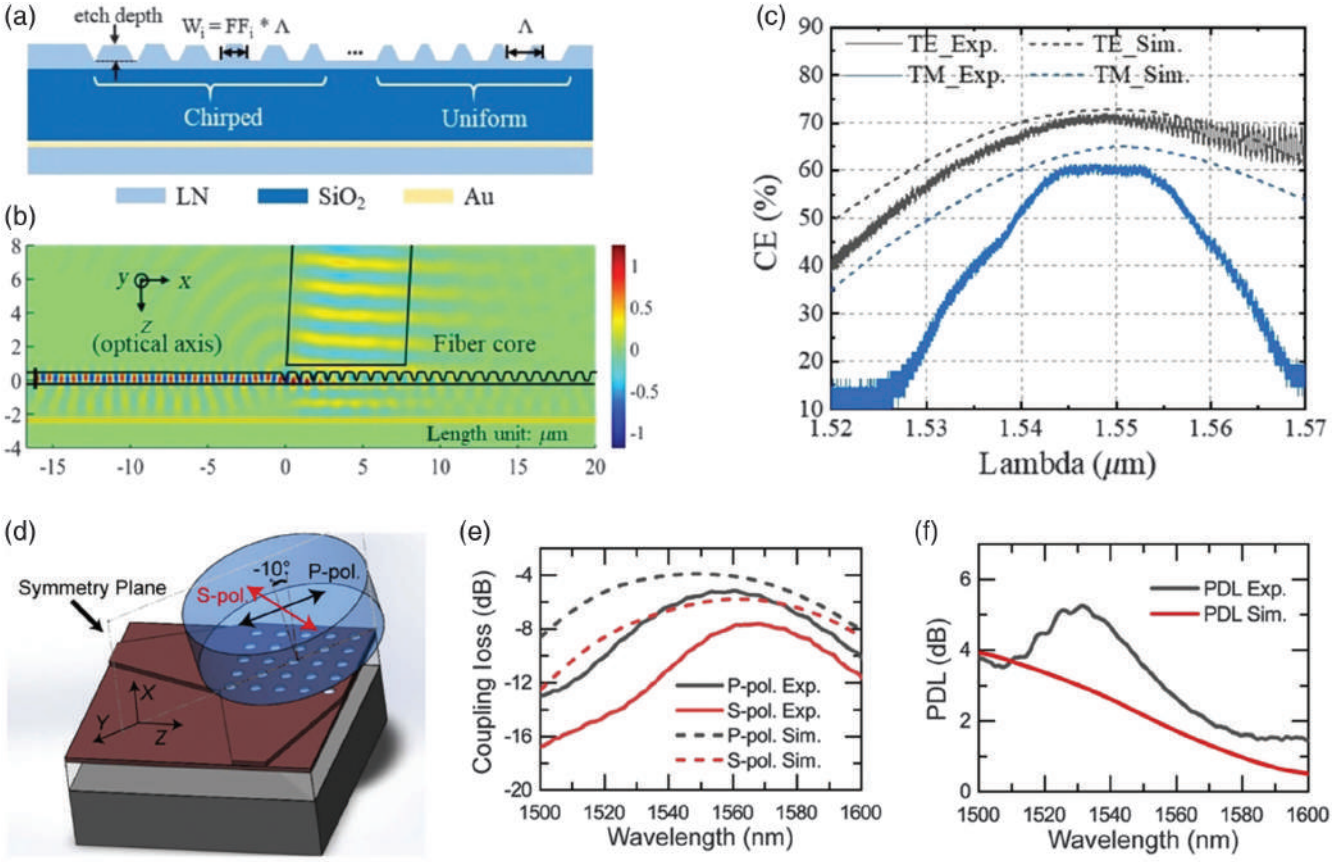

Fig. 8 LN-based GCs. (a) Schematic structure, (b) simulated electric field distribution and (c) measured transmission spectrum of 1D chirped GC in TFLN. (a)–(c) Adapted with permission from Ref. 259 © 2020 OSA. (d) Schematic structure of a 2D GC in TFLN. Measured and simulated (e) transmission spectra and (f) polarization dependence loss of the TFLN 2D GC. (d)–(f) Adapted with permission from Ref. 265 © 2021 OSA.

4.2 EO devices

4.2.1 Electro-optic modulator

Compared with other material systems, the most attractive feature of LN is its large EO coefficient, which can be used for fabricating high-performance modulators. Different from the plasma dispersion effect-based modulators in silicon photonics[10] and the electro-absorption-based modulators in III–V platforms,[11] there is no carrier dynamic process in LN-based modulators where the speed is mainly limited by the microwave electrode. Therefore, Pockels effect-based linear LN modulators can achieve higher modulation speeds.[31,52] Therefore, LN-based modulators are widely used in current fiber-optical communication systems. For a long time, these modulators have been fabricated in bulk LN crystals using the technologies described in Sec. 2. For example, a Ti-diffused ring resonator in a bulk LN crystal can achieve around a 1.565 pm/V tuning efficiency.[43] However, these bulky devices have a large device size and cannot meet the requirements of dense integration in current/future large capacity optical interconnect systems. The TFLN platform is well poised to solve these problems. In the same year, Guarino et al. demonstrated an EO tunable microring resonator in TFLN using CIS and wafer bonding technology.[181] Its structure is shown in Fig. 10(a), where the Z-cut TFLN is directly etched and inserted between the top and bottom electrodes. As shown in Fig. 10(b), the measured tuning efficiency is about 0.105 pm/V from the observed wavelength shift.[181] Such a value is lower than results demonstrated in bulk LN, which is probably due to the lower electric field strength inside the waveguide and can perhaps be improved by changing the design. Subsequently, with the high-quality TFLN that is now commercially available, various kinds of modulators have been demonstrated.[31,52,88,241–243,272–288] Some of the reported modulators in LN platforms are summarized in Table 5.

In terms of device configuration, there are some structures such as microrings,[272,292] MZIs,[31,52,88,272,274,275,277,278,281–285,287] Michelson interferometers,[273,276,279] PhC cavities,[241] and DBR-FP modulators,[242,243] as shown in Table 5 and Fig. 11. Different configurations have different advantages. For example, microring-based modulators have compact sizes,[272,292] and Michelson interferometer modulators (MIMs) [Fig. 11(f)] can realize reduced half-wave voltage-length product ($V_\pi L$) due to doubled interaction between the light wave and electric field compared with MZI structures.[273,276,279] The improved tuning efficiency of PhC-based [Figs. 11(d) and 11(e)] and DBR-FP-based [Figs. 11(g)–11(i)] modulators is based on a similar principle.[241–243]

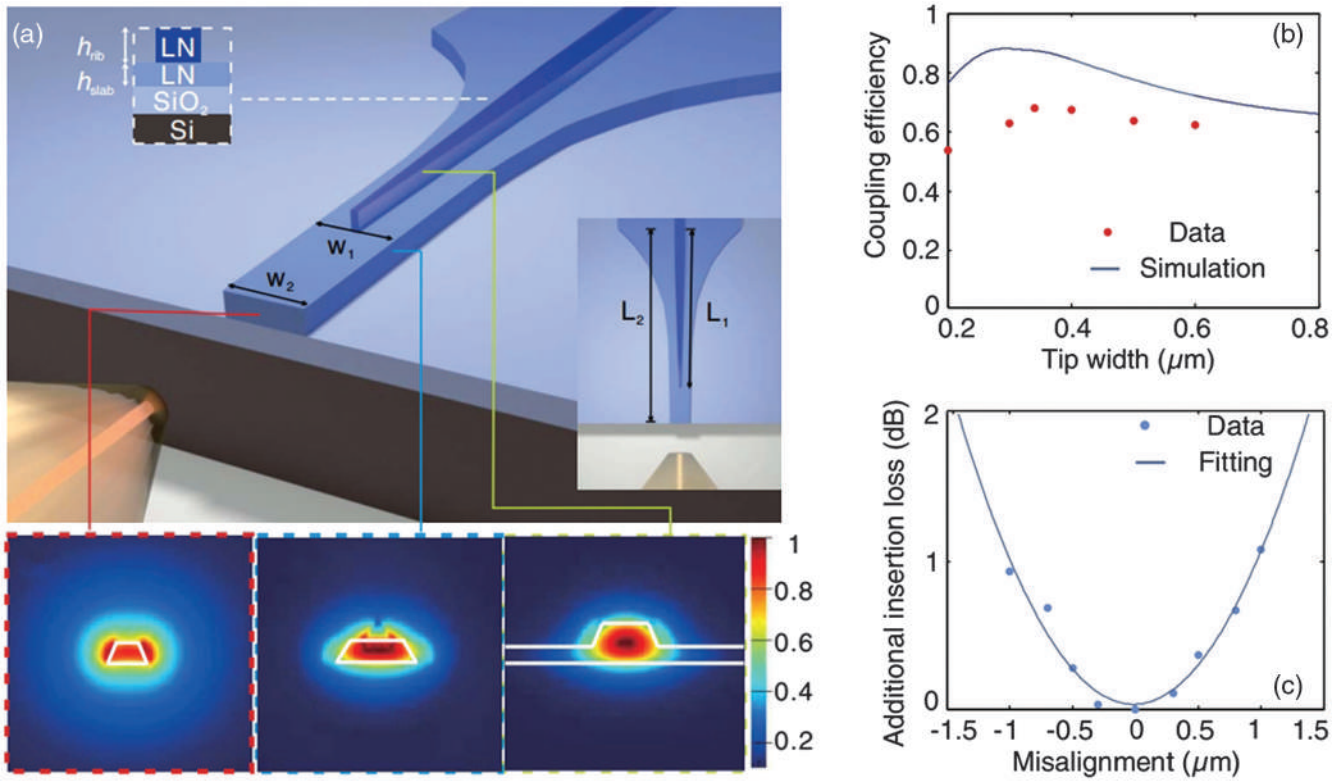

Fig. 9 LN-based edge coupler. (a) Schematic structure of the bilayer edge coupler and its corresponding mode profiles at different positions. (b) Simulated and measured coupling efficiency versus different tip widths in the tapered slab region. (c) Additional insertion loss with respect to coupling misalignment (TE mode). (a)–(c) Adapted with permission from Ref. 246 © 2019 OSA.

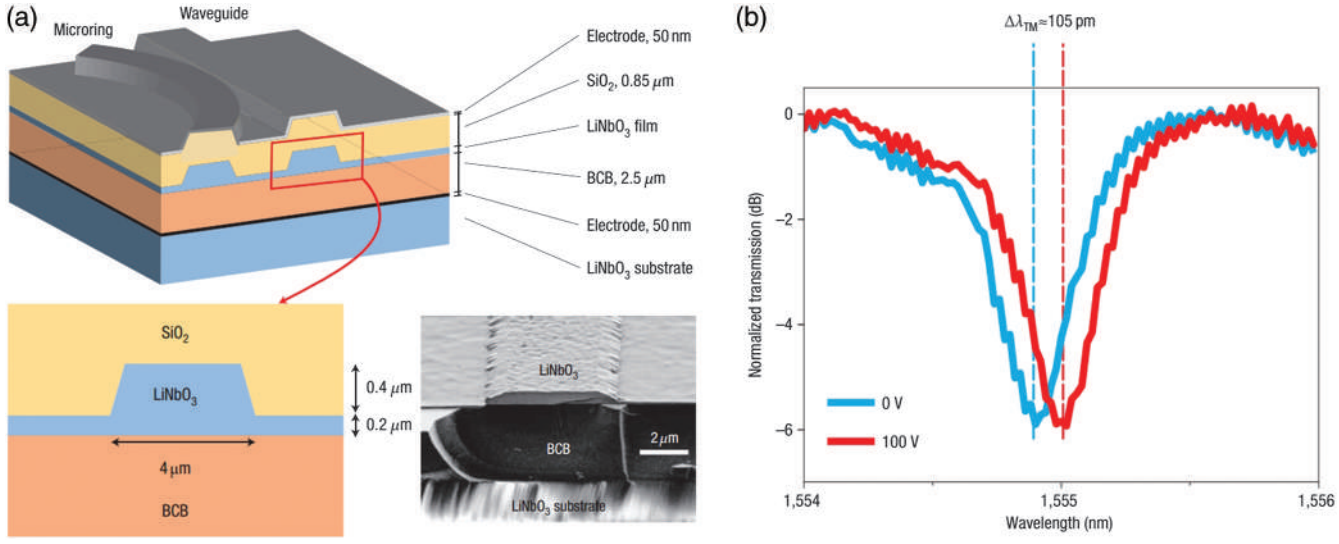

Fig. 10 TFLN EO tunable microring resonator. (a) Schematic structure (top), cross section (bottom left), and SEM images of the Z-cut TFLN microring modulator, and (b) its EO resonance shift curve. (a) and (b) Adapted with permission from Ref. 181 © 2007 Nature Publishing Group.

Table 5 Summary of LN-based EO modulators. HI, heterogeneous integration; DMT, discrete multitone; APE, annealed proton exchange; N.A., not available/applicable.

Year	Cut	Type	$V_\pi L$	Performance	Process	IL[a]/Q factor	Ref.
2002	X-bulk	MZI	~12 V · cm	S_{21}: 30 GHz; ER: 25 dB; data: 40 Gb/s (NRZ)	Ti diffusion	5.4 dB[b]	289
2007	Z-bulk	Ring	N.A.	EO shift: 1.565 nm/V (TM); 0.6912 nm/V (TE)	Ti diffusion and wet etch	N.A.	43
2007	Z-TFLN	Ring	N.A.	EO shift: 0.105 pm/V (TM)	HI and Ar etch	Q: 4×10^3	181
2009	Z-bulk	MZI	5.35 V · cm	ER: 20 dB	Ti diffusion and wet etch	0.5/0.15 dB/cm (TM/TE)	290
2014	X-bulk	PhC	0.0063 V · cm	EO shift: 0.6 nm/V; ER: ~11.2 dB; S_{21}: ~1 GHz	APE and FIB	21 dB[b]	291
2018	Y-TFLN	Ring	N.A.	S_{21}: 4 GHz; EO shift: 0.32 pm/V; ER: >10 dB	Cl_2 ICP	2.3 dB/cm	292
2018	X-TFLN	MZI	2.2 V · cm[c]	S_{21}: 100 GHz (length: 5 mm); data: 210 Gb/s (8-ASK)	Ar ICP-RIE	<0.5 dB/0.2 dB/cm	31
2018	X-TFLN	MZI Ring	1.8 V · cm (MZI) 7 pm/V (ring)	S_{21}: 15 GHz (MZI); S_{21}: 30 GHz (ring)	Ar ICP-RIE	MZI: 2 dB; ring: 1.5 dB	272
2019	X-TFLN	MZI	2.2 V · cm	S_{21}: >70 GHz; data: 100 Gb/s (NRZ)	HI and Ar ICP	2.5 dB	52
2019	X-TFLN	MIM	1.4 V · cm	S_{21}: 12 GHz; data: 35 Gb/s (NRZ)	Ar ICP	4 dB	273
2019	X-TFLN	MZI	5.3 V · cm	ER: >53 dB	ICP	3 dB/cm	274
2019	X-TFLN	MZI	7 to 9 V · cm	V_π: 3.5 to 4.5 V at 5 to 40 GHz	Ar RIE	~1 dB	275
2019	X-TFLN	MIM	1.2 V · cm	S_{21}: 17.5 GHz; data: 40 Gb/s (NRZ); ER: 6.6 dB	HI and Ar ICP	3.3 dB	276
2019	X-TFLN	MZI	7.2 V · cm	S_{21}: 20 GHz	Ti-diffusion	9 dB[d]	293
2020	X-TFLN	PhC	N.A.	EO shift: 16 pm/V; S_{21}: 17.5 GHz; data: 11 Gb/s (NRZ)	Ar ICP	2.2 dB	241
2020	X-TFLN	DBR-FP	N.A.	S_{21}: 60 GHz; data: 100 Gb/s (NRZ); ER: 53.8 dB	Ar ICP	0.2 dB	243
2020	X-TFLN	MZI	2.7 V · cm	S_{21}: >70 GHz; data: 128 Gb/s (PAM4); ER: ~40 dB	Ar ICP	1.8 dB	277
2020	X-TFLN	MZI	2.47 V · cm[c]	S_{21}: >67 GHz (7.5 mm arm); data: 320 Gb/s (16 QAM)	Ar ICP	1.8 dB	88
2021	X-TFLN	MZI	2.74 V · cm	S_{21}: 55 GHz	ICP	8.5 dB	278
2021	X-TFLN	MIM	1.06 V · cm	S_{21}: 40 GHz; data: 70 Gb/s (NRZ)	HI with SiN	4.1 dB	279
2021	X-TFLN	WG	1.91 V · cm	Operating at 1064 nm	CF_4 and Ar ICP	7.7 dB	280
2021	X-TFLN	MZI	0.64 V · cm	S_{21}: 3 GHz	Ion milling	1.77 dB/cm	281
2021	X-TFLN	MZI	2.3 V · cm	S_{21}: >50 GHz; ER: 20 dB	Ar RIE	<1 dB	282
2021	X-TFLN	MZI	1.7 V · cm	S_{21}: >67 GHz	Ar RIE	17 dB[b]	283
2021	X-TFLN	MZI	1.75 V · cm	S_{21}: >40 GHz	Ar ICP	0.7 dB/cm	284
2021	X-TFLN	MZI	3.67 V · cm	S_{21}: 22 GHz; data: 25 Gb/s (NRZ); ER: >20 dB	Ar ICP	6 dB (2 μm)	285
2021	X-TFLN	DBR-FP	N.A.	EO shift: 15.7 pm/V; S_{21}: 18 to 24 GHz; data: 56 Gb/s (NRZ)	ICP	<1.65 dB	242
2021	X-TFLN	MZI	3.068 V · cm	S_{21}: 60 GHz; data: 200.4 Gb/s DMT data	Ar ICP	3 dB[b]	287
2022	X-TFLN	MZI	2.35 V · cm	S_{21}: 110 GHz (1 V); data: 1.96 Tb/s (400 QAM)	Ar ICP	6.5 ± 0.5 dB	294

[a]Insertion loss (IL) is typically defined by the device intrinsic without considering coupling loss if there is no specific noting. Due to different characterization methods reported in the literature, here we also list the propagation loss if the original literature did not report the IL data. For the ring modulator, the Q factor is provided as it also reflects waveguide loss information.

[b]Including coupling loss.

[c]Calculated based on reported data.

[d]Not sure if coupling losses are included.

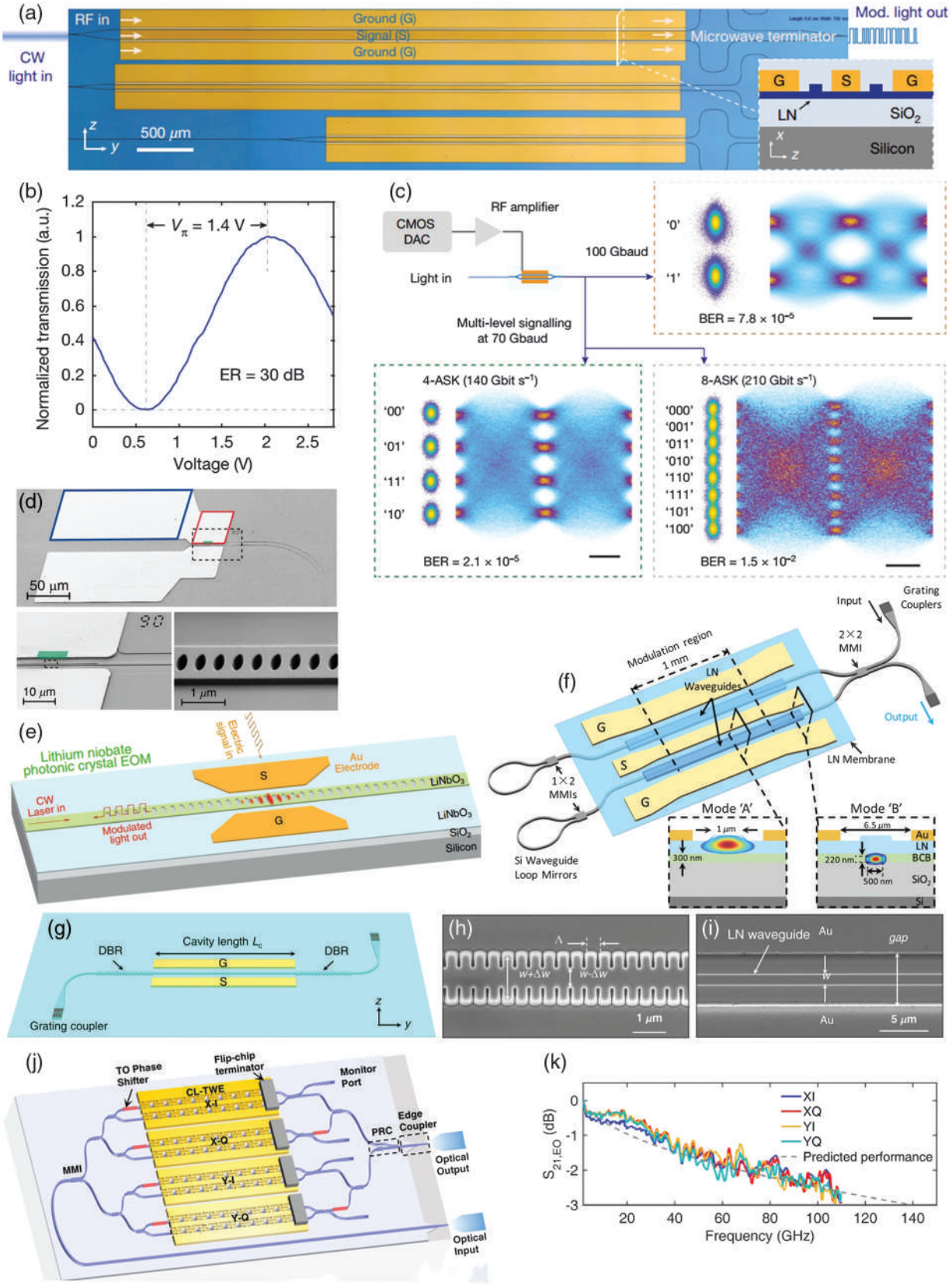

Fig. 11 TFLN-based modulators. (a) Microscopic image of TFLN MZI modulator (inset is its schematic cross section). (b) Measured transmission spectrum of a 2-cm long device. (c) Measured high speed data transmission results of 100 Gb/s NRZ, 140 Gb/s 4-ASK, and 210 Gb/s 8-ASK signals. (a)–(c) Adapted with permission from Ref. 31 © 2018 Springer Nature Limited (SNL).

Fig. 11 (*Continued*) (d) SEM images (top: full SEM image; bottom: zoom-in image of the PhC details). (e) Schematic structure of the TFLN PhC modulator. (d) and (e) Adapted with permission from Ref. 241. (f) Schematic structure of the MIM, and insets are cross section mode profiles at different positions. Adapted from Ref. 276. (g) Schematic structure of the TFLN DBR modulator, and SEM images of the (h) DBR and (i) modulation region. (g)–(i) Adapted with permission from Ref. 242 © 2021 COS. (j) Schematic structure and (k) measured S_{21} curves of the TFLN-based DP-IQ modulator. X and Y represent two orthogonal polarization states, I and Q represent in-phase and quadrature branches. (j) and (k) Adapted with permission from Ref. 294 © 2022 Optica.

In most reported results, the amplitude of the input light is modulated by an applied electrical signal (amplitude modulation). As shown in Figs. 11(a)–11(c), around 100 Gb/s non-return to zero (NRZ) and up to 210 Gb/s 8-ASK (8 level amplitude modulation) are measured using an optimized MZI TFLN modulator. For a 20-mm long arm length, its measured S_{21} (defined as the forward transmission coefficient from port 1 as input to port 2 as output when port 2 is matched for a two-port network and was widely used to characterize the speed of optoelectronic devices) is above 40 GHz. The authors also demonstrated that its S_{21} can be improved up to above 80 GHz by reducing the arm length.[31] Some other modulation dimensions can also be added into the TFLN modulator.[88,294] In 2020, Xu et al. first introduced the phase modulation dimension into a TFLN modulator and realized transmission speeds up to 320 Gb/s based on the 16 quadrature amplitude modulation (QAM) format.[88] More recently, researchers from the same group further demonstrated a TFLN-based dual-polarization in-phase (DP-IQ) modulator with record 1.96 Tb/s data rate.[294] Figures 11(j) and 11(k) show a schematic of the DP-IQ modulator with a 2.35-cm long arm and its corresponding measured S_{21} curves. The researchers used double polarizations and a quadrature amplitude phase modulation format. For each single MZM, the measured S_{21} is above 110 GHz under 1 V voltage. Such a high bandwidth enables 400-QAM and thus realized a record 1.96 Tb/s total data capacity. By engineering the electrode transmission line[282,295] or introducing more multiplexing dimensions, such as mode division multiplexing,[24] the transmission speed/volume can be further improved.

In addition to speed, some other key metrics are also critical to evaluating modulator performance, such as $V_\pi L$, as well as insertion loss (IL). As shown in Table 5, most reported results have an average $V_\pi L$ between 1 and 3 V · cm.[52,88,272,273,276–280,282–285,287] Using a dual-capacitor electrode layout, the $V_\pi L$ can be reduced to as low as 0.64 V · cm.[281] Such a factor is highly related to the device structure and can likely be improved by optimizing the design. The overall low $V_\pi L$ values of LN-based modulators are highly desirable for their application scenarios.

It can be observed from Table 5 that most of the reported LN-based modulators have low IL (excluding coupling loss),[31,52,88,241–243,272,275,277,282,287] which depends on the device dimension and fabrication technology. A typical bulk LN-based modulator is usually fabricated using ion-in diffusion technology. For TFLN modulators, Ar plasma-based dry etching is widely used to pattern the LN waveguide structures, which can realize a low propagation loss (also depends on etching conditions) compared with bulk devices. By optimizing the processing technology, the TFLN waveguide with a more prevailing propagation loss of lower than 0.2 dB/cm can be obtained.[31] Thus, high-performance LN-based modulators with lower IL can be expected in the future.

Extinction ratio (ER) is another metric to characterize a modulator's performance. In most published LN-related results, ER is defined by the valley value [such as the minimum value shown in Fig. 10(b)] of the transmission spectrum.[181] A high ER gives a better modulation signal quality, such as more open eye diagrams during data transmission experiments. The typical ER in literature is between 10 and 30 dB,[282,285,292] which can be improved by optimizing either process technology or design. Take the MZI as an example, and usually the Y-branch is used as the power splitter. However, if the optical power difference between the two arms is too large due to the imperfect fabrication process technology, its ER will be degraded. By optimizing the fabrication process, or changing the Y-branch structure with a multimode interferometer (MMI, more tolerant to fabrication process error compared with Y-branch),[296] a higher ER can be realized. In addition, using cascaded MZI[274] or Bragg grating waveguide,[243] ultrahigh ERs have been demonstrated, which are other examples of improving ER by optimizing design.

In summary, there are many different criteria to evaluate a modulator's performance. Although there are many different kinds of LN-based modulators that have been demonstrated, none of them can realize all the best metrics at the same time. The tradeoffs exist, thus there are still optimizing spaces for the research community.

4.2.2 Other electro-optic devices

The superior EO effect of LN is not only limited to the modulator application, as it can also be extended to various other kinds of application scenarios. One of the key benefits that may result from the development of TFLN is that a variety of different components can be integrated on the same chip to enable more functionality overall. The physics behind them is generally the same as EO modulators, which is by changing the material refractive index and thus the phase. Some typical EO-based applications demonstrated on TFLN platform have been summarized here.

First, the fast EO tuning features can be used in optical fiber communication or optical interconnects. For example, Fig. 12(a) shows EO tunable interleavers,[297] which can be used as tunable filters or wavelength-selective switches. Their measured tuning sensitivity is ∼18 [Fig. 12(b)] and ∼16 pm/V [Fig. 12(c)] for TE and TM modes, respectively. Compared with TO-based tuning, EO tuning enables a much higher speed and thus has broader application perspectives.

Second, the EO effect of LN can also be used for controlling the optical frequency, which enables broad applications, such as advanced photonic computation and frequency-domain photonic quantum computers.[298,299] Figure 13(a) shows an example of a programmable photonic two-level system for controlling gigahertz microwave signals, and its working principle is

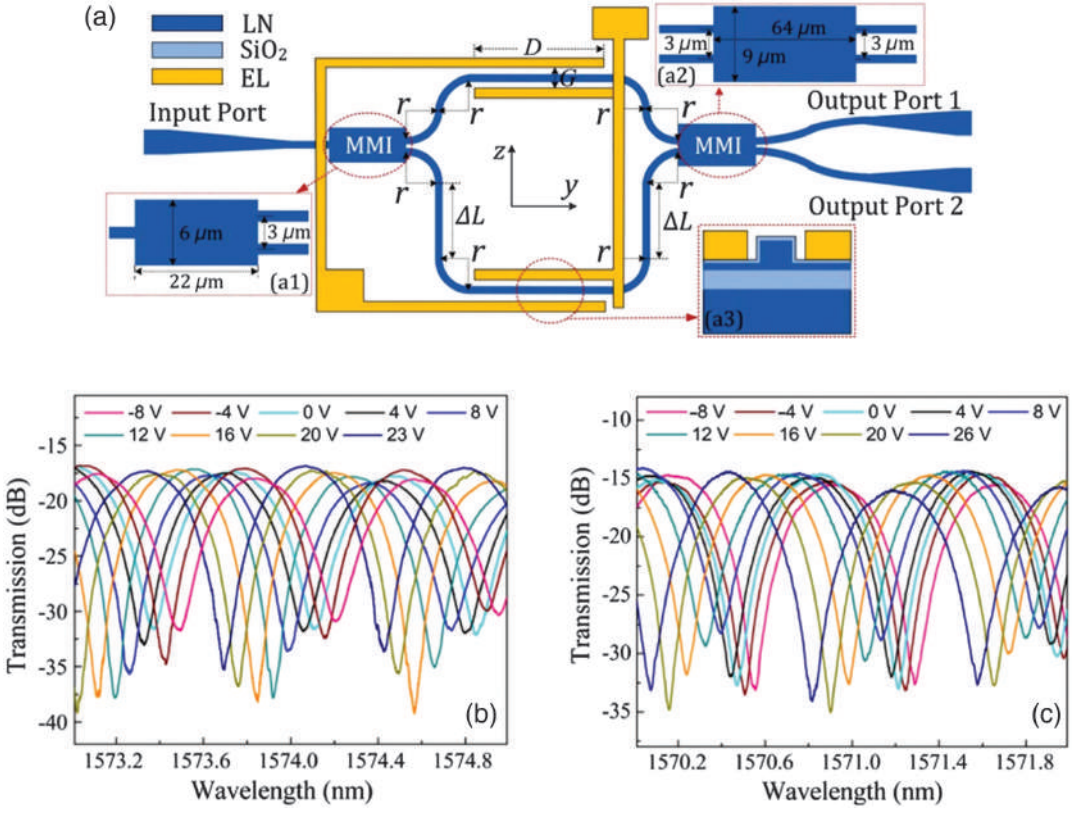

Fig. 12 EO tunable interleaver in TFLN. (a) Schematic structure of TFLN waveguide interleaver, and its measured tunable transmission spectra for (b) TE and (c) TM polarized input light. (a)–(c) Adapted with permission from Ref. 297 © 2018 OSA.

shown in Fig. 13(b).[298] Benefits from the low loss TFLN ring resonator and cointegrated microwave electrode, the authors have demonstrated >30 GHz electrical bandwidth, around 0.5 GHz/V modulation efficiency, and ~2 ns photon lifetime.[298] Figures 13(c)–13(e) show another example of an on-chip EO frequency shifter for frequency controlling using only a single-tone microwave signal.[299] In that work, the authors have realized frequency shifts as high as 28 GHz with an approximately 90% on-chip conversion efficiency (CE) and >0.99 shift ratio (defined as the ratio of the output power at the shifted frequency and the output power inside the bus waveguide). Both works pave the way of efficiently and precisely manipulating light on gigahertz frequency, and open doors to many application scenarios.

Third, an LN-based microwave to optical transducer for quantum networks is another application scenario, especially under the conditions of rapidly developed quantum computation and long-haul quantum communication systems.[300–302] The typical microwave to optical conversion is based on electro-opto-mechanics (EOM) in a bulk optical cavity, which is difficult to operate at the quantum ground state as the mechanical cavity has a limited frequency.[302,303] An LN with the large Pockels effect enables GHz microwave to optical photons conversion and thus attracts significant attention. Holzgrafe et al. used the EO effect in coupled TFLN microrings, realizing an efficient microwave-to-optical transducer [Fig. 14(a)].[300] Its measured on-chip transduction efficiency is up to $(2.7 \pm 0.3) \times 10^{-5}$ [Fig. 14(b)], which can be used to link up superconducting quantum devices with optical fibers. McKenna et al. demonstrated a similar microwave-to-optical transducer,[301] and the TFLN sits on a sapphire platform. Its device structure is shown in Fig. 14(c), which consists of triple resonators. According to the measured results shown in Fig. 14(d), such a device converts microwave photons to optical photons with an on-chip efficiency of around 6.6×10^{-6}. More recently, Xu et al. demonstrated an improved CE up to 1.02% in coupled ring resonators,[302] as shown in Figs. 14(e) and 14(f). Such an improvement is realized using an air-cladding structure to mitigate the prominent photorefractive (PR) effect, which is supposed to be the main limiting factor of CE.[302] Even though the highest CE in TFLN is still under expectation considering its high Pockels effects, we believe the gap between a typical EOM-based scheme (highest CE of 47%[303]) and a TFLN-based EO structure [currently of $(2.7 \pm 0.3) \times 10^{-5}$[300] or 6.6×10^{-6}[301]] can be further narrowed down by optimizing the design and fabrication technology. TFLN-based integrated transducers will play a significant role in future quantum networks.

The last example is a dynamic integrated Fourier-transform spectroscopy based heterogeneously integrated SiN on LN hybrid structure (detail about such integration technology can be found in Sec. 3.3), and its device details are shown in Fig. 15,[171] where the EO properties of TFLN have been exploited for retrieving a complete spatial interferogram. This prototype device is capable of completely sampling the standing waves from signals over a 500-nm bandwidth. Using such a device, the authors have demonstrated a measured interferogram

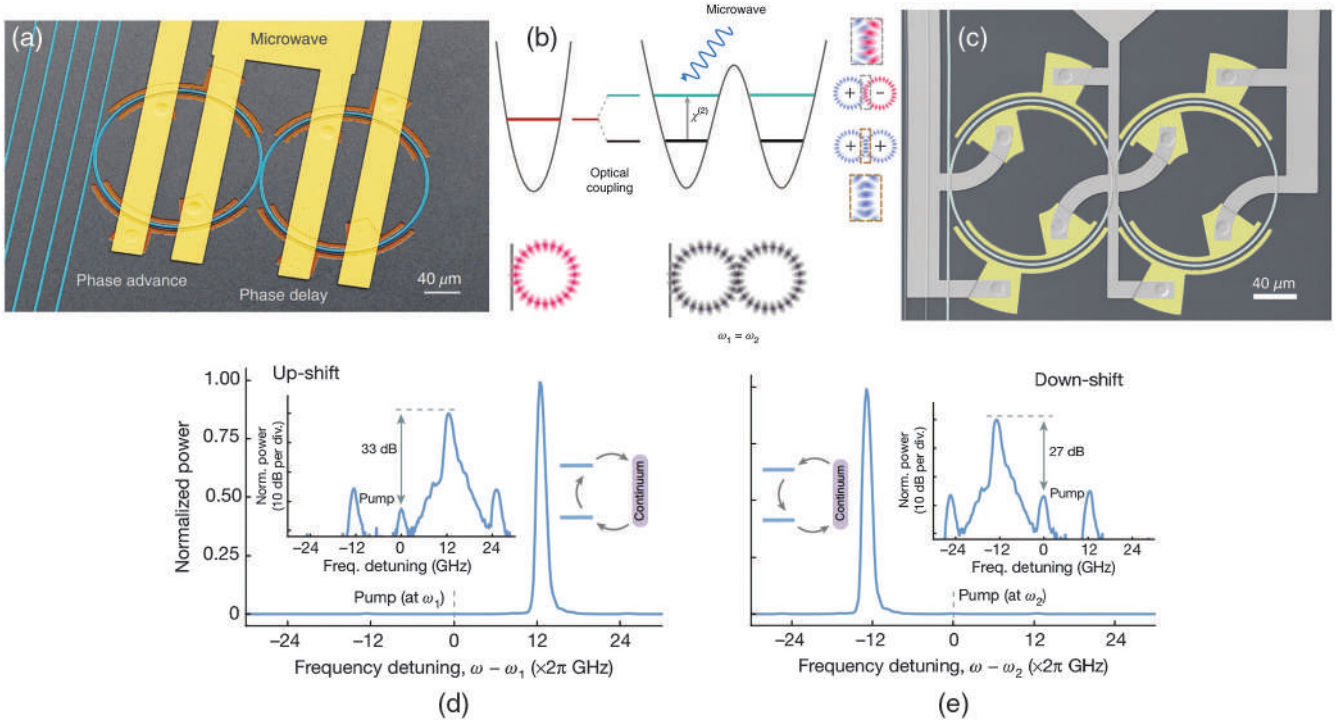

Fig. 13 TFLN-based EO devices for optical frequency controlling. (a) False colored SEM image of an EO tunable coupled microring resonator. (b) The programmable photonic molecule consists of a pair of identical coupled rings (resonant frequency $\omega_1 = \omega_2$). Such a system has two distinct energy levels: symmetric (blue/blue shading) and antisymmetric (red/blue) optical modes are spatially out of phase by π. The microwave field interacts with the two-level system through the large EO effect of TFLN. (a) and (b) Adapted with permission from Ref. 298 © The Author(s), under exclusive license to SNL 2018. (c) SEM image of a reconfigurable electro-optic frequency shifter. (d) Upshift and (e) downshift under 12.5 GHz microwave frequency and at 1601.2 nm wavelength (ω_1) show measured 80% CE and >0.99 shift ratio (defined as the ratio of the output power at the shifted frequency and the output power inside the bus waveguide). Inset shows the directions of energy flow and the spectra in dB scale. (c)–(e) Adapted with permission from Ref. 299 © The Author(s), under exclusive license to SNL 2021.

for a broadband optical signal from a super-luminescent light emitting diode, which has a 1550 nm center wavelength and a 50 nm 3 dB bandwidth. The above-discussed results are just a few examples based on the EO effect of LN for extended applications. We believe the applications are not limited to these and more advanced devices/PICs will be demonstrated in the future.

4.3 Nonlinear and Quantum Photonic Devices

LN is also an excellent platform for various nonlinear and quantum photonic applications due to its significant nonlinear effects. In typical bulk LN, nonlinear applications are mainly limited to areas of frequency conversion. For TFLN, on the other hand, due to the convenience of dispersion engineering, some applications such as optical frequency comb and supercontinuum generations typically demonstrated on silicon photonics platforms can also be realized with superior performance contributed by its improved confinement and better overlap with light.

The nonlinear dynamics in both bulk LN and TFLN need to satisfy the phase-matching condition for conservation of momentum, which can be achieved using birefringent phase matching.[80] Such a method is difficult to realize in both bulk LN and TFLN waveguide structures and has lots of challenges, such as low effective nonlinear effects and inconvenient phase-matching temperatures and angles.[304] An alternative method is called quasiphase matching (QPM) and can be realized by periodically inverting (poling) LN ferroelectric domains to point alternatively to the $+c$ and $-c$ directions to form PPLN.[80] Compared with bulk LN, an advantage of TFLN structures is their flexibility in dispersion engineering by varying the waveguide dimension,[55,79] which provides an additional degree of freedom for fine-tuning the phase-matching condition.

LN-based devices for nonlinear and quantum photonic applications are summarized in Table 6. One of the main categories is frequency conversion, which can be realized either by frequency upconversion with SHG,[12,13,54–56,58–61,63,65,66] SFG,[67,68] and THG[62,69] or by frequency downconversion with DFG.[44] In bulk LN-based devices, their bending loss is typically large due to the small refractive index contrast available, and thus results in a large device size and also degrades the interaction between the light and nonlinear medium. For example, the CE of SHG in bulk PPLN is usually at the level of $600\%/(\mathrm{W}\cdot\mathrm{cm}^2)$.[12] In contrast, a nanophotonic thin film periodically poled lithium

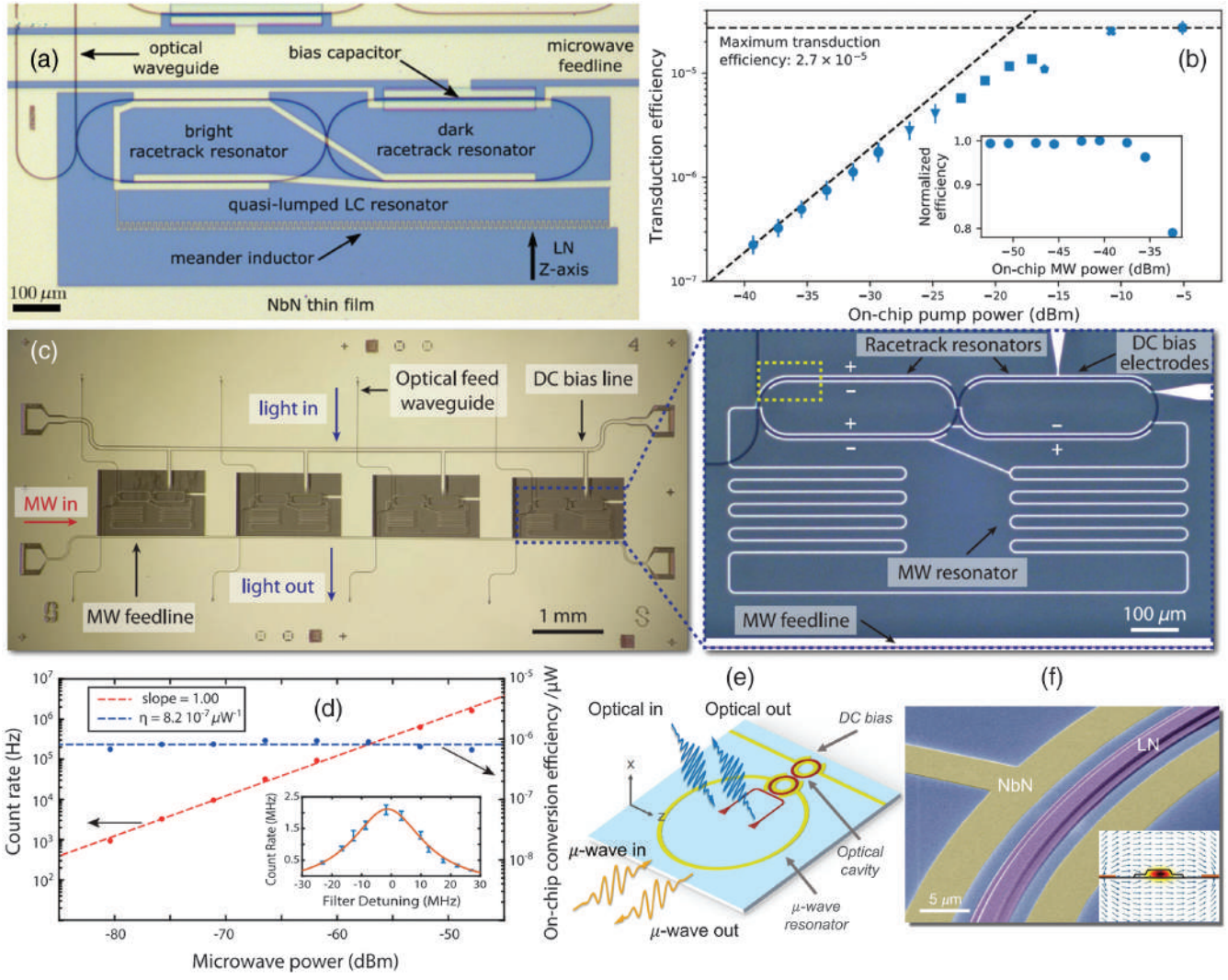

Fig. 14 EO-based microwave to optical transducer in TFLN. (a) Microscopic image of a TFLN-based transducer, and (b) its corresponding measured maximum transduction efficiency with respect to optical pump powers. (a) and (b) Adapted with permission from Ref. 300 © 2020 OSA. (c) Microscopic image of a triply resonant LN on sapphire transducer (zoom in: device details), and (d) its measured photon count rate versus microwave drive frequency with respect to different input microwave powers. (c) and (d) Adapted with permission from Ref. 301 © 2020 OSA. (e) Schematic of an EO converter in TFLN based on two coupled microring resonators (red) and a cointegrated superconducting resonator (yellow). DC bias is applied for optical mode tuning. (f) False color SEM image of the EO converter detail. Inset is the electric field distribution. (e) and (f) Adapted with permission from Ref. 302.

niobate (TFPPLN) waveguide can have CE as high as $2600\%/(\mathrm{W}\cdot\mathrm{cm}^2)$.[58] Assisted by a high-Q cavity, a high CE of 250,000%/W SHG has been demonstrated in a periodically poled TFLN microring,[63] as shown in Figs. 16(a)–16(c). Such a record ultrahigh CE is achievable from the ultralow loss/ultrahigh Q factor ($\sim 10^5$) microring resonator fabricated on a TFLN wafer with a large refractive index contrast. With future development of LN patterning and etching technologies, as well as material quality, an even higher CE can be expected on LN platforms. For example, as discussed in Sec. 4.1.1, the Q factor can be improved up to around 10^8 using an optimized patterning technology,[224] which would enable a greater nonlinear interaction of the optical field with the LN crystal. In addition, metasurface structures can also be used to improve nonlinear conversion in TFLN.[306] Some experimental results will be summarized and introduced in Sec. 4.6.2. It is worth mentioning that devices in thicker (several micron-thick) LN films have some advantages in high-power frequency conversion, such as watt-level frequency generation, as they exhibit a higher power damaging threshold compared with submicron film-based devices. As shown in Table 6, around 1 W of second harmonic can be generated in a thicker LN film,[153,154] using the lapping and polishing method (details in Sec. 3.2.2). The larger waveguide core also enables high global efficiency (considering insertion loss) due to its larger mode profile.[29,30,148–154]

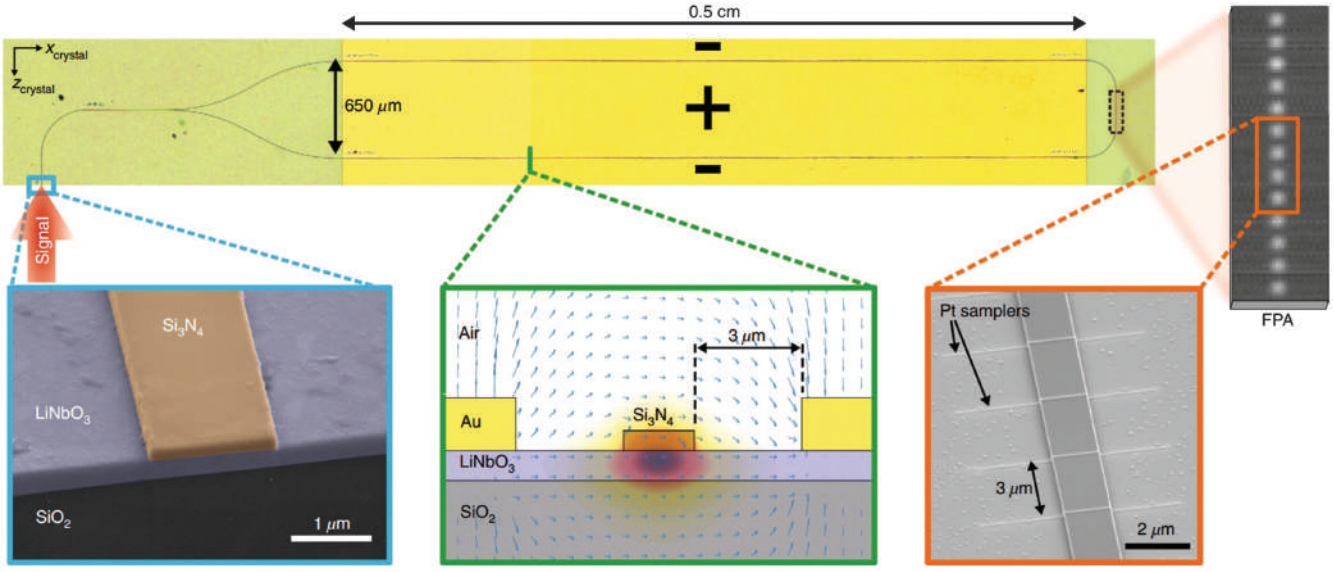

Fig. 15 EO waveguide spectrometer in TFLN. Microscopic image and device details of an EO TFLN waveguide spectrometer. Adapted with permission from Ref. 171 © The Author(s), under exclusive license to SNL 2019.

The optical frequency comb with periodic optical frequency lines has also been demonstrated in the TFLN platform[77] while it is typically difficult to realize in bulk LN. Based on a dispersion-engineered microring with a high Q factor, Kerr comb generation has been demonstrated in the TFLN platform.[63,74,75] Figure 16(d) shows one example of an on-chip photonic integrated circuit (PIC) containing both Kerr comb generation and filtering.[76] The microresonator frequency comb generator is based on the third order ($\chi^{(3)}$) nonlinear effect, while the add-drop filter is based on the second-order ($\chi^{(2)}$) EO effect. Its generated comb has a line spacing of ~250 GHz, and spans of ~300 and ~700 nm for TM and TE modes, respectively. Compared with a third-order nonlinearity-based comb, an EO phase modulation-based comb features high stability and controllability, which has also been demonstrated in the TFLN platform.[77] Such an EO comb is based on ring modulators and has over 80 nm bandwidth and more than 900 comb lines with a slope of 1 dB/nm, as shown in Fig. 16(e). Both the Kerr and EO combs show that TFLN is an excellent platform for comb generation.

TFLN can also be used for supercontinuum generation based on its second- and third-order nonlinear effects. Figure 16(f) shows an example of a supercontinuum spanning 2.58 octaves using dispersion-engineered TFLN waveguides. Its performance is highly related to the waveguide geometries. Benefiting from its large refractive index contrast, dispersion engineering becomes easy and more demonstrations on comb and supercontinuum generations can thus be expected.

Based on the strong second-order nonlinearity in TFLN, a broadband OPA[70] and an ultralow threshold OPO[71] have also been realized in dispersion-engineered TFLN devices. Figure 16(g) shows the principle of OPA in dispersion-engineered periodically poled TFLN waveguides. The general idea is to do engineering on the waveguide for low group velocity dispersion and group velocity mismatch, and thus maximize OPA performance.[70] According to the measured results, broadband phase-sensitive amplification is larger than 45 dB/cm for a 2.5-mm long waveguide with pump pulse energy of only 0.8 pJ. Such a result paves the way for chip-based light sources.[70] Raman scattering is another important nonlinearity and has been widely explored in other materials systems. Yu et al. demonstrated multiwavelength Raman lasing in a TFLN microring and analyzed the underlying physical process,[73] which provides guidance for TFLN-based SRS dynamics.

In addition to the above classical applications, LN is ideally suited for quantum applications based on its large nonlinearity, such as photon pair generation.[15,80–83,149] Although bulk LN has been used for quantum applications for a long time, the recently developed TFLN makes integrated and higher-efficiency devices possible. Figures 16(h)–16(j) show an example of a quantum photon source based on a TFLN microring.[81] Its measured photon pair generation rate (PGR) is around 36.3 MHz using 13.4 μW pump power, while its measured coincidence to accidental ratio (CAR) is above 100 at high rates and reaches $14{,}682 \pm 4427$ at a low pump power. Both of these values are much higher than previous reported results, and such benefits mainly come from having highly confined TFLN devices together with the superior nonlinear effect. In general, with the development of recent advances in the TFLN platform, advantages of LN with its large $\chi^{(2)}$ and $\chi^{(3)}$ are increasingly being exploited. It is believed that many new phenomena and applications will be demonstrated based on the unique nonlinear properties of LN and will further contribute to the development of quantum photonic devices.

4.4 AO Devices

LN is also an ideal platform for the demonstration of AO devices due to its large photo-elastic constant,[2] as such devices can be used in the area of optical networking and signal processing.[16] For a long time, surface acoustic wave (SAW) derived AO devices have been extensively explored in bulk LN in combination with Ti diffusion/PE technology.[307] Due to the weak mode confinement caused by the poor refractive index contrast available with those technologies, the interaction between the

Table 6 Summary of LN-based devices for nonlinear and quantum photonic applications. MgLN, MgO-doped lithium niobate; ZnLN, Zn-doped lithium niobate; ZnOLN, ZnO-doped lithium niobate; PE, proton exchange; HI, heterogeneous integration; PIC, photonic integrated circuit; N.A., not available/applicable.

Year	Cut	Type	Application	Performance	Fabrication	Ref.
1993	Z-cut	Bulk PPLN WG	SHG	CE: 600%/(W · cm^2)	PE and electrical poling	12
1996	Z-MgLN	Bulk PPLN WG	SHG	CE: 4.5%/(W · cm^2)[a]	Wet etching and electrical poling	13
2002	N.A.	Bulk PPLN WG	Photon-pair	CE: 2×10^{-6}	PE and electrical poling	80
2004	N.A.	Bulk PPLN WG	SFG	CE: 330 ± 10%/(W · cm^2)	PE	67
2006	Z-ZnLN	TFPPLN ridge	SHG	CE: 370%/(W · cm^2)	Lapping and polishing, dicing	29
2009	Z-MgLN	Bulk PPLN disk	THG	CE: 1.5%/W^2	Mechanical polishing	69
2010	Z-ZnOLN	TFPPLN ridge	SHG	CE: 2400%/W	Lapping and polishing, dry etching	30
2016	Y-MgLN	TFPPLN ridge	SHG	CE: 189%/(W · cm^2); output power: 0.86 W	Lapping and polishing	152
2016	X-cut	TFPPLN WG	SHG	CE: 160%/(W · cm^2)	HI and electrical poling	54
2016	ZnLN	TFPPLN ridge	Photon-pair	Rate: 1456 Hz/μW; efficiency: 64.1%	Lapping and polishing	149
2016	Z-cut	TFPPLN ridge	SHG	CE: 204%/W	Lapping and polishing, dicing	148
2017	Z-MgLN	TFPPLN	SFG	CE: 3.3%/W; BW: 15.5 nm	HI and bonding	305
2017	X-cut	TFLN WG	SHG	CE: 1660%/(W · cm^2); phase matching free	Ar ICP-RIE	55
2017	X-cut	TFLN WG	SHG	CE: 41%/(W · cm^2)	Ar ICP-RIE	56
2018	N.A.	TFPPLN ridge	Comb	Mid-infrared span	Lapping and polishing	150
2018	X-MgLN	TFPPLN WG	SHG	CE: 2600%/(W · cm^2)	Ar ICP-RIE and electrical poling	58
2019	X-cut	TFLN WG	SHG	CE: 1160%/(W · cm^2)	HI	59
2019	X-MgLN	TFPPLN ring	SHG	CE: 230,000%/W	Ion-milling and electrical poling	60
2019	X-cut	TFLN WG	SHG	CE: 2200%/(W · cm^2)	Ion-milling and electrical poling	61
2019	X-cut	TFLN disk	SHG; THG	SHG: 9.9%/mW; THG: 1.05%/mW^2	Femtosecond-laser ablation and FIB polishing	62
2019	Z-cut	TFPPLN ring	SHG	CE: 250,000%/W	Ar etching and electrical poling	63
2019	Z-cut	TFLN WG	SCG	Span: 1.5 octaves	Ar ICP	78
2019	Z-cut	TFPPLN ridge	SFG	CE: 85%/W	Lapping and polishing, dicing	151
2019	X-cut	TFLN PIC	Comb	Comb generation and modulation (PIC)	Ar ICP-RIE	76
2019	X-cut	TFLN WG	SCG	Span: 2.58 octaves	Ar ICP-RIE	79
2019	X-cut	TFLN ring	Comb	Span: >80 nm	Ar ICP-RIE	77
2019	MgLN	TFPPLN ridge	SHG	CE: 6.29%/(W · cm^2); output power: 1.1 W	Lapping and polishing, dicing	154
2020	N.A.	TFLN disk	SHG	CE: 10^{-2}% (282.7 nm)	Simulation	306
2020	Z-cut	TFPPLN ring	Photon-pair	PGR: 36.3 MHz; CAR: >100	Ion-milling and electrical poling	81
2020	X-cut	TFLN WG	SHG	CE: 3061%/(W · cm^2)	ICP and electrical poling	65
2020	Z-cut	TFLN disk	SFG	CE: 2.22×10^{-6}/mW	FIB and wet etching	68
2020	X-cut	TFLN ring	SRS	Pump-to-Stokes CE: 46%	Ar ICP-RIE	73
2020	X-MgLN	TFPPLN WG	Photon-pair	PCR: 11.4 MHz; CAR: 668	Electrical poling	82
2021	X-MgLN	TFPPLN WG	OPA	Amplification: >45 dB/cm	Ar etching and electrical poling	70
2021	Z-cut	TFPPLN ring	OPO	Threshold: ~30 μW; CE: 11%	Ar ICP-RIE and electrical poling	71
2021	Z-cut	TFPPLN ridge	SHG	CE: 22%/(W · cm^2); output power: 1 W	Lapping and polishing, dicing	153
2021	X-MgLN	TFPPLN WG	DFG	CE: 200%/(W · cm^2)	Ar etching and electrical poling	44
2021	X-cut	TFPPLN WG	SHG	CE: 435.5%/(W · cm^2)	ICP and electrical poling	66
2021	X-cut	TFPPLN WG	Photon-pair	Rate: 2.79×10^{11} Hz/mW; SHG: 2270%/(W · cm^2)	ICP and electrical poling	83

[a]Calculated based on reported data.

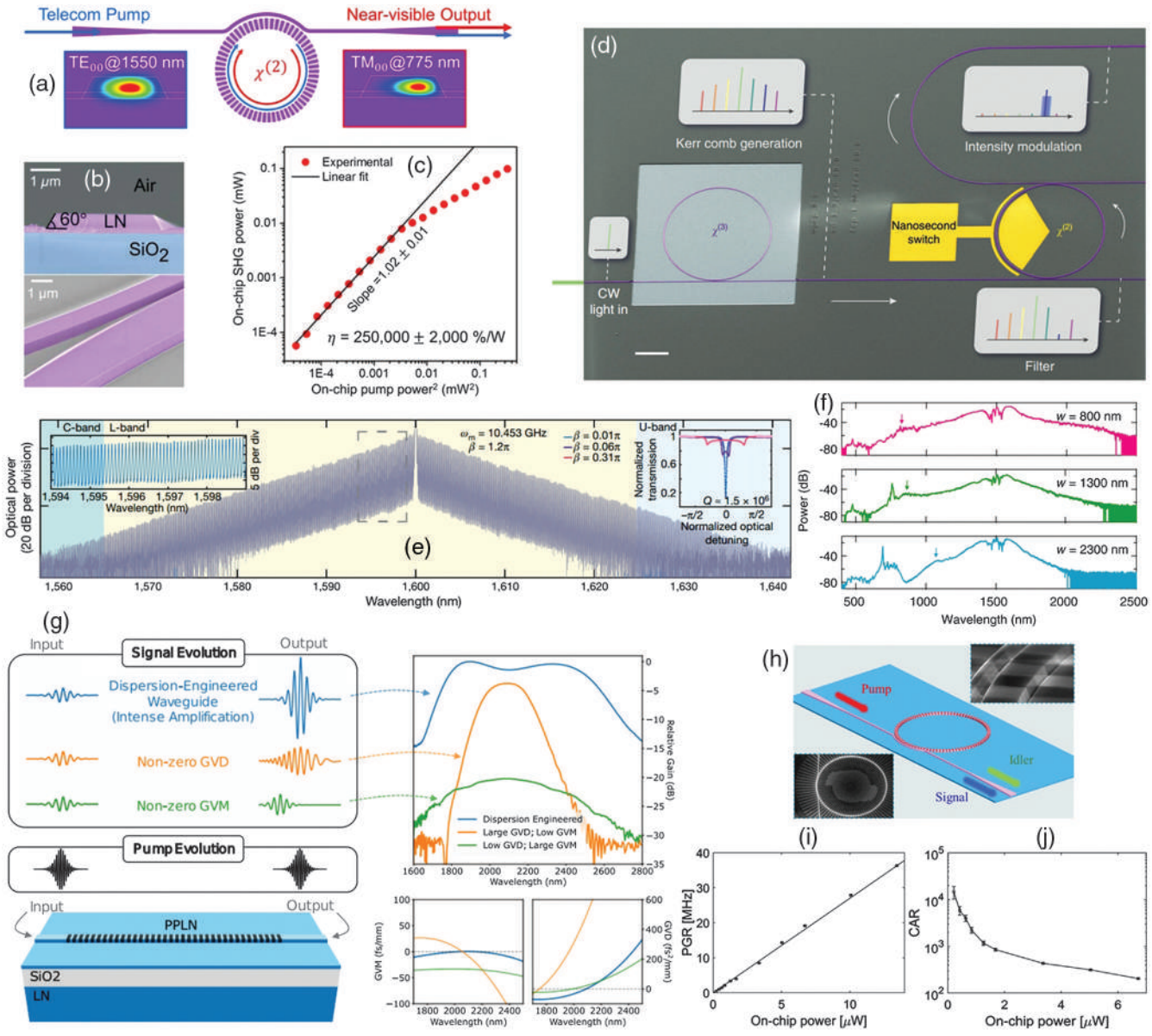

Fig. 16 LN-based nonlinear and quantum photonic devices. (a) Schematic structure of the TFPPLN microring. (b) False-color SEM images of the device cross section and coupling region detail. (c) Experimentally measured SHG power versus pump power. (a)–(c) Adapted with permission from Ref. 63 © 2019 OSA. (d) False color SEM image of TFLN PIC containing Kerr comb and EO add-drop filter. Adapted with permission from Ref. 76. (e) Measured transmission spectrum of the EO comb. Left inset shows a magnified view of several comb lines. Right inset shows measured transmission spectrum for several different modulation indices. Adapted with permission from Ref. 77 © The Author(s), under exclusive license to SNL 2019. (f) Measured transmission spectra with respect to different waveguide width. Adapted with permission from Ref. 79 © 2019 OSA. (g) Principle of OPA in dispersion engineered PPLN waveguide and simulated relative gain spectrum for three dispersion cases. Adapted with permission from Ref. 70 © 2022 OPTICA. (h) Schematic structure of the PPLN microring. Insets are the SEM images of the device details. Measured (i) PGR and (j) CAR. (h)–(j) Adapted with permission from Ref. 81 © 2020 American Physical Society (APS).

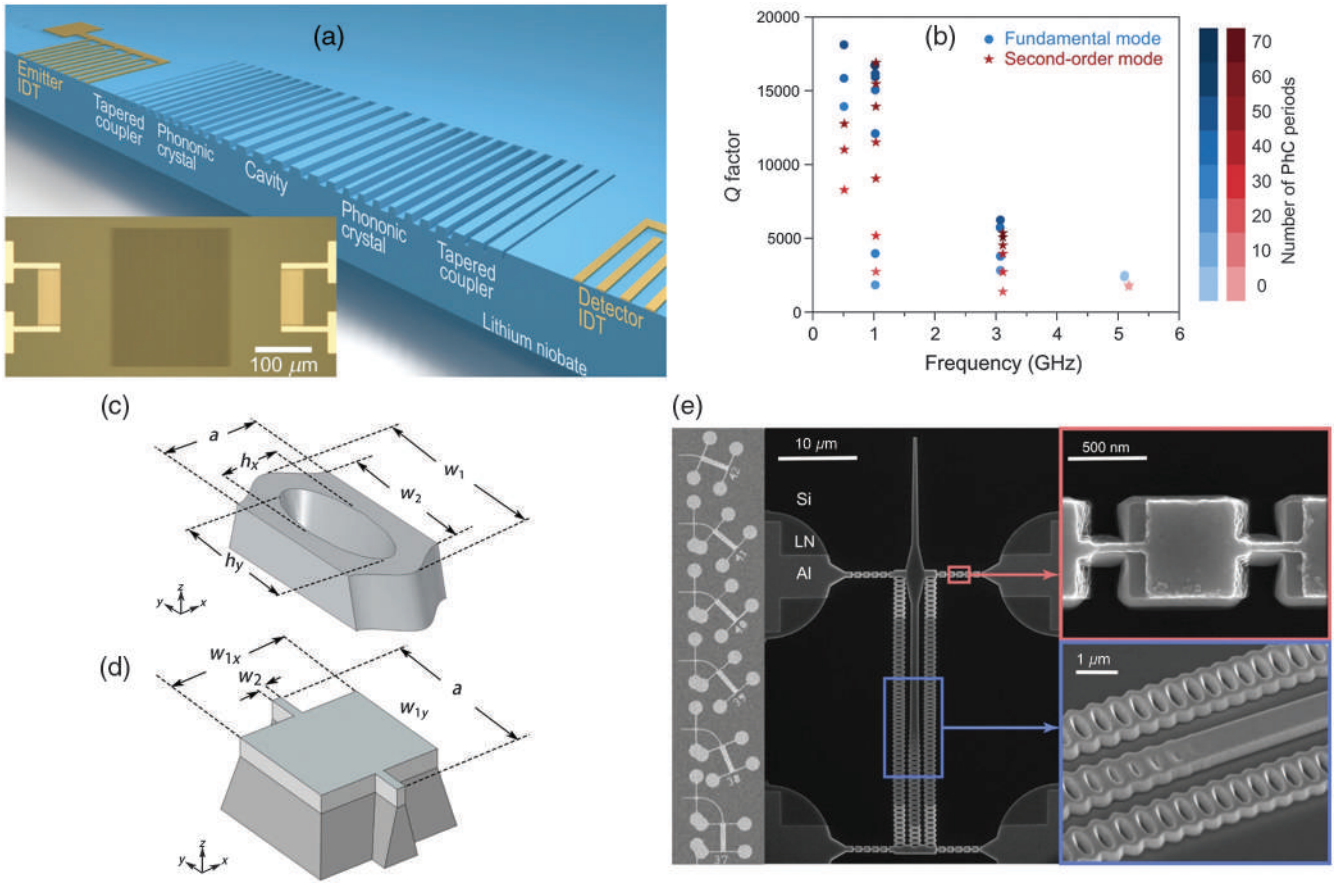

Fig. 17 Cavity optomechanics devices in LN. (a) Schematic of a band structure engineered surface acoustic resonator on TFLN. Inset is the microscopic image of the fabricated device. (b) Measured Q factor with respect to different resonator frequencies. (a) and (b) Adapted with permission from Ref. 311 © 2019 APS. Unit cell geometries of the (c) nanobeam optomechanical crystal and (d) 1D photonic shield. (e) SEM image of a 1D PhC cavity resonator for optomechanical mode generation. Left: full view of the device. Middle: top view of one device. Top right: top view of the 1D photonic shield region. Bottom right: SEM image of the nanobeam reflector coupling region. (c)–(e) Adapted with permission from Ref. 310 © 2019 OSA.

transmitted light and acoustic waves is not as high as desired. The recently developed TFLN platform provides an attractive choice for integrated AO devices. In 2010, Kadota et al. realized a high-frequency (4.5 and 6.3 GHz) Lamb wave resonator using direct c-axis TFLN by the CVD method,[308] which validates TFLN's advantages for AO devices. In this part, we will focus on the latest results about TFLN-based AO devices. Selected bulk LN-based results will also be covered for comparison.

4.4.1 Cavity optomechanics

Benefiting from commercially available high-quality TFLN and well-developed LN etching technologies, high Q factor and small phonon mode size SAW resonators at gigahertz frequencies have been demonstrated by the engineering of photonic band structures,[197,309–311] something that is inapplicable in the typical bulk LN platform. Figure 17(a) shows an SAW resonator based on chirping a quasi-1D PhC period, and its measured Q factor is 6240 at a fundamental mode frequency of 3.07 GHz [Fig. 17(b)], which results in an $f \cdot Q$ product of 2×10^{13} Hz.[311] In another optimized PhC structure, as shown in Figs. 17(c)–17(e), a mechanical mode frequency close to 2 GHz with a Q factor of around 17,000 at 4 K was obtained, which corresponds to around 3.4×10^{13} Hz.[310] These demonstrated high $f \cdot Q$ product optomechanics resonators pave the way toward hybrid quantum systems, enabling the control of solid-state electronic spins, AO modulators, gigahertz frequency optical comb generation, and performing microwave to optical conversion.[17,311]

4.4.2 Acousto-optic modulators

AO modulators have already been demonstrated in LN platforms.[16,17,312,313] Different from high speed EO modulators, AO modulators can be enhanced by a mechanical quality factor with bandpass frequency selectivity and also have no critical requirement of placing interdigitated transducers (IDTs) close to the optical waveguide, since acoustic waves have a low propagation loss.[312] Thus, AO modulators can be a good complement to existing EO modulators.

Surface elastic waves can be generated by mechanical coupling of a shear or compressional wave transducer.[314] However, for better interaction between acoustic and optical waves, the IDT structure is more frequently used.[314] Figure 18(a) shows

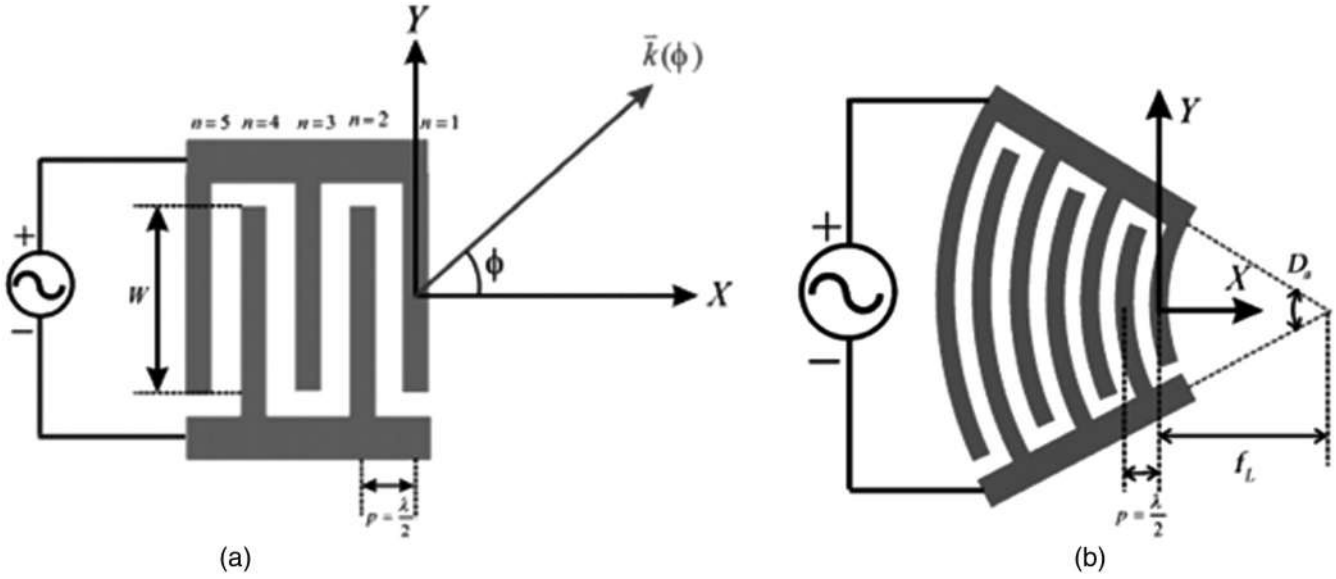

Fig. 18 Design of IDTs. Schematics of (a) straight and (b) concentric IDTs. (a) and (b) Adapted with permission from Ref. 315 © 2005 IEEE.

a typical straight IDT structure, which consists of spatially periodic electrodes. Its key metrics involve the finger length (W), finger number (n), and finger period (p). Based on the angular spectrum of plane wave theory, the amplitude field of the IDT can be calculated.[315] To further improve the acoustic–photonic interaction, a concentric IDT is proposed, as shown in Fig. 18(b). In such a structure, the interdigitated electrodes are designed with circular arc shapes and hence can achieve higher intensity acoustic fields.[315,316]

AO devices have been demonstrated in bulk LN platform. In 1992, Cheng et al. demonstrated an AO frequency shifter with a measured 121 MHz tunable bandwidth (center frequency is 0 MHz) in the visible band based on Y-cut bulk LN.[317] Passive waveguides are formed through Ti diffusion; thus, the device volume is typically in the cubic centimeter range. Kakio et al. demonstrated an AO modulator in a 128-deg rotated Y-cut LN crystal. Under a 17 V and 195 MHz driving voltage, about 84% diffractive efficiency was obtained.[318] Similarly, such a device is based on a Ti diffused waveguide and thus presents a large device size (with an IDT length of 2 or 3 mm). In addition, due to the large device size in bulk LN, the modulation frequency is typically limited to several hundreds of megahertz. The TFLN platform can compensate for these drawbacks and thus realize more compact and efficient AO devices.[312,313,319,320]

Figures 19(a)–19(c) show both MZI and microring-based AO modulators in a TFLN platform, which uses IDTs for launching the SAW to reduce reflection losses.[16] The photoelastic coefficient p_{eff} was extracted to be 0.053 from experimental data, which agrees well with the theoretical value. Based on the acoustic optic resonator/modulator, high-performance microwave to optical conversion has been demonstrated in TFLN.[17] As shown in Figs. 19(d) and 19(e), in a suspended IDT-coupled TFLN MZI AO resonator, enhanced microwave to optical conversion at 2.24 and 3.33 GHz acoustic resonance modes is observed. From such an experimental result, the V_π is estimated to be around 4.6 V, and $V_\pi L$ is around 0.046 V · cm (acoustic resonator length is 100 μm). It is known that the introduction of a resonant acoustic cavity will degrade the bandwidth of an AO modulator, and Hassanien et al. demonstrated a wideband (140 MHz) operation AO modulator without using any acoustic cavity.[312] Its principle is shown in Fig. 19(f), which consists of a PhC waveguide for light confinement, and a split IDT designed to generate S_0 mode Lamb waves. Such a device is power efficient, with phase shifts up to 0.0166 rad/$\sqrt{\text{mW}}$ over a 45-μm modulation length, and its measured bandwidth is up to 140 MHz under a 1.9 GHz center frequency [Fig. 19(g)]. More recently, photonics BIC has also been demonstrated to realize high-performance AO modulation.[319,320] As discussed in Sec. 3.3, BIC structures can realize low loss light transmission without the need for etching of TFLN and thus enable various integrated devices/circuits. Figure 19(h) shows an example of GHz AO modulation based on a photonics BIC waveguide.[320] Compared with a typical bulk LN device, the improved modulation frequency is a consequence of the reduced device size and enhanced acoustic-photonics interaction.

4.4.3 Acoustic delay line

In addition, TFLN is also suitable for the fabrication of an acoustic delay line (ADL) that can be used for radio frequency (RF) acoustic signal processing.[321] By choosing the fundamental symmetrical (S_0) mode, low IL and large fractional bandwidth (FBW) at a high frequency can be realized,[321–323] which overcomes the drawback of fundamental shear horizontal (SH_0) mode[313] or first order antisymmetric (A_1) mode-based devices.[308] Figures 20(a) and 20(b) show an optical image of a fabricated ADL in TFLN operating in the S_0 mode, which realized 1 dB IL and 4.1% FBW at 300 MHz [Fig. 20(c)].[321]

4.5 Rare Earth Doped Devices

Rare earth doped optical fibers (silica) have been used as optical amplifiers and lasers, which makes the great success of current fiber-optic communications systems possible.[324,325] Similarly, LN crystals can be doped with rare earth ions to realize integrated amplifiers and laser sources. Compared with the oxide materials, rare earth doped LN has more advantages as LN

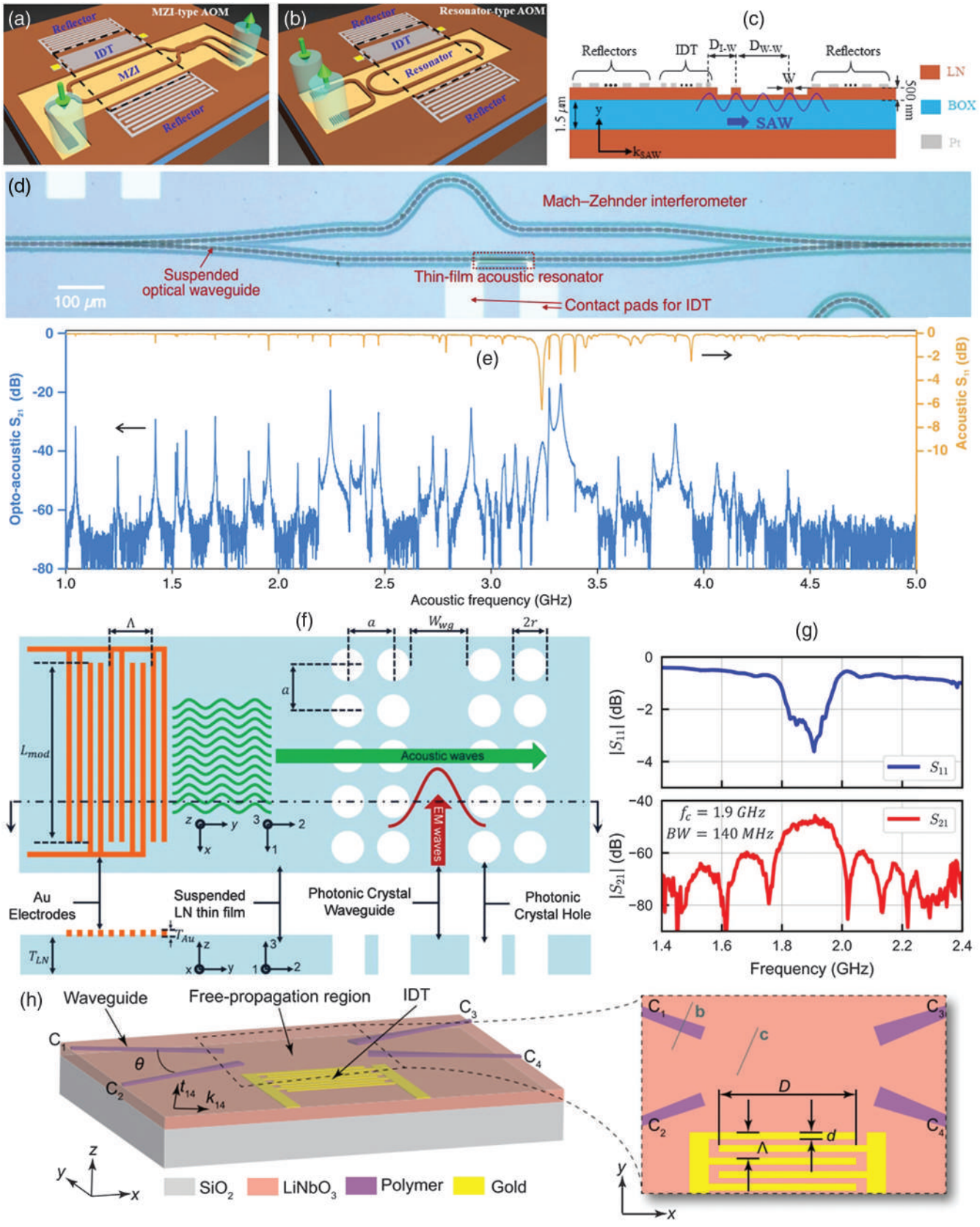

Fig. 19 LN-based AO modulators. Schematics of (a) MZI and (b) microring type AO modulators. (c) Cross section of the AO modulator. (a)–(c) Adapted with permission from Ref. 16 © 2019 Chinese Laser Press (CLP). (d) Microscopic image of a suspended AO MZI. (e) S_{11} and S_{21} spectra of microwave to optical conversion. The optical power detected by photodetector (PD) is

Fig. 19 (*Continued*) 0.25 mW. (d) and (e) Adapted with permission from Ref. 17 © 2019 OSA. (f) Principal illustration of one AO modulator without resonator cavity. (g) Measured S_{11} and S_{21} spectra. (f) and (g) Adapted with permission from Ref. 312 © 2021 CLP. (h) Schematic of AO frequency shifter based on photonic BIC. Adapted with permission from Ref. 320 © 2021 American Chemical Society (ACS).

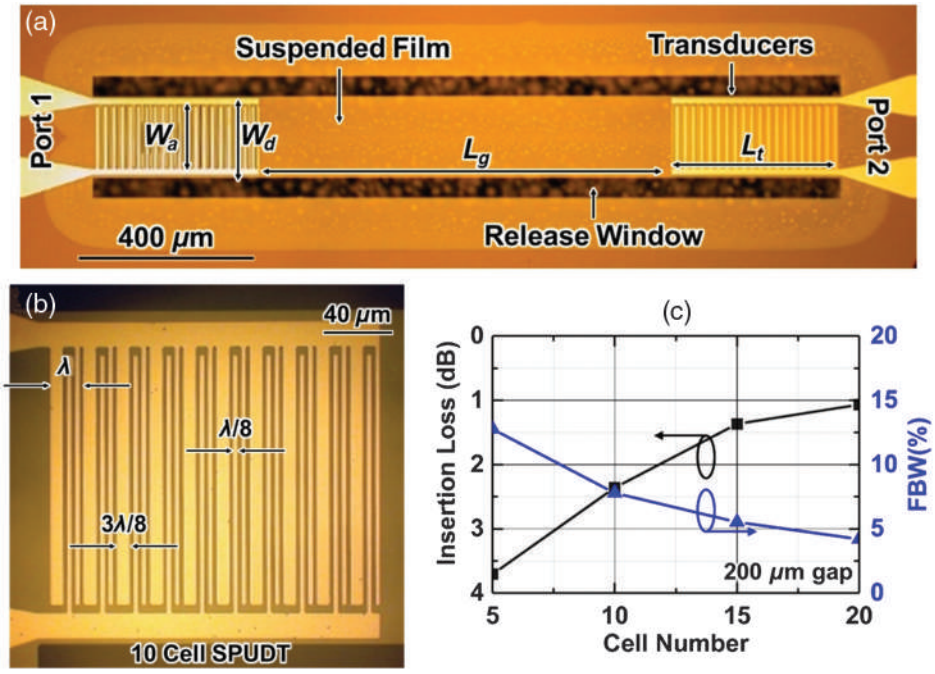

Fig. 20 LN-based ADL. (a) Microscopic image of the fabricated ADL. (b) Microscopic image of zoomed in view of the device. (c) Extracted IL and FBW of ADLs with respect to cell numbers. (a)–(c) Adapted with permission from Ref. 321 © 2018 IEEE.

has various other unique features, as introduced in Sec. 2. By incorporating these functions together, many different devices can be fabricated on the same chip. With recently developed TFLN technology, a chip scale PIC simultaneously containing integrated lasers/light emission, light modulation, amplification, routing, etc. is foreseeable in the near future.

4.5.1 Rare earth doped bulk devices

In bulk LN crystals, rare earth doping has been explored for a long time. Nd^{3+} and Er^{3+} are the two main ions used for doping in Ti-diffused or PE bulk LN devices.[91] For a Nd^{3+} doped bulk LN device, the amplifier gain has been measured to be around 7.5 dB[326] and with a lasing threshold near 1.5 mW,[327] while in Er^{3+} doped and Ti-diffused bulk LN waveguides, a 13.8 dB gain[328] at 1531 nm and 8 mW[329] lasing threshold has been demonstrated. In these reported results, the device performance was not as good as expected and the main reason is likely poor optical mode confinement caused by a low refractive index contrast. TFLN provides an alternative for improved device performance in the future.

4.5.2 Rare earth doped TFLN devices

Dutta et al.[94] demonstrated that Tm^{3+} doped TFLN exhibits identical optical lifetimes to those measured in bulk crystals, as shown in Figs. 21(a)–21(c). Such a result opens the door to applications in rare earth doped TFLN. Many types of integrated amplifiers/lasers based either on microresonators or straight waveguides have been demonstrated successively.[33,92,93,95,238,330–334] Doping of rare earth ions can be either by implantation[95] or can take place during LN crystal growth.[33,92–94,238,330–334] Figures 21(d)–21(f) show one example of an Er^{3+} implanted TFLN device.[95] The researchers have shown that ion implantation damage can be repaired by postannealing. As can be seen from the measured results shown in Fig. 21(e), a Q factor up to 9.2×10^5 can be measured after 550°C postannealing, and its mean value is 5×10^5. Other reports rely on high-quality TFLN with Er^{3+} doping achieved during crystal growth using CIS technology, which has been introduced in Sec. 2. Both high-performance amplifiers[33,92,333] and chip scale laser sources[93,238,330–332,334] have been realized in such a platform. On-chip optical amplification with an 18-dB internal net gain was obtained using a 3.6-cm TFLN waveguide [Figs. 21(g)–21(i)], where the pump wavelength is 980 nm.[33] Benefiting from the microring with an ultrahigh Q factor (1.25×10^6 near 971.5 nm, 4.27×10^5 near 1531.8 nm) in TFLN, an on-chip laser with ~20 μW threshold is realized [Figs. 21(j) and 21(k)], and differential CE was around 6.61×10^{-5}%.[330] In addition, these chip scale lasers also enable an emission wavelength tuning either by changing the pump power[93] or using the EO effect of LN.[334] Wang et al.

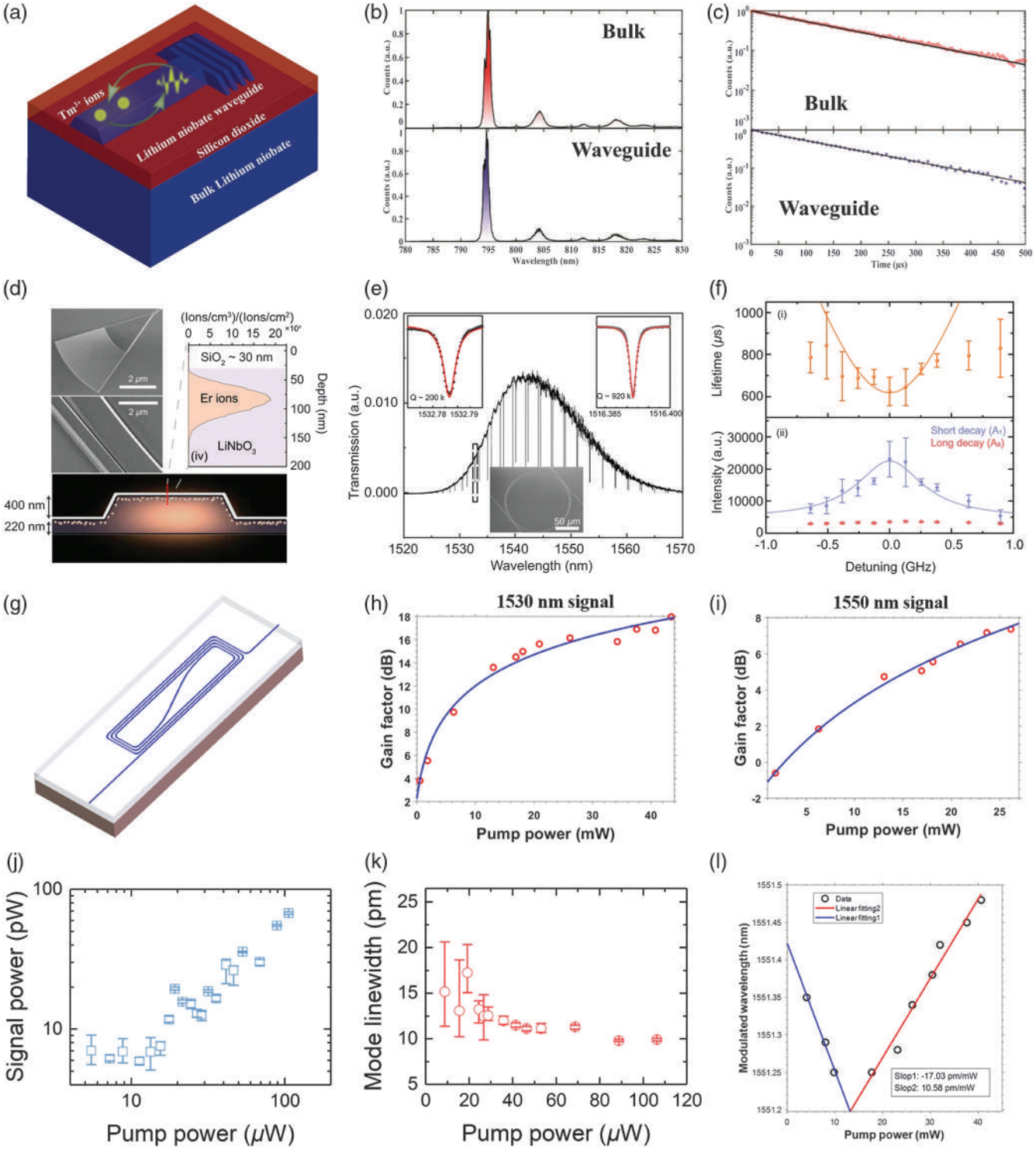

Fig. 21 Rare-earth-doped devices in LN. (a) Schematic structure of a Tm^{3+} doped TFLN device. Measured (b) photoluminescence spectra and (c) time-resolved photoluminescence in Tm^{3+} doped bulk LN and TFLN, respectively. (a)–(c) Adapted with permission from Ref. 94 © 2019 ACS. (d) Top left: SEM images of GC and microring patterned in TFLN. Top right: the stopping and range of ions in matter (SRIM) simulation of Er^{3+} implantation depth distribution. Bottom: schematic electrical field distribution. (e) Transmission spectrum of a TFLN microring. (f) Measured fluorescence decay when the pumping frequency is detuned from the ring resonance. (d)–(f) Adapted from Ref. 95. (g) Schematic structure of an Er^{3+} doped TFLN waveguide-based amplifier. Gain characterization with respect to different pump power when signal wavelength is (h) 1530 nm and (i) 1550 nm. (g)–(i) Adapted with permission from Ref. 33 © 2021

Fig. 21 (*Continued*) Wiley-VCH GmbH. (j) Signal power and (k) mode linewidth with respect to different pump powers. (j) and (k) Adapted with permission from Ref. 330 © 2021 OSA. (l) Modulated wavelength of microdisk laser with respect to pump power. Adapted with permission from Ref. 93 © 2021 OSA.

measured a ~ -17.03 pm/mW tuning efficiency with a pump power below 13 mW, and 10.58 pm/mW with a pump power above 13 mW,[93] as shown in Fig. 21(l). Another example of a monolithically integrated electrical tunable microring laser is based on the EO effect of LN with estimated EO coefficient of around 0.33 pm/V.[334] It is worth noting that there is also a heterogeneously integrated III-V laser recently demonstrated on TFLN based on transfer printing.[335] Benefiting from a mature design in III-V semiconductors generally, its performance is better than that of rare earth doped devices. However, the reduced fabrication complexity and monolithic integration features make rare earth doped device a promising alternative.

In summary, rare earth doping of LN is an interesting topic for both research and industrial applications. Combined with other effects (demonstrated in Sec. 2) of LN, more chip scale PIC functionality can be realized.

4.6 Other Devices

In addition to the above major device categories, LN is also used for other applications as well. With the rapid development of TFLN, some devices that have been conventionally hard to realize in bulk LN, such as metasurface structures, can be realized in TFLN with greater ease. Therefore, we will introduce the latest results demonstrated in TFLN in this section.

4.6.1 Pyroelectric devices

As discussed in Sec. 2, LN has a strong pyroelectric coefficient, which is suitable for the fabrication of a pyroelectric PD.[48,336] As the pyroelectrical current is inversely proportional to the dielectric thickness,[337] a thinner LN thickness is preferred in such devices.[338] However, in the typical bulk LN platform, it is challenging to reduce the LN thickness down to several micrometers,[339] whereas this will be quite easy when transferring this technology to the TFLN platform. For example, Chauvet et al. demonstrated improved pyroelectric effect-based beam self-trapping in an 8-μm-thick LN thin film made using the lapping and polishing method.[338] The recently developed thinner LN film using CIS technology enables the reliability of some more functional pyroelectric devices. As shown in Fig. 22, Suen et al. demonstrated a type of metamaterial absorber-based pyroelectrical detector in TFLN, which works over a wide wavelength range from 8 to 11 μm.[18] The metamaterial structure contributes a high field concentration and thus has a better performance. Such an advantage can be clearly seen from the measured results shown in Fig. 22(d), where pyroelectric PD without the metamaterial pattern has no response, while with a metamaterial pattern it shows a strong response peak. Through appropriate design of the metamaterial absorber, the working wavelength of the pyroelectric detector could be tuned. More recently, Guan et al. combined the pyroelectric effect of X-cut LN with graphene and realized a broadband (405 to 2000 nm) and high detectivity ($\sim 8.65 \times 10^{14}$ Jones) graphene PD.[336] Compared with other pyroelectric material platforms, the high pyroelectrical coefficient feature of LN will continually get attention, especially for some applications such as gas sensing.

4.6.2 Nonlinear metasurface devices

Another research topic in LN photonics is the nonlinear metasurface devices.[340–343] As discussed in Secs. 2.3 and 4.3, LN has large second- and third-order nonlinear coefficients and therefore has been used for various nonlinear functionalities with both bulk LN[12,13,67,69,80] and TFLN waveguide devices.[55,56,59,61] Metasurfaces, consisting of subwavelength elements, can manipulate light–matter interaction with compact forms. Very recently, metasurfaces also provide another pathway for nonlinear devices.[344–346] Due to the recent developments in high-quality TFLN and patterning technology, nonlinear optical conversions have seen enhancement effects with resonator metasurface structures, and they also enrich the research of meta-optics in general. Figures 23(a) and 23(b) illustrate the schematic and experimental results of a metasurface made of TFLN for enhanced SHG.[341] Such a device exhibits Mie-type resonance at a 1550 nm wavelength. According to the measured SHG shown in Fig. 23(b), its CE is round 10^{-6} for 0.88 mW average input power (3.3 kW peak power/4.3 GW/cm^2 peak intensity). As described in Sec. 2, LN has a wide transparency window, ranging from visible to mid-infrared, so that Carletti et al. were able to demonstrate nonlinear meta-optics in the visible range using a TFLN metasurface.[342] The diffraction mechanism of such a

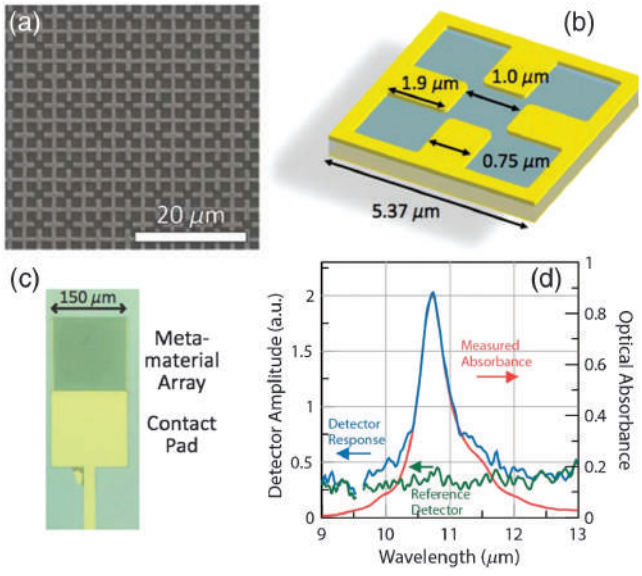

Fig. 22 TFLN-based pyroelectric infrared detector. (a) SEM image of the metamaterial top surface. (b) Schematic of the unit cell. (c) Microscopic image of the pyroelectric PD. (d) Measured detector response and optical absorption of pyroelectric PD with and without metamaterial structure. (a)–(d) Adapted with permission from Ref. 18 © 2017 OSA.

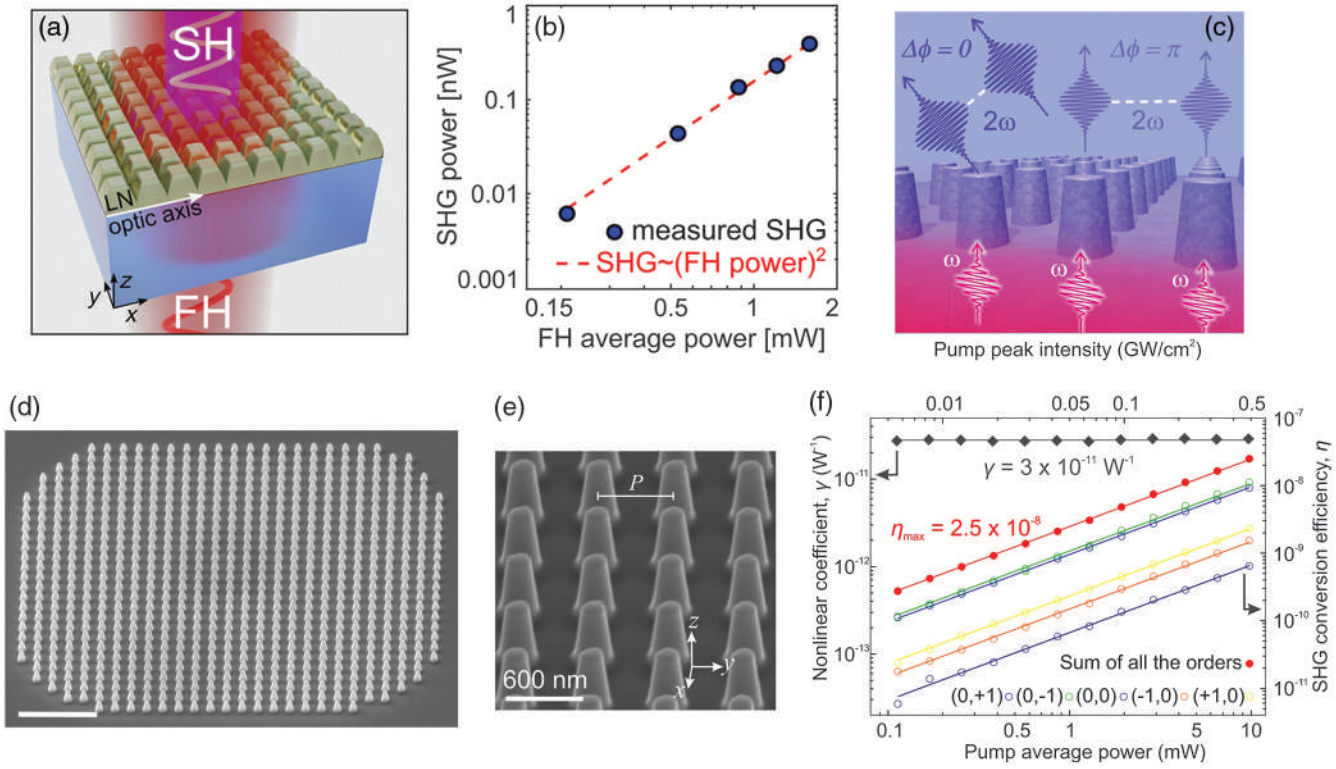

Fig. 23 Nonlinear metasurface devices in LN. (a) Schematic structure of TFLN metasurface for SHG. (b) Measured SHG power with respect to fundamental harmonic average power. (a) and (b) Adapted with permission from Ref. 341 © 2020 ACS. (c) Schematic structure of the diffraction mechanism in the metasurface. SEM images of the (d) full view metasurface (scale bar is 3 μm) and (e) zoom in nanopillars. (f) SHG CE of the diffraction orders with respect to pump power. (c)–(f) Adapted with permission from Ref. 342.

metasurface structure is shown in Fig. 23(c). Their device is fabricated by ion beam milling, which enables high aspect-ratio structures as well as very fine feature sizes. SEM images of their fabricated device are shown in Figs. 23(d) and 23(e). According to the measured results shown in Fig. 23(f), the SHG CE is about 2.4×10^{-8} at a pump intensity as low as 0.5 GW/cm^2. Hence, more results combining the advantages of LN and metasurface design can be expected in the future.

4.6.3 Visible photonics devices

Most of the reported LN-based devices so far are operating in the near-infrared regime, especially for EO devices. This is mainly due to the fact that it matches the current telecom/datacom wavelength range. Compared with other material platforms, such as Si and InP, the transparency window of LN is broad (400 nm to 5 μm) and notably covers the entire visible wavelength range. Therefore, LN is an attractive material platform for visible photonics, which is of great interest for applications ranging from consumer electronics, quantum optics, metrology, to biosensing and biomedicine. Recently, Desiatov et al. have demonstrated both passive and active blocks operated at visible wavelengths based on the TFLN platform.[42] Figures 24(a)–24(c) show an example of their demonstrated TFLN EO modulator operating at visible wavelength range. According to the measured results, the V_π is 8 V for a 2-mm long device (corresponding to $V_\pi L$ of 1.6 V · cm), and its 3-dB EO bandwidth is around 10 GHz. The researchers attribute the lower bandwidth to limitations in the measurement setup. Although the currently reported device performance in the visible range is still not as good as that in the near-infrared range, we believe it can be improved by design and process optimization. Integrated LN-based visible photonics devices will become an area of significant interest in the foreseeable future.

4.6.4 Superconducting nanowire single-photon detector

As discussed in Sec. 4.3, the rich nonlinear effects in LN in combination with its EO property make it an attractive platform for quantum applications. Integrating an efficient single photon detector in LN will broaden such application scenarios in the quantum area. Recently, superconducting nanowire-based SPDs (SNSPDs) have been successfully integrated on Ti diffused LN[347] and TFLN platforms.[172,348,349] Figures 25(a)–25(c) show an example of integrated amorphous tungsten silicide SNSPD on Ti in-diffused LN waveguide, which validates the possibility of evanescent coupled SNSPD in LN. In TFLN, both niobium nitride (NbN)[172,348] and niobium titanium nitride (NbTiN)[349] have been deposited onto LN passive circuits. Figure 25(d) shows an example of a waveguide integrated SNSPD on TFLN, which consists of a 1D GC, a TFLN waveguide, and a U-shaped NbN SNSPD.[172] Its measured on-chip detection efficiency (OCDE), dark count rate (DCR), and noise equivalent power (NEP) are shown in Figs. 25(e) and 25(f). When biased at a 95% switching

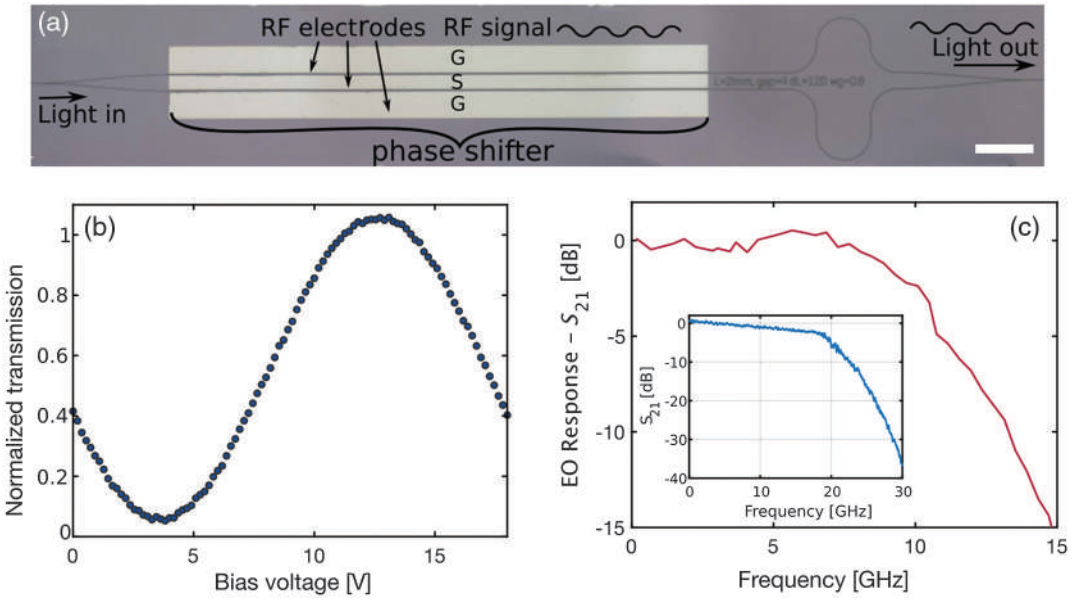

Fig. 24 TFLN modulator operated at visible wavelength range. (a) Microscopic image of the TFLN EO modulator. (b) Measured transmission spectrum and (c) S_{21} curve. (a)–(c) Adapted with permission from Ref. 42 © 2019 OSA.

current of the nanowire (I_{SW}), the DCR is measured to be around 13 Hz with 46% OCDE. While at 95% I_{SW} (switching current), the NEP is measured to be 1.42×10^{-18} W/$\sqrt{\text{Hz}}$. All these measured results are close to other kinds of waveguide-integrated SNSPDs.[350] Another example realized a more functional PIC,[349] as shown in Fig. 25(g), which integrated an EO MZI modulator (MZM) together with two waveguide SNSPDs. Here, the researchers use U-shaped NbTiN nanowires as the detection material. The measured OCDEs for the two SNSPDs are 24% and 27%, respectively, under a critical current of 14 and 12.5 μA. Such a performance is worse than that of an NbN SNSPD mainly due to the process technology, although NbTiN has a lower kinetic inductance compared with NbN.[349] The researchers also characterized the PIC performance (simultaneous operation of EO modulator and SNSPDs). Figure 25(h) shows the count rate traces from two SNSPDs placed at the two output ports of the MZM while MZM is driven with a 1-kHz sawtooth wave. A small reduction of the EO coefficient of the TFLN waveguide at cryogenic temperatures is observed, which is consistent with what has been observed in bulk LN modulators.[351,352] High-performance SNSPD is an essential building block for constructing a fully chip-scale integrated quantum photonic circuit. Current reports with limited performance provide a direction and show the emerging trend for integrated SNSPDs on both bulk LN and TFLN platforms.

4.6.5 Heterogeneously integrated photodetector

Compared with bulk LN devices, the TFLN platform not only can realize better device performance but also enables the integration of different photonic components together on the same chip to realize versatile functional PIC. There are already many examples that have been demonstrated, such as a Kerr comb generation and filtering PIC demonstrated by Wang et al.[76] Although LN by itself cannot realize detection, an on-chip detector is possible by integrating another material on it.[34,172,349] As discussed in Sec. 4.6.4, NbN and NbTiN can be deposited onto TFLN to form SNSPDs for quantum applications, while for telecommunication-related applications operated in the near-infrared or visible wavelength window, one possible solution is by HI of Si, germanium or III–V absorber layers.[22,34,270,353,354] Figures 26(a) and 26(b) show an example of the integration of a Si metal–semiconductor–metal PD with LN passive devices, with a measured 37-mA/W responsivity at 850 nm wavelength.[34] In Sec. 4.5, we discussed chip scale amplifier and laser emitter based on rare earth doped TFLN devices. Therefore, all the functions, including light emission, modulation, signal processing, transmission, and detection, can be integrated on the same TFLN chip, which paves the way for large-scale PIC in TFLN.

4.6.6 Wafer scale fabricated devices

Most of currently reported LN photonics devices (both bulk LN and TFLN) are fabricated in the laboratory (Lab). With the rapid development of integrated LN photonics, wafer scale fabrication/production (from Lab to Fab) is already on the agenda. There are already some pioneering works based on TFLN/LNOI, which is very similar to typical SOI. Luke et al. demonstrated a measured propagation loss as low as 0.27 dB/cm using wafer-scale deep ultraviolet lithography.[355] Safian et al. demonstrated a platform for fabricating TFLN devices bonded on top of silicon photonics chips—a method that has a good compatibility with silicon foundry.[356] Both works pave the way for large-scale production of integrated LN devices in foundry mode. As most of the process flows of TFLN devices are compatible with CMOS (can be fabricated using CMOS line equipment), the biggest challenge is the TFLN wafer size. In current CMOS lines, most advanced machines can only handle 8/12-inch wafers for low-cost mass production. We believe high quality and large size TFLN wafers will be available in the near future with technology development. From there, TFLN devices fabricated in foundry mode can be expected.

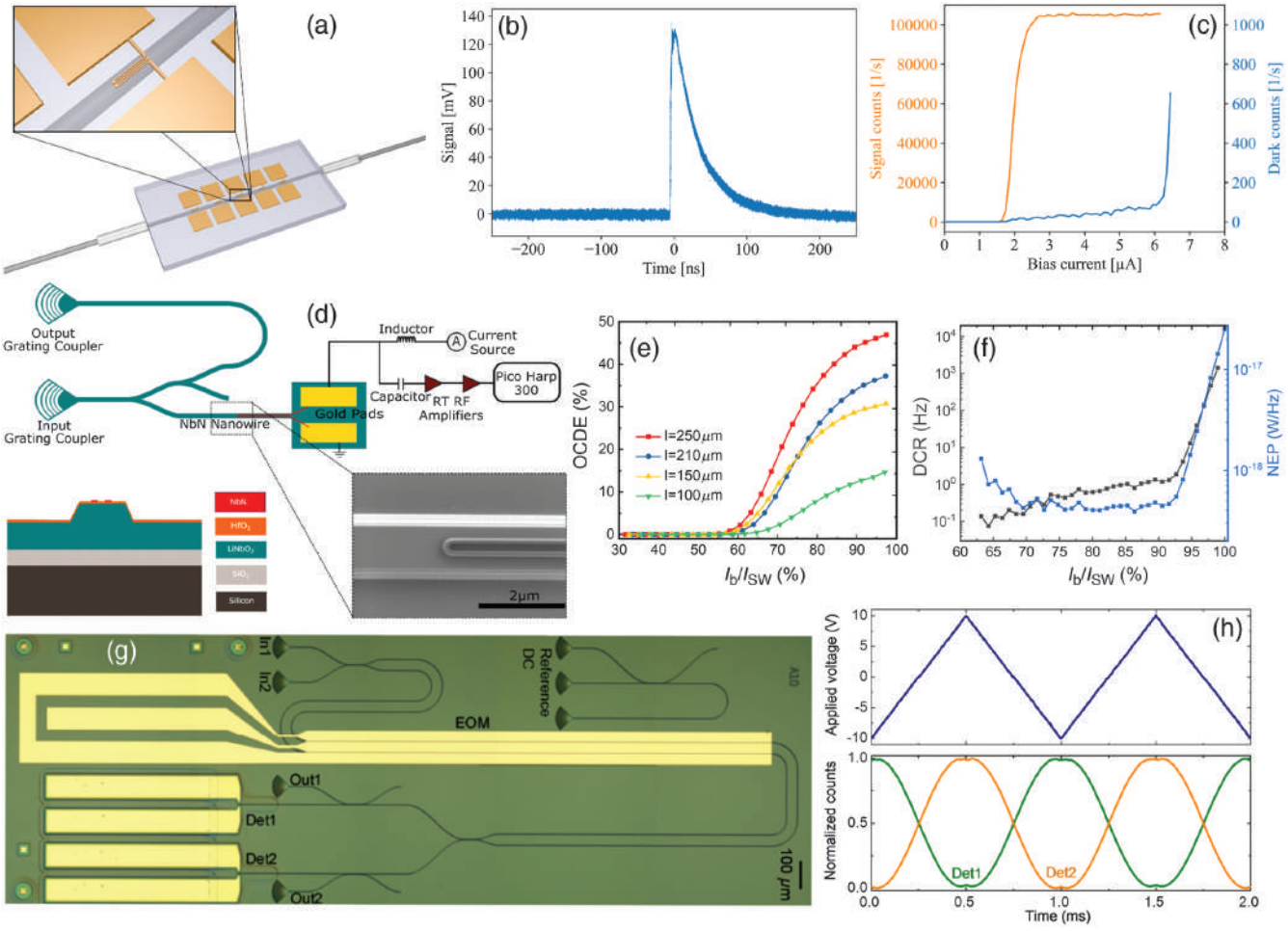

Fig. 25 Integrated SNSPD in LN. (a) Schematic structure of Ti diffused LN waveguide integrated with five in-line SNSPDs. Inset shows the detail of single SNSPD, which has 400 μm length and 160 nm width. (b) Measured response time of an integrated SNSPD. (c) Measured signal and dark counts of the integrated SNSPD under different bias current. (a)–(c) Adapted with permission from Ref. 347. Published by IOP Publishing Ltd. (d) Top: schematic of a TFLN GC coupling light into an integrated U-shaped NbN SNSPD. Bottom left: device cross section. Bottom right: SEM image of the device detail. (e) Measured OCDE, (f) DCR and NEP with respect to I_b/I_{SW} for a 250-μm long detector. I_{SW}, switching current; I_b, bias current. (d)–(f) Adapted from Ref. 172. (g) Microscopic image of the on-chip integrated circuit containing one TFLN EO modulator and two NbTiN SNSPDs. (h) Measured count rates collected from the SNSPDs with a time tagging module (bottom) when EO modulator is driven with a ramp function with an amplitude of 20 V_{pp} and frequency of 1 kHz (top). (g) and (h) Adapted with permission from Ref. 349.

5 Summary and Outlook

We have given a comprehensive review of advances in LN photonics, involving material properties, key processing technologies, and functional devices based on both bulk LN and TFLN. Compared with Si, LN has a large EO coefficient, which is its most significant feature and advantage. In addition, the presence of large second- and third-order nonlinear coefficients of LN also makes it a suitable platform for various nonlinear applications. LN can also be used for fabrication of AO devices due to its large AO coefficient. With the development of TFLN, integrated AO devices with enhanced performance make it more attractive. Rare earth doped LN can provide integrated solutions for optical amplification and laser emission. Some other properties of LN were also discussed along with their corresponding fabricated devices. All of them prove that LN is an excellent platform for photonics applications. With the rapid development of large wafer sizes and high-quality TFLN, more compact and integrable devices are preferred. LN photonics has experienced great development during the past decades, especially when TFLN recently became commercially available. We have tried to cover different aspects of LN-related researches in this review. However, some of the work in the literature will probably not be included in this paper for many reasons, such as publication date after we prepare this paper. We believe these excellent noncited results are also based on the basic properties discussed in Sec. 2.

Looking forward to the development of LN photonics, there are several key directions that can be considered.

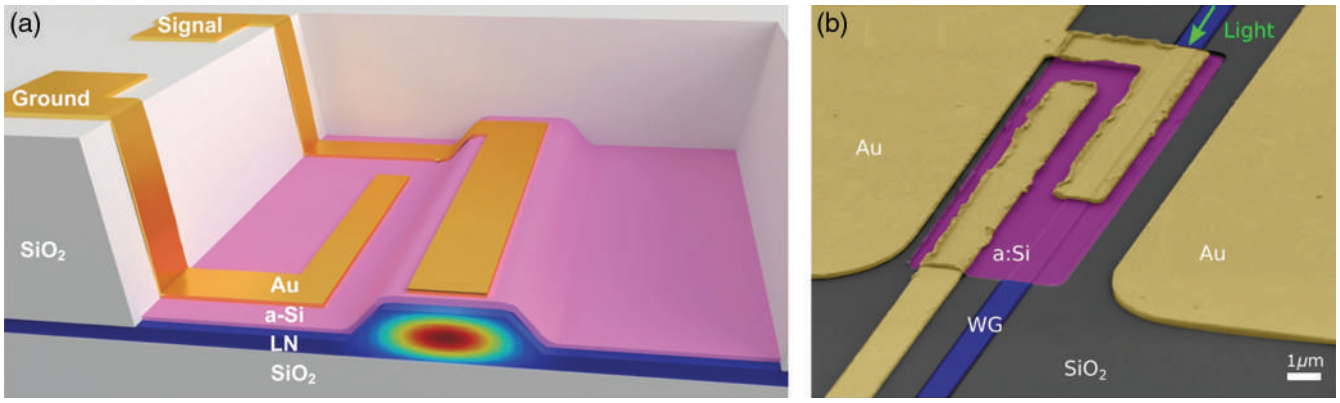

Fig. 26 Integrated Si PD onto LN passive circuit. (a) Schematic structure and (b) false colored SEM image of a TFLN waveguide with integrated Si PD. (a) and (b) Adapted from Ref. 34.

5.1 Integrated LN Photonics

Integrated TFLN photonics will still be one of the best supplements to bulk LN devices due to the large refractive index contrast available. With the high quality of commercially available TFLN, functional blocks with an increasingly greater capability will be demonstrated using a similar design methodology to that of existing material platforms, such as silicon photonics. Such a trend is ongoing and will continue in the foreseeable future as evidenced by the various kinds of passive and active blocks demonstrated in Sec. 4.1. New design methods or structures demonstrated in other material platforms can be transferred into the integrated LN platform, such as inverse design[357,358] and deep learning.[359]

With high performance device-level demonstration, integrating different functional blocks (relying on multiple properties) on the same chip to realize a truly chip-scale PIC system will be another interesting trend. There are already some good attempts, and a part of them have been discussed in Sec. 4.[34,76] We believe denser PIC will be demonstrated in the future and some integration methods can be adopted from other material systems. For example, heterogeneous integration of III–V semiconductors with TFLN is still seldom explored so far and will be an interesting area in the future.

It is worth mentioning that TFLN devices will not completely replace bulk LN devices, as bulk LN devices have certain noteworthy advantages. For example, there is still a gap between bulk LN- and TFLN-based EO devices for CE, as discussed in Sec. 4.2.2. Bulk LN is also regarded as an integrated platform even though its integration density is low.[352] Therefore, we believe both the bulk and TFLN will exist together and complement each other to make integrated LN photonics more attractive in research and applicable in industry.

5.2 High Performance Electro-Optic Devices

One of the most unique features of LN is its large EO coefficient, which makes it a good material of choice for an EO modulator. Although numerous LN-based EO modulators have been demonstrated during the past year, there is still plenty of room for improvements in the reported device performance. For example, even though TFLN modulators with speeds up to 100 Gb/s NRZ have been demonstrated,[31] the speed can be further improved either by shortening the MZI arm length or using more advanced modulation schemes.[88,360] In addition, as shown in the discussion of Sec. 4.2.1, there are many performance metrics to characterize a modulator. It is usually difficult to achieve all the best metrics at the same time. There is a lot of work that can be done to optimize the overall performance or enhance one specific metric to adapt these devices to different application scenarios. It is also worth mentioning that the strong EO effect of LN can not only be used for realizing high performance modulators but it can also be used for other areas where EO modulation shows advantages, such as the EO frequency comb.[77] Some more examples can be found in Sec. 4.2.

5.3 Nonlinear and Quantum Photonics

Based on high second- and third-order nonlinear effects inside LN, various nonlinear applications have been demonstrated in both bulk LN and TFLN. Compared with bulk LN, stronger mode confinement inside TFLN, better interaction between light and the LN medium is achieved, thus enabling a greater nonlinear converting efficiency. Challenges remain on how to further improve the nonlinear CE. Possible solutions include optimizing the phase-matching condition by either new designs or processes,[54] waveguide dispersion engineering,[79] and using optical field enhancement structures such as metasurfaces.[55]

LN can also play a significant role in quantum photonics (quantum communication, computing, etc.) based on its nonlinear effects. For a long time, bulk LN has been used for quantum application demonstrations.[15,361] The emerging TFLN makes more compact devices reality. We have discussed certain heterogeneously integrated high-performance SNSPDs in TFLN.[172,349] At the current stage, the challenges are with how to implement new concepts and ideas based on LN platforms with better performance, especially for TFLN. Some related results have already been demonstrated recently.[81,82] We believe chip-scale fully integrated quantum circuits can be expected in the near future.

5.4 Acousto-Optic Devices

LN is also a good material platform for AO devices due to its significant photoelastic effect, which can be used in microwave photonics and quantum information processing. In the typical

bulk LN device, the performance of AO devices has been mainly restricted due to its weak light confinement. The newly developed TFLN compensates for such a drawback. Looking forward to the further development, ultrahigh Q factor optomechanics microcavities and highly efficient AO modulators/frequency shifters based on TFLN should be able to attract more interest and attention.

5.5 Rare Earth Doped Devices

Rare earth doped devices have not received enough attention, although there is a potential for integrated amplifiers/lasers, and some results have been demonstrated recently.[33,330,331] Compared with heterogeneously integrated III-V amplifiers/lasers, there are still some gaps to be closed in the development of rare earth doped LN devices. This issue can be addressed by optimizing the fabrication process or device designs.[33,92,330,331]

5.6 Wafer Scale Fabrication

With the development of LN photonics, wafer-scale fabrication of LN devices using foundry pilot will receive much more attention, especially for industrial applications. Meanwhile, there will undoubtedly be some technology challenges that must be overcome. Currently, there are already some attempts in such areas as discussed in Sec. 4.6.6, and there will be more effort devoted in the near future. It is believed that with more mature process technologies and advanced theory, LN photonics will be further developed in the near future.

Acknowledgments

This work was supported by the National Research Foundation, Singapore, under its Competitive Research Programme (CRP Award No. NRF-CRP24-2020-0003). This work was also supported by the program for HUST Academic Frontier Youth Team (2018QYTD08). This work was partially supported by A*STAR (Agency for Science, Technology and Research), Singapore, under the RIE2020 Advanced Manufacturing and Engineering (AME) IAF-PP Grant, No. A19B3a0008. The authors thank Dr. Di Zhu for useful discussions. The authors declare no conflicts of interest.

References

1. B. Matthias and J. Remeika, "Ferroelectricity in the ilmenite structure," *Phys. Rev.* **76**(12), 1886–1887 (1949).
2. R. Weis and T. Gaylord, "Lithium niobate: summary of physical properties and crystal structure," *Appl. Phys. A* **37**(4), 191–203 (1985).
3. E. L. Wooten et al., "A review of lithium niobate modulators for fiber-optic communications systems," *IEEE J. Sel. Top. Quantum Electron.* **6**(1), 69–82 (2000).
4. L. Arizmendi, "Photonic applications of lithium niobate crystals," *Phys. Stat. Solidi A* **201**(2), 253–283 (2004).
5. D. Janner et al., "Micro-structured integrated electro-optic $LiNbO_3$ modulators," *Laser Photonics Rev.* **3**(3), 301–313 (2009).
6. G. Poberaj et al., "Lithium niobate on insulator (LNOI) for micro-photonic devices," *Laser Photonics Rev.* **6**(4), 488–503 (2012).
7. A. Boes et al., "Status and potential of lithium niobate on insulator (LNOI) for photonic integrated circuits," *Laser Photonics Rev.* **12**(4), 1700256 (2018).
8. A. Honardoost, K. Abdelsalam, and S. Fathpour, "Rejuvenating a versatile photonic material: thin-film lithium niobate," *Laser Photonics Rev.* **14**(9), 2000088 (2020).
9. Y. Jia, L. Wang, and F. Chen, "Ion-cut lithium niobate on insulator technology: recent advances and perspectives," *Appl. Phys. Rev.* **8**(1), 011307 (2021).
10. G. T. Reed et al., "Silicon optical modulators," *Nat. Photonics* **4**(8), 518–526 (2010).
11. M. Smit et al., "An introduction to InP-based generic integration technology," *Semicond. Sci. Technol.* **29**(8), 083001 (2014).
12. M. Yamada et al., "First-order quasi-phase matched $LiNbO_3$ waveguide periodically poled by applying an external field for efficient blue second-harmonic generation," *Appl. Phys. Lett.* **62**(5), 435–436 (1993).
13. K. Mizuuchi, K. Yamamoto, and M. Kato, "Harmonic blue light generation in bulk periodically poled MgO:$LiNbO_3$," *Electron. Lett.* **32**(22), 2091–2092 (1996).
14. K. R. Parameswaran et al., "Highly efficient second-harmonic generation in buried waveguides formed by annealed and reverse proton exchange in periodically poled lithium niobate," *Opt. Lett.* **27**(3), 179–181 (2002).
15. S. Saravi, T. Pertsch, and F. Setzpfandt, "Lithium niobate on insulator: an emerging platform for integrated quantum photonics," *Adv. Opt. Mater.* **9**(22), 2100789 (2021).
16. L. Cai et al., "Acousto-optical modulation of thin film lithium niobate waveguide devices," *Photonics Res.* **7**(9), 1003–1013 (2019).
17. L. Shao et al., "Microwave-to-optical conversion using lithium niobate thin-film acoustic resonators," *Optica* **6**(12), 1498–1505 (2019).
18. J. Y. Suen et al., "Multifunctional metamaterial pyroelectric infrared detectors," *Optica* **4**(2), 276–279 (2017).
19. R. Schmidt and I. Kaminow, "Metal-diffused optical waveguides in $LiNbO_3$," *Appl. Phys. Lett.* **25**(8), 458–460 (1974).
20. J. Jackel and C. Rice, "Topotactic $LiNbO_3$ to cubic perovskite structural transformation in $LiNbO_3$ and $LiTaO_3$," *Ferroelectrics* **38**(1), 801–804 (1981).
21. J. L. Jackel, C. Rice, and J. Veselka, "Proton exchange for high-index waveguides in $LiNbO_3$," *Appl. Phys. Lett.* **41**(7), 607–608 (1982).
22. G. Chen et al., "High speed and high power polarization insensitive germanium photodetector with lumped structure," *Opt. Express* **24**(9), 10030–10039 (2016).
23. G. Chen et al., "Switchable in-line monitor for multi-dimensional multiplexed photonic integrated circuit," *Opt. Express* **24**(13), 14841–14850 (2016).
24. G. Chen, Y. Yu, and X. Zhang, "Monolithically mode division multiplexing photonic integrated circuit for large-capacity optical interconnection," *Opt. Lett.* **41**(15), 3543–3546 (2016).
25. M. Ye et al., "On-chip WDM mode-division multiplexing interconnection with optional demodulation function," *Opt. Express* **23**(25), 32130–32138 (2015).
26. D. Zhou et al., "Germanium photodetector with distributed absorption regions," *Opt. Express* **28**(14), 19797–19807 (2020).
27. Y. Yu et al., "Intra-chip optical interconnection based on polarization division multiplexing photonic integrated circuit," *Opt. Express* **25**(23), 28330–28336 (2017).
28. G. Chen, Y. Yu, and X. Zhang, "Optical phase erasure and wavelength conversion using silicon nonlinear waveguide with reverse biased PIN junctions," *IEEE Photonics J.* **7**(5), 7102808 (2015).
29. S. Kurimura et al., "Quasi-phase-matched adhered ridge waveguide in $LiNbO_3$," *Appl. Phys. Lett.* **89**(19), 191123 (2006).
30. T. Umeki, O. Tadanaga, and M. Asobe, "Highly efficient wavelength converter using direct-bonded PPZnLN ridge waveguide," *IEEE J. Quantum Electron.* **46**(8), 1206–1213 (2010).
31. C. Wang et al., "Integrated lithium niobate electro-optic modulators operating at CMOS-compatible voltages," *Nature* **562**(7725), 101–104 (2018).

32. P. De Nicola et al., "Fabrication of smooth ridge optical waveguides in $LiNbO_3$ by ion implantation-assisted wet etching," *J. Lightwave Technol.* **31**(9), 1482–1487 (2013).
33. J. Zhou et al., "On-chip integrated waveguide amplifiers on erbium-doped thin-film lithium niobate on insulator," *Laser Photonics Rev.* **15**(8), 2100030 (2021).
34. B. Desiatov and M. Lončar, "Silicon photodetector for integrated lithium niobate photonics," *Appl. Phys. Lett.* **115**(12), 121108 (2019).
35. Z. Yu et al., "High-dimensional communication on etchless lithium niobate platform with photonic bound states in the continuum," *Nat. Commun.* **11**, 2602 (2020).
36. K. Nassau, H. Levinstein, and G. Loiacono, "Ferroelectric lithium niobate. 1. Growth, domain structure, dislocations and etching," *J. Phys. Chem. Solids* **27**(6-7), 983–988 (1966).
37. K. Nassau, H. Levinstein, and G. Loiacono, "Ferroelectric lithium niobate. 2. Preparation of single domain crystals," *J. Phys. Chem. Solids* **27**(6-7), 989–996 (1966).
38. S. Abrahams, J. M. Reddy, and J. Bernstein, "Ferroelectric lithium niobate. 3. Single crystal X-ray diffraction study at 24°C," *J. Phys. Chem. Solids* **27**(6-7), 997–1012 (1966).
39. S. Abrahams, W. C. Hamilton, and J. Reddy, "Ferroelectric lithium niobate. 4. Single crystal neutron diffraction study at 24°C," *J. Phys. Chem. Solids* **27**(6-7), 1013–1018 (1966).
40. S. Abrahams, H. Levinstein, and J. Reddy, "Ferroelectric lithium niobate. 5. Polycrystal X-ray diffraction study between 24° and 1200°C," *J. Phys. Chem. Solids* **27**(6-7), 1019–1026 (1966).
41. R. W. Boyd, "The electrooptic and photorefractive effects," in *Nonlinear Optics*, pp. 511–541, 3rd ed., Academic Press, Elsevier, Inc. (2008).
42. B. Desiatov et al., "Ultra-low-loss integrated visible photonics using thin-film lithium niobate," *Optica* **6**(3), 380–384 (2019).
43. T.-J. Wang, C.-H. Chu, and C.-Y. Lin, "Electro-optically tunable microring resonators on lithium niobate," *Opt. Lett.* **32**(19), 2777–2779 (2007).
44. J. Mishra et al., "Mid-infrared nonlinear optics in thin-film lithium niobate on sapphire," *Optica* **8**(6), 921–924 (2021).
45. C. Thierfelder et al., "Do we know the band gap of lithium niobate?" *Phys. Stat. Solidi C* **7**(2), 362–365 (2010).
46. V. G. Dmitriev, G. G. Gurzadyan, and D. N. Nikogosyan, *Handbook of Nonlinear Optical Crystals*, Vol. **64**, Springer (2013).
47. M. Bache and R. Schiek, "Review of measurements of Kerr nonlinearities in lithium niobate: the role of the delayed Raman response," arXiv:1211.1721 (2012).
48. A. Savage, "Pyroelectricity and spontaneous polarization in $LiNbO_3$," *J. Appl. Phys.* **37**(8), 3071–3072 (1966).
49. S. Yao et al., "Growth, optical and thermal properties of near-stoichiometric $LiNbO_3$ single crystal," *J. Alloys Compd.* **455**(1-2), 501–505 (2008).
50. L. Moretti et al., "Temperature dependence of the thermo-optic coefficient of lithium niobate, from 300 to 515 K in the visible and infrared regions," *J. Appl. Phys.* **98**(3), 036101 (2005).
51. A. W. Warner, M. Onoe, and G. A. Coquin, "Determination of elastic and piezoelectric constants for crystals in class (3m)," *J. Acoust. Soc. Am.* **42**(6), 1223–1231 (1967).
52. M. He et al., "High-performance hybrid silicon and lithium niobate Mach–Zehnder modulators for 100 Gbit s^{-1} and beyond," *Nat. Photonics* **13**(5), 359–364 (2019).
53. L. Gui et al., "Local periodic poling of ridges and ridge waveguides on X- and Y-cut $LiNbO_3$ and its application for second harmonic generation," *Opt. Express* **17**(5), 3923–3928 (2009).
54. L. Chang et al., "Thin film wavelength converters for photonic integrated circuits," *Optica* **3**(5), 531–535 (2016).
55. C. Wang et al., "Metasurface-assisted phase-matching-free second harmonic generation in lithium niobate waveguides," *Nat. Commun.* **8**, 2098 (2017).
56. C. Wang et al., "Second harmonic generation in nano-structured thin-film lithium niobate waveguides," *Opt. Express* **25**(6), 6963–6973 (2017).
57. R. Luo et al., "Highly tunable efficient second-harmonic generation in a lithium niobate nanophotonic waveguide," *Optica* **5**(8), 1006–1011 (2018).
58. C. Wang et al., "Ultrahigh-efficiency wavelength conversion in nanophotonic periodically poled lithium niobate waveguides," *Optica* **5**(11), 1438–1441 (2018).
59. A. Boes et al., "Improved second harmonic performance in periodically poled LNOI waveguides through engineering of lateral leakage," *Opt. Express* **27**(17), 23919–23928 (2019).
60. J.-Y. Chen et al., "Ultra-efficient frequency conversion in quasi-phase-matched lithium niobate microrings," *Optica* **6**(9), 1244–1245 (2019).
61. J.-Y. Chen et al., "Efficient parametric frequency conversion in lithium niobate nanophotonic chips," *OSA Continuum* **2**(10), 2914–2924 (2019).
62. J. Lin et al., "Broadband quasi-phase-matched harmonic generation in an on-chip monocrystalline lithium niobate microdisk resonator," *Phys. Rev. Lett.* **122**(17), 173903 (2019).
63. J. Lu et al., "Periodically poled thin-film lithium niobate microring resonators with a second-harmonic generation efficiency of 250,000%/W," *Optica* **6**(12), 1455–1460 (2019).
64. M. Jankowski et al., "Ultrabroadband nonlinear optics in nanophotonic periodically poled lithium niobate waveguides," *Optica* **7**(1), 40–46 (2020).
65. Y. Niu et al., "Optimizing the efficiency of a periodically poled LNOI waveguide using in situ monitoring of the ferroelectric domains," *Appl. Phys. Lett.* **116**(10), 101104 (2020).
66. B. Mu et al., "Locally periodically poled LNOI ridge waveguide for second harmonic generation," *Chin. Opt. Lett.* **19**(6), 060007 (2021).
67. R. V. Roussev et al., "Periodically poled lithium niobate waveguide sum-frequency generator for efficient single-photon detection at communication wavelengths," *Opt. Lett.* **29**(13), 1518–1520 (2004).
68. X. Ye et al., "Sum-frequency generation in lithium-niobate-on-insulator microdisk via modal phase matching," *Opt. Lett.* **45**(2), 523–526 (2020).
69. K. Sasagawa and M. Tsuchiya, "Highly efficient third harmonic generation in a periodically poled $MgO:LiNbO_3$ disk resonator," *Appl. Phys Express* **2**(12), 122401 (2009).
70. L. Ledezma et al., "Intense optical parametric amplification in dispersion-engineered nanophotonic lithium niobate waveguides," *Optica* **9**(3), 303–308 (2022).
71. J. Lu et al., "Ultralow-threshold thin-film lithium niobate optical parametric oscillator," *Optica* **8**(4), 539–544 (2021).
72. M. Leidinger et al., "Strong forward-backward asymmetry of stimulated Raman scattering in lithium-niobate-based whispering gallery resonators," *Opt. Lett.* **41**(12), 2823–2826 (2016).
73. M. Yu et al., "Raman lasing and soliton mode-locking in lithium niobate microresonators," *Light Sci. Appl.* **9**(1), 9 (2020).
74. Z. Gong et al., "Soliton microcomb generation at 2 μm in z-cut lithium niobate microring resonators," *Opt. Lett.* **44**(12), 3182–3185 (2019).
75. Y. He et al., "Self-starting bi-chromatic $LiNbO_3$ soliton microcomb," *Optica* **6**(9), 1138–1144 (2019).
76. C. Wang et al., "Monolithic lithium niobate photonic circuits for Kerr frequency comb generation and modulation," *Nat. Commun.* **10**, 978 (2019).
77. M. Zhang et al., "Broadband electro-optic frequency comb generation in a lithium niobate microring resonator," *Nature* **568**(7752), 373–377 (2019).
78. J. Lu et al., "Octave-spanning supercontinuum generation in nanoscale lithium niobate waveguides," *Opt. Lett.* **44**(6), 1492–1495 (2019).

79. M. Yu et al., "Coherent two-octave-spanning supercontinuum generation in lithium-niobate waveguides," *Opt. Lett.* **44**(5), 1222–1225 (2019).
80. S. Tanzilli et al., "PPLN waveguide for quantum communication," *Eur. Phys. J. D* **18**(2), 155–160 (2002).
81. Z. Ma et al., "Ultrabright quantum photon sources on chip," *Phys. Rev. Lett.* **125**(26), 263602 (2020).
82. J. Zhao et al., "High quality entangled photon pair generation in periodically poled thin-film lithium niobate waveguides," *Phys. Rev. Lett.* **124**(16), 163603 (2020).
83. G.-T. Xue et al., "Ultrabright multiplexed energy-time-entangled photon generation from lithium niobate on insulator chip," *Phys. Rev. Appl.* **15**(6), 064059 (2021).
84. W. B. Tiffany, "Introduction and review of pyroelectric detectors," *Proc. SPIE* **0062**, 153–158 (1976).
85. X. Liu et al., "Highly efficient thermo-optic tunable microring resonator based on an LNOI platform," *Opt. Lett.* **45**(22), 6318–6321 (2020).
86. G. Chen et al., "Integrated thermally tuned mach-zehnder interferometer in Z-cut lithium niobate thin film," *IEEE Photonics Technol. Lett.* **33**(13), 664–667 (2021).
87. G. Chen, H.-L. Lin, and A. Danner, "Highly efficient thermal tuning interferometer in lithium niobate thin film using air bridge," *IEEE Photonics J.* **13**(3), 6600409 (2021).
88. M. Xu et al., "High-performance coherent optical modulators based on thin-film lithium niobate platform," *Nat. Commun.* **11**, 3911 (2020).
89. E. S. Magden et al., "Frequency domain spectroscopy in rare-earth-doped gain media," *IEEE J. Sel. Top. Quantum Electron.* **24**(5), 3000110 (2018).
90. M. Xin et al., "Optical frequency synthesizer with an integrated erbium tunable laser," *Light Sci. Appl.* **8**(1), 122 (2019).
91. W. Sohler, "Rare earth doped $LiNbO_3$ waveguide amplifiers and lasers," in *Waveguide Optoelectronics*, J. H. Marsh and R. M. De La Rue, Eds., pp. 361–394, Springer, Dordrecht (1992).
92. Z. Chen et al., "Efficient erbium-doped thin-film lithium niobate waveguide amplifiers," *Opt. Lett.* **46**(5), 1161–1164 (2021).
93. Z. Wang et al., "On-chip tunable microdisk laser fabricated on Er^{3+}-doped lithium niobate on insulator," *Opt. Lett.* **46**(2), 380–383 (2021).
94. S. Dutta et al., "Integrated photonic platform for rare-earth ions in thin film lithium niobate," *Nano Lett.* **20**(1), 741–747 (2020).
95. S. Wang et al., "Incorporation of erbium ions into thin-film lithium niobate integrated photonics," *Appl. Phys. Lett.* **116**(15), 151103 (2020).
96. M. Armenise, "Fabrication techniques of lithium niobate waveguides," *IEE Proc.* **135**(2), 85–91 (1988).
97. I. Kaminow and J. Carruthers, "Optical waveguiding layers in $LiNbO_3$ and $LiTaO_3$," *Appl. Phys. Lett.* **22**(7), 326–328 (1973).
98. J. Noda et al., "Electro-optic amplitude modulation using three-dimensional $LiNbO_3$ waveguide fabricated by TiO_2 diffusion," *Appl. Phys. Lett.* **27**(1), 19–21 (1975).
99. J. R. Carruthers, I. P. Kaminow, and L. W. Stulz, "Diffusion kinetics and optical waveguiding properties of outdiffused layers in lithium niobate and lithium tantalate," *Appl. Opt.* **13**(10), 2333–2342 (1974).
100. R. L. Holman, P. J. Cressman, and J. F. Revelli, "Chemical control of optical damage in lithium niobate," *Appl. Phys. Lett.* **32**(5), 280–283 (1978).
101. G. D. Boyd, R. V. Schmidt, and F. Storz, "Characteristics of metal-diffused $LiNbO_3$ for acoustic devices," *J. Appl. Phys.* **48**(7), 2880–2881 (1977).
102. M. Fukuma, J. Noda, and H. Iwasaki, "Optical properties in titanium-diffused $LiNbO_3$ strip waveguides," *J. Appl. Phys.* **49**(7), 3693–3698 (1978).
103. M. Minakata et al., "Precise determination of refractive-index changes in Ti-diffused $LiNbO_3$ optical waveguides," *J. Appl. Phys.* **49**(9), 4677–4682 (1978).
104. J. Campbell, "Coupling of fibers to Ti-diffused $LiNbO_3$ waveguides by butt-joining," *Appl. Opt.* **18**(12), 2037–2040 (1979).
105. A. Neyer and W. Sohler, "High-speed cutoff modulator using a Ti-diffused $LiNbO_3$ channel waveguide," *Appl. Phys. Lett.* **35**(3), 256–258 (1979).
106. M. Feit, J. Fleck, and L. McCaughan, "Comparison of calculated and measured performance of diffused channel-waveguide couplers," *J. Opt. Soc. Am.* **73**(10), 1296–1304 (1983).
107. J. Ctyroky et al., "3-D analysis of $LiNbO_3$:Ti channel waveguides and directional couplers," *IEEE J. Quantum Electron.* **20**(4), 400–409 (1984).
108. P.-K. Wei and W.-S. Wang, "A TE-TM mode splitter on lithium niobate using Ti, Ni, and MgO diffusions," *IEEE Photonics Technol. Lett.* **6**(2), 245–248 (1994).
109. W.-L. Chen et al., "Lithium niobate ridge waveguides by nickel diffusion and proton-exchanged wet etching," *IEEE Photonics Technol. Lett.* **7**(11), 1318–1320 (1995).
110. Y.-P. Liao et al., "Nickel-diffused lithium niobate optical waveguide with process-dependent polarization," *IEEE Photonics Technol. Lett.* **8**(4), 548–550 (1996).
111. R. Nevado and G. Lifante, "Characterization of index profiles of Zn-diffused $LiNbO_3$ waveguides," *J. Opt. Soc. Am. A* **16**(10), 2574–2580 (1999).
112. D. Ciplys et al., "Guided-wave acousto-optic diffraction in Zn:$LiNbO_3$," *Electron. Lett.* **42**(22), 1294–1295 (2006).
113. M. Fukuma and J. Noda, "Optical properties of titanium-diffused $LiNbO_3$ strip waveguides and their coupling-to-a-fiber characteristics," *Appl. Opt.* **19**(4), 591–597 (1980).
114. W. Minford, S. Korotky, and R. Alferness, "Low-loss Ti:$LiNbO_3$ waveguide bends at $\lambda = 1.3$ μm," *IEEE J. Quantum Electron.* **18**(10), 1802–1806 (1982).
115. D. White et al., "Atomically-thin quantum dots integrated with lithium niobate photonic chips," *Opt. Mater. Express* **9**(2), 441–448 (2019).
116. G. Sia et al., "Fabrication and characterization of proton-exchanged waveguide on x-cut $LiNbO_3$," in *IEEE Photonics Global@Singapore*, IEEE (2008).
117. K. Ito and K. Kawamoto, "Dependence of lattice constant deviation and refractive index on proton concentration in proton-exchanged optical waveguides on a single crystal of $LiNbO_3$," *Jpn. J. Appl. Phys.* **31**, 3882–3887 (1992).
118. V. M. Passaro et al., "$LiNbO_3$ optical waveguides formed in a new proton source," *J. Lightwave Technol.* **20**(1), 71–77 (2002).
119. W. J. Liao et al., "Proton-exchanged optical waveguides fabricated by glutaric acid," *Opt. Laser Technol.* **36**(8), 603–606 (2004).
120. T. Fujiwara et al., "Comparison of photorefractive index change in proton-exchanged and Ti-diffused $LiNbO_3$ waveguides," *Opt. Lett.* **18**(5), 346–348 (1993).
121. L. Cai, Y. Kang, and H. Hu, "Electric-optical property of the proton exchanged phase modulator in single-crystal lithium niobate thin film," *Opt. Express* **24**(5), 4640–4647 (2016).
122. P. Suchoski, T. K. Findakly, and F. Leonberger, "Stable low-loss proton-exchanged $LiNbO_3$ waveguide devices with no electro-optic degradation," *Opt. Lett.* **13**(11), 1050–1052 (1988).
123. S. T. Vohra, A. R. Mickelson, and S. E. Asher, "Diffusion characteristics and waveguiding properties of proton-exchanged and annealed $LiNbO_3$ channel waveguides," *J. Appl. Phys.* **66**(11), 5161–5174 (1989).
124. J. Rams, F. Agullo-Rueda, and J. Cabrera, "Structure of high index proton exchange $LiNbO_3$ waveguides with undegraded nonlinear optical coefficients," *Appl. Phys. Lett.* **71**(23), 3356–3358 (1997).
125. O. Stepanenko et al., "Highly confining proton exchanged waveguides on Z-cut $LiNbO_3$ with preserved nonlinear coefficient," *IEEE Photonics Technol. Lett.* **26**(15), 1557–1560 (2014).
126. L. Cai et al., "Channel waveguides and y-junctions in x-cut single-crystal lithium niobate thin film," *Opt. Express* **23**(22), 29211–29221 (2015).

127. M. L. Shah, "Optical waveguides in $LiNbO_3$ by ion exchange technique," *Appl. Phys. Lett.* **26**(11), 652–653 (1975).
128. J. Jackel, "High-Δn optical waveguides in $LiNbO_3$:thallium-lithium ion exchange," *Appl. Phys. Lett.* **37**(8), 739–741 (1980).
129. Y. X. Chen et al., "Characterization of $LiNbO_3$ waveguides exchanged in $TlNO_3$ solution," *Appl. Phys. Lett.* **40**(1), 10–12 (1982).
130. J. L. Jackel and C. Rice, "Variation in waveguides fabricated by immersion of $LiNbO_3$ in $AgNO_3$ and $TlNO_3$: the role of hydrogen," *Appl. Phys. Lett.* **41**(6), 508–510 (1982).
131. M. Zhang et al., "Electro-optic reconfigurable two-mode (de)-multiplexer on thin-film lithium niobate," *Opt. Lett.* **46**(5), 1001–1004 (2021).
132. G. Destefanis, P. Townsend, and J. Gailliard, "Optical waveguides in $LiNbO_3$ formed by ion implantation of helium," *Appl. Phys. Lett.* **32**(5), 293–294 (1978).
133. G. Destefanis et al., "The formation of waveguides and modulators in $LiNbO_3$ by ion implantation," *J. Appl. Phys.* **50**(12), 7898–7905 (1979).
134. G. Destefanis, J. Gailliard, and P. Townsend, "Optical waveguides in $LiNbO_3$ formed by ion implantation," *Radiat. Eff.* **48**(1-4), 63–67 (1980).
135. H. Karge et al., "Radiation damage and refractive index of ion-implanted $LiNbO_3$," *Nucl. Instrum. Methods* **182–183**(Part 2), 777–780 (1981).
136. S. Al-Chalabi, "Transient annealing of planar waveguides formed by $^4He^+$ ion implantation into $LiNbO_3$," *Radiat. Eff.* **98**(1-4), 227–231 (1986).
137. I. Skinner et al., "The modelling of lithium outdiffusion in He^+ implanted optical waveguides in $LiNbO_3$," *Solid-State Electron.* **30**(1), 85–88 (1987).
138. G. Si et al., "Suspended slab and photonic crystal waveguides in lithium niobate," *J. Vac. Sci. Technol. B* **28**(2), 316–320 (2010).
139. G. Griffel, S. Ruschin, and N. Croitoru, "Linear electro-optic effect in sputtered polycrystalline $LiNbO_3$ films," *Appl. Phys. Lett.* **54**(15), 1385–1387 (1989).
140. D. K. Fork and G. B. Anderson, "Epitaxial MgO on GaAs(111) as a buffer layer for z-cut epitaxial lithium niobate," *Appl. Phys. Lett.* **63**(8), 1029–1031 (1993).
141. Y. Sakashita and H. Segawa, "Preparation and characterization of $LiNbO_3$ thin films produced by chemical-vapor deposition," *J. Appl. Phys.* **77**(11), 5995–5999 (1995).
142. M. Levy et al., "Fabrication of single-crystal lithium niobate films by crystal ion slicing," *Appl. Phys. Lett.* **73**(16), 2293–2295 (1998).
143. A. Radojevic et al., "Large etch-selectivity enhancement in the epitaxial liftoff of single-crystal $LiNbO_3$ films," *Appl. Phys. Lett.* **74**(21), 3197–3199 (1999).
144. T. A. Ramadan, M. Levy, and R. Osgood Jr., "Electro-optic modulation in crystal-ion-sliced z-cut $LiNbO_3$ thin films," *Appl. Phys. Lett.* **76**(11), 1407–1409 (2000).
145. P. Rabiei and P. Gunter, "Optical and electro-optical properties of submicrometer lithium niobate slab waveguides prepared by crystal ion slicing and wafer bonding," *Appl. Phys. Lett.* **85**(20), 4603–4605 (2004).
146. G. Poberaj et al., "Ion-sliced lithium niobate thin films for active photonic devices," *Opt. Mater.* **31**(7), 1054–1058 (2009).
147. T. Volk and M. Wöhlecke, *Lithium Niobate: Defects, Photorefraction and Ferroelectric Switching*, Vol. **115**, Springer Science and Business Media, Springer-Verlag, Berlin (2008).
148. M. Chauvet et al., "High efficiency frequency doubling in fully diced $LiNbO_3$ ridge waveguides on silicon," *J. Opt.* **18**(8), 085503 (2016).
149. M. Bock et al., "Highly efficient heralded single-photon source for telecom wavelengths based on a PPLN waveguide," *Opt. Express* **24**(21), 23992–24001 (2016).
150. A. S. Kowligy et al., "Mid-infrared frequency comb generation via cascaded quadratic nonlinearities in quasi-phase-matched waveguides," *Opt. Lett.* **43**(8), 1678–1681 (2018).
151. L. Lehmann et al., "Single photon MIR upconversion detector at room temperature with a PPLN ridge waveguide," *Opt. Express* **27**(14), 19233–19241 (2019).
152. R. Bege et al., "Watt-level second-harmonic generation at 589 nm with a PPMgO:LN ridge waveguide crystal pumped by a DBR tapered diode laser," *Opt. Lett.* **41**(7), 1530–1533 (2016).
153. V. Pecheur et al., "Watt-level SHG in undoped high step-index PPLN ridge waveguides," *OSA Continuum* **4**(5), 1404–1414 (2021).
154. S. A. Berry et al., "Zn-indiffused diced ridge waveguides in MgO:PPLN generating 1 watt 780 nm SHG at 70% efficiency," *OSA Continuum* **2**(12), 3456–3464 (2019).
155. M. E. Solmaz et al., "Vertically integrated As_2S_3 ring resonator on $LiNbO_3$," *Opt. Lett.* **34**(11), 1735–1737 (2009).
156. Y. S. Lee et al., "Hybrid Si-$LiNbO_3$ microring electro-optically tunable resonators for active photonic devices," *Opt. Lett.* **36**(7), 1119–1121 (2011).
157. L. Chen and R. M. Reano, "Compact electric field sensors based on indirect bonding of lithium niobate to silicon microrings," *Opt. Express* **20**(4), 4032–4038 (2012).
158. P. Rabiei et al., "Heterogeneous lithium niobate photonics on silicon substrates," *Opt. Express* **21**(21), 25573–25581 (2013).
159. L. Cao et al., "Hybrid amorphous silicon (a-Si:H)–$LiNbO_3$ electro-optic modulator," *Opt. Commun.* **330**, 40–44 (2014).
160. L. Chen et al., "Hybrid silicon and lithium niobate electro-optical ring modulator," *Optica* **1**(2), 112–118 (2014).
161. F. Bo et al., "Lithium-niobate–silica hybrid whispering-gallery-mode resonators," *Adv. Mater.* **27**(48), 8075–8081 (2015).
162. S. Jin et al., "$LiNbO_3$ thin-film modulators using silicon nitride surface ridge waveguides," *IEEE Photonics Technol. Lett.* **28**(7), 736–739 (2016).
163. S. Li et al., "Waveguides consisting of single-crystal lithium niobate thin film and oxidized titanium stripe," *Opt. Express* **23**(19), 24212–24219 (2015).
164. A. Rao et al., "Heterogeneous microring and Mach-Zehnder modulators based on lithium niobate and chalcogenide glasses on silicon," *Opt. Express* **23**(17), 22746–22752 (2015).
165. A. Rao et al., "High-performance and linear thin-film lithium niobate Mach–Zehnder modulators on silicon up to 50 GHz," *Opt. Lett.* **41**(24), 5700–5703 (2016).
166. L. Chang et al., "Heterogeneous integration of lithium niobate and silicon nitride waveguides for wafer-scale photonic integrated circuits on silicon," *Opt. Lett.* **42**(4), 803–806 (2017).
167. J. D. Witmer et al., "High-Q photonic resonators and electro-optic coupling using silicon-on-lithium-niobate," *Sci. Rep.* **7**, 46313 (2017).
168. A. N. R. Ahmed et al., "Subvolt electro-optical modulator on thin-film lithium niobate and silicon nitride hybrid platform," *Opt. Lett.* **45**(5), 1112–1115 (2020).
169. A. N. R. Ahmed et al., "High-efficiency lithium niobate modulator for K band operation," *APL Photonics* **5**(9), 091302 (2020).
170. N. Boynton et al., "A heterogeneously integrated silicon photonic/lithium niobate travelling wave electro-optic modulator," *Opt. Express* **28**(2), 1868–1884 (2020).
171. D. Pohl et al., "An integrated broadband spectrometer on thin-film lithium niobate," *Nat. Photonics* **14**(1), 24–29 (2020).
172. A. A. Sayem et al., "Lithium-niobate-on-insulator waveguide-integrated superconducting nanowire single-photon detectors," *Appl. Phys. Lett.* **116**(15), 151102 (2020).
173. Z. Yu et al., "Photonic integrated circuits with bound states in the continuum," *Optica* **6**(10), 1342–1348 (2019).
174. Y. Yu et al., "Ultralow-loss etchless lithium niobate integrated photonics at near-visible wavelengths," *Adv. Opt. Mater.* **9**(19), 2100060 (2021).
175. G. Chen et al., "Analysis of perovskite oxide etching using argon inductively coupled plasmas for photonics applications," *Nanoscale Res. Lett.* **16**(1), 32 (2021).

176. J. Jian et al., "High-efficiency hybrid amorphous silicon grating couplers for sub-micron-sized lithium niobate waveguides," *Opt. Express* **26**(23), 29651–29658 (2018).
177. Z. Ruan et al., "Metal based grating coupler on a thin-film lithium niobate waveguide," *Opt. Express* **28**(24), 35615–35621 (2020).
178. J. L. Jackel et al., "Reactive ion etching of $LiNbO_3$," *Appl. Phys. Lett.* **38**(11), 907–909 (1981).
179. H. Nagata et al., "Growth of crystalline LiF on CF_4 plasma etched $LiNbO_3$ substrates," *J. Cryst. Growth* **187**(3-4), 573–576 (1998).
180. H. Nagata et al., "Chemical deterioration of Al film prepared on CF4 plasma-etched $LiNbO_3$ surface," *J. Mater. Res.* **15**(2), 476–482 (2000).
181. A. Guarino et al., "Electro–optically tunable microring resonators in lithium niobate," *Nat. Photonics* **1**(7), 407–410 (2007).
182. Z. Ren et al., "Etching characteristics of $LiNbO_3$ in reactive ion etching and inductively coupled plasma," *J. Appl. Phys.* **103**(3), 034109 (2008).
183. S. Benchabane et al., "Highly selective electroplated nickel mask for lithium niobate dry etching," *J. Appl. Phys.* **105**(9), 094109 (2009).
184. H. Hu, R. Ricken, and W. Sohler, "Lithium niobate photonic wires," *Opt. Express* **17**(26), 24261–24268 (2009).
185. J. Deng, G. Si, and A. J. Danner, "Dry etching of $LiNbO_3$ using inductively coupled plasma," in *Photonics Global Conf.*, IEEE (2010).
186. G. Si et al., "Nanoscale arrays in lithium niobate fabricated by interference lithography and dry etching," *Int. J. Nanosci.* **9**(4), 311–315 (2010).
187. G. Ulliac et al., "Ultra-smooth $LiNbO_3$ micro and nano structures for photonic applications," *Microelectron. Eng.* **88**(8), 2417–2419 (2011).
188. D. Jun et al., "Deep anisotropic $LiNbO_3$ etching with SF_6/Ar inductively coupled plasmas," *J. Vac. Sci. Technol. B* **30**(1), 011208 (2012).
189. C.-M. Chang et al., "A parametric study of ICP-RIE etching on a lithium niobate substrate," in *10th IEEE Int. Conf. Nano/Micro Eng. and Mol. Syst.*, IEEE (2015).
190. G. Ulliac et al., "Argon plasma inductively coupled plasma reactive ion etching study for smooth sidewall thin film lithium niobate waveguide application," *Opt. Mater.* **53**, 1–5 (2016).
191. I. Krasnokutska et al., "Ultra-low loss photonic circuits in lithium niobate on insulator," *Opt. Express* **26**(2), 897–904 (2018).
192. M. Zhang et al., "Monolithic ultra-high-Q lithium niobate microring resonator," *Optica* **4**(12), 1536–1537 (2017).
193. M. Bahadori et al., "High performance fully etched isotropic microring resonators in thin-film lithium niobate on insulator platform," *Opt. Express* **27**(15), 22025–22039 (2019).
194. A. A. Osipov, S. E. Alexandrov, and G. A. Iankevich, "The effect of a lithium niobate heating on the etching rate in SF_6 ICP plasma," *Mater. Res. Express* **6**(4), 046306 (2019).
195. C. Shen et al., "A comparative study of dry-etching nanophotonic devices on a $LiNbO_3$-on-insulator material platform," *Proc. SPIE* **11781**, 117810X (2021).
196. A. A. Osipov et al., "Deep etching of $LiNbO_3$ using inductively coupled plasma in SF_6-based gas mixture," *J. Microelectromech. Syst.* **30**(1), 90–95 (2021).
197. H. Liang et al., "High-quality lithium niobate photonic crystal nanocavities," *Optica* **4**(10), 1251–1258 (2017).
198. T. L. Ting, L. Y. Chen, and W. S. Wang, "Wet etching X-cut $LiNbO_3$ using diluted joint proton source," *Microwave Opt. Technol. Lett.* **48**(10), 2108–2111 (2006).
199. F. Laurell et al., "Wet etching of proton-exchanged lithium niobate-a novel processing technique," *J. Lightwave Technol.* **10**(11), 1606–1609 (1992).
200. H. Lee and S.-Y. Shin, "Lithium niobate ridge waveguides fabricated by wet etching," *Electron. Lett.* **31**(4), 268–269 (1995).
201. R.-S. Cheng, T.-J. Wang, and W.-S. Wang, "Wet-etched ridge waveguides in Y-cut lithium niobate," *J. Lightwave Technol.* **15**(10), 1880–1887 (1997).
202. T.-J. Wang et al., "A novel wet-etching method using electric-field-assisted proton exchange in $LiNbO_3$," *J. Lightwave Technol.* **22**(7), 1764–1771 (2004).
203. I. Azanova et al., "Chemical etching technique for investigations of a structure of annealed and unannealed proton exchange channel $LiNbO_3$ waveguides," *Ferroelectrics* **374**(1), 110–121 (2008).
204. Y. Li et al., "Research of selective etching in $LiNbO_3$ using proton-exchanged wet etching technique," *Mater. Res. Express* **7**(5), 056202 (2020).
205. H. Hu et al., "Lithium niobate ridge waveguides fabricated by wet etching," *IEEE Photonics Technol. Lett.* **19**(6), 417–419 (2007).
206. L. Wang et al., "Selective etching in $LiNbO_3$ combined of MeV O and Si ion implantation with wet-etch technique," *Surf. Coat. Technol.* **201**(9-11), 5081–5084 (2007).
207. H. Hartung et al., "Ultra thin high index contrast photonic crystal slabs in lithium niobate," *Opt. Mater.* **33**(1), 19–21 (2010).
208. F. Lacour et al., "Nanostructuring lithium niobate substrates by focused ion beam milling," *Opt. Mater.* **27**(8), 1421–1425 (2005).
209. G. Si et al., "Photonic crystal structures with ultrahigh aspect ratio in lithium niobate fabricated by focused ion beam milling," *J. Vac. Sci. Technol. B* **29**(2), 021205 (2011).
210. R. Geiss et al., "Photonic crystals in lithium niobate by combining focused ion beam writing and ion-beam enhanced etching," *Phys. Stat. Solidi A* **211**(10), 2421–2425 (2014).
211. M. Qu et al., "Homogenous and ultra-shallow lithium niobate etching by focused ion beam," *Precis. Eng.* **62**, 10–15 (2020).
212. N. Courjal et al., "High aspect ratio lithium niobate ridge waveguides fabricated by optical grade dicing," *J. Phys. D Appl. Phys.* **44**(30), 305101 (2011).
213. M. F. Volk et al., "Low loss ridge waveguides in lithium niobate thin films by optical grade diamond blade dicing," *Opt. Express* **24**(2), 1386–1391 (2016).
214. J. Lin et al., "Fabrication of high-Q lithium niobate microresonators using femtosecond laser micromachining," *Sci. Rep.* **5**, 8072 (2015).
215. Z. Fang et al., "Fabrication of high quality factor lithium niobate double-disk using a femtosecond laser," *Int. J. Optomechatron.* **11**(1), 47–54 (2017).
216. S. Liu, Y. Zheng, and X. Chen, "Cascading second-order nonlinear processes in a lithium niobate-on-insulator microdisk," *Opt. Lett.* **42**(18), 3626–3629 (2017).
217. M. Wang et al., "On-chip electro-optic tuning of a lithium niobate microresonator with integrated in-plane microelectrodes," *Opt. Express* **25**(1), 124–129 (2017).
218. R. Wu et al., "Lithium niobate micro-disk resonators of quality factors above 10^7," *Opt. Lett.* **43**(17), 4116–4119 (2018).
219. R. Wu et al., "Long low-loss-litium niobate on insulator waveguides with sub-nanometer surface roughness," *Nanomaterials* **8**(11), 910 (2018).
220. M. Wang et al., "Chemo-mechanical polish lithography: a pathway to low loss large-scale photonic integration on lithium niobate on insulator," *Quantum Eng.* **1**(1), e9 (2019).
221. J. Zhang et al., "Fabrication of crystalline microresonators of high quality factors with a controllable wedge angle on lithium niobate on insulator," *Nanomaterials* **9**(9), 1218 (2019).
222. Z. Fang et al., "Real-time electrical tuning of an optical spring on a monolithically integrated ultrahigh Q lithium nibote microresonator," *Opt. Lett.* **44**(5), 1214–1217 (2019).
223. N. Yao et al., "Efficient light coupling between an ultra-low loss lithium niobate waveguide and an adiabatically tapered single mode optical fiber," *Opt. Express* **28**(8), 12416–12423 (2020).
224. R. Gao et al., "Lithium niobate microring with ultra-high Q factor above 10^8," *Chin. Opt. Lett.* **20**(1), 011902 (2022).

225. X. C. Tong, "Characterization methodologies of optical waveguides," in *Advanced Materials for Integrated Optical Waveguides*, pp. 53–102, Springer, New York City (2014).
226. S. Y. Siew et al., "Rib microring resonators in lithium niobate on insulator," *IEEE Photonics Technol. Lett.* **28**(5), 573–576 (2016).
227. J. Moore et al., "Continuous-wave cascaded-harmonic generation and multi-photon Raman lasing in lithium niobate whispering-gallery resonators," *Appl. Phys. Lett.* **99**(22), 221111 (2011).
228. C. Wang et al., "Integrated high quality factor lithium niobate microdisk resonators," *Opt. Express* **22**(25), 30924–30933 (2014).
229. C. Wang et al., "Integrated lithium niobate nonlinear optical devices," in *Conf. Lasers and Electro-Opt.*, IEEE (2015).
230. J. Wang et al., "High-*Q* lithium niobate microdisk resonators on a chip for efficient electro-optic modulation," *Opt. Express* **23**(18), 23072–23078 (2015).
231. Y. He et al., "Dispersion engineered high quality lithium niobate microring resonators," *Opt. Express* **26**(13), 16315–16322 (2018).
232. L. Ge et al., "Quality improvement and mode evolution of high-*Q* lithium niobate micro-disk induced by 'light annealing'," *Opt. Mater. Express* **9**(4), 1632–1639 (2019).
233. S. Liu et al., "Effective four-wave mixing in the lithium niobate on insulator microdisk by cascading quadratic processes," *Opt. Lett.* **44**(6), 1456–1459 (2019).
234. L. Zhang et al., "Microdisk resonators with lithium-niobate film on silicon substrate," *Opt. Express* **27**(23), 33662–33669 (2019).
235. Y. Zheng et al., "High-*Q* exterior whispering-gallery modes in a double-layer crystalline microdisk resonator," *Phys. Rev. Lett.* **122**(25), 253902 (2019).
236. J. Ling et al., "Athermal lithium niobate microresonator," *Opt. Express* **28**(15), 21682–21691 (2020).
237. R. Wang and S. A. Bhave, "Lithium niobate optomechanical disk resonators," in *Joint Conf. IEEE Int. Freq. Control Symp. and Int. Symp. Appl. Ferroelectr.*, IEEE (2020).
238. R. Gao et al., "On-chip ultra-narrow-linewidth single-mode microlaser on lithium niobate on insulator," *Opt. Lett.* **46**(13), 3131–3134 (2021).
239. B. Pan et al., "Compact racetrack resonator on $LiNbO_3$," *J. Lightwave Technol.* **39**(6), 1770–1776 (2021).
240. Y. Xu et al., "Mitigating photorefractive effect in thin-film lithium niobate microring resonators," *Opt. Express* **29**(4), 5497–5504 (2021).
241. M. Li et al., "Lithium niobate photonic-crystal electro-optic modulator," *Nat. Commun.* **11**, 4123 (2020).
242. M. Xu et al., "Integrated thin film lithium niobate Fabry–Perot modulator," *Chin. Opt. Lett.* **19**(6), 060003 (2021).
243. D. Pohl et al., "100-GBd waveguide Bragg grating modulator in thin-film lithium niobate," *IEEE Photonics Technol. Lett.* **33**(2), 85–88 (2021).
244. Z. Gong et al., "Optimal design of DC-based polarization beam splitter in lithium niobate on insulator," *Opt. Commun.* **396**, 23–27 (2017).
245. L. Cai and G. Piazza, "Low-loss chirped grating for vertical light coupling in lithium niobate on insulator," *J. Opt.* **21**(6), 065801 (2019).
246. L. He et al., "Low-loss fiber-to-chip interface for lithium niobate photonic integrated circuits," *Opt. Lett.* **44**(9), 2314–2317 (2019).
247. A. Kar et al., "Realization of alignment-tolerant grating couplers for z-cut thin-film lithium niobate," *Opt. Express* **27**(11), 15856–15867 (2019).
248. I. Krasnokutska et al., "High coupling efficiency grating couplers on lithium niobate on insulator," *Opt. Express* **27**(13), 17681–17685 (2019).
249. I. Krasnokutska, J.-L. J. Tambasco, and A. Peruzzo, "Nanostructuring of LNOI for efficient edge coupling," *Opt. Express* **27**(12), 16578–16585 (2019).
250. A. Pan et al., "Fundamental mode hybridization in a thin film lithium niobate ridge waveguide," *Opt. Express* **27**(24), 35659–35669 (2019).
251. Q. Xu et al., "A theoretical study on rib-type photonic wires based on $LiNbO_3$ thin film on insulator," *Adv. Theor. Simul.* **2**(10), 1900115 (2019).
252. Z. Chen, Y. Ning, and Y. Xun, "Chirped and apodized grating couplers on lithium niobate thin film," *Opt. Mater. Express* **10**(10), 2513–2521 (2020).
253. Z. Gong et al., "Tunable microwave photonic filter based on LNOI polarization beam splitter and waveguide grating," *IEEE Photonics Technol. Lett.* **32**(13), 787–790 (2020).
254. C. C. Kores, M. Fokine, and F. Laurell, "UV-written grating couplers on thin-film lithium niobate ridge waveguides," *Opt. Express* **28**(19), 27839–27849 (2020).
255. Y. Liu et al., "TE/TM-pass polarizers based on lateral leakage in a thin film lithium niobate–silicon nitride hybrid platform," *Opt. Lett.* **45**(17), 4915–4918 (2020).
256. D. Pohl et al., "Tunable Bragg grating filters and resonators in lithium niobate-on-insulator waveguides," in *CLEO: Sci. and Innov.*, Optical Society of America (2020).
257. A. Prencipe, M. A. Baghban, and K. Gallo, "Ultra-narrowband Bragg grating filters in $LiNbO_3$ on insulator photonic wires," in *Integrated Photonics Res., Silicon and Nanophotonics*, Optical Society of America (2020).
258. G. Qian et al., "Design and fabrication of cantilevered fiber-to-waveguide mode size converter for thin-film lithium niobate photonic integrated circuits," *Proc. SPIE* **11455**, 1145587 (2020).
259. K. Shuting et al., "High-efficiency chirped grating couplers on lithium niobate on insulator," *Opt. Lett.* **45**(24), 6651–6654 (2020).
260. S. Tan et al., "Two-dimensional beam steering based on LNOI optical phased array," in *CLEO: Science and Innov.*, Optical Society of America (2020).
261. H. Xu et al., "Proposal for an ultra-broadband polarization beam splitter using an anisotropy-engineered Mach–Zehnder interferometer on the x-cut lithium-niobate-on-insulator," *Opt. Express* **28**(8), 10899–10908 (2020).
262. L. Zhang, X. Fu, and L. Yang, "Polarization-independent, lithium-niobate-on-insulator directional coupler based on a combined coupling-sections design," *Appl. Opt.* **59**(28), 8668–8673 (2020).
263. J.-X. Zhou et al., "Electro-optically switchable optical true delay lines of meter-scale lengths fabricated on lithium niobate on insulator using photolithography assisted chemo-mechanical etching," *Chin. Phys. Lett.* **37**(8), 8084201 (2020).
264. K. Abdelsalam et al., "Tunable dual-channel ultra-narrowband Bragg grating filter on thin-film lithium niobate," *Opt. Lett.* **46**(11), 2730–2733 (2021).
265. B. Chen et al., "Two-dimensional grating coupler on an X-cut lithium niobate thin-film," *Opt. Express* **29**(2), 1289–1295 (2021).
266. C. Hu et al., "High-efficient coupler for thin-film lithium niobate waveguide devices," *Opt. Express* **29**(4), 5397–5406 (2021).
267. Y. Liu et al., "Ultra-compact mode-division multiplexed photonic integrated circuit for dual polarizations," *J. Lightwave Technol.* **39**(18), 5925–5932 (2021).
268. E. Lomonte, F. Lenzini, and W. H. P. Pernice, "Efficient self-imaging grating couplers on a lithium-niobate-on-insulator platform at near-visible and telecom wavelengths," *Opt. Express* **29**(13), 20205–20216 (2021).
269. S. Yang et al., "Low loss ridge-waveguide grating couplers in lithium niobate on insulator," *Opt. Mater. Express* **11**(5), 1366–1376 (2021).
270. G. Chen, Y. Yu, and X. Zhang, "A dual-detector optical receiver for PDM signals detection," *Sci. Rep.* **6**, 26469 (2016).
271. R. Alferness et al., "Efficient single-mode fiber to titanium diffused lithium niobate waveguide coupling for $\lambda = 1.32$ μm," *IEEE J. Quantum Electron.* **18**(10), 1807–1813 (1982).
272. C. Wang et al., "Nanophotonic lithium niobate electro-optic modulators," *Opt. Express* **26**(2), 1547–1555 (2018).

273. J. Jian et al., "High modulation efficiency lithium niobate Michelson interferometer modulator," *Opt. Express* **27**(13), 18731–18739 (2019).
274. M. Jin et al., "High-extinction electro-optic modulation on lithium niobate thin film," *Opt. Lett.* **44**(5), 1265–1268 (2019).
275. T. Ren et al., "An integrated low-voltage broadband lithium niobate phase modulator," *IEEE Photonics Technol. Lett.* **31**(11), 889–892 (2019).
276. M. Xu et al., "Michelson interferometer modulator based on hybrid silicon and lithium niobate platform," *APL Photonics* **4**(10), 100802 (2019).
277. S. Sun et al., "Bias-drift-free Mach–Zehnder modulators based on a heterogeneous silicon and lithium niobate platform," *Photonics Res.* **8**(12), 1958–1963 (2020).
278. J. Hu et al., "Folded thin-film lithium niobate modulator based on a poled Mach–Zehnder interferometer structure," *Opt. Lett.* **46**(12), 2940–2943 (2021).
279. X. Huang et al., "40 GHz high-efficiency Michelson interferometer modulator on a silicon-rich nitride and thin-film lithium niobate hybrid platform," *Opt. Lett.* **46**(12), 2811–2814 (2021).
280. N. Jagatpal et al., "Thin film lithium niobate electro-optic modulator for 1064 nm wavelength," *IEEE Photonics Technol. Lett.* **33**(5), 271–274 (2021).
281. M. Jin et al., "Efficient electro-optical modulation on thin-film lithium niobate," *Opt. Lett.* **46**(8), 1884–1887 (2021).
282. P. Kharel et al., "Breaking voltage–bandwidth limits in integrated lithium niobate modulators using micro-structured electrodes," *Optica* **8**(3), 357–363 (2021).
283. X. Liu et al., "Low half-wave-voltage, ultra-high bandwidth thin-film $LiNbO_3$ modulator based on hybrid waveguide and periodic capacitively loaded electrodes," arXiv:2103.03684 (2021).
284. Y. Liu et al., "Low V_π thin-film lithium niobate modulator fabricated with photolithography," *Opt. Express* **29**(5), 6320–6329 (2021).
285. B. Pan et al., "Demonstration of high-speed thin-film lithium-niobate-on-insulator optical modulators at the 2-μm wavelength," *Opt. Express* **29**(12), 17710–17717 (2021).
286. X. Ye et al., "High-speed programmable lithium niobate thin film spatial light modulator," *Opt. Lett.* **46**(5), 1037–1040 (2021).
287. P. Ying et al., "Low-loss edge-coupling thin-film lithium niobate modulator with an efficient phase shifter," *Opt. Lett.* **46**(6), 1478–1481 (2021).
288. G. Chen et al., "Integrated electro-optic modulator in z-cut lithium niobate thin film with vertical structure," *IEEE Photonics Technol. Lett.* **33**(23), 1285–1288 (2021).
289. J. Kondo et al., "40-Gb/s X-cut $LiNbO_3$ optical modulator with two-step back-slot structure," *J. Lightwave Technol.* **20**(12), 2110–2114 (2002).
290. M. García-Granda et al., "Design and fabrication of novel ridge guide modulators in lithium niobate," *J. Lightwave Technol.* **27**(24), 5690–5697 (2009).
291. H. Lu et al., "Optical and RF characterization of a lithium niobate photonic crystal modulator," *IEEE Photonics Technol. Lett.* **26**(13), 1332–1335 (2014).
292. M. Mahmoud et al., "Lithium niobate electro-optic racetrack modulator etched in Y-cut LNOI platform," *IEEE Photonics J.* **10**(1), 6600410 (2018).
293. Y. Yamaguchi et al., "Experimental evaluation of wavelength-dependence of thin-film $LiNbO_3$ modulator with an extinction-ratio-tunable structure," in *24th OptoElectron. and Commun. Conf. and Int. Conf. Photonics Switch. and Comput.*, IEEE (2019).
294. M. Xu et al., "Dual-polarization thin-film lithium niobate in-phase quadrature modulators for terabit-per-second transmission," *Optica* **9**(1), 61–62 (2022).
295. X. Zhang et al., "An optical switch based on electro-optic mode deflection in lithium niobate waveguide," *IEEE Photonics Technol. Lett.* **32**(20), 1295–1298 (2020).
296. G. Chen et al., "Design and fabrication of high-performance multimode interferometer in lithium niobate thin film," *Opt. Express* **29**(10), 15689–15698 (2021).
297. X. P. Li, K. X. Chen, and L. F. Wang, "Compact and electro-optic tunable interleaver in lithium niobate thin film," *Opt. Lett.* **43**(15), 3610–3613 (2018).
298. M. Zhang et al., "Electronically programmable photonic molecule," *Nat. Photonics* **13**(1), 36–40 (2019).
299. Y. Hu et al., "On-chip electro-optic frequency shifters and beam splitters," *Nature* **599**(7886), 587–593 (2021).
300. J. Holzgrafe et al., "Cavity electro-optics in thin-film lithium niobate for efficient microwave-to-optical transduction," *Optica* **7**(12), 1714–1720 (2020).
301. T. P. McKenna et al., "Cryogenic microwave-to-optical conversion using a triply resonant lithium-niobate-on-sapphire transducer," *Optica* **7**(12), 1737–1745 (2020).
302. Y. Xu et al., "Bidirectional interconversion of microwave and light with thin-film lithium niobate," *Nat. Commun.* **12**, 4453 (2021).
303. A. P. Higginbotham et al., "Harnessing electro-optic correlations in an efficient mechanical converter," *Nat. Phys.* **14**(10), 1038–1042 (2018).
304. L. E. Myers et al., "Quasi-phase-matched optical parametric oscillators in bulk periodically poled $LiNbO_3$," *J. Opt. Soc. Am. B* **12**(11), 2102–2116 (1995).
305. G. Li et al., "Broadband sum-frequency generation using d_{33} in periodically poled $LiNbO_3$ thin film in the telecommunications band," *Opt. Lett.* **42**(5), 939–942 (2017).
306. Y. Li et al., "Optical anapole mode in nanostructured lithium niobate for enhancing second harmonic generation," *Nanophotonics* **9**(11), 3575–3585 (2020).
307. S. Kakio et al., "Diffraction properties and beam-propagation analysis of waveguide-type acoustooptic modulator driven by surface acoustic wave," *Jpn. J. Appl. Phys.* **44**(6B), 4472–4476 (2005).
308. M. Kadota et al., "High-frequency lamb wave device composed of MEMS structure using $LiNbO_3$ thin film and air gap," *IEEE Trans. Ultrason. Ferroelectr. Freq. Control* **57**(11), 2564–2571 (2010).
309. W. C. Jiang and Q. Lin, "Chip-scale cavity optomechanics in lithium niobate," *Sci. Rep.* **6**, 36920 (2016).
310. W. Jiang et al., "Lithium niobate piezo-optomechanical crystals," *Optica* **6**(7), 845–853 (2019).
311. L. Shao et al., "Phononic band structure engineering for high-Q gigahertz surface acoustic wave resonators on lithium niobate," *Phys. Rev. Appl.* **12**(1), 014022 (2019).
312. A. E. Hassanien et al., "Efficient and wideband acousto-optic modulation on thin-film lithium niobate for microwave-to-photonic conversion," *Photonics Res.* **9**(7), 1182–1190 (2021).
313. C. J. Sarabalis et al., "Acousto-optic modulation of a wavelength-scale waveguide," *Optica* **8**(4), 477–483 (2021).
314. R. M. White and F. W. Voltmer, "Direct piezoelectric coupling to surface elastic waves," *Appl. Phys. Lett.* **7**(12), 314–316 (1965).
315. T.-T. Wu et al., "Analysis and design of focused interdigital transducers," *IEEE Trans. Ultrason. Ferroelectr. Freq. Control* **52**(8), 1384–1392 (2005).
316. M. S. Kharusi and G. W. Farnell, "On diffraction and focusing in anisotropic crystals," *Proc. IEEE* **60**(8), 945–956 (1972).
317. Z. Cheng and C. Tsai, "Baseband integrated acousto-optic frequency shifter," *Appl. Phys. Lett.* **60**(1), 12–14 (1992).
318. S. Kakio, "Acousto-optic modulator driven by surface acoustic waves," *Acta Phys. Pol. A* **127**(1), 15–19 (2015).
319. Z. Yu and X. Sun, "Acousto-optic modulation of photonic bound state in the continuum," *Light Sci. Appl.* **9**(1), 1 (2020).
320. Z. Yu and X. Sun, "Gigahertz acousto-optic modulation and frequency shifting on etchless lithium niobate integrated platform," *ACS Photonics* **8**(3), 798–803 (2021).
321. R. Lu et al., "S0-mode lithium niobate acoustic delay lines with 1 dB insertion loss," in *IEEE Int. Ultrason. Symp.*, IEEE (2018).

322. R. Lu et al., "Gigahertz low-loss and wideband S0 mode lithium niobate acoustic delay lines," *IEEE Trans. Ultrason. Ferroelectr. Freq. Control* **66**(8), 1373–1386 (2019).
323. R. Lu et al., "GHz broadband SH0 mode lithium niobate acoustic delay lines," *IEEE Trans. Ultrason. Ferroelectr. Freq. Control* **67**(2), 402–412 (2020).
324. R. J. Mears et al., "Low-noise erbium-doped fibre amplifier operating at 1.54 μm," *Electron. Lett.* **23**(19), 1026–1028 (1987).
325. G. P. Agrawal, *Fiber-Optic Communication Systems*, Vol. **222**, John Wiley and Sons, Hoboken (2010).
326. E. Lallier et al., "Nd:MgO:$LiNbO_3$ waveguide laser and amplifier," *Opt. Lett.* **15**(12), 682–684 (1990).
327. E. Lallier et al., "Laser oscillation of single-mode channel waveguide in Nd:MgO:$LiNbO_3$," *Electron. Lett.* **25**(22), 1491–1492 (1989).
328. I. Baumann et al., "Er-doped integrated optical devices in $LiNbO_3$," *IEEE J. Sel. Top. Quantum Electron.* **2**(2), 355–366 (1996).
329. R. Brikmann, W. Sohler, and H. Suche, "Continuous-wave erbium-diffused $LiNbO_3$ waveguide laser," *Electron. Lett.* **27**(5), 415–417 (1991).
330. Q. Luo et al., "On-chip erbium-doped lithium niobate microring lasers," *Opt. Lett.* **46**(13), 3275–3278 (2021).
331. Y. Liu et al., "On-chip erbium-doped lithium niobate microcavity laser," *SCIENCE CHINA Phys. Mech. Astron.* **64**(3), 234262 (2021).
332. Q. Luo et al., "Microdisk lasers on an erbium-doped lithium-niobite chip," *SCIENCE CHINA Phys. Mech. Astron.* **64**(3), 234263 (2021).
333. Q. Luo et al., "On-chip erbium-doped lithium niobate waveguide amplifiers," *Chin. Opt. Lett.* **19**(6), 060008 (2021).
334. D. Yin et al., "Electro-optically tunable microring laser monolithically integrated on lithium niobate on insulator," *Opt. Lett.* **46**(9), 2127–2130 (2021).
335. C. Op de Beeck et al., "III/V-on-lithium niobate amplifiers and lasers," *Optica* **8**(10), 1288–1289 (2021).
336. H. Guan et al., "Broadband, high-sensitivity graphene photodetector based on ferroelectric polarization of lithium niobate," *Adv. Opt. Mater.* **9**(16), 2100245 (2021).
337. S. Liu and D. Long, "Pyroelectric detectors and materials," *Proc. IEEE* **66**(1), 14–26 (1978).
338. M. Chauvet et al., "Fast-beam self-trapping in $LiNbO_3$ films by pyroelectric effect," *Opt. Lett.* **40**(7), 1258–1261 (2015).
339. K. K. Gopalan et al., "Mid-infrared pyroresistive graphene detector on $LiNbO_3$," *Adv. Opt. Mater.* **5**(4), 1600723 (2017).
340. B. Gao et al., "Lithium niobate metasurfaces," *Laser Photonics Rev.* **13**(5), 1800312 (2019).
341. A. Fedotova et al., "Second-harmonic generation in resonant nonlinear metasurfaces based on lithium niobate," *Nano Lett.* **20**(12), 8608–8614 (2020).
342. L. Carletti et al., "Steering and encoding the polarization of the second harmonic in the visible with a monolithic $LiNbO_3$ metasurface," *ACS Photonics* **8**(3), 731–737 (2021).
343. J. Ma et al., "Nonlinear lithium niobate metasurfaces for second harmonic generation," *Laser Photonics Rev.* **15**(5), 2000521 (2021).
344. G. Li, S. Zhang, and T. Zentgraf, "Nonlinear photonic metasurfaces," *Nat. Rev. Mater.* **2**(5), 17010 (2017).
345. I. Staude, T. Pertsch, and Y. S. Kivshar, "All-dielectric resonant meta-optics lightens up," *ACS Photonics* **6**(4), 802–814 (2019).
346. L. Wang et al., "Nonlinear wavefront control with all-dielectric metasurfaces," *Nano Lett.* **18**(6), 3978–3984 (2018).
347. J. P. Höpker et al., "Integrated superconducting nanowire single-photon detectors on titanium in-diffused lithium niobate waveguides," *J. Phys. Photonics* **3**(3), 034022 (2021).
348. M. Colangelo et al., "Superconducting nanowire single-photon detector on thin-film lithium niobate photonic waveguide," in *CLEO: Sci. and Innov.*, Optical Society of America (2020).
349. E. Lomonte et al., "Single-photon detection and cryogenic reconfigurability in lithium niobate nanophotonic circuits," *Nat. Commun.* **12**, 6847 (2021).
350. W. H. P. Pernice et al., "High-speed and high-efficiency travelling wave single-photon detectors embedded in nanophotonic circuits," *Nat. Commun.* **3**, 1325 (2012).
351. C. Herzog, G. Poberaj, and P. Günter, "Electro-optic behavior of lithium niobate at cryogenic temperatures," *Opt. Commun.* **281**(4), 793–796 (2008).
352. F. Thiele et al., "Cryogenic electro-optic polarisation conversion in titanium in-diffused lithium niobate waveguides," *Opt. Express* **28**(20), 28961–28968 (2020).
353. G. Chen et al., "Bandwidth improvement for germanium photodetector using wire bonding technology," *Opt. Express* **23**(20), 25700–25706 (2015).
354. G. Chen et al., "Integration of high-speed GaAs metal-semiconductor-metal photodetectors by means of transfer printing for 850 nm wavelength photonic interposers," *Opt. Express* **26**(5), 6351–6359 (2018).
355. K. Luke et al., "Wafer-scale low-loss lithium niobate photonic integrated circuits," *Opt. Express* **28**(17), 24452–24458 (2020).
356. R. Safian et al., "Foundry-compatible thin-film lithium niobate electro-optic modulators," *Proc. SPIE* **11283**, 112832F (2020).
357. A. Y. Piggott et al., "Inverse design and demonstration of a compact and broadband on-chip wavelength demultiplexer," *Nat. Photonics* **9**(6), 374–377 (2015).
358. S. Molesky et al., "Inverse design in nanophotonics," *Nat. Photonics* **12**(11), 659–670 (2018).
359. Y. Shen et al., "Deep learning with coherent nanophotonic circuits," *Nat. Photonics* **11**(7), 441–446 (2017).
360. X. Chen et al., "Single-wavelength and single-photodiode 700 Gb/s entropy-loaded PS-256-QAM and 200-GBaud PS-PAM-16 transmission over 10-km SMF," in *Eur. Conf. Opt. Commun.* (2020).
361. O. Alibart et al., "Quantum photonics at telecom wavelengths based on lithium niobate waveguides," *J. Opt.* **18**(10), 104001 (2016).

Guanyu Chen received his PhD in optical engineering from Huazhong University of Science and Technology (HUST), China. During his PhD period, he was as a joint PhD student at Ghent University (UGent), Belgium, with a research focus on silicon photonics. After graduation, he worked as a research fellow at the National University of Singapore (NUS), Singapore, with a research focus on lithium niobate photonics. His current research interests include integrated photonics, high performance optoelectronic devices, and applications in quantum information science and engineering.

Nanxi Li is a scientist at Institute of Microelectronics (IME), A*STAR. He received his BE degree (first class honors) in electrical and electronic engineering from Nanyang Technological University in 2012. In 2013, he started his graduate study at Harvard University, where he received his MS degree in 2015 and his PhD in 2018, both in applied physics. His research interests include silicon photonics, MEMS-based chemical sensors, metasurfaces, and fiber optics.

Yu Yu received his PhD from HUST, Wuhan, China, in 2009. From 2009 to 2010, he was with the Centre for Photonic Systems, Department of Engineering, University of Cambridge, Cambridge, United Kingdom, as a research associate. He is currently with the Wuhan National Laboratory for Optoelectronics, HUST, as a professor. His research interests include integrated device and all-optical signal processing.

Aaron J. Danner is an associate professor at NUS, Singapore. He received his PhD in electrical engineering from the University of Illinois at Urbana-Champaign, USA. Before joining NUS, he was with Avago Technologies.

Biographies of the other authors are not available.

Research Article

ADVANCED PHOTONICS

Electro-optic tuning of a single-frequency ultranarrow linewidth microdisk laser

Jintian Lin,[a,b,†] Saeed Farajollahi,[c,†] Zhiwei Fang,[d,†] Ni Yao,[e,f] Renhong Gao,[a,b] Jianglin Guan,[d,g] Li Deng,[d,g] Tao Lu,[c,*] Min Wang,[d,g] Haisu Zhang,[d,g] Wei Fang,[f,h,*] Lingling Qiao,[a,b] and Ya Cheng[a,b,d,g,i,j,k,*]

[a]Chinese Academy of Sciences (CAS), Shanghai Institute of Optics and Fine Mechanics (SIOM), State Key Laboratory of High Field Laser Physics and CAS Center for Excellence in Ultra-Intense Laser Science, Shanghai, China
[b]University of Chinese Academy of Sciences, Center of Materials Science and Optoelectronics Engineering, Beijing, China
[c]University of Victoria, Department of Electrical and Computer Engineering, Victoria, British Columbia, Canada
[d]East China Normal University, School of Physics and Electronic Science, XXL—The Extreme Optoelectromechanics Laboratory, Shanghai, China
[e]Research Center for Intelligent Sensing, Zhejiang Lab, Hangzhou, China
[f]Zhejiang University, College of Optical Science and Engineering, The Interdisciplinary Center for Quantum Information, State Key Laboratory of Modern Optical Instrumentation, Hangzhou, China
[g]East China Normal University, State Key Laboratory of Precision Spectroscopy, Shanghai, China
[h]Jiaxing Institute of Zhejiang University, Intelligent Optics & Photonics Research Center, Jiaxing, China
[i]Shanxi University, Collaborative Innovation Center of Extreme Optics, Taiyuan, China
[j]Shandong Normal University, Collaborative Innovation Center of Light Manipulations and Applications, Jinan, China
[k]Shanghai Research Center for Quantum Sciences, Shanghai, China

Abstract. Single-frequency ultranarrow linewidth on-chip microlasers with a fast wavelength tunability play a game-changing role in a broad spectrum of applications ranging from coherent communication, light detection and ranging, to metrology and sensing. Design and fabrication of such light sources remain a challenge due to the difficulties in making a laser cavity that has an ultrahigh optical quality (Q) factor and supports only a single lasing frequency simultaneously. Here, we demonstrate a unique single-frequency ultranarrow linewidth lasing mechanism on an erbium ion-doped lithium niobate (LN) microdisk through simultaneous excitation of high-Q polygon modes at both pump and laser wavelengths. As the polygon modes are sparse within the optical gain bandwidth compared with the whispering gallery mode counterpart, while their Q factors (above 10 million) are even higher due to the significantly reduced scattering on their propagation paths, single-frequency lasing with a linewidth as narrow as 322 Hz is observed. The measured linewidth is three orders of magnitude narrower than the previous record in on-chip LN microlasers. Finally, enabled by the strong linear electro-optic effect of LN, real-time electro-optical tuning of the microlaser with a high tuning efficiency of ~50 pm/100 V is demonstrated.

Keywords: lasers; lithium niobate; microcavities; integrated optics.

Received Nov. 23, 2021; revised manuscript received Feb. 24, 2022; accepted for publication Mar. 30, 2022; published online May 3, 2022.

[DOI: 10.1117/1.AP.4.3.036001]

1 Introduction

Broad transparency window and high piezoelectric, acousto-optic, second-order nonlinear, and electro-optic (EO) coefficients characterize crystalline lithium niobate (LN) as the "silicon in photonics."[1–7] Recent breakthroughs in the nanofabrication technology on thin-film LN platforms[4] gave birth to a variety of integrated photonic devices such as high-performance EO modulators,[8,9] broadband optical frequency combs,[10–12] and high efficiency frequency converters.[13–15] To build a monolithic integrated photonic system on an LN chip, the capacity of microlaser

*Address all correspondence to Tao Lu, taolu@ece.uvic.ca; Wei Fang, wfang08@zju.edu.cn; Ya Cheng, ya.cheng@siom.ac.cn.

†These authors contributed equally to the work.

fabrication on this platform is essential. The high EO coefficient of LN ensures that such lasers outperform all other on-chip counterparts in broad range and real-time wavelength tunability. However, similar to silicon, LN itself does not provide optical gain for lasing. Therefore, to functionalize LN, doping of the gain medium is necessary. In particular, to make lasers operating at widely needed telecom wavelengths, the erbium ion (Er^{3+}) is a favorable choice of dopant.[16–22] More importantly, to enable many applications and outperform silicon counterparts, such lasers should operate at a single frequency with an ultranarrow linewidth and fast wavelength tunability.[23–27] According to the Schawlow–Townes theory, the laser fundamental linewidth is quadratic inversely proportional to the undoped cavity Q factor.[28–30] Therefore, increasing the Q factor will quadratically reduce the linewidth of a microlaser. The highest Q factors demonstrated to date are those of whispering gallery mode (WGM) microcavities where light confinement is achieved by continuous total internal reflection at the smooth resonator periphery.[31] However, the dense WGMs within the optical gain bandwidth would easily lead to multifrequency lasing in a microcavity. To reduce the number of modes, attempts have been made to reduce the microcavity size,[23] which inevitably increases the radiation loss and decreases the mode volume, leading to a reduction of both the Q factor and optical gain in the microcavity. Consequently, the pump threshold increases while the laser power remains low.

The polygon-shaped modes in large LN microdisks have demonstrated high Q factors due to reduced scattering losses on their propagation paths.[32] In this work, by exciting polygon modes and avoiding the dense WGMs, we demonstrated single-frequency lasing in large Er^{3+}-doped LN microdisks with an ultranarrow linewidth. EO tuning of the laser wavelength was realized with a high linear tuning efficiency of 50 pm/100 V.

2 Construction of the Microlaser

2.1 Active Microdisk Fabrication

The fabrication process of the microdisk begins from the preparation of an Er^{3+}-doped Z-cut LN thin-film wafer by ion slicing. The doping concentration of Er^{3+} is 1% (mole fraction). The fabrication flow of the microdisk resonators mainly consists of four steps. First, a chromium (Cr) thin layer was coated on the LN thin-film wafer and then patterned into microdisks using femtosecond laser micromachining. The removal of the Cr thin film with a high spatial resolution was achieved by femtosecond laser ablation. Second, the microdisk pattern was transferred from the Cr layer to the LN thin film via chemo-mechanical polishing. Third, the microelectrodes were fabricated on the Cr layer again using the space-selective femtosecond laser ablation. Finally, the silica layer underneath the LN disk was partially undercut to form the supporting pedestals for supporting the LN thin-film microdisks. The details of the fabrication can be found in Refs. 17 and 33. An optical micrograph of the fabricated microdisk integrated with electrodes is shown in the inset of Fig. 1 (bottom right). The distance between the microelectrodes is 35 μm. The zoom-in scanning electron microscope (SEM) image of the fabricated microcavity without microelectrodes is also shown in the inset of Fig. 1 (bottom middle), which consists of an Er^{3+}-doped LN microdisk with a thickness of 700 nm and a diameter ~29.8 μm, indicating an ultrasmooth surface. The microdisk is supported by a thin silica pedestal (with a diameter of ~8 μm) on the LN substrate. The principal dielectric axes x, y of LN are illustrated in the inset of Fig. 1.

2.2 Experimental Setup

The experimental setup is illustrated in Fig. 1. A narrow-linewidth tunable diode laser (Model: TLB-6719, New Focus, Inc.)

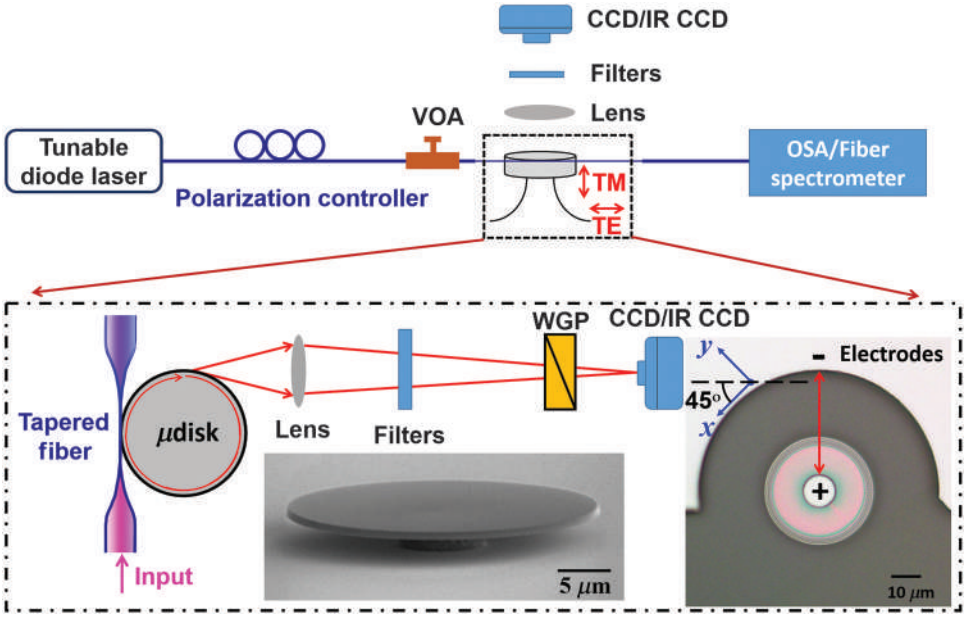

Fig. 1 The experimental setup for lasing and polarization measurement. A variable optical attenuator (VOA) was used to tune the input power into the Z-cut microdisk. TM and TE represent transverse magnetic and transverse electric polarization states, respectively. Inset: SEM image of the microdisk (without electrodes) and optical micrograph of the microdisk integrated with Cr electrodes.

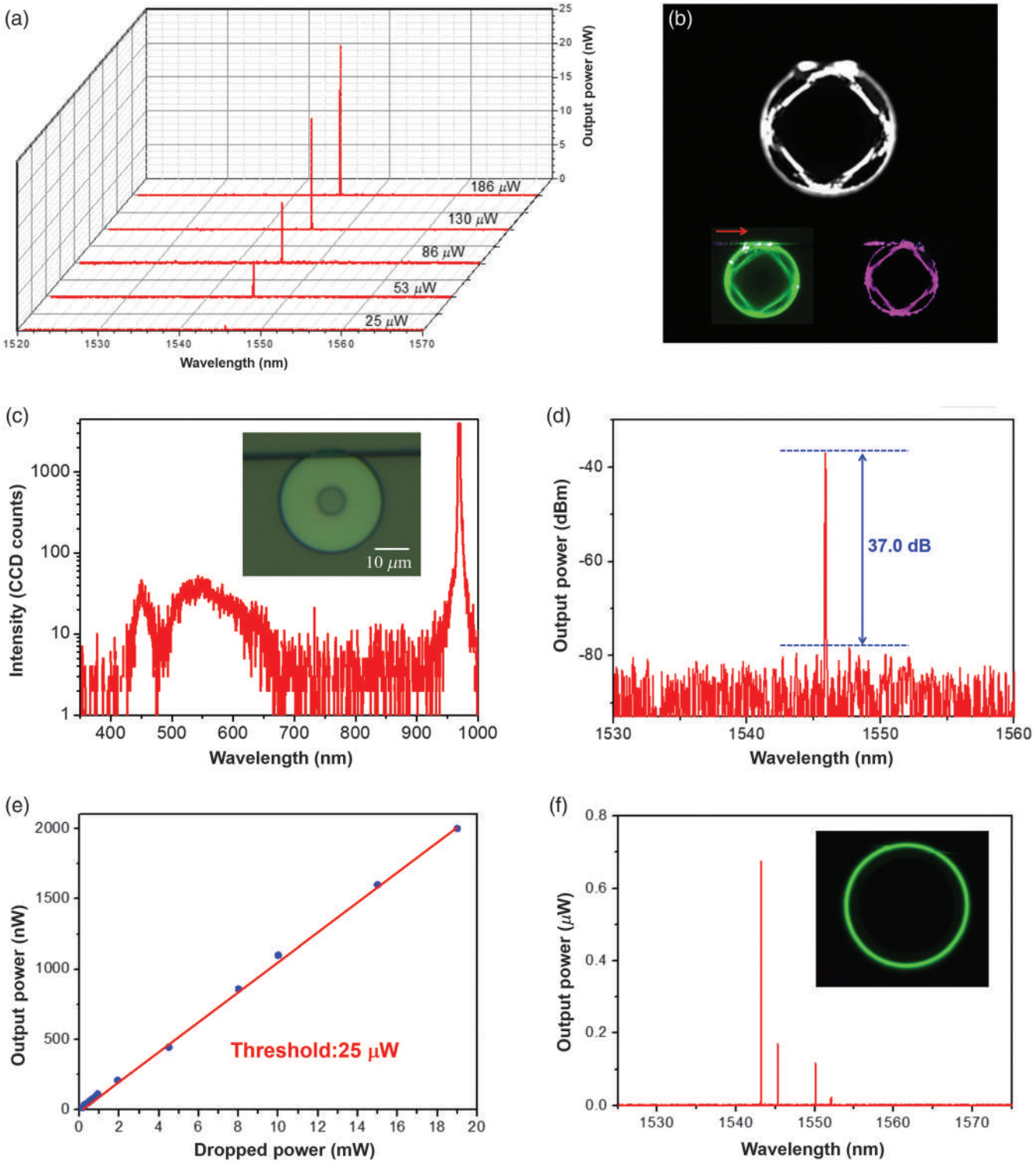

Fig. 2 (a) Spectra of the microlaser output powers at different pump power levels. (b) The optical micrograph of the square lasing mode at 1546-nm wavelength. Inset: the optical micrographs of the square modes of the upconversion fluorescence around the 550-nm wavelength (left) and the pump light (right). (c) Spectrum of the upconversion fluorescence and the pump light. Inset: optical micrograph of the tapered fiber coupled with the microdisk. (d) Spectrum of lasing. (e) Laser output power versus pump power dropped to the cavity shows a pump threshold of 25 μW. (f) Spectrum of multiple-mode lasing when pumping with a WGM at 971.5-nm wavelength. Inset: the optical micrograph of the upconversion fluorescence, showing a circular pattern along the disk periphery.

was used as the pump light source, and the pump laser wavelength was tuned to be resonant with a specific transverse electric (TE) polarized cavity mode around 968 nm. The laser was coupled to the microdisk via a tapered fiber with a waist size of 2 μm. The position between the tapered fiber and the microdisk was adjusted by a three-dimensional (3D) piezo stage with a 20-nm resolution. An optical imaging system consisting of a microscope objective lens with a numerical aperture (NA) of 0.42, long-pass filters (Thorlabs, Inc., Model: FELH1100), and an infrared (IR) charge-coupled device (CCD) was used to monitor the coupling system from the top and capture the intensity profile of the lasing modes around 1550-nm wavelength. To capture the intensity profiles of the pump mode and upconversion fluorescence signal in the microdisk, a visible CCD and a set of long-pass filters and short-pass filters (Thorlabs, Inc., Model: FEL800 and FES800) were used to take the place of the IR CCD and long-pass filters in the optical micrograph system for blocking the upconversion fluorescence, and combination of the pump light and the lasing signal, respectively. The generated emission from the microdisk was coupled out by the same tapered fiber and sent into either an optical spectrum analyzer (OSA for short, YOKOGAWA, Inc., Model AQ6370D, detection range: 600 to 1700 nm) or a fiber spectrometer [Ocean Optics, Inc., Model USB2000+ (VIS-NIR), detection range: 350 to 1000 nm] for spectral analysis. Meanwhile, the polarization states of the pump and lasing modes were checked via a precalibrated wire grating polarizer (WGP) by collecting the signals scattered from the edge of the microdisk. The resolutions of the OSA and the spectrometer were set as 0.01 and 1.5 nm, respectively.

2.3 Polygon Mode Formation

When the relative position between the tapered fiber and the center of the microdisk was adjusted to 13.37 μm [inset in Fig. 2(c)], the single-mode laser peaking at 1546-nm wavelength was observed in TE polarization, as shown in Fig. 2(a). The IR CCD captured the top view of the lasing mode in Fig. 2(b), which displays a square pattern in the microdisk. The large overlap between the lasing mode pattern and those of the pump mode at 968 nm and the upconversion fluorescence at ~550-nm wavelengths [shown in Fig. 2(b)], ensures that conventional high-density WGMs circulating around the circumference of the disk cannot be efficiently excited. The relatively large free spectral range (FSR) of 11.5 nm facilitates single-mode lasing within the gain bandwidth of Er^{3+}. Figure 2(d) confirms that the laser exhibits a side mode suppression ratio of 37.0 dB. The output power of the laser signal as a function of the pump power is plotted in Fig. 2(e), indicating a lasing threshold of merely ~25 μW. The maximum output power of the microlaser was measured as 2 μW (i.e., −27.0 dBm) when the dropped pump power was 20 mW. For comparison, we also pumped the microdisk to exhibit a conventional WGM at the pump laser wavelength of 971.5 nm, giving rise to the multiple-mode lasing shown in Fig. 2(f).

2.4 Mode Structure Measurements

In principle, WGMs feature ultrahigh Q factors based on the nature of total internal reflection. In reality, however, these modes suffer from the inevitable surface roughness introduced during fabrication, as their optical pathways overlap with the

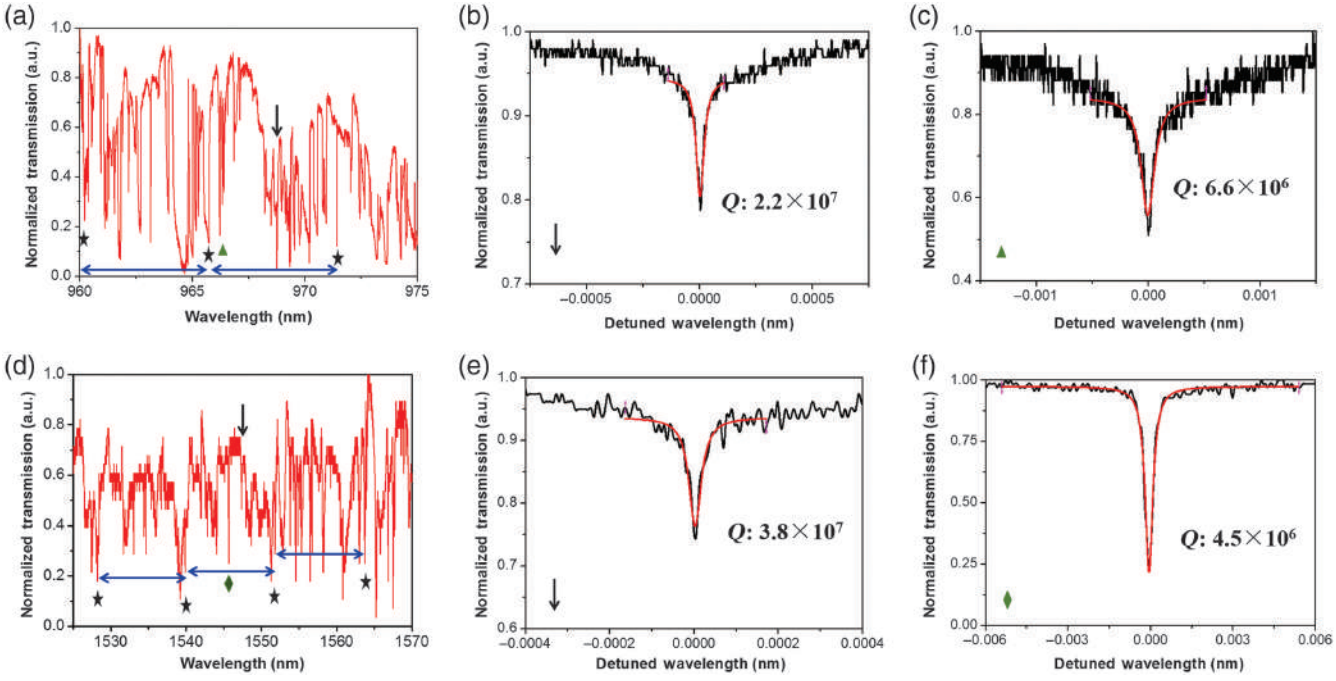

Fig. 3 Transmission spectra of the tapered fiber coupled with the microdisk. (a) Transmission spectrum around the pump wavelength, where each blue line segment with two arrows indicates an FSR. (b) The Q factor of the pump mode. (c) The measured highest Q factor of the conventional WGM [indicated with a green triangle in (a)] within one FSR. (d) Spectrum around the lasing wavelength. (e) The Q factor of the lasing mode. (f) The measured highest Q factor of the conventional WGM [indicated with a green rhombus in (d)] within one FSR.

periphery of the cavity. The polygon modes have their main propagation paths away from the boundary yet preserve the total internal reflection condition at the bouncing points. Thus, polygon modes can have competitively high Q factors over those of WGMs. This was proved experimentally based on an undoped microdisk that had the same geometry as the microlaser. Figures 3(a) and 3(d) show the transmission spectra around 968 and 1546 nm when two tunable diode lasers (Model: TLB-6719 & 6728, New Focus, Inc.) with an output power of 5 μW were used to investigate the modes at the pump and lasing wavelength range. The tapered fiber was placed at the same location as the microlaser experiment, so that polygon modes were excited in both wavelength regions. The loaded Q factors of polygon modes at 968- and 1546-nm wavelength [Figs. 3(b) and 3(e)] were both measured to be above 10^7, about one order of magnitude higher than that of conventional WGMs in the vicinity [Figs. 3(c) and 3(f)].

2.5 Linewidth Characterization

With such a high Q factor, a laser based on the polygon mode can have an ultranarrow linewidth based on the relationship between the laser linewidth and the Q factor of an undoped cavity.[32] As shown in Fig. 4(a), we measured the linewidth by heterodyning two independently pumped single-mode microlasers.[34] Since the two microdisks have the same diameter, a relative lasing frequency difference of ~1 MHz can be achieved by adjusting the pump powers.[16–19,22] The two laser signals were photo-mixed with a 3-dB optical directional coupler and converted to electrical signals with a balanced photodetector for spectral analysis in the radio frequency (RF) domain, as illustrated in Fig. 4(a). Here, a polarization controller was used at the output of one of the microlasers to ensure the two laser signals were of the same polarization state when photo-mixing. The Lorentzian-shaped power spectrum of the beat note signal was captured by a real-time spectrum analyzer (RSA for short, Tektronix RSA5126B) with a resolution bandwidth of ~1 Hz. Figure 4(b) shows the RF spectrum around 1 MHz when the output powers of both microlasers were ~2 μW. The full width at half maximum of the detected signal was measured as 643 Hz. Accordingly, the linewidth of the microlaser was 322 Hz, assuming that the microdisks were identical. The power spectral density of the frequency noise was also recorded by the spectrum analyzer in the phase noise analysis mode, as shown in

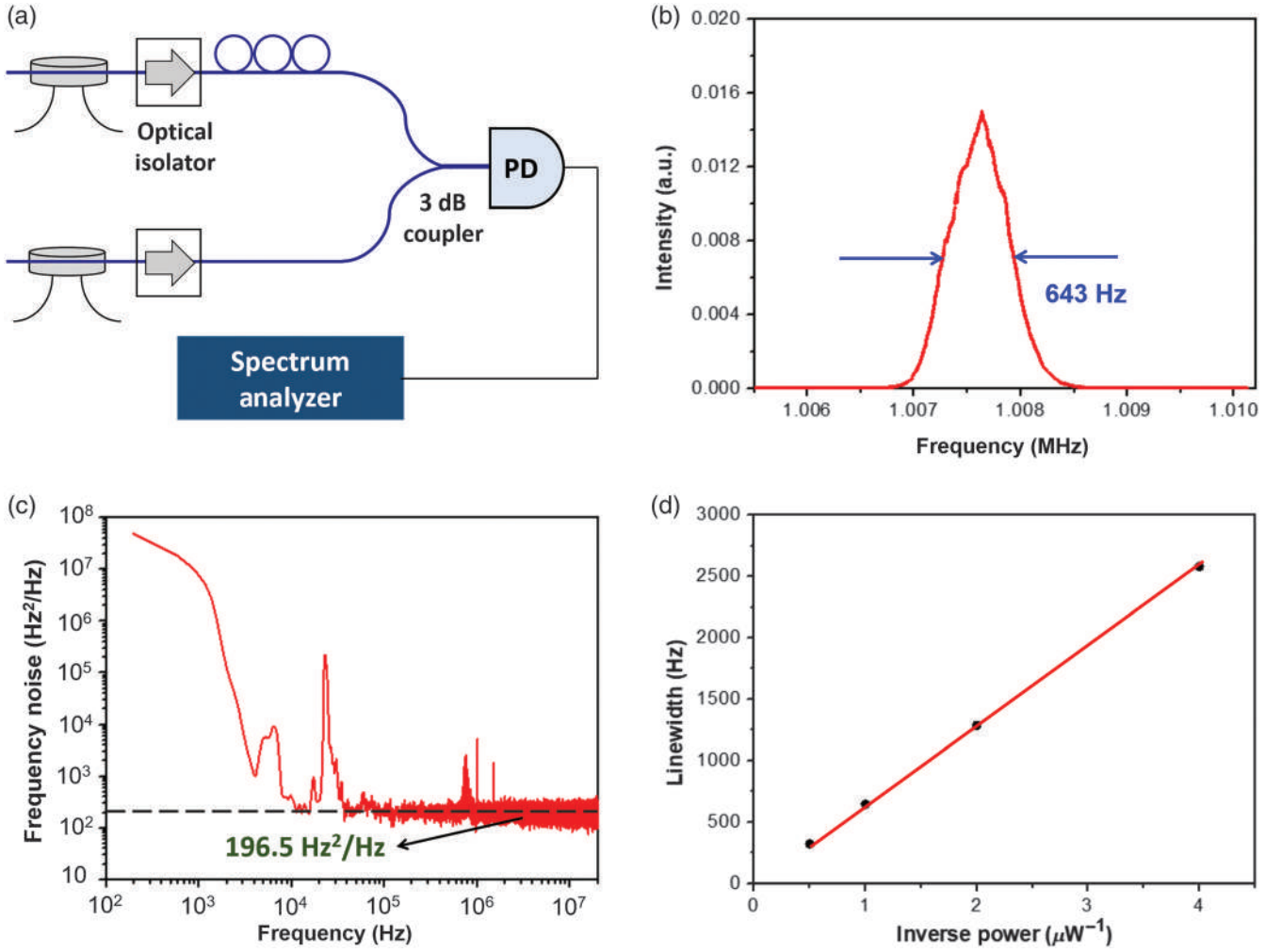

Fig. 4 Linewidth measurement. (a) The experimental setup. (b) The spectrum of the detected beating signal for an output power of 2 μW. (c) The measured frequency noise. (d) The linewidth is a function of the output power of the microlaser.

Fig. 4(c). At the high-frequency range (>0.5 MHz), the frequency noise is almost flat around 196.5 Hz^2/Hz, indicating a linewidth of 309 Hz, which is consistent with the result shown in Fig. 4(b). The linewidth of the microlaser as a function of the output power was further characterized. The inverse linear dependence of the linewidth versus output power agrees well with the Schawlow–Townes formula,[28–30] suggesting our microlaser linewidth is quantum noise limited. The measured linewidth is three orders of magnitude narrower than the previous record in on-chip LN microlasers.[16–22] In addition, the tuning of the microlaser as a function of the pump power in the MHz range can be resolved from the beat note signal captured by the RSA, which has been provided in the Supplementary Material. Here, the tuning efficiency agrees well with the results measured by the OSA.

2.6 Real-Time Wavelength Tuning

For the sake of application, the ability of wavelength tuning is usually required, especially for lasers with an ultranarrow linewidth. The wavelength of an LN microlaser can be tuned via temperature or pump power control.[16–19,22] The pump power tuning based on the combined significant photorefractive and thermo-optic effect is a spontaneous yet limited way.[22,35,36] As shown in Figs. 5(a) and 5(b), when the pump power dropped to the cavity increased from 1.92 to 20.00 mW, the laser wavelength shifted from 1545.633 to 1545.866 nm, corresponding to a wavelength tuning rate of 12.3 pm/mW (i.e., 1.54 MHz/μW). To achieve a fast wavelength tuning, the EO-based mechanism is the more favorable way, enabled by the strong linear EO effect of LN.[4] To introduce a refractive index change in the microdisk via the EO effect, a bias was applied between the circular microelectrode on the microdisk and the plane electrode integrated into the LN-on-insulator (LNOI) surface using two metal probes. The microelectrode integrated on the microdisk possesses a radius of 5 μm, as shown in the inset of Fig. 1. The electric potential and the electric field distribution are plotted in Figs. 5(c) and 5(d), respectively. The electric field distributed in the microdisk is mainly oriented in the radial direction. When the applied voltage was 1 V, the electric field strength was $\sim 2.08 \times 10^4$ V/m in the mode volume. Here, the EO coefficient r_{22} (6.8 pm/V) was utilized, and the details of the electrode design can be found in the Supplementary Material.[37,38] Figures 5(e) and 5(f) show the EO performance of the microlaser. When the voltage was tuned from −300 to 300 V, the lasing wavelength was redshifted from 1545.716 to 1546.017 nm, indicating a high linear tuning efficiency of 50 pm/100 V, which roughly agrees with the theoretically calculated value of 80 pm/100 V.[37] To access the largest EO coefficient r_{33} (30.9 pm/V), an X-cut LNOI substrate and TE polarized modes should be utilized. External wires can be directly integrated on the chip using air-bridge wiring[37] in future work.

3 Numerical Modeling

The underlying physics behind the polygon modes can be further explained by performing a 2D finite element simulation using COMSOL. In our simulation, the extraordinary and ordinary refractive indices of LN used in the simulation are $n_e = 2.1622$ and $n_o = 2.2393$ for the pump wavelength and $n_e = 2.1361$ and $n_o = 2.2113$ for the laser wavelength.[39] To provide sufficient perturbation for polygon modes, a tapered fiber is placed on top of the disk and we use the effective index method to compute the effective refractive index of the fiber-disk overlap

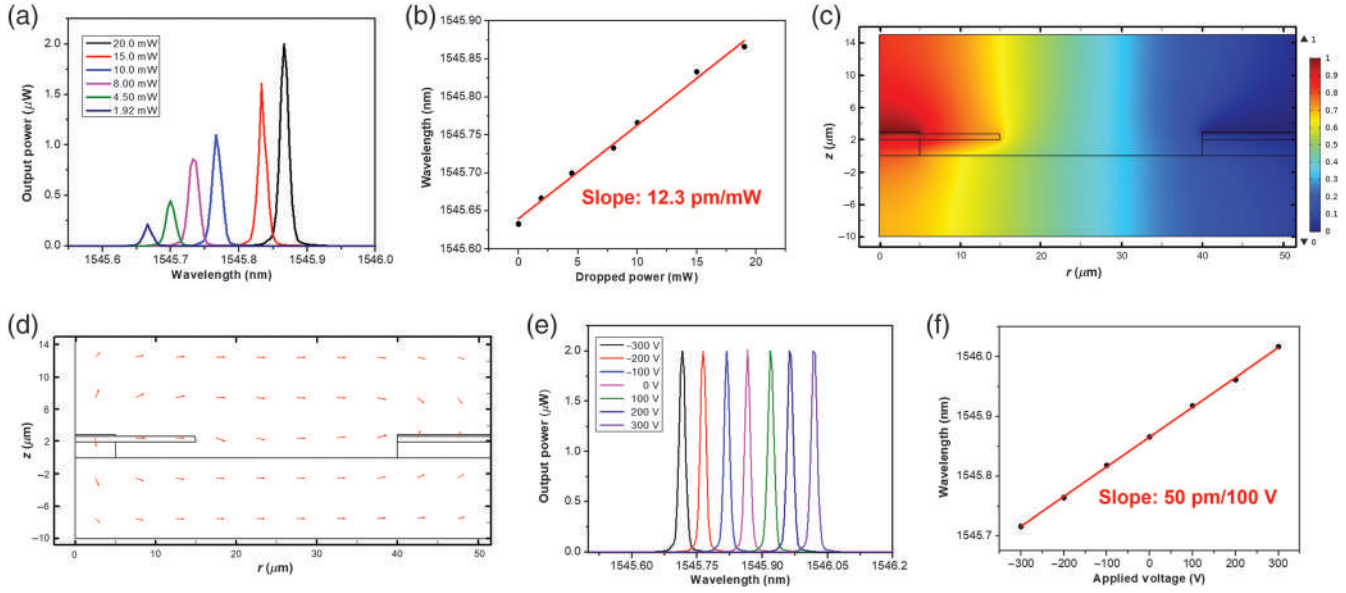

Fig. 5 (a) Lasing wavelength drift with different pump powers. (b) Lasing wavelength versus pump power. The linear fitting (red curve) shows a slope of 12.3 pm/mW. Distributions of (c) the scalar electric potential and (d) the vectorial electric field in the microdisk. The arrows denoting the vectorial electric field have a length proportional to the logarithm of the electric field magnitude. The material layers from top to bottom were Cr, LN, silica, and LN, respectively. (e) Lasing wavelength drift with the applied voltage. (f) Lasing wavelength versus applied voltage, showing a high tuning efficiency of 50 pm/100 V.

regime.[40,41] Figures 6(a) and 6(b) show the intensity profiles of the square mode and fundamental WGM at the pump wavelengths while Figs. 6(c), 6(f), and 6(i) display the square mode, fundamental, and high order WGMs, respectively. It is worth mentioning that within one FSR around each of the laser and pump wavelengths, multiple numbers of WGMs coexist but only the single square mode will appear due to the stringent requirement for polygon mode formation. We then compute the overlap factor Γ between different laser and pump modes defined by

$$\Gamma = \iiint \hat{I}_p \cdot \hat{I}_l \mathrm{d}v. \tag{1}$$

Here, $\hat{I}_p$ and $\hat{I}_l$ are normalized pump (I_p) and laser (I_l) intensities such that $\hat{I}_{p,l} = \frac{I_{p,l}}{\sqrt{\iiint I_{p,l}^2 \mathrm{d}v}}$ and $\iiint(\cdot)\mathrm{d}v$ is the volume integral over full space. The minimum pump threshold occurs when the laser and pump mode intensity overlap Γ is maximized, which can be found in the Supplementary Material.[42]

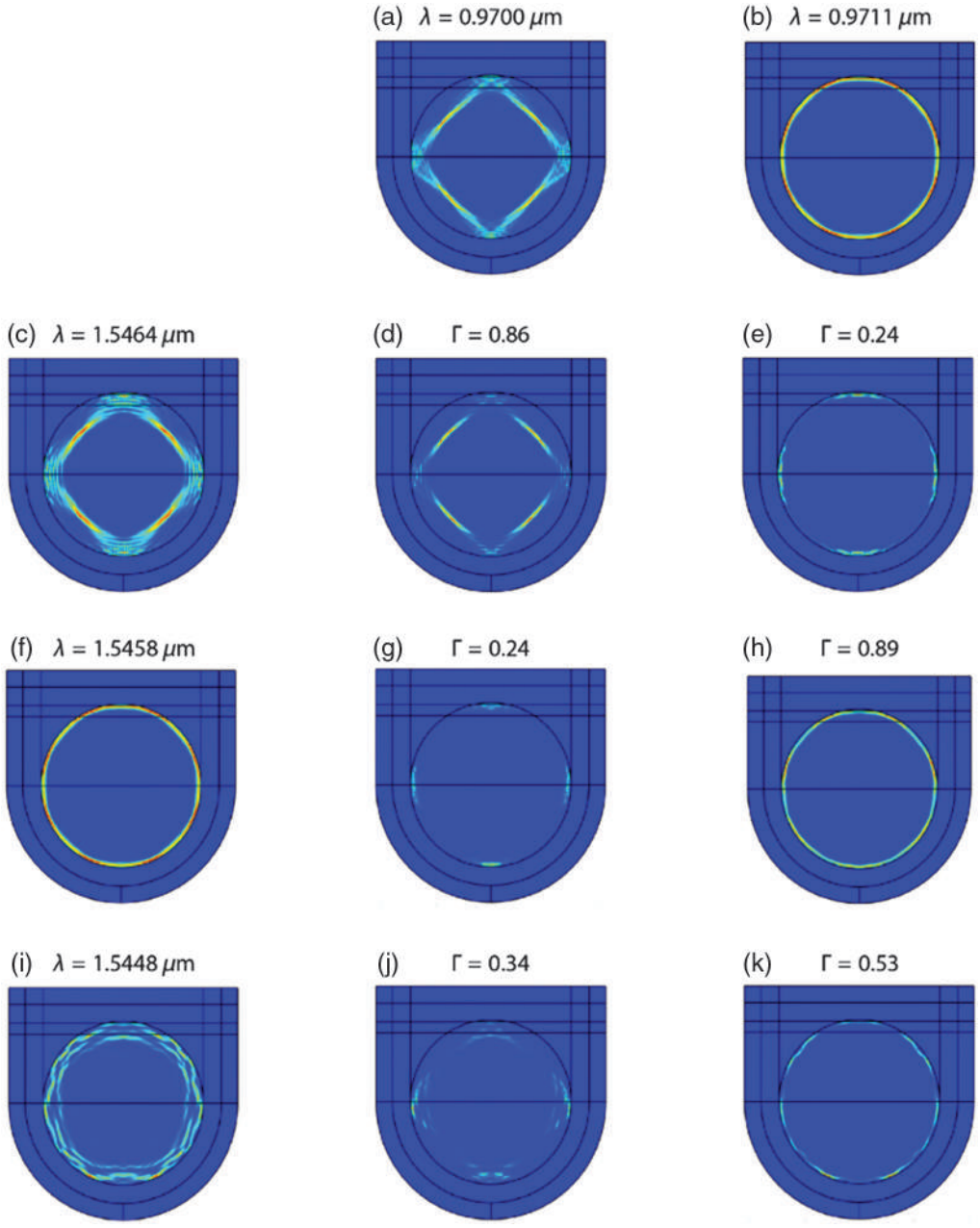

Fig. 6 The intensity distributions of (a) the square mode and (b) the fundamental WGM at the pump wavelengths. Left column: (c) the square mode, (f) the fundamental WGM, and (i) high order WGM at lasing wavelengths. (d)–(k) The intensity distributions of the integrand between each laser mode in the left column and either pump mode in the top row. Here, the larger overlap ($\Gamma = 0.53$) in (k) between the pump fundamental WGM and laser high-order WGM suggests that both the fundamental and high-order WGMs are likely to simultaneously lase, while in the case of being pumped by a square mode, the high-order WGM will not lase due to a lower overlap ($\Gamma = 0.34$).

The distributions of the integrand between different pump and laser modes are displayed in the rest of the subplots in Fig. 6. As shown, when the pump is in the square mode, its overlap factor with a square mode at the laser wavelength is $\Gamma = 0.86$ [Fig. 6(d)] while its overlap factor with the fundamental and high-order WGM can be as low as $\Gamma = 0.24$ [Fig. 6(g)] and $\Gamma = 0.34$ [Fig. 6(j)]. The significantly higher overlap coefficient ensures that only the square mode will have a sufficient optical gain for lasing. In addition, the FSR is larger than the gain bandwidth of Er^{3+}. Therefore, the square mode at neighboring FSRs will not be excited either due to lower gain. Consequently, single mode operation can be achieved when the polygon mode is formed at the pump wavelength. In contrast, when a regular WGM is formed by the pump, multiple WGMs within the gain bandwidth may lase simultaneously as the Γ of the laser and pump WGMs are close in value [e.g., the overlap between the pump fundamental WGM and high order laser mode can be as high as $\Gamma = 0.53$ (Fig. 6(k)]. Finally, it is also worth mentioning that the two-dimensional (2D) simulation will not allow the precise evaluation of the overall quality factor of the coupled cavity due to the unphysically large reflection incurred at the fiber-to-disk interfaces. The issue can be overcome with a full-wave 3D mode match method, which will be applied in future research.[40,41] Nevertheless, the 2D simulation results capture the essence of the polygon mode microlaser, which faithfully reproduces the main features of the observed microdisk laser mode as shown above.

4 Conclusions and Discussion

The formation of coherent polygon modes with ultrahigh Q factors has allowed for the realization of single-mode narrow-linewidth microlasers in single LN microdisks, which has significant implications for the miniaturization of optical systems in which highly coherent laser sources must be incorporated. To achieve a fully integrated EO tunable polygon mode microdisk laser, the suspended microdisk can be replaced with a microdisk sitting on the fused silica substrate to achieve better mechanical stability. A cladding layer of fused silica is then coated on the LNOI microdisk, which is flattened by polishing to support a coupling waveguide. Then, the fiber taper can be replaced with a waveguide lithographically fabricated on top of the fused silica cladding, and the polygon mode is formed by controlling the coupling location of the upper waveguide and lower LNOI microdisk, allowing for the construction of a fully integrated narrow-linewidth EO tunable polygon mode microdisk laser. Further exploration of the strong piezoelectric, acousto-optic, and second-order nonlinear properties of the LN will promote the performance and functionality of the single-mode microdisk laser in a straightforward manner without the necessity of heterogeneous integration.

Acknowledgments

T.L. and S.F. would like to acknowledge CMC Microsystems. The work was supported by the National Key R&D Program of China (2019YFA0705000), the National Natural Science Foundation of China (12192251, 62122079, 11734009, 62035013, 61635009, 62075192, 11874375, and 11874154), Shanghai Municipal Science and Technology Major Project (2019SHZDZX01), Science and Technology Commission of Shanghai Municipality (21DZ1101500), the Quantum Joint Funds of the Natural Foundation of Shandong Province (ZR2020LLZ007), the Fundamental Research Funds for the Central University, Nature Science and Engineering Research Council of Canada (NSERC) Discovery (RGPIN-2020-05938), and the Youth Innovation Promotion Association of Chinese Academy of Sciences (2020249). The authors declare no conflicts of interest related to this paper.

References

1. M. Kösters et al., "Optical cleaning of congruent lithium niobate crystals," *Nat. Photonics* **3**(9), 510–513 (2009).
2. Y. Kong et al., "Recent progress in lithium niobate: optical damage, defect simulation, and on-chip devices," *Adv. Mater.* **32**(3), 1806452 (2020).
3. A. Boes et al., "Status and potential of lithium niobate on insulator (LNOI) for photonic integrated circuits," *Laser Photonics Rev.* **12**(4), 1700256 (2018).
4. J. Lin et al., "Advances in on-chip photonic devices based on lithium niobate on insulator," *Photonics Res.* **8**(12), 1910–1936 (2020).
5. Y. Qi and Y. Li, "Integrated lithium niobate photonics," *Nanophotonics* **9**(6), 1287–1320 (2020).
6. Y. Jia, L. Wang, and F. Chen, "Ion-cut lithium niobate on insulator technology: recent advances and perspectives," *Appl. Phys. Rev.* **8**(1), 011307 (2021).
7. D. Zhu et al., "Integrated photonics on thin-film lithium niobate," *Adv. Opt. Photonics* **13**(2), 242–352 (2021).
8. M. Zhang et al., "Integrated lithium niobate electro-optic modulators: when performance meets scalability," *Optica* **8**(5), 652–667 (2021).
9. M. Xu et al., "High-performance coherent optical modulators based on thin-film lithium niobate platform," *Nat. Commun.* **11**(1), 3911 (2020).
10. C. Wang et al., "Monolithic lithium niobate photonic circuits for Kerr frequency comb generation and modulation," *Nat. Commun.* **10**(1), 978 (2019).
11. Y. He et al., "Self-starting bi-chromatic $LiNbO_3$ soliton microcomb," *Optica* **6**(9), 1138–1144 (2019).
12. Z. Gong et al., "Near-octave lithium niobate soliton microcomb," *Optica* **7**(10), 1275–1278 (2020).
13. J. Lin et al., "Broadband quasi-phase-matched harmonic generation in an on-chip monocrystalline lithium niobate microdisk resonator," *Phys. Rev. Lett.* **122**(17), 173903 (2019).
14. R. Luo et al., "Highly tunable efficient second-harmonic generation in a lithium niobate nanophotonic waveguide," *Optica* **5**(8), 1006–1011 (2018).
15. G.-T. Xue et al., "Ultrabright multiplexed energy-time-entangled photon generation from lithium niobate on insulator chip," *Phys. Rev. Appl.* **15**(6), 064059 (2021).
16. Y. Liu et al., "On-chip erbium-doped lithium niobate microcavity laser," *Sci. China Phys. Mech. Astron.* **64**(3), 234262 (2021).
17. Z. Wang et al., "On-chip tunable microdisk laser fabricated on Er^{3+}-doped lithium niobate on insulator," *Opt. Lett.* **46**(2), 380–383 (2021).
18. R. Gao et al., "On-chip ultra-narrow-linewidth single-mode microlaser on lithium niobate on insulator," *Opt. Lett.* **46**(13), 3131–3134 (2021).
19. Q. Luo et al., "On-chip erbium-doped lithium niobate microring lasers," *Opt. Lett.* **46**(13), 3275–3278 (2021).
20. T. Li et al., "A single-frequency single-resonator laser on erbium-doped lithium niobate on insulator," *APL Photonics* **6**(10), 101301 (2021).
21. R. Zhang et al., "Integrated lithium niobate single-mode lasers by the Vernier effect," *Sci. China Phys. Mech. Astron.* **64**(9), 294216 (2021).
22. Z. Xiao et al., "Single-frequency integrated laser on erbium-doped lithium niobate on insulator," *Opt. Lett.* **46**(17), 4128–4131 (2021).

23. T. Lu et al., "A narrow-linewidth on-chip toroid Raman laser," *IEEE J. Quantum Electron.* **47**(3), 320–326 (2011).
24. L. He et al., "Detecting single viruses and nanoparticles using whispering gallery microlasers," *Nat. Nanotechnol.* **6**(7), 428–432 (2011).
25. L. Feng et al., "Single-mode laser by parity-time symmetry breaking," *Science* **346**(6212), 972–975 (2014).
26. H. Rong et al., "A continuous-wave Raman silicon laser," *Nature* **433**(7027), 725–728 (2005).
27. T. Lu et al., "On-chip green silica upconversion microlaser," *Opt. Lett.* **34**(4), 482–484 (2009).
28. A. Schawlow and C. H. Townes, "Infrared and optical masers," *Phys. Rev.* **112**(6), 1940–1949 (1958).
29. C. H. Henry, "Theory of the linewidth of semiconductor lasers," *IEEE J. Quantum Electron.* **18**(2), 259–264 (1982).
30. P. Goldberg, P. W. Milonni, and B. Sundaram, "Theory of the fundamental laser linewidth," *Phys. Rev. A* **44**(3), 1969–1985 (1991).
31. K. J. Vahala, "Optical microcavities," *Nature* **424**(6950), 839–846 (2003).
32. Z. Fang et al., "Polygon coherent modes in a weakly perturbed whispering gallery microresonator for efficient second harmonic, optomechanical, and frequency comb generations," *Phys. Rev. Lett.* **125**(17), 173901 (2020).
33. R. Wu et al., "Lithium niobate microdisk resonators of quality factors above 107," *Opt. Lett.* **43**(17), 4116–4119 (2018).
34. D. Derickson, *Fiber Optic Test and Measurement*, Prentice Hall, Upper Saddle River, New Jersey (1998).
35. H. Jiang et al., "Fast response of photorefraction in lithium niobate microresonators," *Opt. Lett.* **42**(17), 3267–3270 (2017).
36. J. Wang et al., "Thermo-optic effects in on-chip lithium niobate microdisk resonators," *Opt. Express* **24**(19), 21869–21879 (2016).
37. T.-J. Wang et al., "On-chip optical microresonators with high electro-optic tuning efficiency," *J. Lightwave Technol.* **38**(7), 1851–1857 (2020).
38. A. Yariv and P. Yeh, *Photonics: Optical Electronics in Modern Communications*, 6th ed., Oxford University Press, New York (2007).
39. D. N. Nikogosyan, *Nonlinear Optical Crystals: A Complete Survey*, Springer, New York (2006).
40. X. Du, S. Vincent, and T. Lu, "Full-vectorial whispering-gallery-mode cavity analysis," *Opt. Express* **21**(19), 22012–22022 (2013).
41. X. Du et al., "Generalized full-vector multi-mode matching analysis of whispering gallery microcavities," *Opt. Express* **22**(11), 13507–13514 (2014).
42. A. Yariv, *Quantum Electronics*, 3rd ed., Wiley, New York (1991).

Jintian Lin is an associate professor at Shanghai Institute of Optics and Fine Mechanics, CAS. He received his BS degree in optical information science and technology from Sun Yat-sen University in 2009 and his PhD in optics from the University of Chinese Academy of Sciences in 2014. His current research interests include integrated optics, nonlinear optics, and micro/nano-processing.

Biographies of the other authors are not available.

Research Article

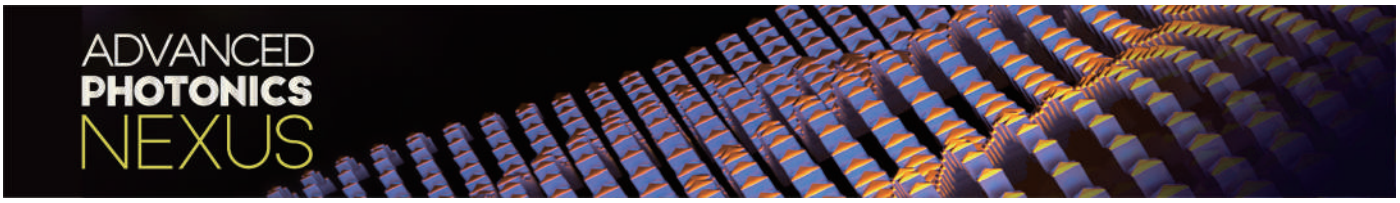

Ultra-broadband and low-loss edge coupler for highly efficient second harmonic generation in thin-film lithium niobate

Xiaoyue Liu,[a] Shengqian Gao,[a] Chi Zhang,[b] Ying Pan,[a] Rui Ma,[a] Xian Zhang,[a] Lin Liu,[a] Zhenda Xie,[b] Shining Zhu,[b] Siyuan Yu,[a] and Xinlun Cai[a,*]

[a]Sun Yat-sen University, School of Electronics and Information Technology, State Key Laboratory of Optoelectronic Materials and Technologies, Guangzhou, China

[b]Nanjing University, College of Electronic Science and Engineering, School of Physics, Nanjing, China

Abstract. Thin-film lithium niobate is a promising material platform for integrated nonlinear photonics, due to its high refractive index contrast with the excellent optical properties. However, the high refractive index contrast and correspondingly small mode field diameter limit the attainable coupling between the waveguide and fiber. In second harmonic generation processes, lack of efficient fiber-chip coupling schemes covering both the fundamental and second harmonic wavelengths has greatly limited the overall efficiency. We design and fabricate an ultra-broadband tri-layer edge coupler with a high coupling efficiency. The coupler allows efficient coupling of 1 dB/facet at 1550 nm and 3 dB/facet at 775 nm. This enables us to achieve an ultrahigh overall second harmonic generation normalized efficiency (fiber-to-fiber) of 1027% W^{-1} cm^{-2} (on-chip second harmonic efficiency ~3256% W^{-1} cm^{-2}) in a 5-mm-long periodically-poled lithium niobate waveguide, which is two to three orders of magnitude higher than that in state-of-the-art devices.

Keywords: thin-film lithium niobate; ultrabroadband coupler; second harmonic generation.

Received May 26, 2022; accepted for publication May 30, 2022; published online Jun. 29, 2022.

[DOI: 10.1117/1.APN.1.1.016001]

1 Introduction

Lithium niobate is an ideal material for nonlinear photonics due to its exceptional nonlinear-optic properties, wide transparency range, and ferroelectric properties.[1,2] Periodically poled lithium niobate (PPLN) waveguides, where the periodic domain inversion allows for a quasi-phase-matched (QPM) second-order nonlinear [$\chi^{(2)}$] process, have been widely used in wavelength conversion,[3,4] optical parametric oscillation,[5–8] photon pair generation,[9–12] and supercontinuum generation.[13–15] As the strength of the nonlinear interaction is proportional to the optical intensity, the employment of high-contrast waveguides with strong optical confinement can greatly improve nonlinear optical efficiency. Unfortunately, the legacy PPLN waveguides are based on weakly confined waveguides with index contrasts of ~0.02, leading to low nonlinear interaction strengths. Therefore, the traditional PPLN device requires a long interaction length for high conversion efficiency, making it difficult for large-scale photonic integrated circuits. In recent years, thin-film lithium niobate (TFLN) has emerged as an attractive platform for compact and high-performance optical modulators[16–18] and $\chi^{(2)}$ nonlinear optical devices[19–24] due to the high refractive index contrast ($\Delta n \sim 0.7$) offered by TFLN waveguides. TFLN-based PPLN devices have been demonstrated that outperform their legacy counterparts in both nonlinear optical efficiency and device footprint.[25–28] For instance, the efficiency of second harmonic generation (SHG) has been improved over 20 times in TFLN-based PPLN devices.[26] However, TFLN-based PPLN devices face a major challenge of how to achieve efficient and broadband off-chip coupling. For example, in Ref. 29 an on-chip SHG conversion efficiency as high as 3757% W^{-1} cm^{-2} was achieved in a 5-mm PPLN waveguide, but the collected second harmonic (~780 nm) power is only several μW when the input pump (~1560 nm) power is nearly about 100 mW due to the lack of a well-designed coupling mechanism. For SHG, an ideal device requires an efficient coupling scheme

*Address all correspondence to Xinlun Cai, caixlun5@mail.sysu.edu.cn

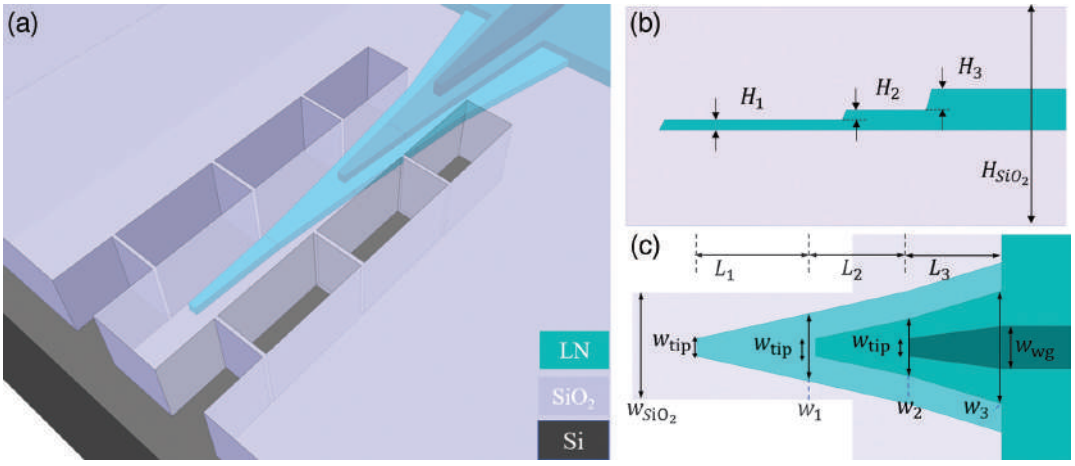

Fig. 1 (a) Three-dimensional structure schematic diagram of the coupler; (b) cross-sectional view and (c) top view of coupler.

for both the near-infrared (~1550 nm) and near-visible (~775 nm) bands. Recently, several off-chip coupling schemes based on an edge coupler have been demonstrated for efficient coupling at 1550 nm.[30–32] Nonetheless, an efficient edge coupler that can cover both near-infrared (~1550 nm) and near-visible (~775 nm) has not been reported yet.

In this paper, we propose and demonstrate an efficient and ultra-broadband edge coupler in an x-cut TFLN platform for the fundamental transverse electric (TE_{00}) mode by employing a low-index SiO_2 waveguide and a tri-layer TFLN waveguide taper structure. The measured off-chip coupling loss for 1550 and 775 nm is 1 and 3 dB/facet, respectively. In addition, we demonstrate a highly efficient SHG in a TFLN-based PPLN waveguide with this ultra-broadband edge coupler, exhibiting an ultra-high overall SHG normalized efficiency of 1027% $W^{-1}\,cm^{-2}$ and a corresponding on-chip efficiency of 3256% $W^{-1}\,cm^{-2}$, respectively.

2 Design and Simulation

The proposed edge coupler is based on an x-cut TFLN platform (from NANOLN) with 360-nm lithium niobate and 2-μm SiO_2 on silicon (Si) substrate. As illustrated schematically in Fig. 1(a), the coupler consists of a suspended SiO_2 waveguide, and a tri-layer spot size converter (SSC) including top-, middle-, and bottom-layer tapers. The light from lensed fiber is first coupled into SiO_2 waveguide, and then transferred to the TFLN rib waveguides through the SSC. The TFLN rib waveguides have a top width of 1.2 μm, a slab thickness of 180 nm, and a rib height of 180 nm. A cross sectional view of the coupler is depicted in Fig. 1(b), where H_1, H_2, and H_3 represent the thickness of the bottom-, middle-, and top-layer of the SSC, respectively. Figure 1(c) shows the top-view of the SSC, in which L_i, w_i ($i = 1, 2, 3$), and w_{tip} denote the lengths, widths, and tip width of tapers. We note here that the w_{tip} is usually larger than 80 nm, which is limited by the fabrication process.

We select 1550 and 775 nm as the target wavelengths for designing the SiO_2 waveguide and the TFLN SSC. First, we calculate the mode overlap between the SiO_2 waveguide and lensed fiber to optimize the size of the SiO_2 waveguide. The mode field diameters of lensed single-mode optical fibers are set to be 3.5 μm at 1550 nm and 2.5 μm at 775 nm, respectively. As shown in Fig. 2(a), the size of the SiO_2 waveguide is set to be 4 μm × 4 μm to ensure a mode overlap efficiency of >95% for both wavelengths. Secondly, we carefully designed the SSC, especially the thickness and the tip-width of the bottom layer, to achieve adiabatic mode transition from SiO_2 waveguide to the TFLN rib waveguide. We calculated the coupling loss between the SiO_2 waveguide and LN bottom layer as functions of the tip-width at both 775 nm [Fig. 2(b)] and 1550 nm [Fig. 2(c)]. These results are obtained by eigenmode expansion (EME) method by setting a sufficiently long length of LN bottom taper. In Fig. 2(b), for a thickness $H_1 > 120$ nm, the coupling loss between the SiO_2 waveguide and LN bottom layer is more than 2 dB at 775 nm if the tip-width is larger than 80 nm. This reveals that a double layer SSC with a bottom layer thicknesses of 180 nm cannot achieve an efficient coupling for 775-nm light. Thus, we adopt a TFLN SSC with tri-layer structure. The tip width of the tri-layer structure is 100 nm, and the thicknesses of bottom-, middle-, and top-layer are set as 90, 90, and 180 nm, respectively. With this bottom tip size, the minimum coupling loss from the SiO_2 waveguide to the LN bottom layer can be <0.5 dB at both wavelengths. Additionally, we simulated the lengths of the SSC by EME solver. As shown in Figs. 2(d)–2(f), the taper lengths were designed to be $L_1 \sim 200$ μm, $L_2 \sim 100$ μm, and $L_3 \sim 100$ μm to allow a sufficient mode transfer. All the other parameters of the SSC are given in Table 1.

Figure 3(a) shows the transverse electric (TE_{00}) mode field distribution of 1550 and 775 nm at different cross-sections of the designed edge coupler. We can see that the mode fields of both wavelengths are first well-confined in the SiO_2 waveguide [labeled I in Fig. 3(a)]. Subsequently, the 775- and 1550-nm wavelength light is coupled to the TFLN rib waveguide via the bottom-, middle-, and top-layer of SSC. Figures 3(b) and 3(c) show the snapshot of the mode evolution process at both wavelengths. A simulated coupling loss of 0.5 dB/facet at 1550 nm and 1 dB/facet at 775 nm is obtained for TE_{00} mode after optimization, while that for the transverse magnetic (TM_{00}) mode is more than 3 and 7 dB/facet at the two wavelengths, showing a polarization dependence of the designed coupler. This is advantageous for nonlinear frequency conversion based on x-cut TFLN platform, where the TE_{00} mode is usually used to exploit the maximum nonlinear coefficient d_{33} of lithium niobate.

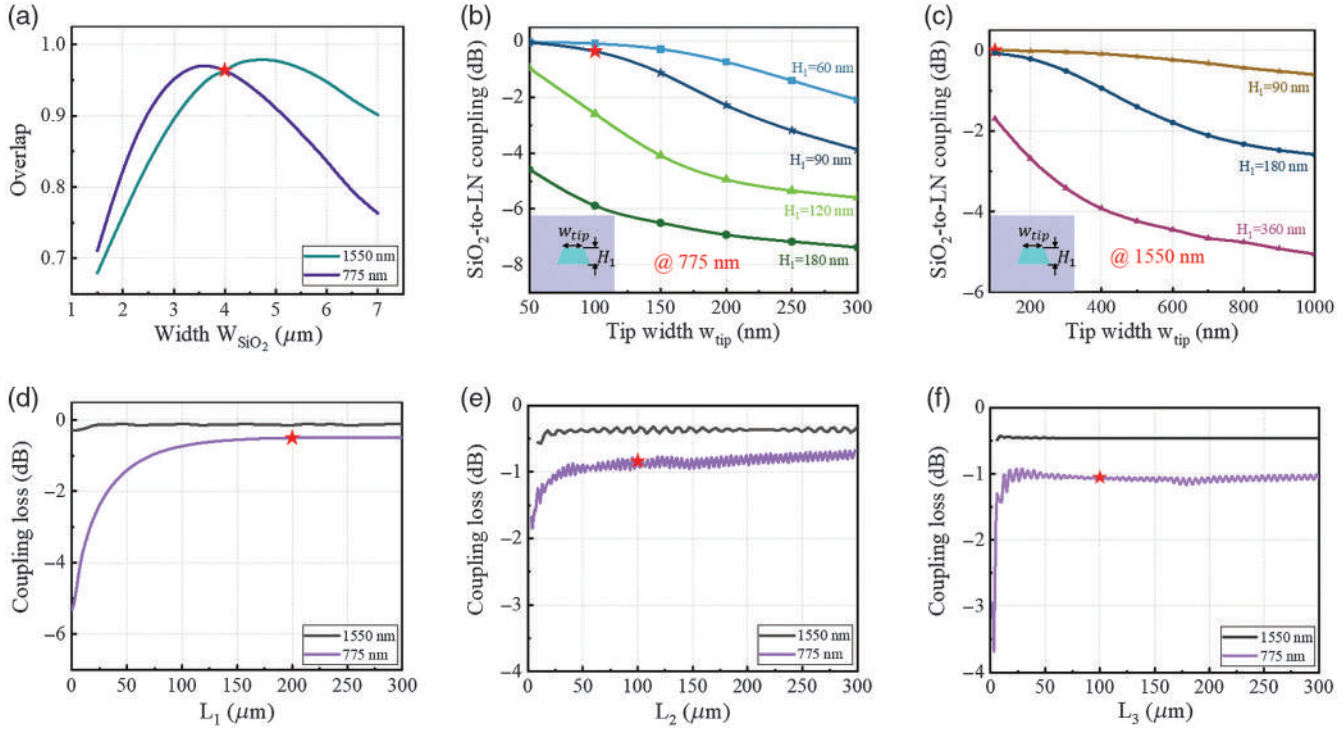

Fig. 2 (a) The simulated overlap between the lensed fiber mode and the SiO_2 waveguide mode at 1550 and 775 nm under different waveguide widths. Coupling loss from the SiO_2 waveguide to the LN bottom layer at (b) 775 nm and (c) 1550 nm with different bottom dimensions (inset: dimensional parameters of the bottom cone). The simulated curves of coupling lengths (d) L_1, (e) L_2, and (f) L_3 at 1550 and 775 nm. The red stars represent the designed parameter values of the coupler.

Table 1 Parameters of the designed coupler.

Parameter	Value (μm)	Parameter	Value (μm)	Parameter	Value (μm)
MFD for 1550 nm/775 nm	3.5/2.5	H_3	0.18	w_{wg}	1.2
H_{SiO_2}	4	w_{tip}	0.1	L_1	200
W_{SiO_2}	4	w_1	1.5	L_2	100
H_1	0.09	w_2	1.5	L_3	100
H_2	0.09	w_3	4	—	—

For comparison, we calculated the coupling efficiencies of the proposed edge coupler with tri-layer SSC and the traditional coupler with double layer SSC, respectively. As illustrated in Figs. 4(a) and 4(b), these simulated results clearly show that the present edge coupler with tri-layer SSC (the solid curves) features ultra-broadband operation covering both 1550- and 775-nm bands, while the edge coupler with double layer SSC (the dotted curves) only works well in the 1550-nm band.

3 Fabrication

The device fabrication process is as follows. First, the rib waveguides and the top layer of SSC are defined with HSQ resist by electron-beam lithography (EBL), and transferred to TFLN by using Ar ion in inductively coupled plasma (ICP) system. The etching depth of waveguide is 180 nm. Then, the middle- and bottom-layers of the SCC are prepared by EBL, photolithography, and ICP etching. Figures 5(a), 5(b), and 5(c) show the scanning electron microscope (SEM) pictures of the tips of the bottom-, middle-, and top-layer, respectively. After the fabrication of the SSC, a 2-μm-thick SiO_2 is deposited by plasma-enhanced chemical vapor deposition. The SiO_2 waveguides with supporting arms are patterned by photolithography and etched by CHF_3/Ar chemistry. Finally, the underlying silicon substrate is removed by two-step etching processes. An isotropic etching with SF_6 is first utilized to suspend the SiO_2 waveguide, while a Bosch deep silicon anisotropic dry etch process with SF_6/C_4F_8 is used to expose the coupling interface between optical fiber and chip. A smooth sidewall and coupling interface are observed in the SEM pictures in Figs. 5(d) and 5(e).

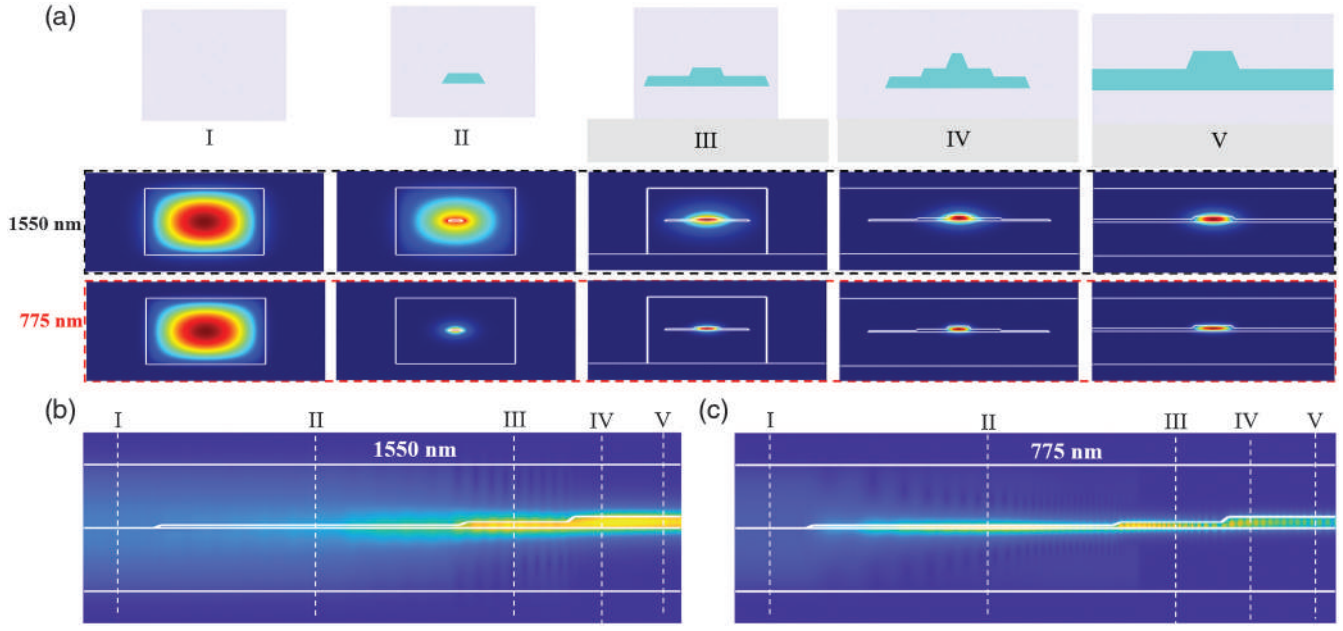

Fig. 3 (a) The simulated distribution of TE_{00} mode of 1550 and 775 nm at different cross sections I, II, III, IV, and V; simulated mode propagation in the designed coupler at wavelengths (b) 1550 nm and (c) 775 nm.

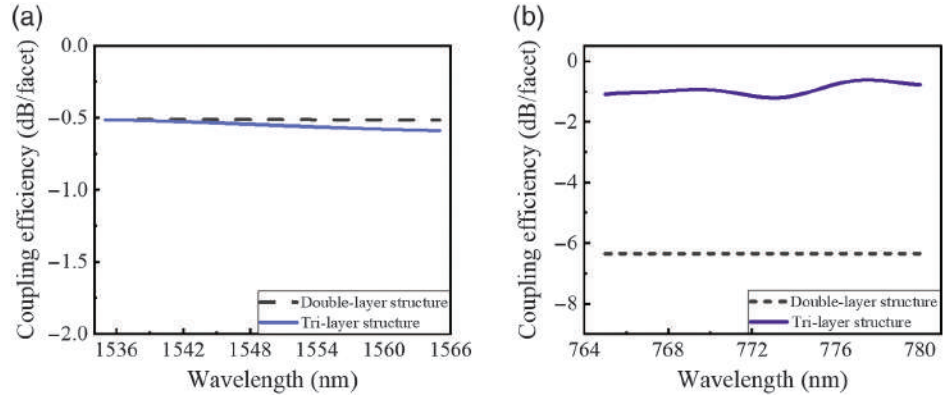

Fig. 4 The simulated coupling efficiency of double-layer structure and tri-layer structure at (a) 1550- and (b) 775-nm band.

4 Results and discussions

4.1 Coupling Efficiency Characterization

The coupling efficiency of the edge coupler is characterized by several 5-mm-long reference waveguides. The propagation losses of the waveguides are 0.3 dB/cm at 1550 nm and 0.5 dB/cm at 775 nm. Two lensed fibers and a fiber polarization controller (FPC) are applied for TE_{00} mode coupling. We measured the coupling transmission spectra at near-infrared band (1535 to 1565 nm) and near-visible band (765 to 780 nm). Figures 6(a) and 6(b) show the mean values of coupling losses for the TE_{00} mode and its standard deviation over six devices on the same wafer. The mean coupling losses are 1 dB/facet at 1550 nm and ~3 dB/facet at 775 nm, respectively. The measured results show lower coupling efficiency than the simulated one, which is predominately originated from the scattering losses of the multi-layer structure and propagation loss of SiO_2 waveguide with supporting arm which are estimated to less than 0.5 dB at 1550 nm and 0.25 dB at 775 nm according to 3D FDTD simulation.

4.2 Second Harmonic Generation

We also fabricate 5-mm-long PPLN waveguides along with designed edge coupler for SHG. The width and thickness of the PPLN waveguide is designed as 1.2 μm and 180 nm. According to the QPM condition $\Lambda = \frac{\lambda_{\text{pump}}}{2(n_{\text{SH}} - n_{\text{pump}})}$, we obtained the poling period for type-0 scheme by simulating the TE_{00} mode effective indexes at second harmonic (~775 nm) and pump (~1550 nm) wavelength. Taking fabrication error into consideration, several PPLN waveguides with poling periods ranging from 3.10 to 3.18 μm in 10-nm steps are prepared in experiment. The

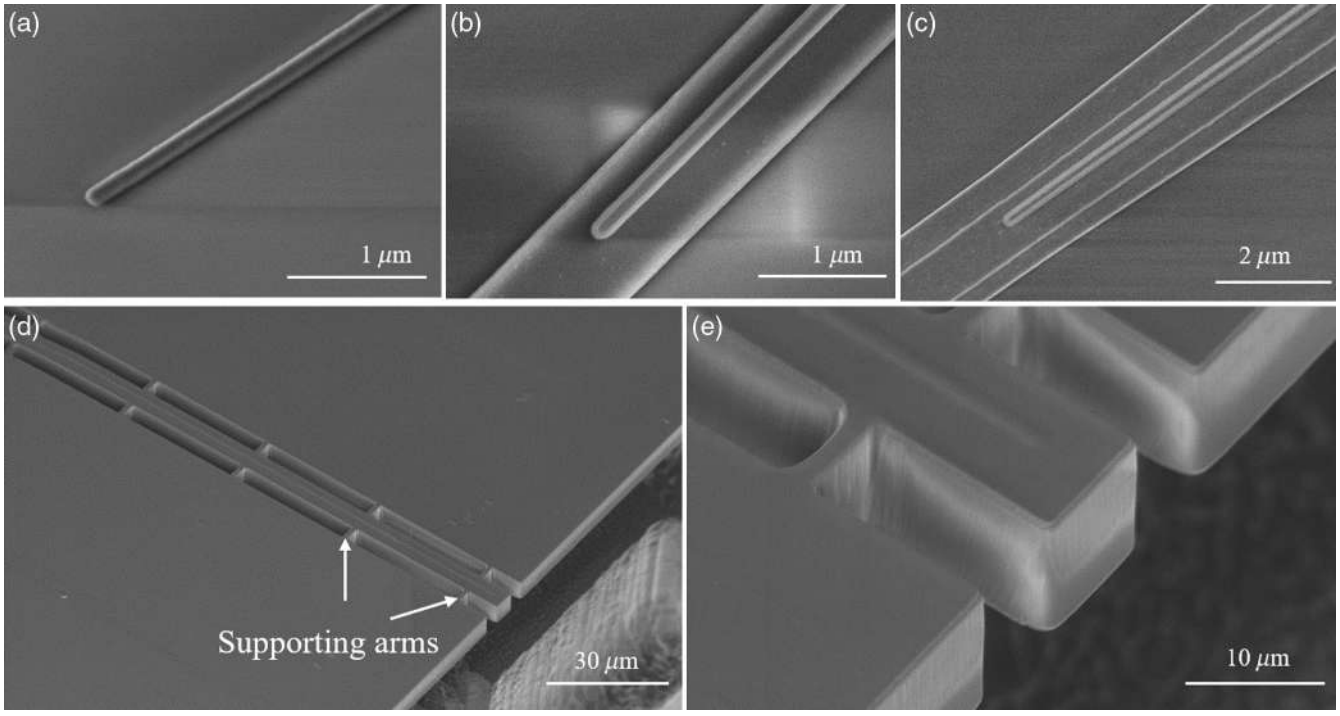

Fig. 5 SEM pictures of (a) bottom tip, (b) middle tip, and (c) top tip. (d) SEM picture and (e) larger view of suspended SiO_2 waveguide.

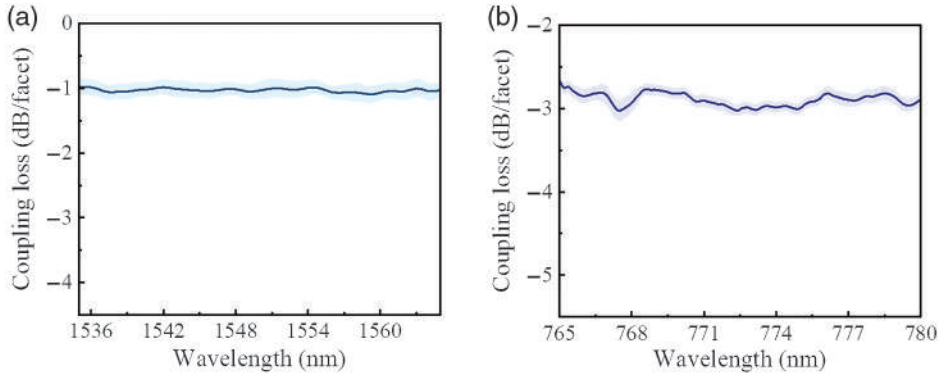

Fig. 6 The coupling losses of the fabricated edge couplers at (a) 1535 to 1565 nm and (b) 765 to 780 nm. Shadowed areas show the standard deviation measured over six devices.

periodic poling process can be divided into two steps.[21] First, the comb-shaped electrodes consisting of 30-nm NiCr and 40-nm Au were deposited on the *x*-cut TFLN before the fabrication of waveguide. Then several high-voltage pulses about 300 V were applied, and the period domains were checked via SHG imaging technique using confocal microscope to optimize the pulse duration time and the number of pulses. Figure 7(a) shows the period domain observed by SHG-confocal microscope imaging, which shows the domain-inverted region with duty cycle close to 50:50 (red frame).

The experimental setup for SHG is shown in Fig. 7(b). The pump light from a C-band tunable laser is adjusted to TE_{00} via an FPC, and subsequently coupled from the lensed fiber into the PPLN waveguide utilizing the edge coupler. The generated second harmonic signal is coupled out from the chip by a second lensed fiber and finally monitored with a Si photodiode power sensor or an optical spectrum analyzer (OSA). We first investigate the SHG spectral profile of the PPLN waveguide by scanning the pump wavelength. As depicted in Fig. 7(c), the main QPM peak is centered at 1563.1 nm with a full width at half-maximum bandwidth of 1.5 nm. By fixing the pump wavelength at 1563.1 nm and gradually increasing the pump power, we obtain the quadratic power dependence of the second harmonic wave on the pump light [see Fig. 7(d)] and a slope of 814% W^{-1} is extracted by linearly fitting the experimental data. The normalized efficiency is calculated to be 3256% $W^{-1}\,cm^{-2}$, which is 70% of the theoretical efficiency (~4600% $W^{-1}\,cm^{-2}$).[33] The lower maximum efficiency is mainly caused by the inhomogeneity of the thin-film thickness over the 5-mm waveguide length.[34,35] We define an overall normalized efficiency

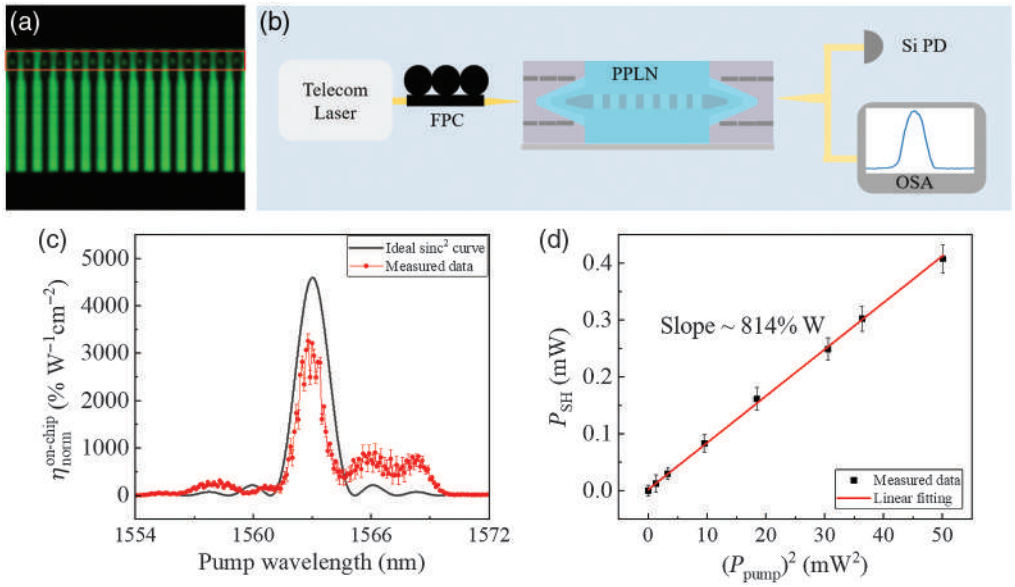

Fig. 7 (a) Period domain observed by SHG-confocal microscope imaging; red frame is the domain-inverted region. (b) Experimental setup for SHG. FPC, fiber polarization controller; OSA, optical spectrum analyzer. (c) Measured normalized SHG conversion efficiency versus pump wavelengths. (d) Quadratic power dependence of the SH wave on the pump wave.

Table 2 A comparison with other SHG works based on periodically poled TFLN waveguides.

Ref.	Length (mm)	$\eta_{on\text{-}cp}$ (% W^{-1} cm^{-2})	$\eta_{overall}$ (% W^{-1} cm^{-2})	Pump/SH coupling loss (dB/facet)
21	6	3061	3[a]	10/10
24	0.6	4600	57.5[a]	6/7
26	4	2600	2.6[a]	10/10
29	5	3757	9.65[a]	6.7/12.5
This work	5	3256	1027	1/3

[a]The value was calculated according to the data in reference.

by dividing the collected second harmonic power by the square of the input pump light and the square of the poled waveguide length. By taking account of the off-chip coupling efficiency $k_{pump} \sim 80\%$ (1 dB per facet) at 1563.1 nm and $k_{SH} \sim 50\%$ (3 dB per facet) at 781.55 nm, the overall normalized efficiency is counted to be 1027% W^{-1} cm^{-2} according to formula of $\eta_{on\text{-}chip} = \frac{\eta_{overall}}{k_{SH} \cdot k_{pump}^2}$.

5 Conclusions

We implement an edge coupler featuring low coupling loss and ultra-broad bandwidth. The off-chip efficiency at 755 and 1550 nm is 3 and 1 dB/facet, respectively. The experimental coupling efficiency of the coupler in the near-visible light band is 3 dB higher than the simulated efficiency of the traditional two-layer structure. Based on this designed coupling scheme, we acquire an ultrahigh overall SHG normalized efficiency of 1027% W^{-1} cm^{-2} in a 5-mm-long PPLN waveguide, corresponding to a high on-chip SHG normalized efficiency of 3256% W^{-1} cm^{-2}. Compared with the state-of-the-art (Table 2), the overall conversion efficiency of the present PPLN devices is increased by two to three orders of magnitude, benefitting from the improvement of coupling efficiency at the pump light and second harmonic wave. This high-efficiency and ultra-broadband edge coupler greatly reduces the power consumption in the process of nonlinear frequency conversion, showcasing obvious advantages in practical nonlinear applications.

Acknowledgments

This research is sponsored by the National Key R&D Program of China (Grant No. 2019YFA0705000) and the National Natural Science Foundation of China (Grant Nos. 11690031 and 11761131001). The authors declare no conflicts of interest.

References

1. V. Gopalan et al., "Defect-domain wall interactions in trigonal ferroelectrics," *Annu. Rev. Mater. Res.* **37**(1), 449–489 (2007).
2. R. S. Weis et al., "Lithium niobate: summary of physical properties and crystal structure," *Appl. Phys. A* **37**(4), 191–203 (1985).
3. J. Zhang et al., "Flexible wavelength conversion via cascaded second order nonlinearity using broadband SHG in MgO-doped PPLN," *Opt. Express* **16**(10), 6957–6962 (2008).

4. M. Gong et al., "All optical wavelength broadcast based on simultaneous type I QPM broadband SFG and SHG in MgO:PPLN," *Opt. Lett.* **35**(16), 2672–2674 (2010).
5. A. V. Okishev et al., "Intracavity-pumped Raman laser action in a mid-IR, continuous-wave (CW) MgO:PPLN optical parametric oscillator," *Opt. Express* **14**(25), 12169–12173 (2006).
6. I.-H. Bae et al., "Low-threshold singly-resonant continuous-wave optical parametric oscillator based on MgO-doped PPLN," *Appl. Phys. B* **103**(2), 311–319 (2011).
7. T. Wang et al., "Electro-optically spectrum switchable, multi-wavelength optical parametric oscillators based on aperiodically poled lithium niobate," *Opt. Lett.* **45**(20), 5848–5851 (2020).
8. J. Lu et al., "Ultralow-threshold thin-film lithium niobate optical parametric oscillator," *Optica* **8**(4), 539–544 (2021).
9. S. Tanzilli et al., "PPLN waveguide for quantum communication," *Eur. Phys. J. D* **18**(2), 155–160 (2002).
10. X. Lu et al., "Chip-integrated visible–telecom entangled photon pair source for quantum communication," *Nature Physics* **15**(4), 373–381 (2019).
11. B. S. Elkus et al., "Generation of broadband correlated photon-pairs in short thin-film lithium-niobate waveguides," *Opt. Express* **27**(26), 38521–38531 (2019).
12. J. Zhao et al., "High quality entangled photon pair generation in periodically poled thin-film lithium niobate waveguides," *Phys. Rev. Lett.* **124**(16), 163603 (2020).
13. C. R. Phillips et al., "Supercontinuum generation in quasi-phase-matched $LiNbO_3$ waveguide pumped by a Tm-doped fiber laser system," *Opt. Lett.* **36**(19), 3912–3914 (2011).
14. M. Yu et al., "Coherent two-octave-spanning supercontinuum generation in lithium-niobate waveguides," *Opt. Lett.* **44**(5), 1222–1225 (2019).
15. J. Lu et al., "Octave-spanning supercontinuum generation in nano-scale lithium niobate waveguides," *Opt. Lett.* **44**(6), 1492–1495 (2019).
16. C. Wang et al., "Nanophotonic lithium niobate electro-optic modulators," *Opt. Express* **26**(2), 1547–1555 (2018).
17. C. Wang et al., "Monolithic lithium niobate photonic circuits for Kerr frequency comb generation and modulation," *Nat. Commun.* **10**, 978 (2019).
18. M. He et al., "High-performance hybrid silicon and lithium niobate Mach–Zehnder modulators for 100 Gbit s^{-1} and beyond," *Nat. Photonics* **13**(5), 359–364 (2019).
19. M. Xu et al., "High-performance coherent optical modulators based on thin-film lithium niobate platform," *Nat. Commun.* **11**, 3911 (2020).
20. J. -Y. Chen et al., "Ultra-efficient frequency conversion in quasi-phase-matched lithium niobate microrings," *Optica* **6**(9), 1244–1245 (2019).
21. Y. Niu et al., "Optimizing the efficiency of a periodically poled LNOI waveguide using *in situ* monitoring of the ferroelectric domains," *Appl. Phys. Lett.* **116**(10), 101104 (2020).
22. J. Lu et al., "Periodically poled thin-film lithium niobite microring resonators with a second-harmonic generation efficiency of 250,000%/W," *Optica* **6**(12), 1455–1460 (2019).
23. G. -T. Xue et al., "Ultrabright multiplexed energy-time-entangled photon generation from lithium niobate on insulator chip, *"Phys. Rev. Appl*. **15**(6), 064059 (2021).
24. A. Rao et al., "Actively-monitored periodic-poling in thin-film lithium niobate photonic waveguides with ultrahigh nonlinear conversion efficiency of 4600 % $W^{-1}cm^{-2}$," *Opt. Express* **27**(18), 25920–25930 (2019).
25. D. Zhu et al., "Integrated photonics on thin-film lithium niobate," *Adv. Opt. Photonics* **13**(2), 242–352 (2021).
26. C. Wang et al., "Ultrahigh-efficiency wavelength conversion in nanophotonic periodically poled lithium niobate waveguides," *Optica* **5**(11), 1438–1441 (2018).
27. X. Liu et al., "Highly efficient thermo-optic tunable micro-ring resonator based on an LNOI platform," *Opt. Lett.* **45**(22), 6318–6321 (2020).
28. R. Gao et al., "Lithium niobate microring with ultra-high Q factor above 10^8," *Chin. Opt. Lett.* **20**(1), 011902 (2022).
29. J. Zhao et al., "Shallow-etched thin-film lithium niobate waveguides for highly-efficient second-harmonic generation," *Opt. Express* **28**(13), 19669–19682 (2020).
30. L. He et al., "Low-loss fiber-to-chip interface for lithium niobate photonic integrated circuits," *Opt. Lett.* **44**(9), 2314–2317 (2019).
31. C. Hu et al., "High-efficient coupler for thin-film lithium niobate waveguide devices," *Opt. Express* **29**(4), 5397–5406 (2021).
32. Y. Pan et al., "Low-loss edge-coupling thin-film lithium niobate modulator with an efficient phase shifter," *Opt. Lett.* **46**(6), 1478–1481 (2021).
33. L. Chang et al., "Thin film wavelength converters for photonic integrated circuits," *Optica* **3**, 531–535 (2016).
34. X.-H. Tian et al., "Effect of dimension variation for second-harmonic generation in lithium niobate on insulator waveguide," *Chin. Opt. Lett.* **19**(6), 060015 (2021).
35. M. Santandrea et al., "Characterisation of fabrication inhomogeneities in $Ti:LiNbO_3$ waveguides," *New J. Phys.* **21**, 123005 (2019).

Biographies of the authors are not available.